



HAL
open science

Characterization of winding insulation of electrical machines fed by voltage waves with high dV/dt

Veronika Gavrilenko

► **To cite this version:**

Veronika Gavrilenko. Characterization of winding insulation of electrical machines fed by voltage waves with high dV/dt . Other. Université Paris-Saclay; Université polytechnique de Tomsk (Russie), 2020. English. NNT: 2020UPAST027 . tel-03102553

HAL Id: tel-03102553

<https://theses.hal.science/tel-03102553>

Submitted on 7 Jan 2021

HAL is a multi-disciplinary open access archive for the deposit and dissemination of scientific research documents, whether they are published or not. The documents may come from teaching and research institutions in France or abroad, or from public or private research centers.

L'archive ouverte pluridisciplinaire **HAL**, est destinée au dépôt et à la diffusion de documents scientifiques de niveau recherche, publiés ou non, émanant des établissements d'enseignement et de recherche français ou étrangers, des laboratoires publics ou privés.

Characterization of winding insulation of electrical machines fed by voltage waves with high dV/dt

Thèse de doctorat de l'université Paris-Saclay et de l'Université Polytechnique de Tomsk

École doctorale n° 575, Electrical, Optical, Bio- physics and Engineering (EOBE)

Spécialité de doctorat : Génie électrique

Unité de recherche : Université Paris-Saclay, ENS Paris-Saclay, CNRS, SATIE, 91190,

Gif-sur-Yvette, France

Référent : ENS Paris-Saclay

Thèse présentée et soutenue en visioconférence totale le 2 décembre 2020, par

Veronika GAVRILENKO

Composition du Jury

Emmanuel ODIC Professeur, CentraleSupélec (GEEPS)	Président
Daniel ROGER Professeur, Université d'Artois (LSEE)	Rapporteur & Examineur
Oleg NOS Professor, Novosibirsk State Technical University - Russia	Rapporteur & Examineur
Gilbert TEYSSEBRE Professeur, Université Paul Sabatier (LAPLACE)	Examineur
Talgat GAZIZOV Associate Professor, Tomsk State University of Control Systems and Radioelectronics - Russia	Examineur
Stéphane LEFEBVRE Professeur des universités, CNAM Paris (SATIE)	Directeur de thèse
Andrey LEONOV Associate Professor, Tomsk Polytechnic University - Russia	Co-Directeur de thèse
Sami HLIOUI Maître de conférences, CNAM Paris (SATIE)	Co-Directeur de thèse

Université Paris-Saclay

Espace Technologique / Immeuble Discovery

Route de l'Orme aux Merisiers RD 128 / 91190 Saint-Aubin, France

Acknowledgements

I would like to express my gratitude to my committee chair, Professor Emmanuel Odic, who presided the thesis defence conducted via video conference and should adapt to these unusual circumstances.

I would like to thank my committee members, Professor Daniel Roger, Professor Oleg Nos, for examining thoroughly my manuscript, and the rest of the committee, Professor Gilbert Teysedre and Associate Professor Talgat Gazizov, for fruitful discussions during the dissertation defence.

It is with the immense gratitude that I acknowledge my research supervisors, Andrey Leonov, Stéphane Lefebvre and Sami Hlioui. Thank you for your support and encouragement, for your guidance, patience, persistent help in both scientific and administrative issues that have been indispensable for the realization of my Ph.D.

I wish to thank my Russian colleagues from the Tomsk Polytechnic University, Andrey Bukharkin, Stanislav Kolesnikov and Tatiana Soldatenko, for your presence, advices and helping hand when I was in Tomsk. I would like to give special gratitude to Boris Ubiyennykh to sharing your immense knowledge, enthusiasm and creativity.

I have had the great pleasure of working with my French colleagues from the SATIE. I am grateful to Yoann Pascal for your patience and help. Many thanks also go to my other colleagues, Mahamat Chabakata, Shuangfeng Zhang, Salim Asfirane, Matthieu Landel,...

I am very grateful to Sophie ABRIET for your support and help with administrative problems quickly and efficiently.

I would like to thank Adrien Dittrick, Tatiana Babicheva and Ekaterina Katia for being my friends and encouraging me from the beginning of my thesis.

Last but not the least, I would like to acknowledge with gratitude, the support and love of my family. My sincere gratitude goes to my boyfriend, Guillaume Valentin, for your love and faith in me, for being by my side, caring about me. Thank you for keep me moving forward.

Résumé détaillé en français

Résumé de thèse intitulée : **Caractérisation des isolants de bobinage des machines électriques alimentées par des ondes de tension à forts dV/dt**

La présente thèse est le fruit d'une collaboration entre l'Université Polytechnique de Tomsk (TPU), en Russie, et l'Université Paris-Saclay, en France. Dans le cadre d'une convention de cotutelle internationale, les travaux de recherche et la formation complémentaire ont été menés au laboratoire Systèmes et Applications des Technologies de l'Information et de l'Énergie (SATIE) de l'ENS Paris-Saclay - France et de la division Power and Electrical Engineering de la TPU - Russie.

L'étude expérimentale et les simulations numériques réalisées dans le cadre de cette thèse se concentrent essentiellement sur les effets des ondes de tension à forts dV/dt et de la fréquence de commutation élevée sur la robustesse de l'isolation du bobinage des machines électriques alimentées par des onduleurs. Par conséquent, les travaux touchent un certain nombre de questions liées à l'entraînement à vitesse variable, à l'électronique de puissance, aux machines électriques, aux matériaux diélectriques et aux décharges partielles (DPs). La pertinence de ce travail est due à la mise en œuvre de composants à semi-conducteurs grand gap, tels que le Carbure de silicium (SiC), dans les convertisseurs de puissance qui peuvent intensifier les contraintes électriques dans les moteurs entraînés, accélérant la défaillance d'isolation d'enroulement du moteur.

Le Chapitre I est consacré à un état de l'art sur les machines électriques basse tension et leurs systèmes d'isolation. Il synthétise les facteurs affectant l'isolation du bobinage des machines électriques lors de leur fabrication (la compatibilité des fils d'enroulement et des compositions d'imprégnation) ainsi que leur fonctionnement (des contraintes thermiques, électriques, et mécaniques, ainsi que des conditions ambiantes). Une attention particulière devrait être accordée aux contraintes électriques dues à la tension d'alimentation du moteur entraîné par un onduleur. Comme on peut le voir dans la littérature, l'isolation des bobinages des moteurs alimentés par des convertisseurs statiques basés sur la modulation de largeur d'impulsion (MLI) est soumise à des contraintes électriques provenant de la forme d'onde de la tension d'alimentation. Les phénomènes de nuisances

électromagnétiques sur l'ensemble de la chaîne de conversion, les ondes réfléchies dans le câble d'alimentation, ainsi que la non-adaptation des impédances du câble et de l'enroulement de la machine, peuvent conduire à l'apparition de surtensions aux bornes de la machine. Les surtensions peuvent être suffisamment élevées pour dépasser la tension d'apparition des décharges partielles (TADP). L'apparition de ces décharges partielles entraîne alors la dégradation des isolants qui, à son tour, amène à une augmentation de la fréquence des impulsions de DPs et de leurs amplitudes. Il en résulte une dégradation de l'isolation entre les spires qui, à terme, peut avoir pour conséquence la défaillance de la machine. Cela est particulièrement critique pour l'isolation de Type I utilisée dans les machines basse tension (jusqu'à 700 V de tension nominale efficace).

Le développement de l'électronique de puissance ne s'arrête pas comme on peut le constater avec l'implémentation des semi-conducteurs à large bande interdite, tels que le SiC, qui permet la réalisation de convertisseurs de forte densité de puissance notamment pour les systèmes d'entraînement à vitesse variable des machines électriques. En raison de vitesses de commutation plus élevées que les composants Silicium (Si), une fréquence de commutation plus importante peut être obtenue avec des dispositifs à large bande interdite, ce qui conduit à des contraintes électriques en dV/dt plus sévères sur l'isolation des enroulements des moteurs alimentés par de tels convertisseurs. Les enroulements de la machine peuvent alors subir des surtensions plus élevées ce qui peut augmenter le risque de DP et accélérer le vieillissement ainsi que la destruction de l'isolant. À cet égard, les contraintes liées à la forme d'ondes de tension à forts dV/dt générée par les onduleurs à base de SiC et leurs effets sur l'isolation du bobinage nécessitent d'une étude profonde.

Faisant suite à l'état de l'art, le Chapitre II présente une étude des surtensions transitoires dans un moteur alimenté par un onduleur qui permet d'estimer les contraintes électriques provoquant la dégradation accélérée de l'isolation du bobinage du moteur. À cet égard, un modèle hautes fréquences (HF) existant dans la littérature a été utilisé pour des simulations du système d'entraînement à vitesse variable. Les modèles HF proposés dans la littérature sont généralement destinés à examiner et prédire les phénomènes transitoires dans les machines asynchrones qui sont les machines électriques les plus utilisées pour les applications industrielles. Or, d'autres types de machines utilisés dans les systèmes d'entraînement à vitesse variable doivent être considérées. Par conséquent, notre étude se concentre sur la modélisation de la machine à réluctance variable (MRV) qui est particulièrement intéressante en raison de sa construction redondante et tolérante aux pannes, sa commande particulière utilisant un convertisseur de puissance en demi-pont asymétrique et son bobinage concentré contrairement aux moteurs asynchrones. De plus, l'absence dans la littérature de modèles de MRV pour l'analyse de leurs comportements à haute fréquence en fait un objet d'études intéressant.

En se basant sur les modèles hautes fréquences développés pour les moteurs asynchrones triphasés, le moteur à réluctance variable à double saillances (triphasé, à 6 dents statorique et à 4 dents rotoriques, $V_{DC} = 300\text{ V}$) a été modélisé par des circuits électriques équivalents aux paramètres RLC discrets. L'identification des paramètres du modèle HF est basée sur des mesures de l'impédance en mode commun et mode différentiel réalisées en utilisant l'analyseur d'impédance (Agilent Technologies E5061B, 5 Hz – 3 GHz) dans la gamme de fréquences de 30 kHz à 30 MHz (Figure 1).

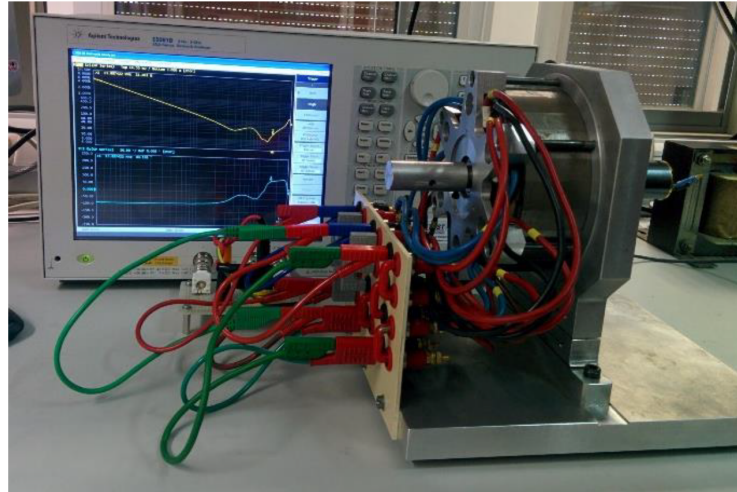


FIGURE 1: Banc expérimental de mesure d'impédances de la machine à réluctance variable.

En faisant une validation du modèle dans le domaine fréquentiel, nous avons observé une bonne corrélation entre les résultats mesurés et simulés présentés ci-dessous dans la Figure 2. Nous avons étudié les surtensions transitoires à l'entrée du moteur combinant le circuit équivalent du moteur suggéré et un modèle de câble d'alimentation composé des associations de cellules élémentaires proposé dans la littérature. Les phases de la machine à réluctance variable pouvant être alimentées indépendamment, nous avons effectué les observations des fronts de tension lors des commutations en mode monophasé. L'onduleur est modélisé par un générateur d'impulsions idéal avec des temps de montée/descente et donc dV/dt spécifiés. Les résultats des simulations confirment que les fronts raides de tension engendrent une surtension importante. Il est à noter qu'en cas de temps de montée extrêmement court, jusqu'à 10 ns, même un mètre de câble d'alimentation représente une longueur critique (Figure 3). De plus, l'augmentation de la longueur de câble intensifie la surtension transitoire, affecte la fréquence d'oscillation et allonge les oscillations transitoires (Figure 4). L'étude réalisée est en corrélation avec les travaux précédents et met en évidence l'importance de la caractérisation des effets des forts dV/dt .

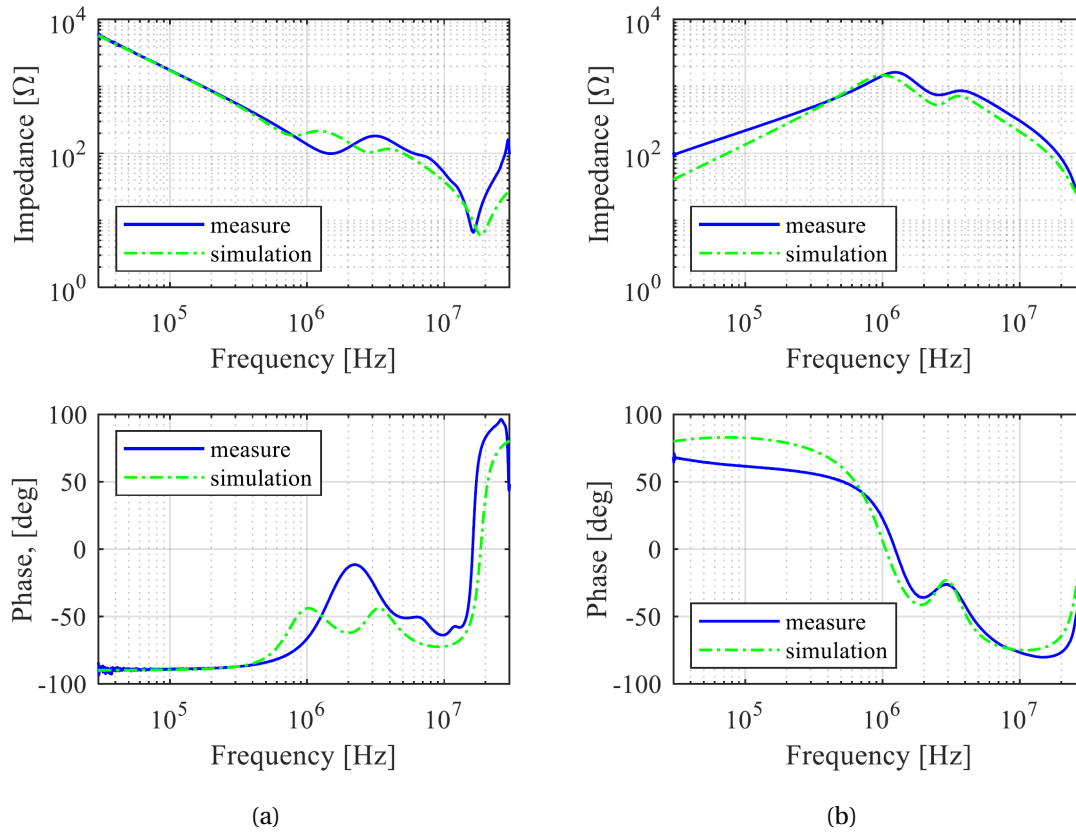


FIGURE 2: Comparaison des impédances mesurées et simulées : (a) mode commun et (b) mode différentiel.

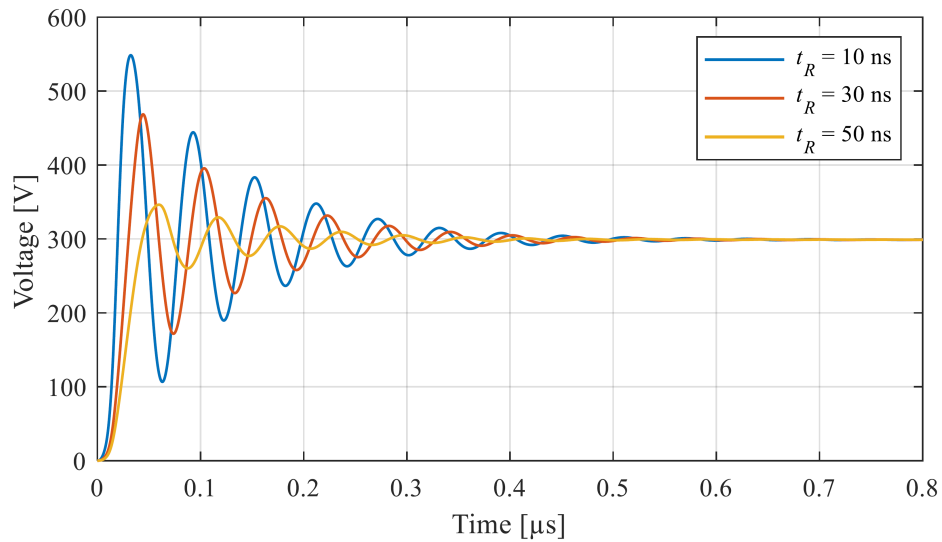


FIGURE 3: Formes d'ondes de tension simulées pour différents temps de montée avec une longueur de câble de 1 m.

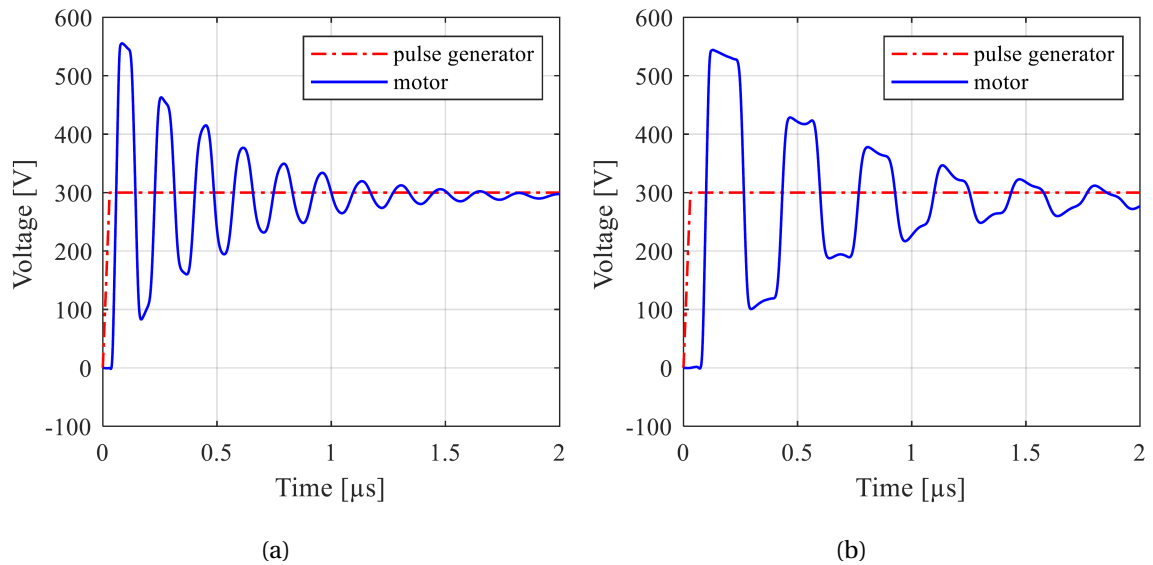


FIGURE 4: Formes d’ondes de tension simulées pour temps de montée $t_R = 30$ ns et une longueur de câble différente : (a) $L = 5$ m and (b) $L = 10$ m.

Afin d’étudier les effets du dV/dt et de la fréquence de commutation, sur l’isolation du bobinage des machines électriques, différentes méthodes d’essai sont proposées dans le Chapitre III. Sachant que l’isolation entre spires est l’élément le plus faible du système d’isolation de la machine électrique, nous avons effectué des essais d’endurance sur des éprouvettes sous forme de paires torsadées constituées de fils émaillés conventionnels et Corona résistants. De plus, une nouvelle forme d’éprouvette présentée dans la Figure 5 est proposée permettant de tester des fils rectangulaires émaillés, ce qui élargit la gamme des moteurs étudiés.

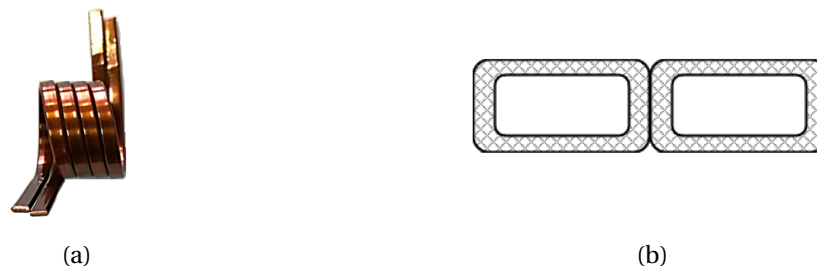


FIGURE 5: Éprouvette sous forme de bobine : (a) photographie et (b) section transversale.

Tout d’abord, le dispositif expérimental utilisé dans le but de comparer des tensions de claquage et une endurance des fils émaillés sous tension sinusoïdale de fréquence nominale de 50 Hz est présenté. Ensuite, je décris les essais d’endurance sous tension impulsionnelle de type MLI ayant des dV/dt relativement faibles de $0.4 \text{ kV}/\mu\text{s}$ avec un temps de montée de $4 \mu\text{s}$. Ce banc d’essai précédemment développé et installé à la TPU (Russie), contient un générateur d’impulsions permettant de reproduire des contraintes électriques proches de celles typiques pour le fonctionnement des moteurs alimentés par

des convertisseurs de puissance à base de silicium. L'association de ce générateur d'impulsions avec une chambre thermique a permis de combiner les contraintes électriques et thermiques au cours des essais d'endurance.

Dans le but d'appliquer sur l'isolation entre spires des contraintes électriques engendrées par des interrupteurs commutant à haute vitesse et fréquences élevées, nous avons développé un nouveau banc intégrant un générateur d'impulsions à base de SiC au sein du laboratoire SATIE (France). Initialement, un onduleur monophasé en demi-pont a été réalisé avec des transistors MOSFET SiC 1200 V (Figure 6). Un transistor de faible capacité de sortie (et donc de résistance à l'état passant élevée) a été sélectionné afin de maximiser les dV/dt en sortie de l'onduleur. Les composants électroniques de puissance utilisés permettent d'appliquer des impulsions de tension d'amplitude maximale égale à 1200 V et de fréquence de commutation inférieure à 64 kHz. Cet onduleur nous a permis d'ores et déjà d'appliquer des fronts raides de tension (jusqu'à 30 kV/ μ s avec une tension de bus DC de 300 V) et nous a servi de premier prototype pour le banc d'essai à forts dV/dt .

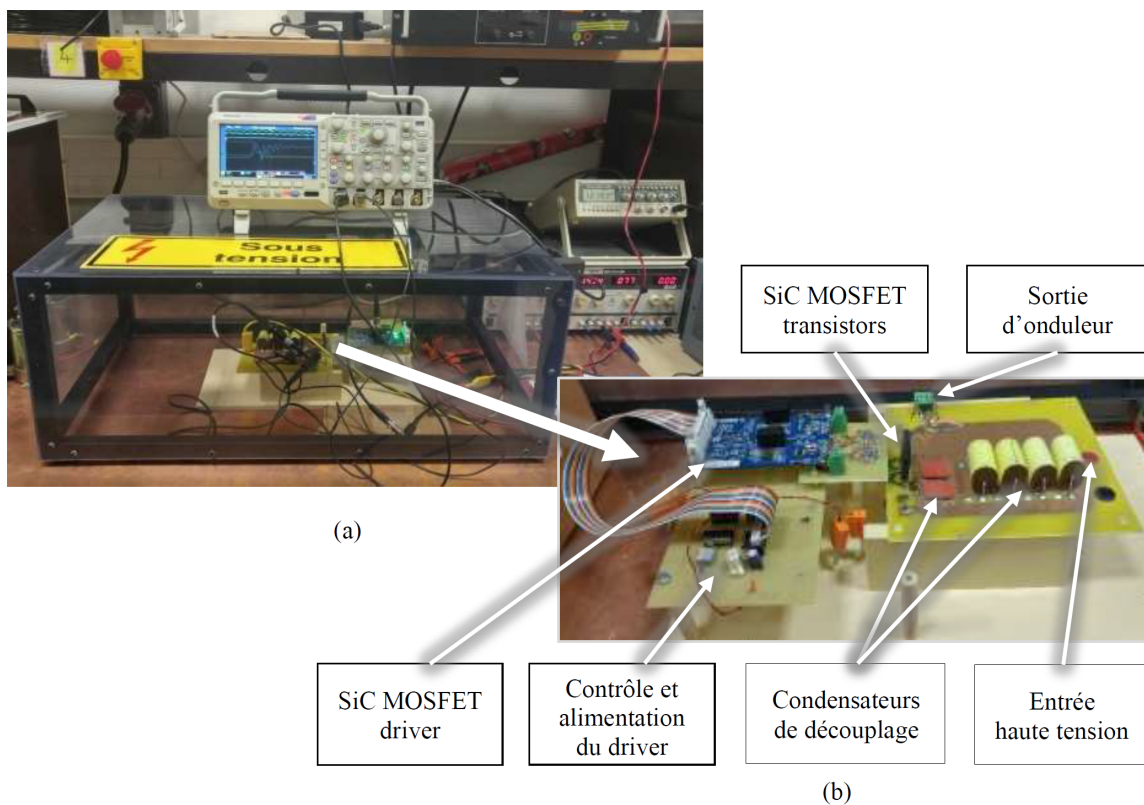


FIGURE 6: Aperçu d'ensemble du montage expérimental (a) et SiC onduleur (b).

Ensuite, un onduleur monophasé en pont complet à base de MOSFET SiC 1700 V a été développé au laboratoire SATIE. Les dispositifs électroniques de puissance utilisés permettent de commuter des tensions allant jusqu'à 1700 V avec une fréquence de commutation maximale jusqu'à 125 kHz. Le banc d'essai à forts dV/dt présenté dans la Figure 7 est assemblé et installé à la TPU. Il comprend un générateur de tension DC, le

générateur d'impulsions à base de SiC, une chambre thermique où les éprouvettes sont installées et le système de mesures. Le générateur d'impulsions produit une tension impulsionnelle à très forts dV/dt : jusqu'à $60 \text{ kV}/\mu\text{s}$ appliqués à l'éprouvette testée. Les paramètres des impulsions générées telles que l'amplitude, la fréquence de découpage et le rapport cyclique sont réglables. En outre, la variation de la température est possible lorsque des éprouvettes sous tension sont placées dans la chambre thermique. La possibilité de varier ces paramètres permet d'examiner leurs effets sur l'apparition des DP et sur le vieillissement du matériau isolant.

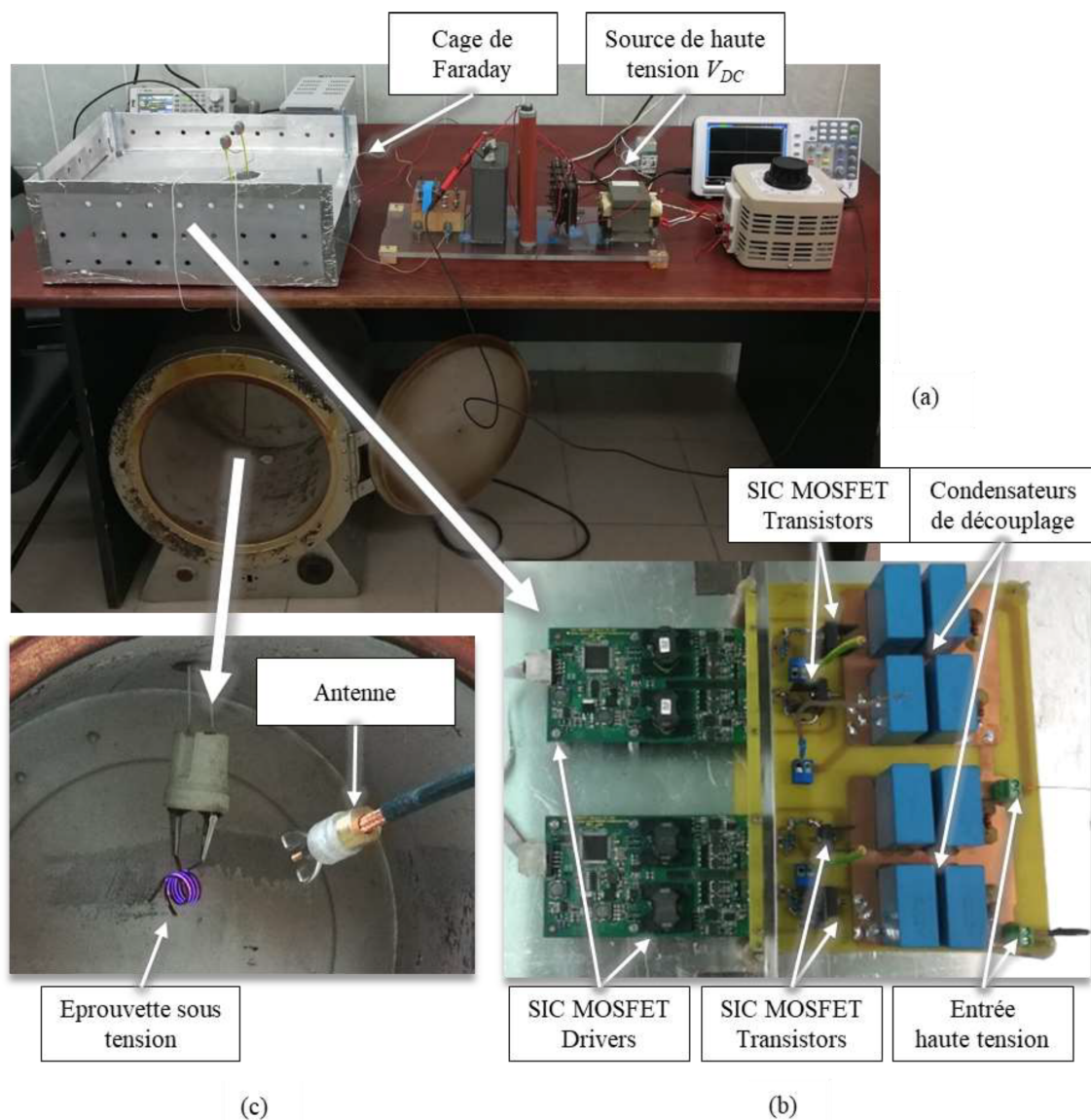


FIGURE 7: Aperçu d'ensemble du montage expérimental (a), SiC onduleur (b), éprouvette testée (c).

Étant donné que les surtensions dans un moteur alimenté par un onduleur peuvent être suffisamment élevées pour dépasser le seuil d'apparition des décharges partielles, tous les essais d'endurance d'isolation entre spires ont été effectués en présence de dé-

charges partielles représentant le principal facteur de vieillissement. Afin de les détecter, j'ai utilisé des méthodes optiques, électromagnétiques et chimiques. Les DP's les plus faibles ont été observées lors de l'application d'une tension sinusoïdale, alors que la tension impulsionnelle à forts dV/dt donne lieu aux DP's les plus intenses.

Les protocoles expérimentaux suivis des résultats obtenus et de leur analyse sont présentés au Chapitre IV. Dans le but d'estimer la résistance des différents fils émaillés (sans imprégnation) aux décharges partielles et l'impact des décharges sur la durée de vie des isolants, les essais sont poursuivis jusqu'à la rupture de l'isolation, ou claquage. Le temps moyen jusqu'au claquage a été systématiquement déterminé en appliquant diverses formes d'ondes de tension : sinusoïdale, impulsionnelle à faibles dV/dt , impulsionnelle à forts dV/dt . Conformément à nos attentes, le fil Corona résistant a montré la meilleure tenue vis-à-vis des décharges partielles par rapport aux fils conventionnels. Le fil de section rectangulaire a également montré un temps moyen jusqu'au claquage plus important que les autres fils conventionnels, ce qui peut être lié à sa classe thermique plus élevée et à son isolation plus épaisse.

En outre, nous avons mené une étude consacrée à l'influence des défauts dans les couches d'email sur l'endurance de l'isolation entre spires. À cet égard, des éprouvettes non-défectueuses non-imprégnées, défectueuses non-imprégnées et défectueuses imprégnées par différentes compositions d'imprégnation, ont été testées sous tension impulsionnelle de type MLI à faible dV/dt . En comparant les temps moyens jusqu'au claquage, nous avons observé que, premièrement, la présence de défaut même sur un seul fil d'une paire torsadée affecte de façon critique l'isolation entre spires lorsqu'ils sont soumis aux DP's et, deuxièmement, l'imprégnation peut ne pas fournir de « recouvrabilité » des défauts d'isolation suffisante ce qui met en évidence l'importance de la compatibilité de l'email et de la composition de l'imprégnation.

Les observations suivantes peuvent être faites suite aux résultats expérimentaux présentés dans le Chapitre IV :

- L'échauffement des éprouvettes dans la chambre thermique à la température correspondante à leur classe thermique lorsqu'elles sont soumises aux DP's accélère considérablement la destruction de l'isolant (mécanisme de défaillance d'origine électrothermique).
- Le claquage d'isolation des éprouvettes testées sous tension sinusoïdale avec une fréquence de 50 Hz et sous une tension d'impulsion de type MLI à faibles dV/dt avec une fréquence porteuse de 5 kHz s'est produit en majorité de cas dans une zone défectueuse; le phénomène de « frost effect » et les endommagements localisés ont été observés sur la surface de l'isolant (dominance des mécanismes de défaillance d'origine électrique et chimique).

- Les effets de carbonisation et de collage des spires ont été observés dans les éprouvettes testées sous la tension impulsionnelle à forts dV/dt d'amplitude élevée avec une fréquence de commutation de 50 kHz (dominance du mécanisme de défaillance d'origine thermique) comme présenté dans la Figure 8.

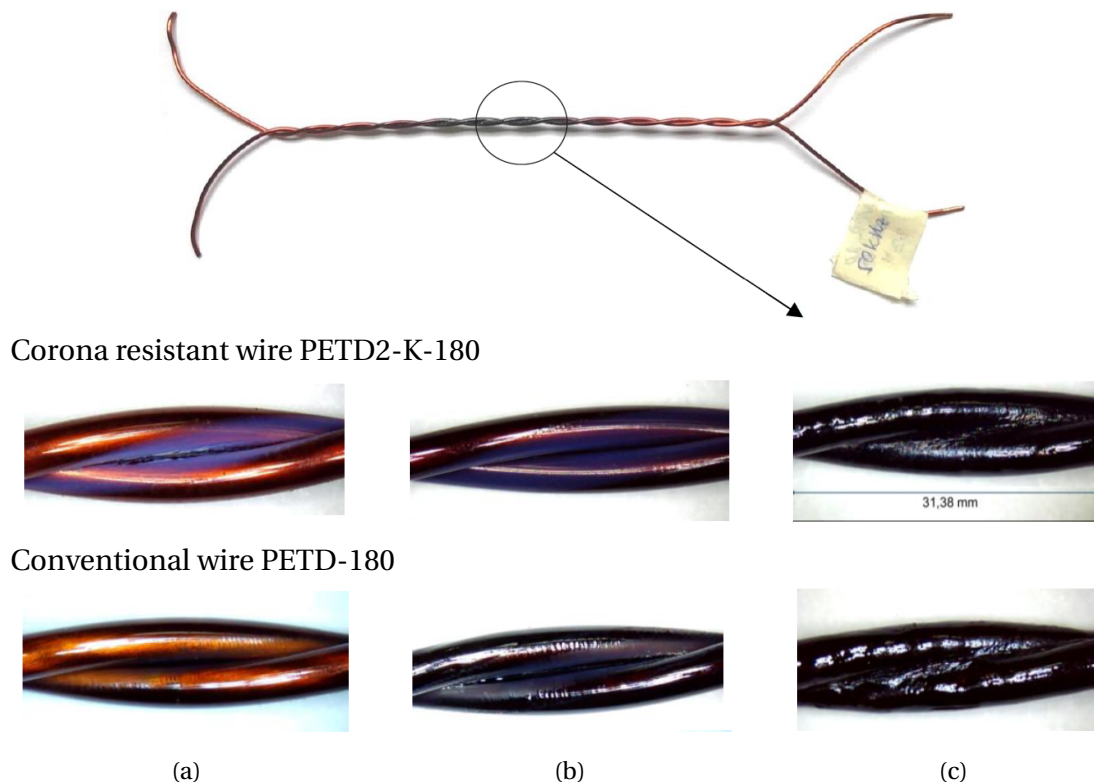


FIGURE 8: Photographie et images microscopiques des éprouvettes testées sous une tension impulsionnelle à fort dV/dt , $T=25^{\circ}\text{C}$, $f_s = 50\text{ kHz}$: (a) $V_{dc} = 1\text{ kV}$; (b) $V_{dc} = 1.2\text{ kV}$ et (c) $V_{dc} = 1.4\text{ kV}$.

Ces observations révèlent que la tension impulsionnelle ayant un temps de montée très court et une fréquence de commutation élevée donnent lieu à une concentration d'ozone plus élevée et à une augmentation significative de la température ce qui raccourcit extrêmement la durée de vie de l'isolation. Malheureusement, les effets des forts dV/dt et de la fréquence de commutation élevée n'ont pas pu être dissociés ce qui a compliqué l'analyse de l'effet du seul dV/dt .

Les résultats expérimentaux présentés ci-dessus m'ont motivé à examiner de manière plus approfondie les processus de détérioration de l'isolation entre spires exposée à une tension impulsionnelle à forts dV/dt , ainsi que les caractéristiques des décharges partielles comme je le décris dans le Chapitre V. Les éprouvettes sous forme de paire torsadée ont été utilisées pour mener cette étude phénoménologique.

En premier lieu, les surtensions causées par la longueur de câblage entre le générateur d'impulsions à base de SiC et la paire torsadée au cours des essais ont été modélisées et analysées en se basant sur l'approche électromagnétique et l'approximation de la ligne de transmission à faibles pertes (Figure 9). Les résultats obtenus mettent en

évidence l'importance de minimiser la longueur du câble pour limiter les oscillations de tension et les surtensions (Figure 10) ce qui est en phase avec les observations présentées dans le Chapitre II.

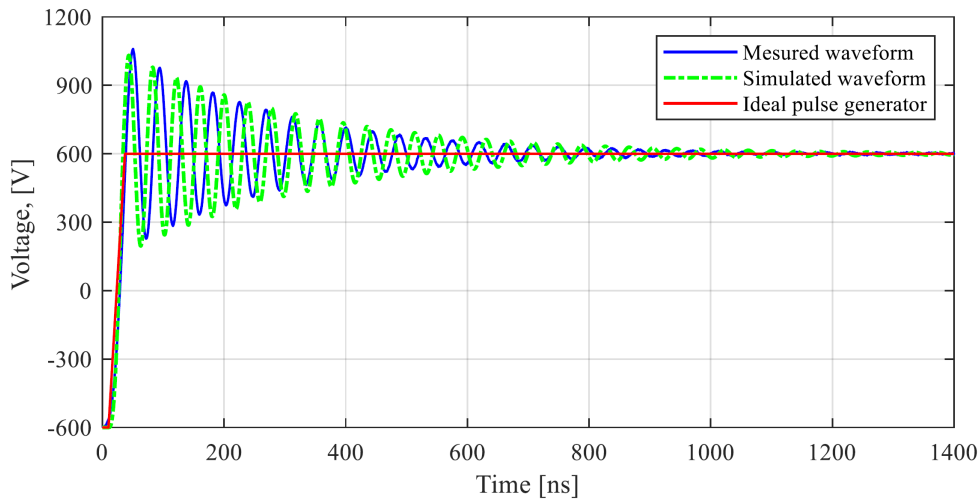


FIGURE 9: Formes d'ondes de tension mesurées sur l'éprouvette mise dans la chambre thermique et modélisées par le circuit équivalent RLC sous LTSpice.

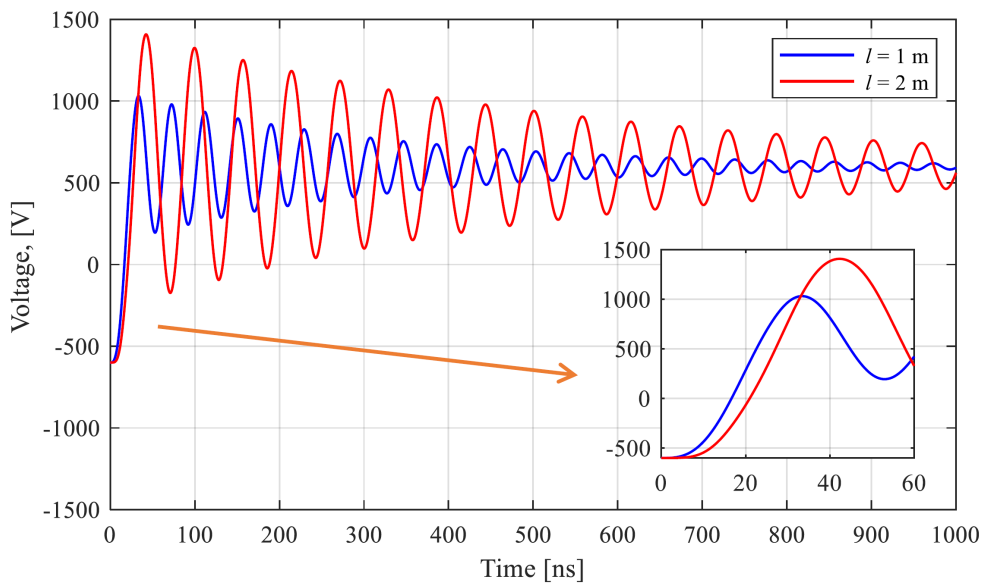


FIGURE 10: Formes d'ondes de tension avec le temps de montée de 27 ns modélisées pour deux longueurs de câble.

Ensuite, nous avons caractérisé les décharges partielles dans la paire torsadée en tant que décharges à barrière diélectrique (DBD) parce qu'elles se produisent dans l'air entre les spires de paires torsadées (entre les deux conducteurs isolés). Ainsi, l'isolation émaillée d'une paire torsadée a été représentée par les barrières diélectriques et modélisée par des capacités. Cela nous a permis d'analyser les caractéristiques de courant-tension obtenues numériquement et expérimentalement, en reliant la géométrie de l'éprou-

vette et la permittivité relative à la TADP ainsi qu'en dissociant le courant de décharges et le courant capacitif, lequel est particulièrement significatif à forts dV/dt . Cependant, les mesures de courant et de tension lorsque les impulsions de tension ont des temps de montée très courts est un défi à surmonter car cela nécessite une précision qui peut être difficile à atteindre avec nos sondes disponibles et conçues en laboratoire. La Figure 11 montre une sonde de courant utilisé (shunt sur la Figure 11a) et des formes d'ondes de tension et de courant mesurées sur les paires torsadées au-dessous (Figure 11b) et au-dessus (Figure 11c) de la tension d'apparition des décharges partielles.

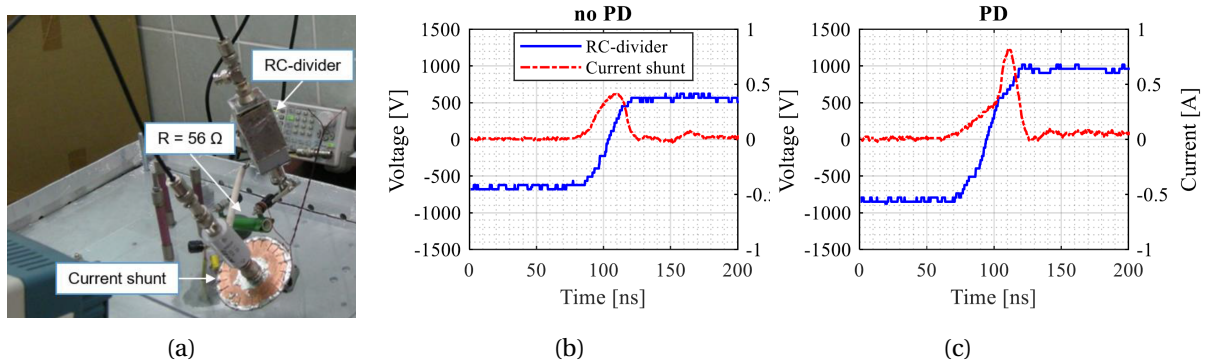
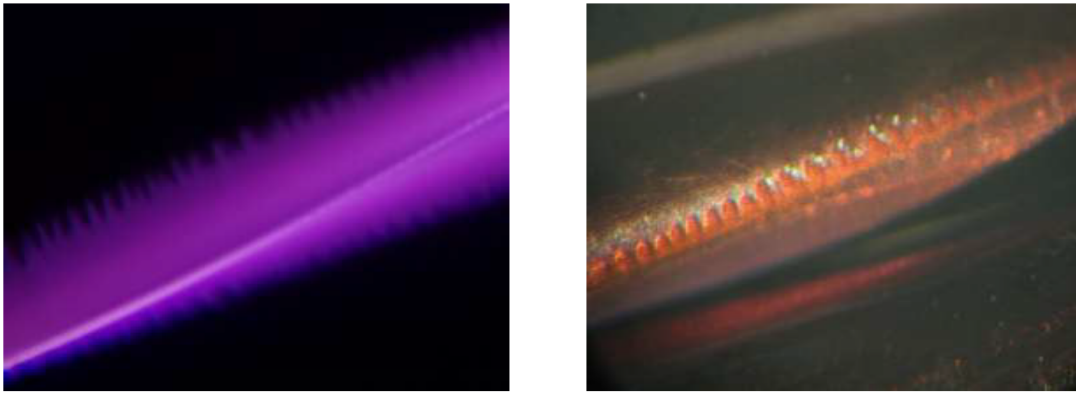


FIGURE 11: Mesure de tension et de courant sur les paires torsadées testées sous forts dV/dt , $f = 20 \text{ kHz}$: (a) dispositifs de mesure, (b) mesure avant apparition de DPs et (c) mesure en présence de DPs.

Les mesures de courant, de température et de spectre d'émission optique montrent une énergie élevée des décharges à barrière diélectrique augmentant avec l'accroissement de la fréquence de commutation, ainsi qu'avec l'intensification du champ électrique (également démontrée par des calculs électrostatiques effectués en utilisant la modélisation par éléments finis). Les images microscopiques des décharges (Figure 12a) et de l'érosion de surface de l'isolant (Figure 12b) mettent en évidence la structure filamenteuse des décharges à barrière en les associant à l'érosion de l'isolant par les attaques chimiques dues aux filaments. Ainsi, le mécanisme de destruction de l'isolation entre spires soumise à une tension impulsionnelle à forts dV/dt correspond au claquage dû à une ionisation. Les décharges entre les barrières diélectriques produisent de la chaleur et du rayonnement ultraviolet (UV), génèrent de l'ozone et des NO_x , accélèrent les bombardements d'électrons et d'ions et réchauffe la surface diélectrique (barrières diélectriques). En fonction de la distribution de l'énergie entre les différents processus, le mécanisme de défaillance d'origine électrochimique ou électrothermique se produira.

Pour aller plus loin dans l'étude expérimentale, nous proposons un banc d'essai synthétique contenant deux sources de tension (la source de tension sinusoïdale permet de chauffer l'éprouvette et le générateur d'impulsions d'appliquer la tension impulsionnelle) et la possibilité de contrôler la pression et le milieu (gaz, liquide) des éprouvettes testées (Figure 13). Un exemple d'utilisation de ce banc d'essai est le test effectué sur des



(a)

(b)

FIGURE 12: Images microscopiques : (a) décharges à barrière avec structure filamentaire et (b) érosion de l'isolant par des attaques chimiques due aux filaments.

paires torsadées sous tension impulsionnelle et basse pression lequel nous a permis de visualiser les points d'isolation les plus faibles en présence de décharges partielles comme le montre la Figure 14. Cette méthode pourrait être utilisée pour l'estimation des défauts d'isolation.

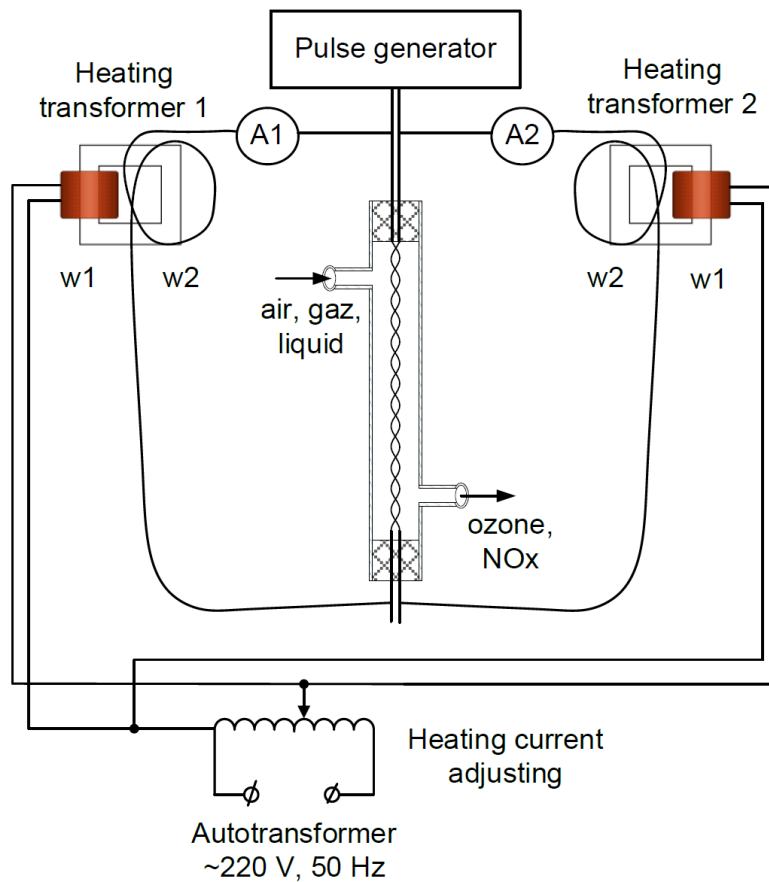


FIGURE 13: Synoptique du banc d'essai synthétique.

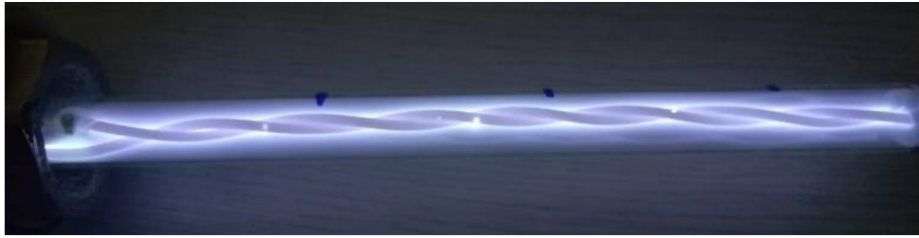


FIGURE 14: Visualisation des défauts d'isolation.

Les principaux résultats et contributions de la présente thèse sont les suivants :

- Élaboration d'un modèle à haute fréquence destiné à étudier des surtensions transitoires aux bornes d'une machine à réluctance variable alimentée par un onduleur.
- Conception d'un banc d'essai qui comprend un générateur d'impulsions à base de SiC fournissant une tension impulsionnelle à forts dV/dt (jusqu'à $60 \text{ kV}/\mu\text{s}$ appliqué à l'éprouvette) avec une amplitude de tension jusqu'à 1700 V et une fréquence de commutation maximale jusqu'à 125 kHz .
- Conception d'une nouvelle forme d'éprouvette pour l'essai des fils émaillés de section rectangulaire.
- Conception d'un banc d'essai synthétique associant deux sources de tension ce qui offre la possibilité d'appliquer la forme d'onde de tension désirée à l'éprouvette et en même temps de contrôler sa température, sa pression et son milieu.
- Estimation des défauts d'isolation à l'aide de la visualisation des défauts lorsque les éprouvettes sont placées sous la basse pression et soumises aux ondes de tension à forts dV/dt dépassant la TADP.
- Caractérisation des décharges partielles dans l'air entre les spires de paires torsadées comme des décharges à barrière diélectrique. Compte tenu du fait que la paire torsadée représente un modèle physique de l'enroulement de la machine, les décharges partielles dans l'enroulement peuvent également être considérées et étudiées comme des décharges à barrière diélectrique.
- Révélation de la structure filamentaire des décharges à barrière diélectrique dans les paires torsadées testées sous tension impulsionnelle à forts dV/dt avec haute fréquence de commutation, ce qui provoque l'apparition de traces d'érosion périodiques sur la surface de l'émail.
- Démonstration de fait qu'en cas de décharges à barrière dans les paires torsadées testées sous tension impulsionnelle à forts dV/dt à haute fréquence de commutation, le mécanisme de défaillance d'origine électrothermique peut prédominer sur celui d'origine électrochimique.

Le travail effectué ouvre des perspectives envisageables au terme de cette recherche parmi lesquelles nous pouvons citer :

- Poursuivre le travail sur la modélisation HF de la machine à réluctance variable intégrant les modèles de l'onduleur et du câble d'alimentation en étendant la gamme de fréquences. Approfondir l'étude de surtension en proposant un modèle permettant de déterminer les répartitions de tension dans le bobinage concentré et distribué.
- Étudier la distribution probable des défauts dans l'isolation du bobinage qui, en association avec la répartition de tension, permettra de prévoir avec plus de précision les zones présentant un risque d'apparition de décharges partielles.
- Approfondir l'étude expérimentale des mécanismes de défaillance de l'isolation entre spires soumise aux ondes de tension à forts dV/dt et hautes fréquences de commutation en contraintes environnementales telles que la basse pression. À l'issue de cette étude, développer un modèle mathématique de la durée de vie de l'isolation compte tenu des nouvelles contraintes imposées par l'utilisations des semi-conducteurs à grand gap tels que le SiC.
- Approfondir l'étude des décharges à barrières diélectriques : déterminer un bilan de puissance (échauffement, production d'ozone, rayonnement UV, pertes diélectriques), examiner l'effet de la permittivité relative et de la capacité des fils sur l'apparition des décharges, améliorer le modèle des barrières diélectrique dans la paire torsadée en tenant compte des capacités dynamiques qui évoluent en présence de décharges, ainsi que la résistance variable caractérisant l'ionisation de l'air.

List of publications

PUBLICATIONS IN THE CONTEXT OF THE THESIS

International Conference Papers With Peer Review

1. V. Bolgova¹, S. Kolesnikov, A. Leonov, S. Lefebvre, S. Hlioui. Effect of High Switching Frequencies on Enamel Insulation Degradation of Motors Fed by SiC-based Inverters // IEEE 2020 International Conference on Dielectrics (ICD) 6-31 July, Virtual Edition (*waiting to be published*).
2. Bolgova Veronika, Andrey Leonov, Lefebvre Stéphane, Hlioui Sami. Aging investigation of inverter-fed low voltage motor winding insulation subjected to high dv/dt // XXVth Symposium on Electromagnetic Phenomena in Nonlinear Circuits (EPNC 2018), 26 – 29 June, 2018, Arras, France.
3. Veronika Bolgova, Stéphane Lefebvre, Sami Hlioui, Nidhal Boucenna, François Costa, Andrey Leonov. Development of testing methods for winding turn-to-turn insulation of low voltage motors fed by PWM converters // 2017 19th European Conference on Power Electronics and Applications (EPE'17 ECCE Europe), 11-14 September 2017, Warsaw, Poland, P.1 - P.10.
4. Bolgova V. A., Leonov A. P., Charkov D. I. Influence of VFD Parameters on Voltage Stresses in Low Voltage Windings // 57th International Scientific Conference on Power and Electrical Engineering of Riga Technical University: proceedings, Riga, Latvia, October 13-14, 2016. - New York: IEEE, 2016 - p. 1-5.
5. A. Leonov, A. Supueva, V. Bolgova. Influence of Defects in Windings Insulation on its Operation Reliability. IEEE Xplore: 2016 IEEE 16th International Conference on Environment and Electrical Engineering (EEEIC) 7-10 June 2016, Florence, Italy, pp.742-745.

¹The former (married) surname is Bolgova and the legal (birth) surname is Gavrilenko

National Conference Papers With Peer Review (France)

6. V Bolgova, S Hlioui, S Lefebvre, A. Leonov. Méthodes d'essais d'isolation entre spires des enroulements de machines électriques alimentés par des convertisseurs de tension // 14ème Conférence des Jeunes Chercheurs en Génie Électrique (JCGE'17), 30 Mai - 1er Juin, Arras, France.
7. Bolgova Veronika, Leonov Andrey, Hlioui Sami, Lefebvre Stéphane. Essais de tenue d'isolation entre spires pour enroulements de machines électriques alimentées par des ondes de tension à très forts dV/dt // 3ème Symposium de Génie Electrique (SGE 2018), 3 – 5 Juillet, Nancy, France.

OTHER PUBLICATIONS***Journal Publications***

8. V.V. Red'ko, A.P. Leonov, L.A. Red'ko, and V.A. Bolgova. Problems of Automatic Test of Insulation in Cable Production. Journal of Physics: Conference Series, Volume 671, conference 1, published online: 18 January 2016.
9. Igor S. Bolgov, Yuriy N. Dementyev, Veronika A. Bolgova, "Simulation Modelling of a Pulse Frequency-Phase Discriminator", Applied Mechanics and Materials, Vol. 792, pp. 95-100, 2015.

International Conference Papers With Peer Review

10. Bolgov I. S., Bolgova V. A. Detailed simulation model of the two-phase brushless DC motor designed for VFD integration // 57th International Scientific Conference on Power and Electrical Engineering of Riga Technical University: proceedings, Riga, October 13-14, 2016. - New York: IEEE, 2016 - p. 1-5.

National Conference Papers With Peer Review (Russia)

11. V.I. Merkulov, A.P. Leonov and V.A. Bolgova. Estimation of time before the breakdown of the polymer insulation. Electromechanical energy converters. Proceedings of the VII International Scientific and Technical Conference; Tomsk Polytechnic University: 24 - 28 October 2015. Tomsk (Language: Russian).
12. V.A. Bolgova. Impact of factors affecting the insulation of low voltage motor windings in VFD. Electromechanical energy converters. Proceedings of the VII International Scientific and Technical Conference; Tomsk Polytechnic University: 24 - 28 October 2015. Tomsk (Language: Russian).

Glossary

AC Alternating Current.

ANOVA analysis of variance.

ASD Adjustable-Speed Drive.

BJT Bipolar Junction Transistor.

CM Common Mode.

CR corona resistant.

CV conventional.

DBD Dielectric Barrier Discharges.

DC Direct Current.

DM Differential Mode.

dV/dt Voltage changing rate (edge).

EMI ElectroMagnetic Interference.

EV Electric Vehicle.

FEM Finite Element Method.

GTO Gate Turn-Off thyristor.

HEV Hybrid Electric Vehicle.

HF High Frequency.

IEC International Electrotechnical Commission.

IGBT Insulated Gate Bipolar Transistor.

IM Induction Machine.

KI Potassium Iodide.

LEV Low Emission Vehicle.

MEA More Electric Aircraft.

MOSFET Metal-oxide-semiconductor Field-effect transistor.

NEMA National Electrical Manufacturers Association.

NO_x Oxides of Nitrogen.

PA polyamide.

PAI polyamide-imide.

PCB Printed Circuit Board.

PD Partial Discharge.

PDF Probability Distribution Function.

PDIV Partial Discharge Inception Voltage.

PE polyester.

PEI polyester-imide.

PI polyimide.

PMSM Permanent Magnet Synchronous Machine.

PU polyurethane.

PWM Pulse Width Modulation.

RLC Resistance, Inductance, Capacitance.

RMS Root Mean Square.

Si Silicon.

SiC Silicon Carbide.

SRM Switched Reluctance Machine.

TEAM Thermal, Electrical, Ambient and Mechanical stresses.

UV Ultraviolet.

VDF Variable Frequency Drive.

VPI Vacuum Pressure Impregnation.

WBG Wide Bandgap.

Contents

Acknowledgements	iii
Résumé détaillé en français	v
List of publications	xix
Glossary	xxi
Contents	xxv
General introduction	3
I Factors affecting low voltage electrical machines fed by inverters: literature survey	11
1 Introduction	12
2 Electrical machines	15
3 Electrical machine winding	21
4 Electrical machine winding insulation system	24
5 Operational factors affecting winding insulation	29
6 Conclusion	39
References	43
II High-frequency modelling of inverter-fed motor drive	57
1 Introduction	58
2 High frequency electrical machine modelling	58
3 High frequency cable modelling	74
4 Simulation of transient overvoltage in inverter-fed motor drive	76
5 Conclusion	79
References	83
III Endurance testing methods for turn insulation of motors fed by inverters	89
1 Introduction	90
2 Review of methods for testing the inverter-fed motors winding insulation	90
3 Testing methodology	94
4 Conclusion	123

References	127
IV Analysis of turn insulation endurance experimental results	137
1 Introduction	138
2 Breakdown voltage tests	138
3 Endurance tests	142
4 Thermal imaging study	167
5 Conclusion	169
References	173
V Deterioration of turn insulation under partial discharges at high dV/dt impulse voltage	177
1 Introduction	178
2 Characterization and modelling of twisted pair	179
3 Study of turn insulation deterioration	198
4 Synthetic experimental setup for turn insulation testing	208
5 Conclusion	211
References	215
Conclusion and future work	221
Appendices	III
Appendix III-A. Wires characteristics	IV
Appendix III-B. RC-divider characteristics	V
Appendix IV-A. Endurance tests results under sinusoidal voltage	VI
Appendix IV-B. Endurance tests results under PWM impulse voltage with low dV/dt	VIII
Appendix IV-C. Endurance tests results under PWM impulse voltage with low dV/dt: effect of defects “healing” by the impregnation	XI
Appendix IV-D. Endurance tests results under rectangular impulse voltage with high dV/dt	XII
Appendix IV-E. Thermal imaging of specimens subjected to PDs under different voltage waveform parameters	XVI
Appendix V-A. LCR meter E7-13	XVII
Appendix V-B. Current shunt and RC-divider	XVIII
List of Figures	XXIII
List of Tables	XXIX

General introduction

General introduction

Context

Electrical insulation quality plays a vital role in providing electrical machines reliability. This essential component of electrical machines operates under combined Thermal, Electrical, Ambient and Mechanical stresses (TEAM) [1], [2], [3], [4] and [5]. It results in ageing and gradual deterioration of insulation properties that can reduce machine's service lifetime. As reported by [2], [6], [7] and [8], one of the most common reasons of induction motor breakdowns is a stator winding turn insulation fault which accounts for 36-37% of all the failures. Thus, the turn insulation, consisting of enamelled wire and impregnating compound, is the weakest element of the machine's insulation system.

The impact of these factors on dielectrics ageing and deterioration depends on the electrical machine's environmental conditions (temperature, humidity and pressure), the power supply and the control system. In case of sinusoidal 50-Hz AC supply voltage, thermal stresses are the main cause of low voltage electrical machines insulation deterioration [2] and [3]. This is due to the fact, that voltage magnitude and surges are not high enough to cause an insulation breakdown or an ionization process.

Nowadays, the energy consumption due to electrical machines utilized in industry represents 40% of the total worldwide generated electrical energy [9]. The objective to reduce the environmental impact of transportation system inspire the hybrid, electric vehicles, and more electric aircrafts technologies continuing development. These advancements can also increase the electrical energy consumption that demands high-efficient motor drives design and electrical machines eco-conception [10], [11], [12], [13] and [14].

Aforementioned challenges highlight the importance of efficient variable-frequency control allowing to reduce energy losses and to adapt the electrical machine torque and speed to the load. At the same time, electrical machines being a part of Variable Frequency Drives (VFDs) are subjected to repetitive surges issued from impulse voltage waveform with steep rising and falling edges when supplied from power converters [3], [4] and [15]. The arising electrical stresses can drastically accelerate the electrical insulation ageing and lead to Partial Discharges (PDs) inception in low voltage electrical machines [16], [17], [18] and [19]. This phenomenon, previously considered only in high voltage electrical equipment, provokes complex physico-chemical processes and decreases notably the

low voltage insulation service life.

The negative effect of impulse voltage becomes more important with the implementation of Wide Bandgap (WBG) power semiconductors as Silicon Carbide (SiC). The modern advances in semiconductors technology allow to create powerful inverters with higher switching speed and frequency range in comparison with Silicon technology, providing losses reduction, compactness, and lower weight [12], [20], [21], [22], [23], [24] and [25]. Due to these features SiC power semiconductor devices are especially attractive for motor drives in automotive, aerospace, and industrial applications where power density and weight are the main factors for power electronics dimensioning [12], [23] and [26]. Nevertheless, resulting electrical stresses are severe for the controlled motors: high dV/dt pulses with very fast rise time (about 10-50 ns), raise of common mode currents and electromagnetic radiation [24], [27] and [28]. Due to this fact, PDs will occur with higher probability and the motor insulation ageing will be accelerated shortening the service life.

Since the presence of PDs in inverter-fed low voltage motors have been recognized, numerous studies were related to characterize PDs, inception conditions and the influence of their presence on the insulation [16], [17], and to compare enamel winding wires' endurance to partial discharges (also referred as corona resistance) [29], [30], [31], [32], or to detect insulation defects [33]. Insulation lifetime models depending on the applied stresses and their interaction are described in [34] and [35]. Thermal, mechanical and electrical stresses effects on turn insulation were studied separately in [36] using experimental setups, without consideration of factors interaction effect. In [37] analysis and predetermination of voltage distribution and spikes in motor windings were carried out. In thesis [4] the voltage distribution modelling in simplified motor winding represented by equivalent circuit and the method to evaluate the risk of PDs occurrence are proposed.

The use of WBG power electronics in motor drives requires new methods and approaches to study PDs effect on motor winding insulation. In reference [27] the experimental setup is performed using SiC components reproducing environmental and operational conditions. Nevertheless, the fact that the tests are conducted on complex motor drive system makes them relatively expensive and difficult to use in order to study the physical processes of dielectric ageing, or to utilize in motors conception. Therefore, ageing and deterioration process in insulation subjected to impulse voltage, in particular, with high dV/dt and high commutation frequency are not thoroughly investigated. Moreover, considering the influence of thermal stresses affecting the insulation during motor operation, the process of electro-thermal ageing needs to be considered.

Objectives and methods

Having regard to the above, this study is dedicated to investigate the constraints applied to solid dielectrics used in inverter fed motors and their effects on motor windings considering the high dV/dt and high switching frequency specific to SiC-based inverters. To achieve these goals, the work is focused on the following axes:

- Develop models for determine voltage transients and surges at machine's terminals characterized by high dV/dt .
- Define the methodology for estimating the endurance of insulating materials used in low voltage electrical machines fed by inverters. In particularly, the turn insulation endurance in presence of partial discharges will be studied.
- Design the experimental test bench for reproducing the constraints imposed by impulse voltage waveform with high dV/dt and high switching frequency. The temperature effect also should be considered.
- Investigate the processes of electro-thermal insulation ageing and destruction due to partial discharges activity in inverter fed machines.

Main contributions

One of the main contributions of this work consists in revealing the influence of combined electrical and thermal effects on the enamel insulation resistance to partial discharges and insulation lifespan. It should be noted, that the high frequency impulse voltage waveform with steep edges is a limiting factor that determines the applicability of insulating materials in inverter fed motors. This is confirmed by experimental results of endurance tests when an accelerated deterioration and a change in insulation destruction mechanism were observed on wires' specimens subjected to voltage pulses having high dV/dt ratio and high switching frequency.

The partial discharges arising in air gaps between turns of winding wire's specimens subjected to high dV/dt impulse voltage having high commutation frequency have been characterized as filamentary dielectric barrier discharges; having regard that the twisted pair represents a physical model of machine's winding part, the PDs within the winding may be also considered and studied as dielectric barrier discharges.

The proposed testing methods and experimental benches allow to conduct accelerated ageing and endurance tests of enamel insulation under electrical stresses engendered by conventional Silicon (Si) and modern SiC inverters. Furthermore, a novel specimen's shape for testing enamelled rectangular winding wires is proposed that expands the range of studied motors.

Another contribution is a method of detecting insulation defects such as air gaps and cracks testing under the impulse voltage at low pressure. The random and artificial defects have been detected during the experimental study of partial discharges phenomenon on winding wire's specimens.

Outline

This thesis is organized into five chapters. The final part provides the main conclusions drawn from this work and future research axes.

The **first chapter** is devoted to factors affecting the insulation reliability of low-voltage electrical machines powered by inverters. The influence of defects and turn insulation components compatibility on mechanical and electric strength is considered. The negative effects of variable frequency control on the motor insulation system are identified, and the main solutions of the mentioned problems proposed in literature are discussed.

In the **second chapter** the high frequency model of the electric drive system composed by inverter, supply cable and motor is suggested. The main goal is to provide the analysis of overvoltage at motor terminals caused by high dV/dt and impedance mismatch between the inverter, cable and the powered motor, which plays an important role for motor insulation robustness. This study is focused on the modelling of a three-phase Switched Reluctance Motor (3-phase, 6-slot, and 4-pole). The high frequency model of the studied motor represents an equivalent circuit model with RLC lumped parameters extracted from common mode and differential mode impedance measurements. The supply cable model existing in literature is used. In the proposed electric drive model, the study of a single commutation is performed. In this regard, the inverter is modelled by an ideal pulse generator.

The **third chapter** presents the experimental study of winding wires endurance when subjected to electrical and thermal stresses provoking partial discharges activity. At the beginning of this chapter, the brief review of existing testing methods aimed to investigate partial discharges in electric motors and winding wires, as well as to determine wires insulation endurance is provided. Then the proposed methods and experimental benches allowing to perform insulation electro-thermal accelerated ageing tests are presented. The original test bench with the objective to study the effect of electrical stresses on motor winding insulation engendering by SiC high-speed switches has been designed.

The **fourth chapter** gathers the experimental protocols and obtained results followed by statistical analysis and main observations. Firstly, the results of breakdown voltage tests carried out under sinusoidal voltage are given. Then, the results of endurance tests conducted on studied winding wires under sinusoidal voltage, Pulse Width Modulation (PWM) low dV/dt impulse voltage (μ s-level of rise time) and rectangular high dV/dt

impulse voltage (ns-level of rise time) are presented. The influence of voltage waveform on turn insulation ageing and endurance, as well as the effect of thermal stresses are discussed.

The **fifth chapter** presents a phenomenological study of deterioration processes in turn insulation under PDs when subjected to high dV/dt impulse voltage. The high dV/dt bench and tested twisted pairs are modelled using different approaches. The partial discharges in twisted pair have been characterized as dielectric barrier discharges that offers an opportunity to apply the methods developed for ozone generators to our study using common aspects. The characterization of insulation deterioration processes in twisted pairs subjected to high frequency impulse voltage with high dV/dt allows a better understanding of winding insulation destruction of motors powered by SiC-based power converters.

The present thesis is a result of collaboration between the National Research Tomsk Polytechnic University (TPU), in Russia, and the Paris-Saclay University, in France. In accordance with the agreement on joint international supervision the research work and complementary training have been conducted at the laboratory of Systems & Applications of Information & Energy Technologies (SATIE) of ENS Paris-Saclay - France and the School of Energy & Power Engineering of TPU - Russia.

**Chapter I : Factors affecting low voltage
electrical machines fed by inverters:
literature survey**

Chapter I

Factors affecting low voltage electrical machines fed by inverters: literature survey

Contents

1 Introduction	12
2 Electrical machines	15
2.1 Induction machine	17
2.2 Switched reluctance machine	18
3 Electrical machine winding	21
3.1 Distributed winding	21
3.2 Concentrated winding	22
4 Electrical machine winding insulation system	24
4.1 Winding wires	24
4.2 Winding impregnation	26
4.3 Impregnating compositions and wires enamel insulation compatibility	27
5 Operational factors affecting winding insulation	29
5.1 Failures in motor windings	31
5.2 Effect of impulse supply voltage on winding insulation	32
6 Conclusion	39
References	43

1 Introduction

Variable Frequency Drives (VDFs) are widely used throughout industry, electrical energy production and transportation systems, providing energy savings and equipment performance improvement due to adjustable speed control of electrical machines. Electrical machines operate converting electrical energy in mechanical energy in “motor” mode or inversely in “generator” mode (regenerative braking). Schematic representation of typical system usually used in industrial applications composed of an induction motor fed by a power converter through a long supply cable is given in Figure I.1 [38].

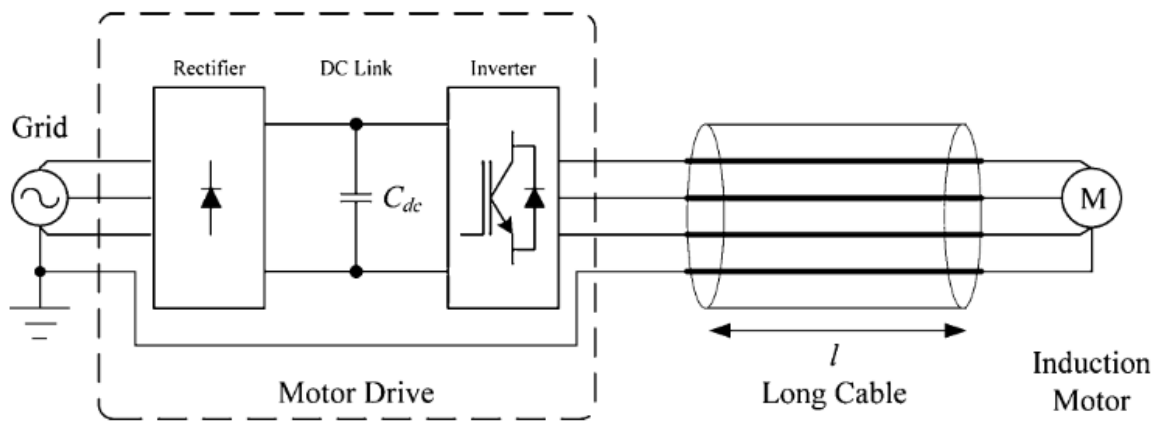


Figure I.1: Typical motor drive system with a long supply cable [38].

Depending on applications, the distance between machine and feeding converter can be shorter. For example, in automotive systems adopted electric propulsion, the traction electric motor and the controlling power electronic block can be disposed in close proximity. Figure I.2 depicts traction and charging power systems installed on-board of Renault’s electric vehicle: ZOE [39].

Another example of propulsion system for electric vehicles is a wheel motor technology [40] and [41]. The Michelin Active Wheel concept (Figure I.3) was firstly presented at “Challenge Bibendum 2004’s edition”. In-wheel electric drive integration is a promising technology, which combines mechanical and electrical components giving opportunities for suspension’s mass reducing and driving strategies optimization. With the purpose to obtain more compact embedded systems, deep converter-integration concepts, consisting of electrical machine and integrated VDF, are designed [14] and [42].

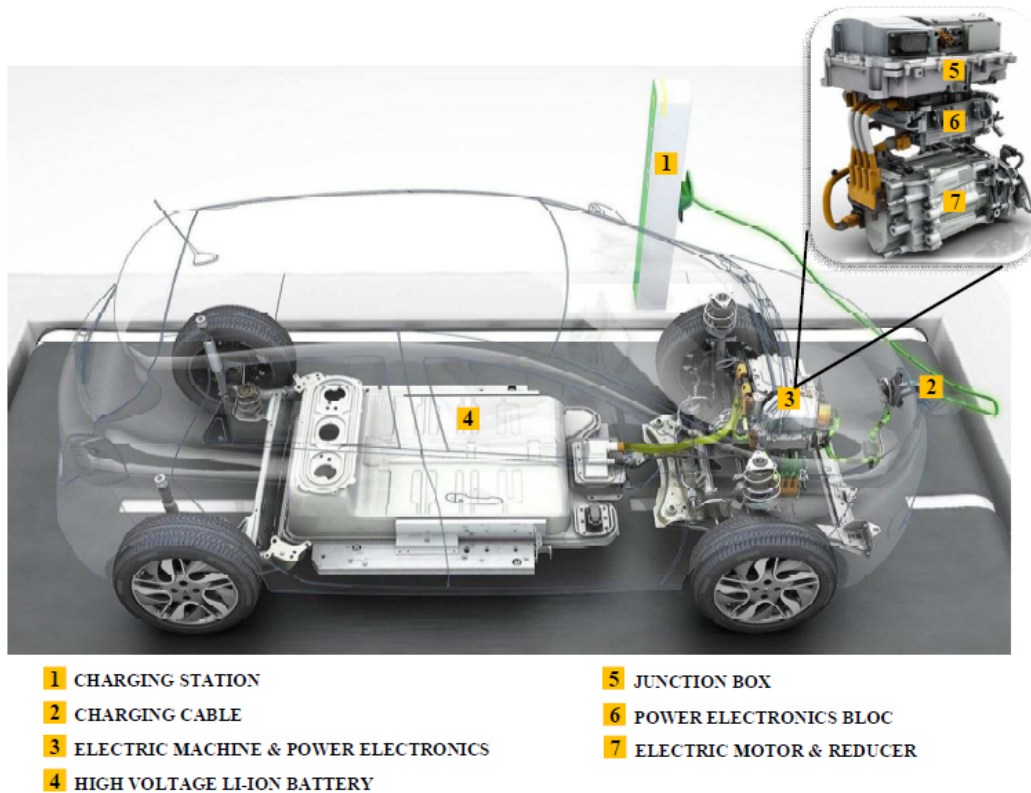


Figure I.2: Traction and charging power trains on-board of Renault's electric vehicle: ZOË [39].

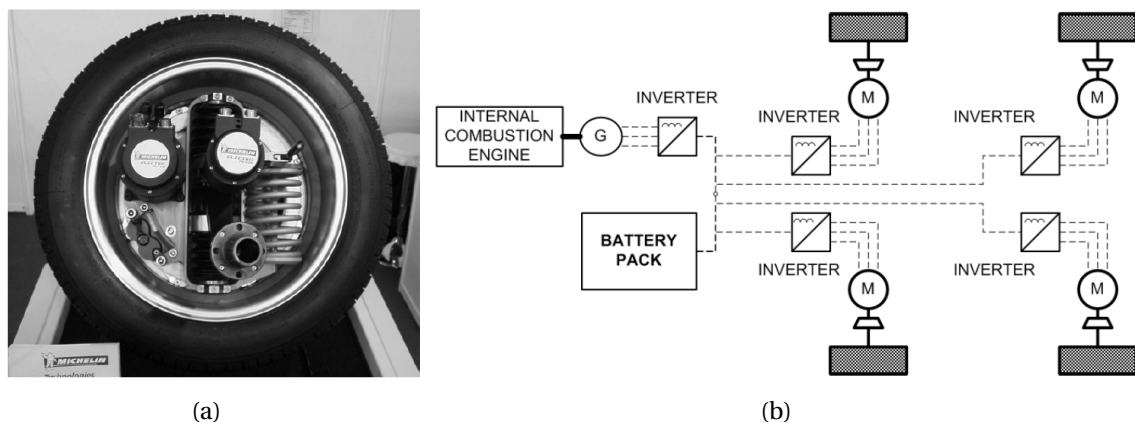


Figure I.3: Michelin Active Wheel System:
 (a) image of propulsion, brake, energy recovery and suspension;
 (b) vehicle powertrain scheme [41].

Regardless of integration technology, electrical machine being part of electric drive, constitutes the final element of a chain of energy conversion; it is at the interface between the power converter and the mechanical system. Therefore, it constitutes a preferred route for the transmission of electromagnetic interferences in the environment and is also influenced by electrical stresses characterized by steep rising and falling pulses with very straight fronts (high dV/dt) generated by Pulse Width Modulation (PWM) converters, reflected waves in cable line, mismatching of cable and motor winding impedance

caused by high frequency component in VDF systems. The complexity of these components, their three-dimensional character, the operational conditions and multi-materials are very difficult objects to study and model in this context. Furthermore, for the power converters used in transport applications, maximum temperature at which they will operate trends to rise to about 120 °C for automobile and 200 °C for aeronautics. This development therefore is due to the use of a new generation of Wide Bandgap (WBG) semiconductors, such as Silicon Carbide (SiC). The modern advances in semiconductors technology allow to create powerful inverters with high temperature capability, higher switching speed and frequency range in comparison with Silicon technology, providing losses reduction, compactness, and lower weight [12], [20], [22], [23], [24], [25] and [26]. Due to these features, SiC power semiconductor devices are especially attractive for motor drives in automotive, aerospace, and industrial applications where power density and weight are the main factors for power electronics sizing (see Figure I.4) [43].

SiC Application Areas – Early Adopters



Figure I.4: SiC Application areas presented in AgileSwitch SiC Product Overview [43].

Figure I.5 shows inverters developed by ROHM demonstrating the power devices technology evolution in sport electric vehicles of Formula E, all-electric-powered FIA (Fédération Internationale de l'Automobile). The new embedded Full SiC Power module makes 200 kW inverters 43% smaller and 6 kg lighter [44] compared with Silicon (Si)-based converters.



Figure I.5: Si and SiC inverters comparison [44].

At the same time, the advent of WBG devices provokes the rising of electrical stresses in controlled motors windings affecting their electrical insulation and shortening the service life. Development in power electronics that provokes changes in motors operation makes it necessary to determine the main influencing constraints and to refine the existing approaches to assess the winding insulation endurance.

Having regard to the above, this Chapter presents a literature survey on low voltage motors and their insulation systems, detailing the key factors affecting motor winding insulation. There, the influence of impulse supply voltage on the electrical machine controlled by PWM inverters will be studied and negative effects caused by long supply cable will be discussed.

2 Electrical machines

Electric motors consume large part of worldwide produced energy. They cover a vast number of applications everywhere in industry, transport, and household appliance, with different sizes and supply voltages. The electric motor is also the central component in Hybrid Electric Vehicles (HEVs) and Electric Vehicles (EVs). Concerning automotive applications, there are many types of motors that could be used in electric traction drives HEVs and EVs [14] and [45] (see Figure I.6).

Regarding aeronautics and aerospace applications, a particular attention is given when selecting electric motor type and drive topology. It is especially crucial in More Electric Aircraft (MEA) where electric driven systems replace conventional mechanical, hydraulic, or pneumatic systems providing technical and economic improvements. An overview of motor drive technologies used for safety-critical MEA applications is given in [46]. According to this overview, the feasible candidate machines are limited to motors

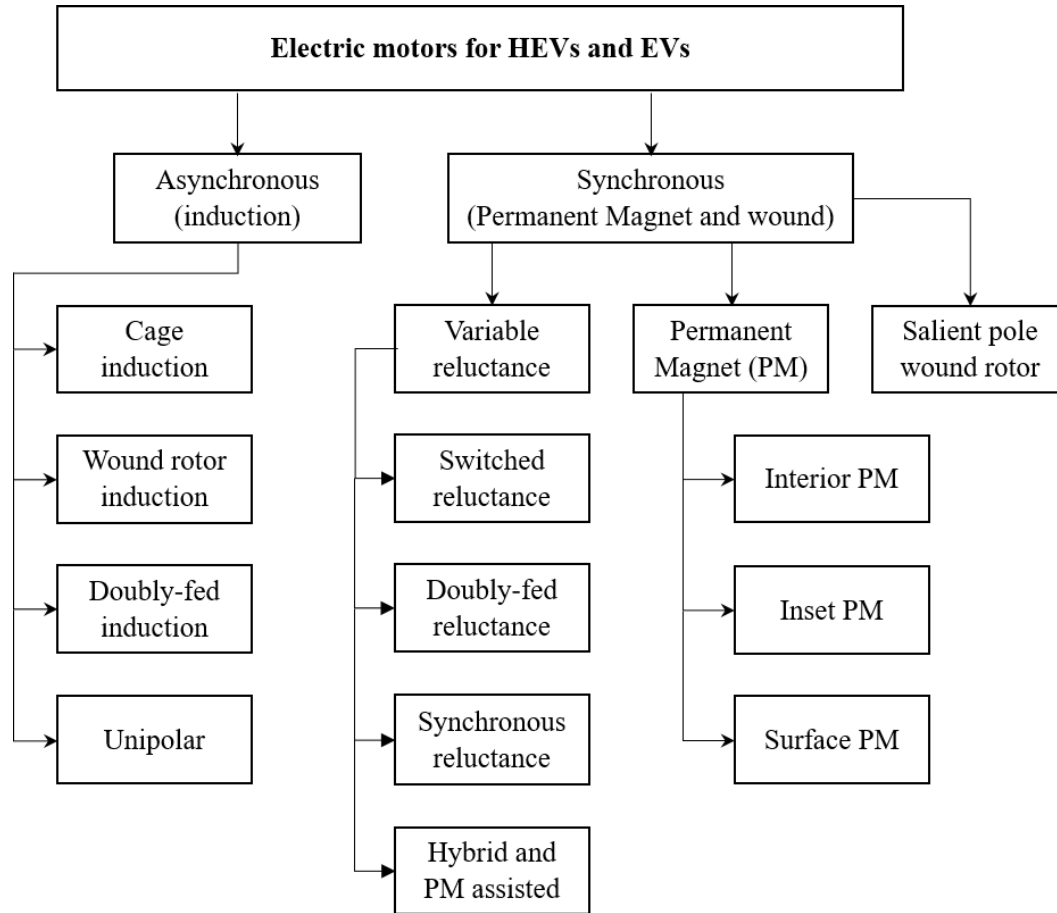


Figure I.6: Chart of possible motor choices for HEVs and EVs [45].

shown in Figure I.7. To ensure safe, reliable and efficient operation, a number of factors should be considered such as environment, thermal robustness, efficiency, weight, volume, life, controllability, torque, speed, power source. Figure I.8 gives a performance comparison of motor technologies that can be used in aerospace applications.

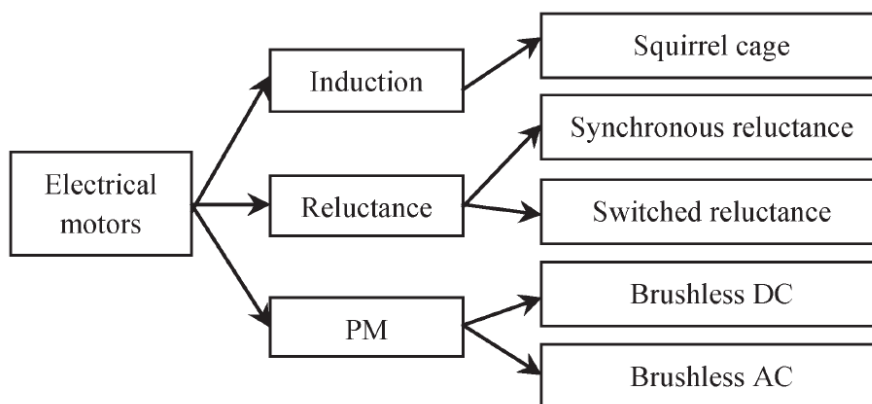


Figure I.7: Machine options for the MEA drive system [46].

Performance	IM-cage	SR	PMAC
Fault tolerance	low	high	high
Power density	moderate	moderate	high
Robustness	√	√	×
Efficiency	moderate	high	high
Cost	low	low	high
Wide speed range	×	√	√
Open-loop control	√	×	×
Close-loop simplicity	√	√	√
Torque ripple	×	high	low
Acoustic noise	×	moderate	low
Areas of application	actuators	high-temp. engine	fuel pump actuators

Figure I.8: Performance comparison of motor technologies [46].

Among electric motors shown in Figures I.6 and I.7, there are traditional widely used motors and recently developed. These motors differ in control and operational modes, costs and efficiency, having their advantages and disadvantages. In this research we will be focused on two types of low-voltage electrical machines¹: Induction Machine (IM) as the most used, and Switched Reluctance Machine (SRM) as competitive and promising for electric vehicles and fault-tolerant aerospace applications.

2.1 Induction machine

The fields of application of induction machines comprise a significant part of the industry applications, owing to their reliability, ruggedness, robust construction, and lower cost of maintenance compared with synchronous electrical machines and DC motors, and also their ability to operate in hostile environments [1], [45], [47] and [48]. In automotive drives IMs are utilized in such vehicles as Renault Kangoo, Daimler Chrysler Durango, Chevrolet Silverado, BMW X5, and Tesla [47]. One of the most widely utilized type of IM is the well-known cage (or squirrel cage) induction motor. The cage induction motor predominance is attributed to the simplicity and ruggedness of the rotor [1]. Figures I.9 and I.10 show the construction and magnetic circuit of an induction motor respectively [8].

Induction motors main drawbacks are high losses (stator copper losses, core (iron) losses, stray and mechanical losses), low efficiency, and low power factor. To improve their efficiency and performance, IMs should be controlled through power converters as shown in Figure I.1 and different minimum-loss control schemes and strategies can be utilized, as described in [49] and [50].

¹According to IEC classification, low-voltage refers to motors that operate at voltages less than 1000 V

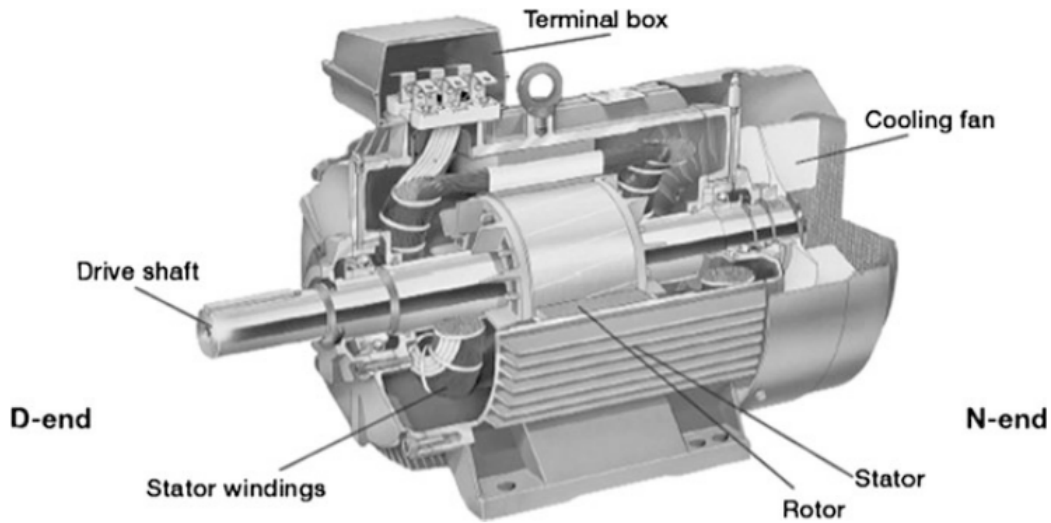


Figure I.9: Construction of an induction motor (dissected view) [8].

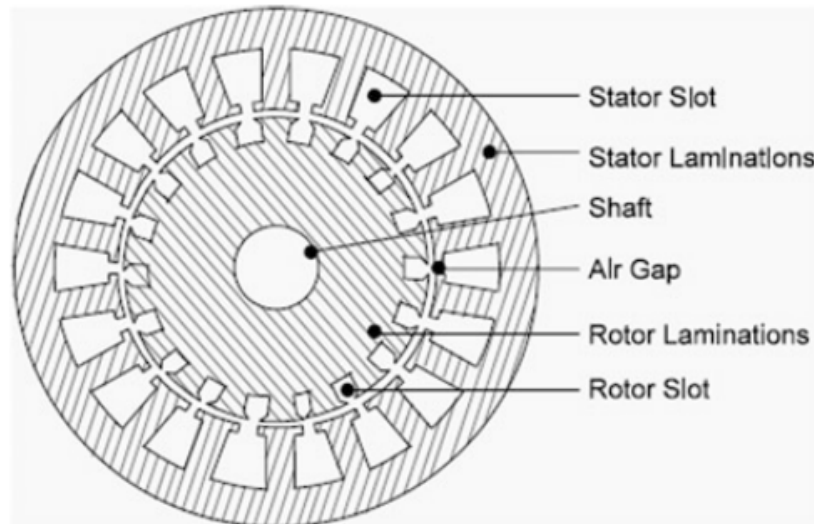


Figure I.10: Magnetic circuit of induction motor's stator and rotor [8].

2.2 Switched reluctance machine

Compared with mature motor technologies such as the induction motor, DC shunt motor, and the more recent brushless Permanent Magnet Synchronous Machine (PMSM), SRM offers a competitive alternative to its counterparts [14] and [51]. The numerous advantages such as high torque density, simple construction, robustness and low manufacturing cost make this type of machines attractive for researchers and manufacturers [52].

The most used conventional SRM have different numbers of salient poles on the stator and rotor. There are two windings of different phases in the each slot of the stator. The rotor does not contain any windings or excitation system which allows reaching very high speeds [53]. Moreover, by contrast with PMSM, this machine do not contain costly rare earth permanent magnets. As an example, the construction of three-phase 12/8 SRM

(12 stator poles and 8 rotor poles) and its magnetic circuit are depicted in Figures I.11a and I.11c respectively [54].

The SRM operation principle is based on variable reluctance. The torque is produced by the tendency of the rotor poles to align with the excited stator poles (see Figure I.11b). During rotation of a rotor, the reluctance and, consequently, the phase inductance vary between their minimal and maximal values. When operated as a motor, the phase windings are excited during the period in which the inductance is increasing as the rotor turns. When operated as a generator, the phases are commutated on and off during the period when the inductance is reduced as the rotor turns. The higher the ratio of aligned inductance to the unaligned inductance, the higher the torque [55] and [56].

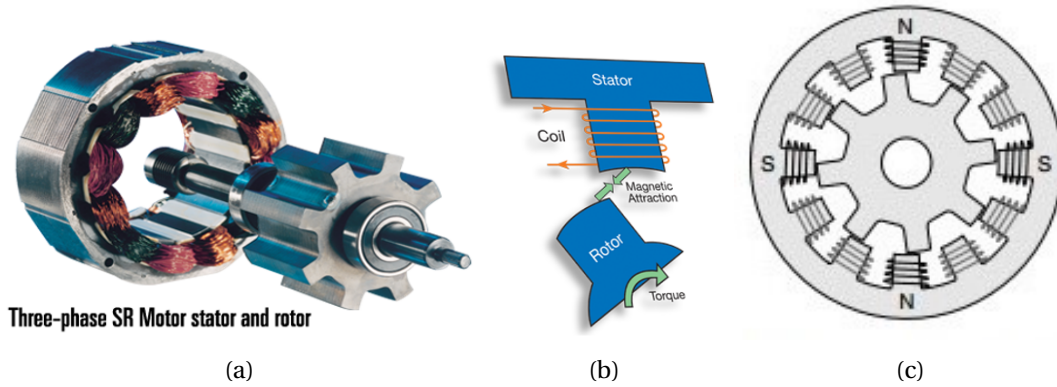


Figure I.11: Three-phase SR Drive® stator and rotor (graphic of NIDEC Motors) [54]: (a) SRM construction; (b) principle of operation; (c) magnetic circuit.

Based on the previously mentioned, the torque T of three-phase SRM can be defined as follows:

$$T = \frac{1}{2} i_a^2 \frac{dL_a}{d\theta} + \frac{1}{2} i_b^2 \frac{dL_b}{d\theta} + \frac{1}{2} i_c^2 \frac{dL_c}{d\theta} \quad (I.1)$$

where i_i and L_i are the corresponding phase currents and inductances; θ is an electrical angle that defines a rotor position. As shown in [52] the mutual inductance between phases for conventional SRM can be neglected due to its winding configuration.

According to the expression I.1, the torque is directly proportional to $\frac{\partial L}{\partial \theta}$ and I^2 , where the last one is always positive regardless of the sign of excited current, so the excitation can be unipolar. Unipolar operation requires nonstandard power electronic modules: SRM is mostly driven by asymmetric half-bridge power converter [57] (see Figure I.12). Another converter's topology can also be employed depending on applications and requirements, *e.g.*, bipolar excitation can be used to increase the torque density and reduce torque pulsations [56] (see Figure I.13).

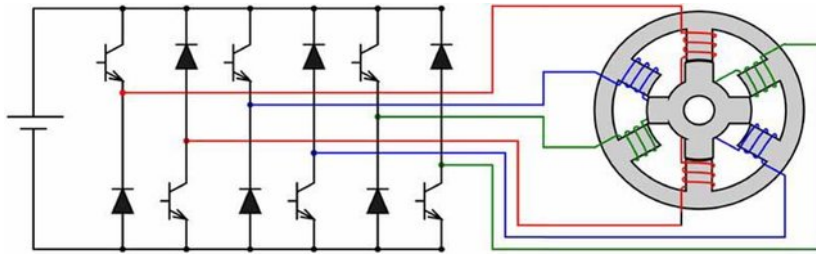


Figure I.12: Three-phase SRM driven by asymmetric half-bridge converter [57].

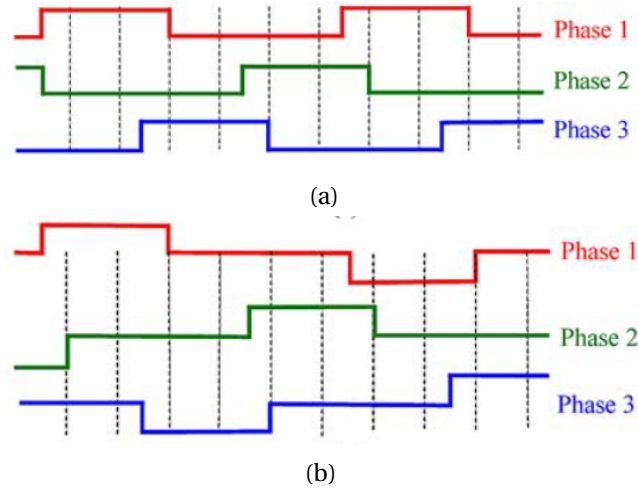


Figure I.13: Conventional excitation (a) and bipolar overlapping excitation (b) [56].

There are different types of SRM, where the stator and rotor poles number combinations and phase's number determine the machine and drive configurations and performances. Increasing stator/rotor poles number allows to produce the higher power factor and torque density with lower torque ripple. On the other hand, it reduces the constant power capability and the overload capability. A larger number of phases improves the reliability and fault tolerance, but complicates the inverter and requires a higher operating frequency for a given speed [55] and [56].

Overviews [14], [45], [47], [56], [58] and research works [53], [59], [60] and [61] on automotive propulsion systems demonstrate that switched reluctance motors are recognized to have a potential for EV/HEV applications. Examples of SRM drives automotive application are Land Rover Defender, presented at the 2013 Geneva Motor Show [62], the Australian hybrid ECOMmodore and hybrid aXcessaustralia Low Emission Vehicle (LEV) [60].

The main disadvantages of this type of electrical machines are the high torque ripple, the acoustic noise and vibrations (especially at low speeds), undesirable in modern vehicles [51]. These drawbacks can be minimized by optimization of control strategy (torque/current control) and motor design. The SRM with controlled torque can find application where standard variable frequency drives are common.

3 Electrical machine winding

As can be seen from the foregoing, two types of electrical machines (cage induction motor and switched reluctance motor) are considered in this work. Thus, only stator winding insulation systems will be discussed.

3.1 Distributed winding

Like most low voltage motors, the cage induction motor has a randomly distributed stator winding. The construction of a random wound winding is given in International Electrotechnical Commission (IEC) standard 60034-18-41:2014 [63] and depicted in Figure I.14; the stator winding photograph is shown in Figure I.15 [64].

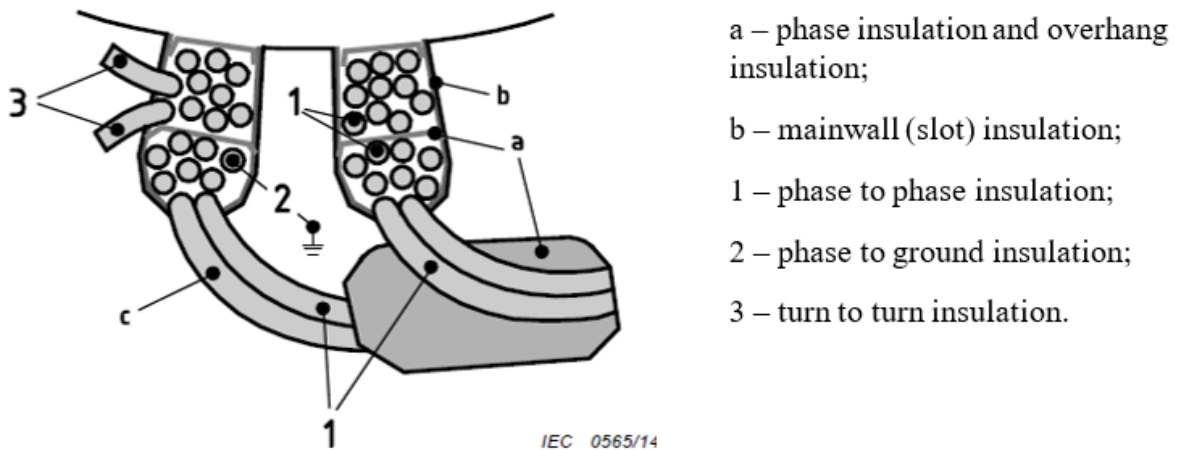


Figure I.14: Section of stator winding [63].

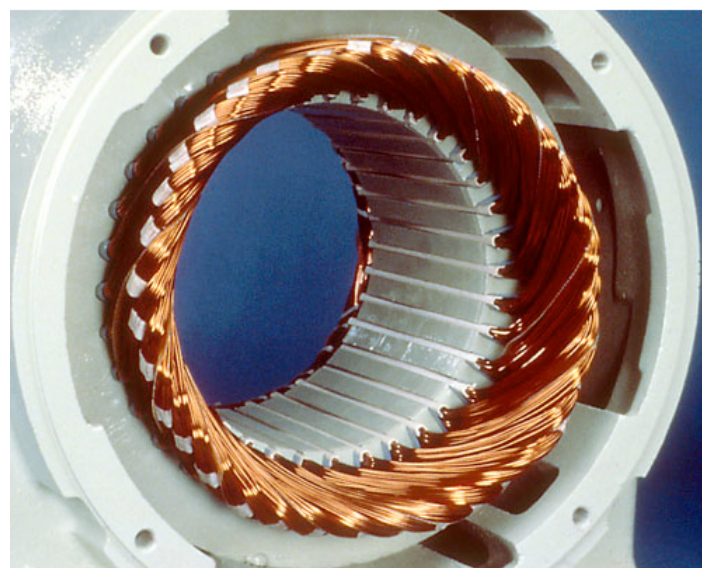


Figure I.15: Distributed stator winding [64].

Random wound winding consists of round insulated conductors, called winding wire or magnet wire. This wire is wound continuously (by using a winding machine or by hand) through slots in the stator magnet core to form a coil: turns of wire connected in series, arranged to link or produce magnetic flux. These turns are placed randomly in coils, thus the term “random”. The first and the last turns can be adjacent, and in this case turn insulation is subjected to the entire voltage of the coil [1]. The winding insulation system’s components will be detailed in Section 4.

3.2 Concentrated winding

By contrast with induction motors, switched reluctance motors usually have a concentrated coil winding configuration. Comparison between distributed and concentrated winding design is demonstrated in Figure I.16 by the example of synchronous permanent magnet machine stator structures given in [65]. As can be seen, overlaps between coils referring to the different phases are eliminated in concentrated winding. The photograph of concentrated stator winding is shown in Figure I.17.

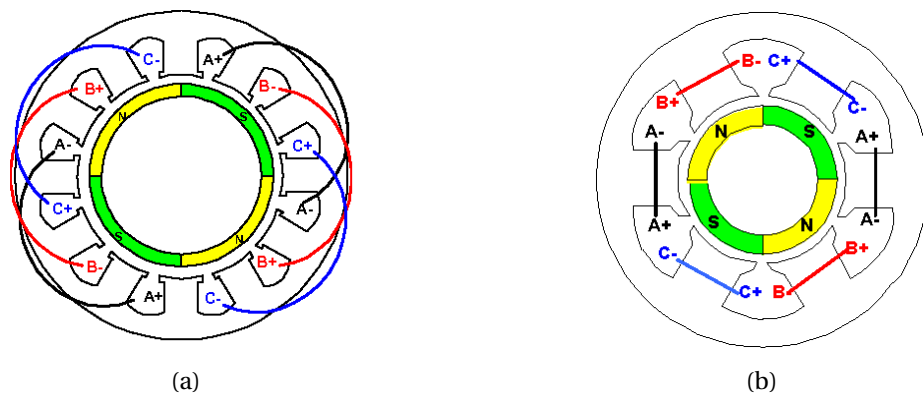


Figure I.16: Distributed (a) and concentrated (b) winding configurations [65].

In case of conventional switched reluctance motor, winding is wound around each tooth of the stator that allows to minimize magnetic coupling between phases and make easier electrical feeding [51] and [52].

Both round and rectangular sections wires can be used to constitute winding coils. The use of rectangular winding wires allows to increase a slot filling factor (or space factor), the ratio between the total conductor area in a slot and slot area, as shown in Figure I.18 [67]. This parameter determines the motor’s rated power. By improving the slot filling factor the power density may be increased and the DC winding losses may be reduced [68].

The coil concentrated winding configuration simplifies mechanical design and manufacturing process as well as machine’s maintainability by offering a stator modularity possibility [68]. It makes possible to arrange turns in winding coils in order to assure better electric field distribution compared with random wound winding.



Figure I.17: Concentrated winding configuration of a Hyundai Sonata 2011 motor [66].

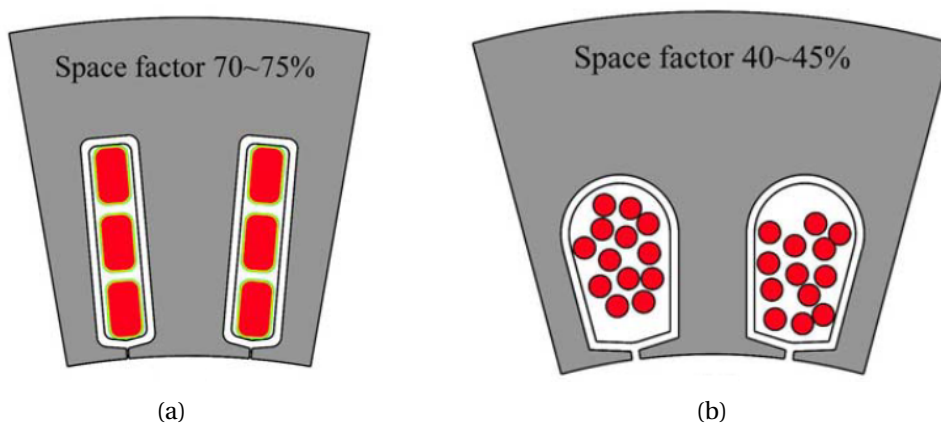


Figure I.18: Difference between rectangular (a) and round (b) conductors placed in stator slot [67].

The multiphase concentrated winding can improve the electrical machine's fault tolerance [69]. Nevertheless, the turn insulation tends to be exposed to higher mechanical stresses during the coil-forming process, creating insulation stretches and cracks [1]. Furthermore, distributed windings demonstrate higher torque and power density performances compared with concentrated winding [68]. The stator winding topology should be selected regarding electrical machines speed and power range, and respecting torque, volume and efficiency requirements.

4 Electrical machine winding insulation system

Electrical machine's insulation system is a combination of dielectric materials. According to IEC 60034-18-1:2010 [70], its role is to provide insulation of conducting parts from each other and grounded ones, to prevent short-circuits between winding turns, and thus to ensure reliable electrical machine operation.

In the following sections components of stator winding insulation systems, as well as the main factors affecting them during machines operation will be discussed.

As previously noted, winding insulation system comprises slot insulation, phase to phase, phase to ground and turn insulation. The slot insulation, phase to phase and phase to ground insulation are usually made of paper or organic laminated materials based on polymers (Nomex®, Mylar®) providing good dielectric strength, flexibility, mechanical toughness and thermal conductivity. This insulation has a greater thickness compared with the turn insulation composed of winding wire and impregnating composition [1], [3], [4] and [71]. Whereas the turn insulation is mostly subjected to failures, this component of insulation system will be studied in detail.

4.1 Winding wires

Winding wires having thin enamel insulation (enamelled wires) are mostly used in low voltage electrical machines windings. The thinner insulation allows to assure a higher slot filling factor. Moreover, overall dimensions of motor can be decreased by reducing the insulation thickness while keeping the energetic parameters [72].

The enamelled winding wire is a copper or aluminium conductor coating with a polymer film insulation composed of one, two, or three types of enamel varnish – insulating layers (Figure I.19). In modern winding wires the combination of different chemical compositions is often used to provide the required electrical, thermal and mechanical parameters [73].

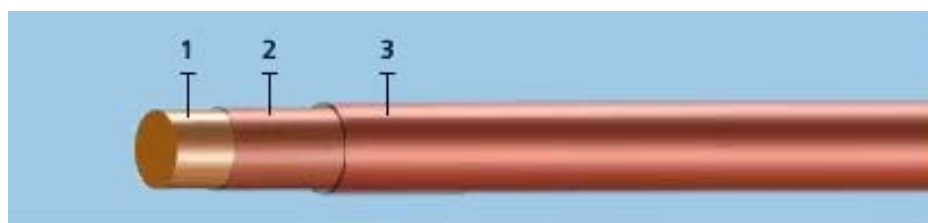


Figure I.19: Enamelled wire with double layer insulation:
1 – copper conductor; 2 – inner insulating layer (base), 3 – outer insulating layer (top).

Enamel varnish is a solution of high-molecular-weight film-forming compounds in organic volatile compounds, where the volume of a dry (solid) substrate in average corresponds to 28-32% [74] and [75]. Depending on required winding wire insulation

properties and motor operation conditions, different chemical compositions can be applied. The most common are the enamel varnish based on polyester (PE), polyimide (PI), polyurethane (PU), polyamide (PA), polyamide-imide (PAI), and polyester-imide (PEI).

The enamel film should be applied to the wire continuously and as thinly as possible. Firstly, it allows to have a good filling factor of wound stator, as it was mentioned above. Secondly, it prevents the falling drops of liquid varnish which tend to distribute unevenly over the wire. Therefore, each insulating layer (of one chemical composition) consists of a number of very thin coats (Figure I.20), which are applied sequentially passing through an enamel applicator. This reduces amount of defects and micro-voids in the enamel insulation resulting from the volatilization of low-molecular additives and solvents. The number of these single layers can reach up to 20-30 μm and the total thickness of the enamel film comes to be from 30 to 60 μm [74] and [75]. Depending on the insulation range of thickness or grade, enamelled wires are categorized in accordance with the IEC 60317-0-1:2013 [76]. The insulation grade is defined by external wire's diameter D ($D_{\text{grade1}} < D_{\text{grade2}} < D_{\text{grade3}}$). Therefore, properties which depend on the thickness of the insulation (*e.g.*, electrical breakdown voltage, resistance to abrasion, springiness, *etc.*) vary from one grade to the next. A higher grade number means that wire has higher electric strength.

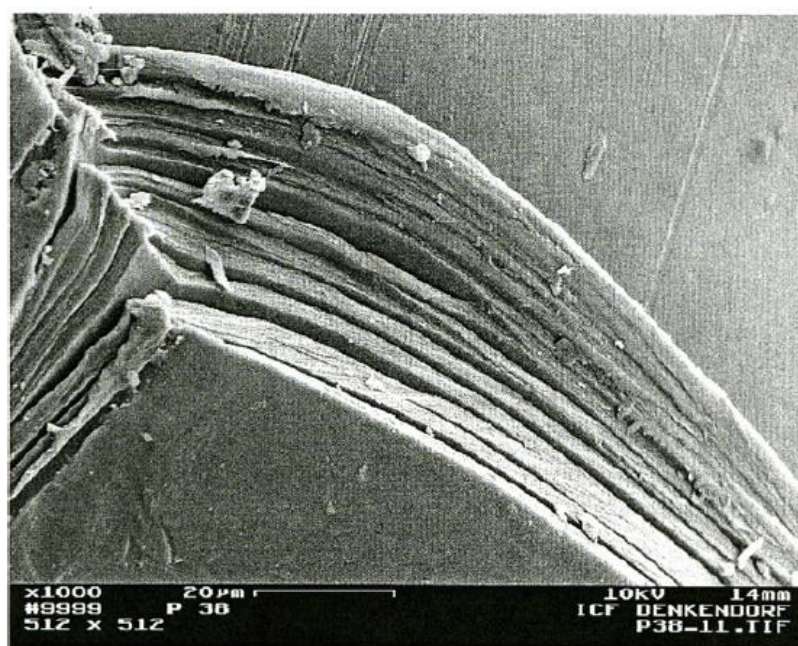


Figure I.20: Scanning electron microscopy image of enamelled wire, chemical composition PAI and PEI, 13 layers, total thickness 50 μm [75].

The copper round enamelled wire is the most prevailing winding wire type by reason of production process features and product quality. The interest in aluminium conductor is based on its lower costs and low-weight properties especially attractive for aircrafts and automotive applications. The main drawback of aluminium is the lower perfor-

mance compared with copper, consisting in higher resistivity, lower tensile strength and higher coefficient of thermal expansion. Moreover, to improve aluminium winding wire quality, special methods and equipment are required in manufacturing processes. Special lacquer layer called “primer” should be firstly applied to assure good enamel film adhesion to aluminium conductor [74]. To this purpose, an additional lacquer unit is used.

Since the electrical equipment operating temperature is often the dominant ageing factor affecting insulating materials, one of the most important parameters of winding wires is their thermal class (or temperature index). A thermal class shall be assigned to the insulation materials and systems used in electrical machines in accordance with IEC 60085:2007 standard [77]. This is a temperature numerically equal to the temperature at which the breakdown voltage (or other parameter) remains above a certain predetermined level for at least 20.000 h. In this regard, the classification of the winding wires is carried out over a long permissible operating temperature. Insulating materials intended for use in rotating electrical machines correspond to the heat resistance classes 130 (B), 155 (F) and 180 (H) [48] and [77]. According to [73] and [74] in Russia enamelled wires having the thermal classes of 155 and 180 are mainly produced. Furthermore, higher winding wire thermal class allows to increase electrical machines power density or to reduce their size and weight that is especially crucial for traction drives.

4.2 Winding impregnation

With the purpose to consolidate winding's turns, the winding is impregnated with a liquid impregnating composition (compound, resin or varnish). Epoxy, polyester or silicon resins are often used. The impregnation reduces air voids inside stator slots and between winding wire's turns, prevents winding moisture and contamination, improves winding mechanical strength and heat transfer.

For wound stator impregnating, dipping, trickling or Vacuum Pressure Impregnation (VPI) technologies can be used. In dipping method, the winding is fully immersed in reservoir containing liquid impregnating varnish until air gaps filling with following curing in an oven and cooling. Trickling impregnation process is performed at a very slowly rotating wound stator and the impregnating material is dripped over. During this process a current circulating in winding increases its temperature due to Joule effect to cure the impregnant. In VPI impregnation processing, the wound stator is placed under vacuum to remove air from winding gaps and pores, and placed in impregnation resin bath. Then the excessive pressure is applied to force impregnating material penetration into the stator winding. After that, draining and baking processes follow to cure the impregnant. VPI impregnation allows to improve air gaps filling between conductor strands minimizing voids in turn insulation and providing a greater bond strength [1].

As an alternative to impregnation self-adherent enamelled wires can be used. Their thermo-adhesive external layer, *e.g.*, made of aromatic polyamide, allows to solidify winding turns by bonding at elevated temperature. To this effect, winding heating is usually achieved by circulating current that cures wires' enamel top coat [3].

4.3 Impregnating compositions and wires enamel insulation compatibility

As far as the winding insulation system includes the winding wire enamel film and the impregnating composition, winding insulation reliability is determined by quality and compatibility of both insulating materials. Differences in chemical and physico-mechanical properties of these components may cause negative effects on insulation system performance [75].

The impregnant, the enamel film and the conductor are held together by adhesive forces. These forces create intermolecular bonding between contacting surfaces and provide system mechanical integrity. System components are forced to be deformed together under thermal cycling or external loads, but differences in materials' coefficient of thermal linear expansion and modulus of elasticity lead to unequal deformations. As a result, subsurface stresses appear in insulation. Engendered mechanical integrity deterioration facilitates penetration of moisture, oxygen and corrosive components into windings, intensifying turn insulation ageing processes and decreasing breakdown voltage [73] and [74].

Solvents contained in impregnating compositions affect enamel insulation during impregnation process and subsequent curing. As a result, enamel insulation softening, swelling or cracking may occur. Swollen enamel film adhesion often decreases while heating that leads to contact imperfections with conductor. Solvent negative influence increases with heating and mechanical stresses in enamel insulation caused by wires stretching and bonding when stator is wound [74]. Depending on impregnating composition (varnish, resin, compound, with solvent or solvent-free), impregnation technique and conductor strands density, turn insulation may have different microstructures. A complete filling of interturn space allows to obtain a monolithic turn insulation microstructure (Figure I.21a). When an impregnant is partially leaked or solvent is evaporated during curing process air pockets (cavities) appear in impregnated winding. The cured impregnating material is distributed around wires as a film with uneven thickness. Such insulation microstructure is called cellular (Figure I.21b) [71].

The real winding usually has mixed microstructure. The monolithic and cellular microstructures ratio depends on used impregnating material, its technological features (viscosity, non-volatile matter content), impregnating method and quality, as well as on wire's diameter, slot filling factor and winding design. Turn insulation microstructure,

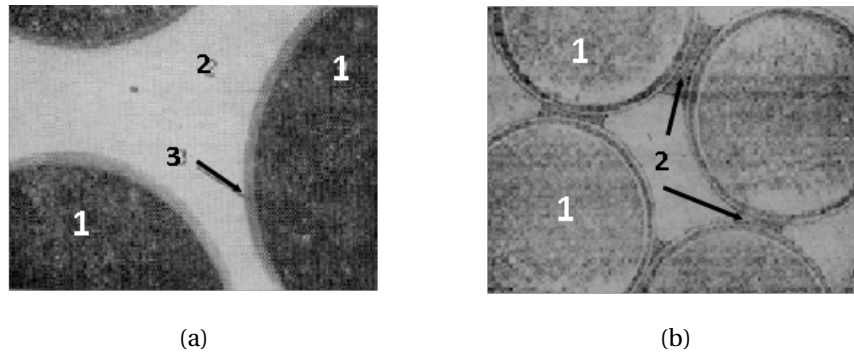


Figure I.21: Turn insulation microstructures microscopy images:

(a) monolithic microstructure; (b) cellular microstructure;

1 – winding wires' conductors, 2 – impregnating material, 3 – enamel insulation film [71].

polymers properties and adhesive forces determine crack formation mechanisms.

The minimum level of impregnant and enamel film adhesion should ensure windings integrity. Adhesion increasing leads to rising internal mechanical stresses in the impregnating material and affects defect formation processes. Therefore, turn insulation destruction processes start with impregnating material cracking caused by internal mechanical stresses. When a crack reaches enamel insulation, its propagation mechanism depends on adhesive forces in “impregnating material - enamelled wire” interface and eventual surfaces imperfections. The mechanism is described in [71]. In front of the crack tip, which is a stress concentrator, the local internal mechanical stresses magnitude is significantly higher than in the rest of the polymer's volume. If interface adhesive force is higher than internal mechanical stresses in impregnating material, the crack can pass through the enamel film and reach the wire's conductor (Figure I.22a). A crack propagation can be suspended if a tensed zone, moving in a form of a wave in front of a crack, causes an appearance of a cavity at the interface (Figure I.22b). The resulting cavity becomes a trap for the crack, and further crack propagation is suspended. The microscopy images of two described cases of the crack propagation in turn insulation are given in Figures I.23a and I.23b [71].

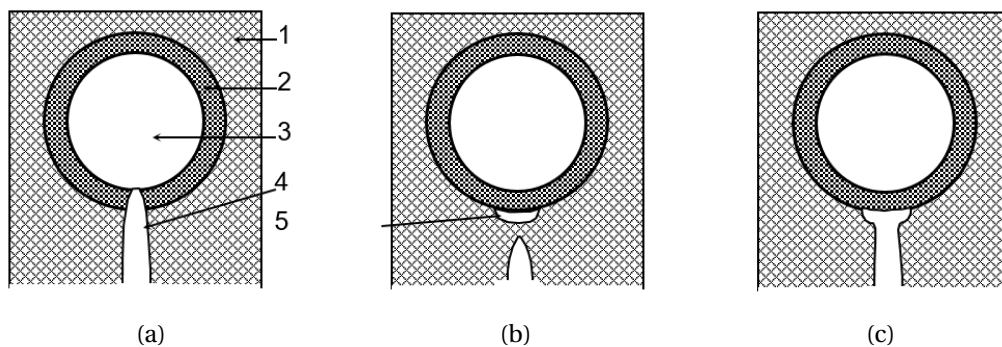


Figure I.22: Crack propagation mechanism in turn insulation:

1 – impregnating material; 2 – enamel film; 3 – conductor; 4 – crack in the impregnating material; 5 – delamination of impregnating material from enamel film (secondary crack) [71].

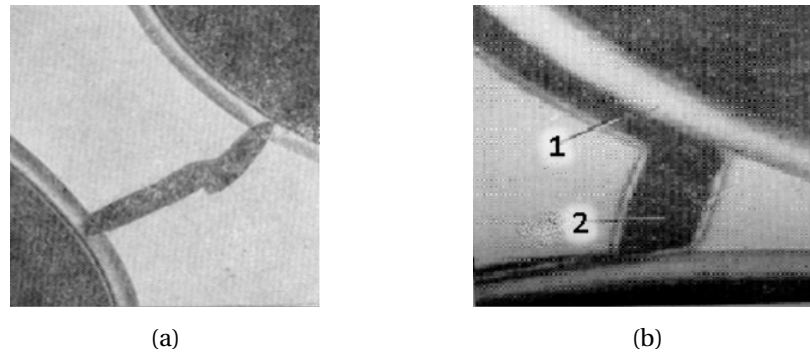


Figure I.23: Crack propagation in turn insulation microscopy images:
(a) crack in impregnating material passed through enamel films and reached conductors;
(b) crack in impregnating material with delamination from enamel film [71].

Having regard on above stated, turn insulation components should be selected considering their chemical and physico-mechanical properties and their compatibility characterized by interface adhesive forces that will allow to obtain the insulation system having minimum defects.

5 Operational factors affecting winding insulation

During production and operation processes, insulation is influenced by Thermal, Electrical, Ambient and Mechanical stresses (TEAM), including also pressure, moisture, and corrosive substances [1], [75], [78], [79] and [80] (see Figure I.24 [80]). It results in ageing and time-dependent deterioration of insulation properties that can reduce motor's service lifetime.

Environmental humidity influences on electrical machines time between failures, because moisture adsorption and sorption processes in insulating materials reduce its dielectric strength. Moisture effect is especially significant in poorly impregnated winding. In this case, moisture penetrates into unfilled space and diffuses into insulation's pores. Reducing insulation resistance and dielectric strength, moisture creates conditions for leakage currents appearance. Chemically active substances, such as oils and solvent vapours, influence on insulation leading to its deterioration. A dust contained in the air has an abrasive effect on insulation and reduces its insulating resistance [3] and [79].

Mechanical and thermomechanical factors can also reduce insulation service life. Thermomechanical loads in electrical machines are the results of windings heating and cooling cycles. Mechanical loads result from electrodynamic forces, centrifugal forces, rotating parts unbalance, shocks and jolts from a drive or a driven mechanism. In automotive transportation systems, electrical machines are also subjected to external vibrations depending on traction mode; these efforts are usually alternating and cyclical. During transients, vibrations magnitudes increase (the quadratic dependence of electrodynamic

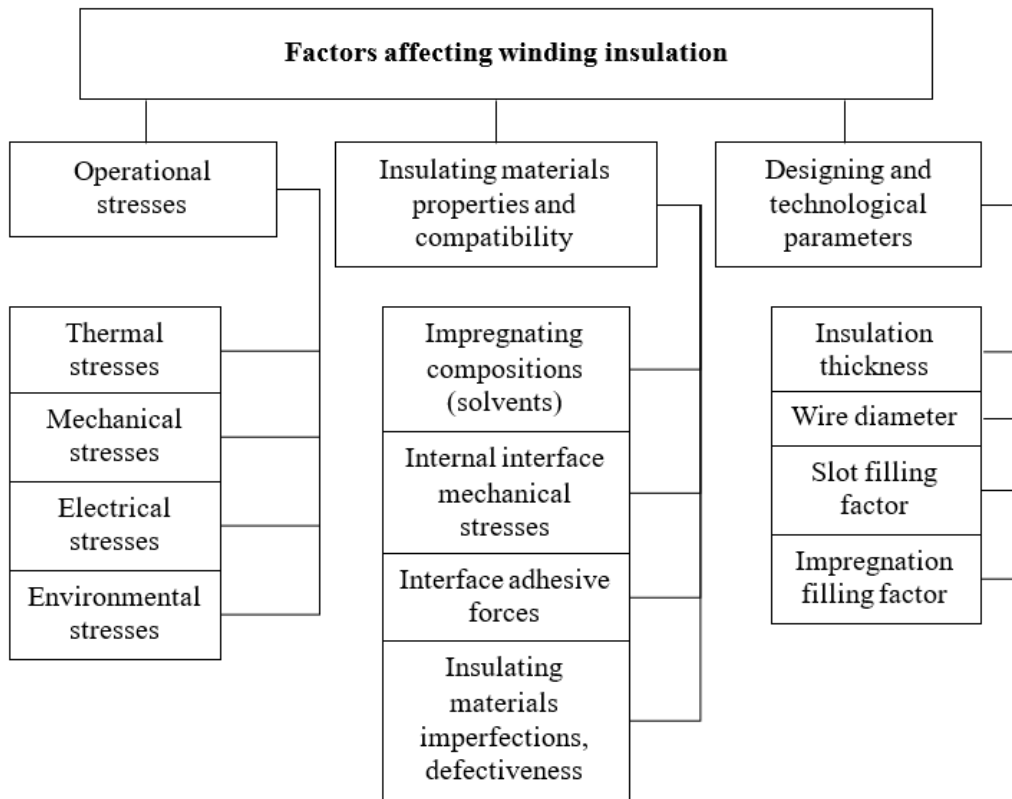


Figure I.24: Main factors affecting winding insulation during electrical machines manufacturing and operational processes [80].

forces on current). Cycles of mechanical and thermomechanical loads damage the insulation system integrity [80].

In case of sinusoidal 50-Hz AC supply voltage, the temperature effect is considered as one of the main operational factor causing the low-voltage insulation properties degradation [1], [2], [3], [8] and [81]. The low-voltage winding insulation is primarily determined by the electrical stress [1].

Prolonged heating during the electrical machine operation is inevitably accompanied by the winding insulation system thermal ageing and deterioration provoked by chemical reactions of oxidation in air-cooled machines [1]. The chemical reaction rate can be estimated using empirical Arrhenius law. In [82] it is proposed to use the Arrhenius chemical reaction rates relationship formulated in the exponential form to predict insulation life depending on expected service temperature:

$$L = Ae^{\frac{-B}{T}} \quad (I.2)$$

where L is insulation life time in hours; T is the absolute temperature in Kelvin, A and B are constants dependent on environmental conditions.

The known “10 °C half-life rule” approximates this equation: every 10 °C increase in operating temperature above the winding insulation system thermal class (temperature limit) reduces the expected insulation service life by half [1], [48] and [83] (Figure I.25 [83]).

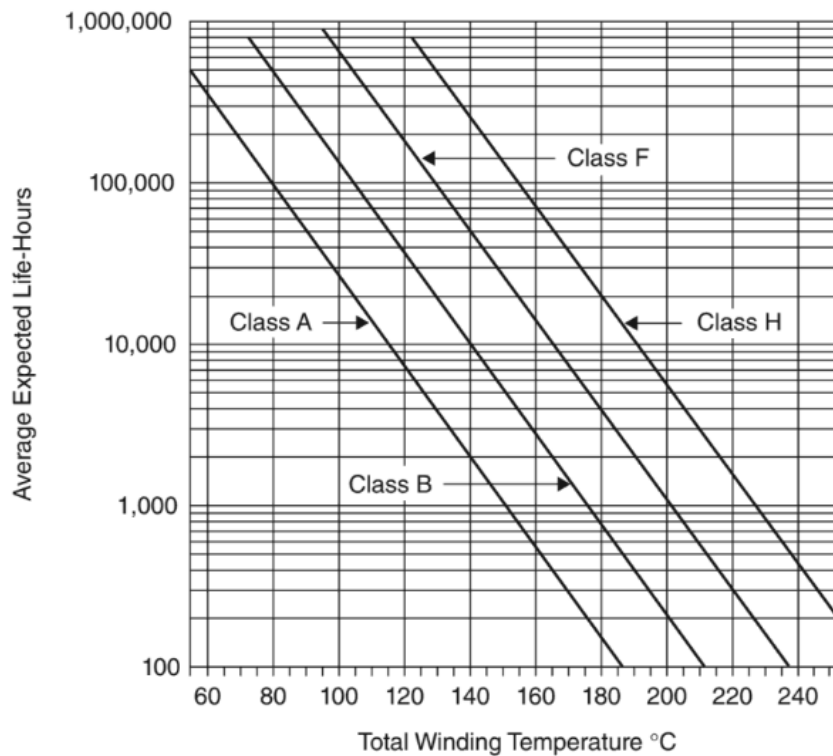


Figure I.25: Expected insulation life vs. operating temperature for different thermal classes [83].

5.1 Failures in motor windings

Electrical machines insulation should be selected considering constraints mentioned above and be able to ensure specified service lifetime. As reported by [2], [6], [7] and [8], one of the most common reasons of induction motor breakdowns is a stator winding turn insulation fault which accounts for 36-37% of all the failures. A significant part of failures occurs during the machine’s running-in period, generally caused by latent defects and imperfections in winding insulation. These defects appear due to wires’ insulating technology, copper conductors having sharp burrs utilization, wires’ stretching and hits during windings manufacturing process, as well as during electrical machines operation.

Figure I.26 demonstrates the following induction machine stator winding failures [8]:

- a inter-turn short circuits between turns of the same phase (turn-to-turn fault);
- b short circuited winding (coil-to-coil fault);
- c short circuits between winding and stator core at the end of the stator slot (coil to ground fault);
- d short circuits between winding and stator core in the middle of the stator slot;
- e short circuit at the leads;
- f short circuit between phases (phase-to-phase fault).

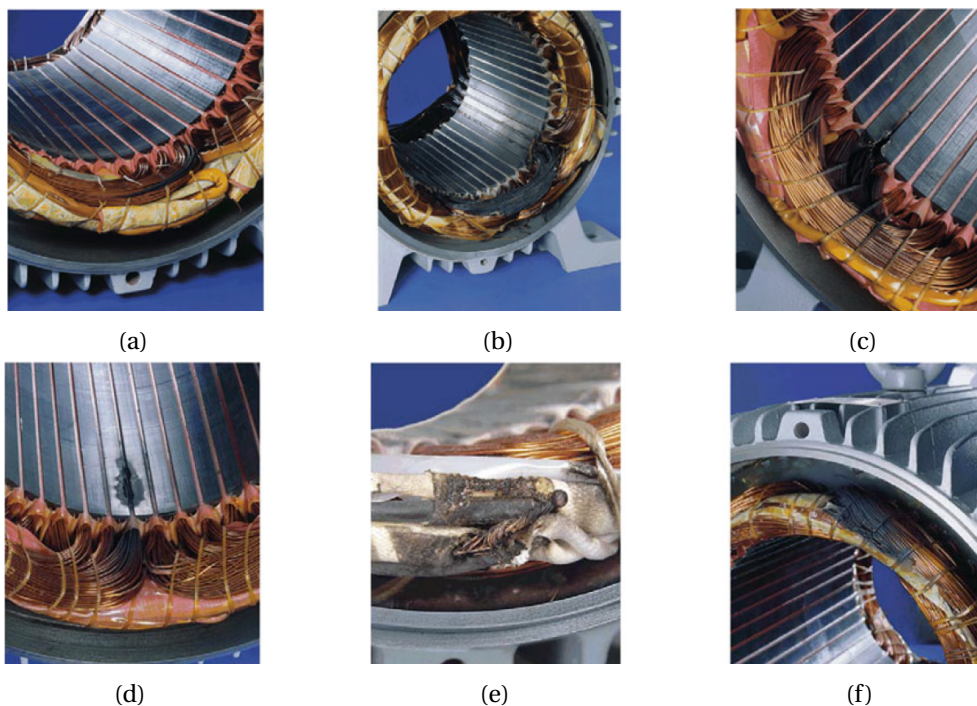


Figure I.26: Insulation damage caused by inter-turn short circuit of the stator windings in three-phase induction motors [8].

5.2 Effect of impulse supply voltage on winding insulation

The impact of described above factors on dielectrics ageing and deterioration depends on the electrical machine's environmental conditions, the power supply and the control system. As previously noted, in case of sinusoidal 50-Hz AC supply voltage, thermal stresses are the main cause of low voltage electrical machines insulation deterioration. This is due to the fact, that voltage magnitude and surges are not high enough to cause an insulation breakdown or an ionization process.

Numerous studies [1], [3], [4], [15], [84], [85], [86], [87] and [88] put into evidence that the use of PWM based inverters increases electrical stresses in low voltage electrical

machines (see Figure I.27). Voltage inverters are made on the basis of power semiconductor devices – electronic switches, e.g., Gate Turn-Off thyristor (GTO), Bipolar Junction Transistor (BJT), Insulated Gate Bipolar Transistor (IGBT) and Metal-oxide-semiconductor Field-effect transistor (MOSFET). Depending on type and characteristics of used semiconductor devices the switching frequency could reach dozens of kHz and the impulse voltage front duration can be from tens of nanoseconds to several microseconds [89] and [90] creating high dV/dt slopes and oscillating frequencies up to several megahertz.

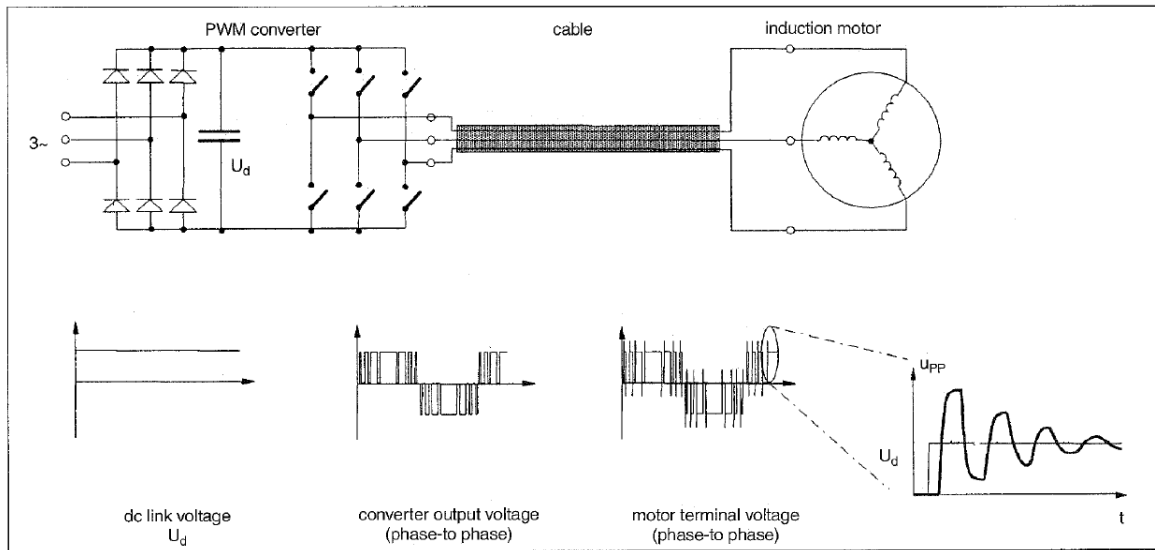


Figure I.27: Principle of induction motor adjustable speed drive with its schematic voltage characteristics [88].

The impulse voltage rise time t_r is defined in IEC 60034-8-41:2014 [63] and IEC TS 60034-25:2014 [91] standards as the time required for the voltage U to rise from 10% to 90% of the peak voltage (from $0,1 U_p$ to $0,9 U_p$ in Figure I.28).

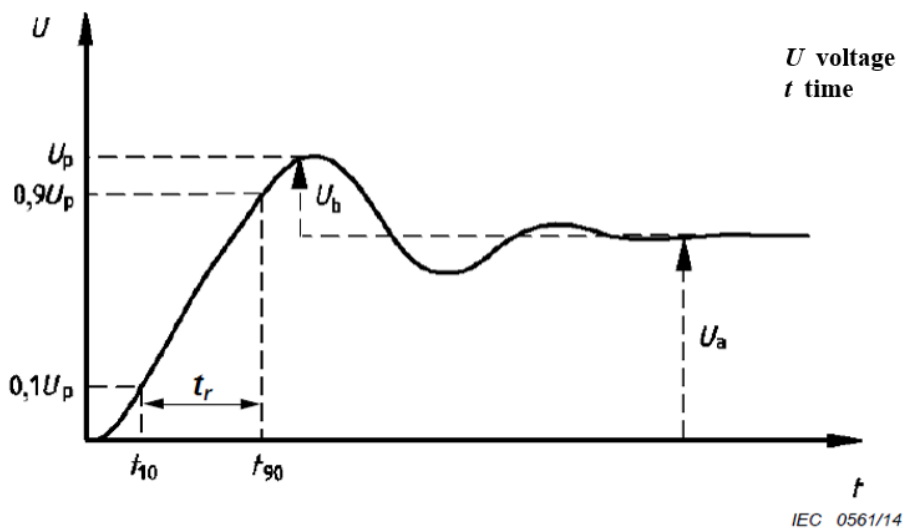


Figure I.28: Voltage impulse waveform parameters [63].

It should be noted, that there are two different definitions for this important parameter. The impulse rise time calculated in accordance with the standard National Electrical Manufacturers Association (NEMA) MG1 Part 31 [92] definition will have a smaller value for the same voltage waveform as it shown in Figure I.29.

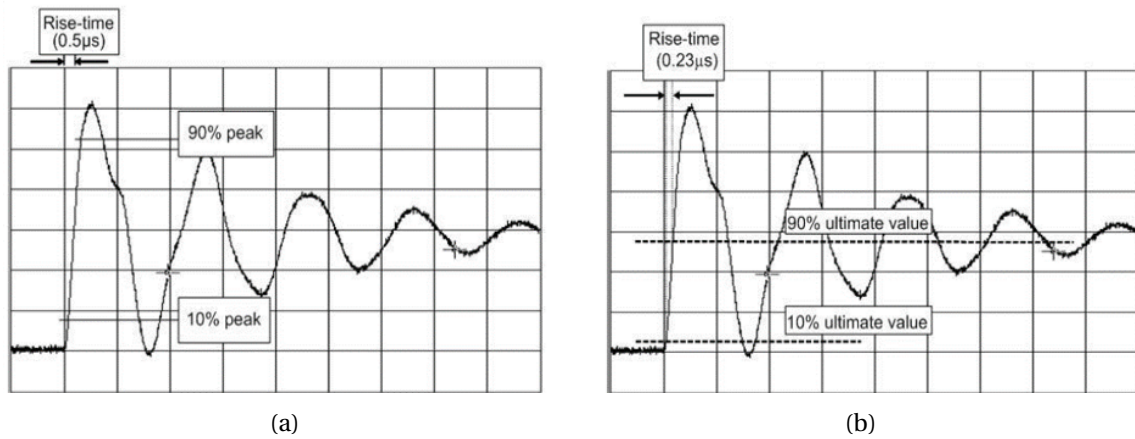


Figure I.29: Different definitions of impulse rise time:
 (a) IEC TS 60034-25:2014 and (b) NEMA MG1 Part 31.

The impulse voltage waveform with steep rising and falling edges creates a nonlinear voltage distribution along feeding motor windings. Indeed, overvoltage at motor terminals can occur due to reflected waves phenomena in cable line caused by mismatching of inverter, supply cable and motor winding impedances [15], [84], [85], [86], [88] and [90]. Overvoltage at motor terminals depending on voltage rise time and drive to motor cable length is shown in Figure I.30 [90].

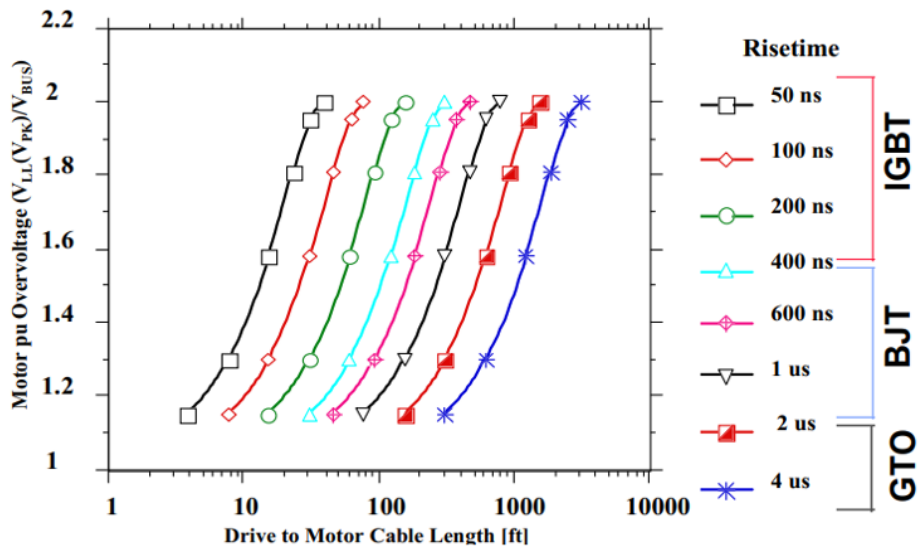


Figure I.30: Inverter fed motor pu overvoltage vs. cable length and impulse voltage risetime [90].

Another example of supply cable length influence on motor voltage waveform is given in Figure I.31. The phase-to-phase voltage was measured at motors connected using different cable lengths [84].

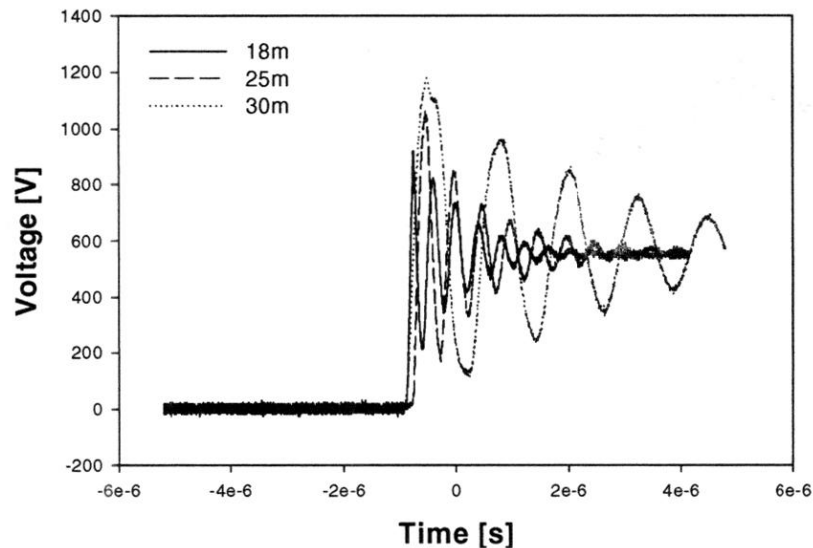


Figure I.31: Phase-to-phase voltage waveforms during motor operation at the motor input with a 30 m, 25 m and 15 m length connecting cable [84].

Moreover, in a random wound motor winding, the first and the last turns of one or more coils may be adjacent and be exposed to the entire terminal voltage [3], [84], [86] and [88]. The increased voltage amplitudes and the transient voltages uneven distribution lead to rise in voltage amplitude stressing the turn insulation up to ten times compared with machines operated at sine AC voltage of 50 or 60 Hz frequency [88].

The negative effect of repetitive impulse voltage becomes more important with the implementation of wide bandgap power semiconductors as Silicon Carbide in inverters. The modern advances in semiconductors technology allow to create inverters with high temperature capabilities, lower conduction and switching losses, higher switching speed and frequency range in comparison with Si technology, providing compactness and lower weight [12], [20], [21], [22], [23], [24] and [26]. Due to these features, SiC power semiconductor devices are very attractive for motor drives in automotive, aerospace, especially for MEA concepts, as well as in industrial applications where power density and weight are one of the main factors for power electronics sizing [12], [20], [22] and [26]. Nevertheless, resulting electrical stresses are severe for the controlled motors: dV/dt with very low rise/fall times (10-50 ns), raise of common mode currents and electromagnetic radiation [3], [24], [27], [28] and [93].

Overvoltage in inverter-fed motor winding can be higher than the value of Partial Discharge Inception Voltage (PDIV) that provokes partial discharges in winding insulation leading to early insulation degradations and/or failures.

According to [90] and [94] partial discharges comprise local discharges on surface or inside insulation such as a corona, a creeping discharge, or an insulation element local breakdown, which shunts a part of insulation between electrodes having different potentials. The corona, local internal and surface discharges are partial discharges that occurs at the threshold applied voltage caused ionization of the air around conductors. These partial discharges lead to failures in local areas with high voltage intensity and weakened insulation. The term “corona” here is used for a surface discharge in electrical machine’s winding insulation (Figure I.32 [95] and [96]).

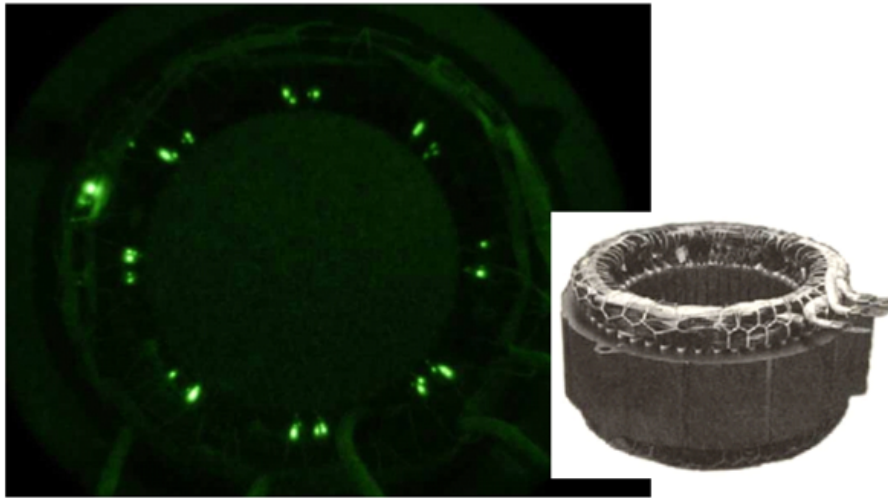


Figure I.32: Electrical discharges in stator windings [95] and [96].

Partial Discharges (PDs) mainly occur in air gaps, voids and defects appearing in insulation due to wires’ insulating technology, windings manufacturing, and electrical machines operation [80] and [97]. In electrical machines corona and PDs can be located in stator end winding contacting with air, stator slot insulation, in the insulation between different phases (in the case where interphase insulating films are not correctly placed),

or between winding's turns (defects of impregnation). The partial discharges activity provokes the complex physico-chemical process caused by accelerated electrons and ions bombardments, gas-discharge radiation, temperature rise, chemically active substances produced by these discharges (nitric oxides and ozone), and increased local electrical intensity in affected areas [17], [18], [19], [98], [99], [100], [101] and [102]. It causes dielectric material erosion and accelerated degradation (Figure I.33 [102]).

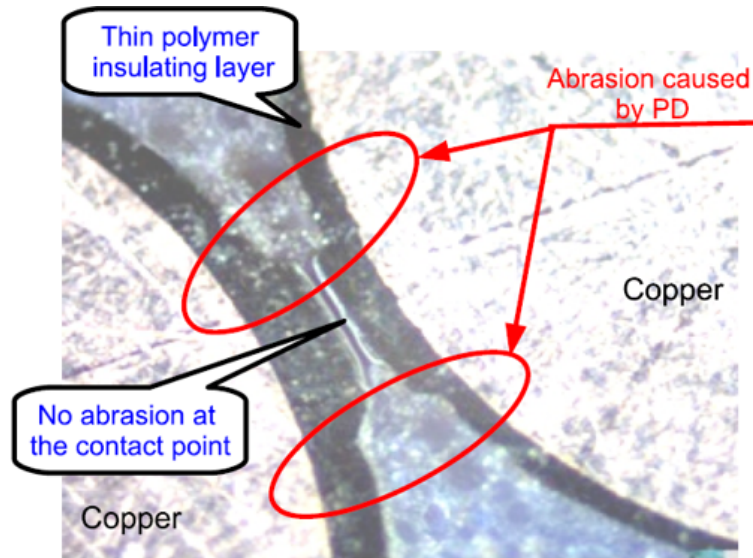


Figure I.33: Microscopy images of turn insulation aged by PDs [102].

As the insulation degrades, the partial discharges number and pulses magnitude will increase shortening the insulation lifetime. In low voltage electrical machines PDs occur as a result of thermal, mechanical and electrical ageing. Under normal operating conditions, PDs appearance is a symptom of the degradation process of the insulation that can lead to a final failure. The studies show that humidity impact on partial discharges appearance has lower significance than the pressure and the temperature one [3], [103] and [104]. Thus the conditions leading to insulation breakdown are the low pressure and high temperature [102]. Typical situation is, for example, encountered in aeronautic applications.

Partial discharges activity accelerates insulation ageing and deterioration processes that requires to change the approach to model the low-voltage insulation lifetime considering the effect of electrical stresses. In this case, the inverse power model has been proposed to describe the effect of voltage level V on the insulation lifetime L in [1] and [101]:

$$L = cV^{-n} \quad (\text{I.3})$$

where c is a material constant and n is the power law constant.

A lot of researches have been devoted to develop PDs detection methods, to eliminate electromagnetic interference effects and to analyse measured characteristics [96], [105], [106], [107], [108], [109], [110] and [111]. In electrical detection methods ultra-high frequency sensors or antennas, high-frequency current transformers and coupling capacitors are employed. Partial discharges in high voltage cables can be detected using acoustic technique (piezoelectric sensor). Optical detection (optical fiber based sensors, ultraviolet cameras) and chemical methods (*e.g.*, analysis of gases dissolved in transformer oil and liquid chromatography) are also proposed.

Partial discharges measurements are often used for insulation condition and fault diagnostics in high voltage cable lines, electrical machines and transformers. This allows to identify insulation defects at the earliest stages of its occurrence, to monitor their propagation, to evaluate insulation current state and further operation. In [84] it is proposed to use partial discharge measurements also for low-voltage electrical machines condition monitoring. However, in case of electric motors having Type I insulation system [63], which are not expected to withstand PDs activity, the presence of partial discharges might indicate a critical insulation condition.

In the order to eliminate or limit electrical discharges in electrical machine's winding different solutions may be employed. Firstly, the risk of partial discharge inception can be decreased by limiting electrical stresses in motor winding insulation using filters to adapt cable impedance and inverter-fed motor impedance [3], [4] and [112]. It reduces surges and inverter voltage front steepness, and can also decrease the voltage distribution non-linearity in motor winding. Another way is to use a multi-level inverter topology. The use of multi-level inverter creates a higher number of voltage levels and, therefore, increases the number of impulse voltage fronts, but decreases their amplitude, which reduces overvoltage and extends insulation lifetime [63] and [113] (Figure I.34). However, this solution leads to a rise in electric drive cost and size.

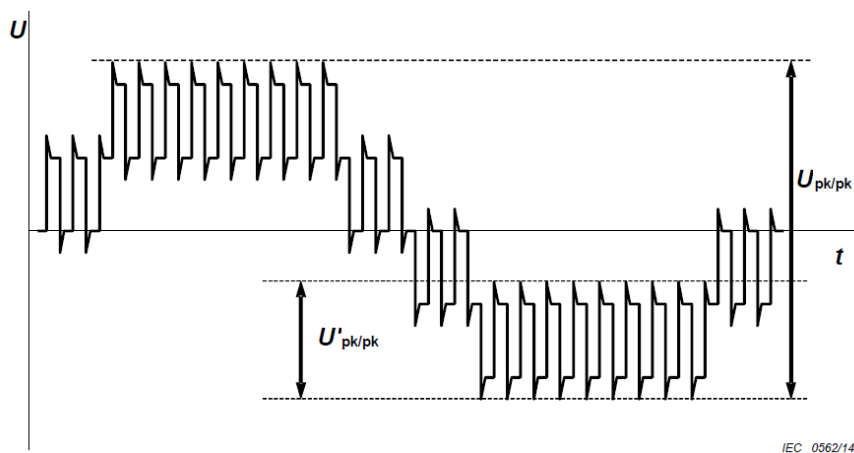


Figure I.34: Five step phase to phase voltage at the terminals of a machine fed by a 3-level converter [63].

On the other hand, inverter-fed motor windings can be designed considering the risk of partial discharges activity. In order to improve the electrical machine winding reliability, corona resistant enamelled wires containing inorganic nanoparticles, *e.g.* aluminium oxide filler, can be used. The specific composition of the corona resistant nano-filled wire makes possible a better resistance to degradation caused by partial discharges, providing improvement in terms of mechanical and chemical erosion due to PDs, electrical breakdown/endurance behaviour, and space charge mitigation compared with conventional enamelled wires [29], [32] and [114]. The filled enamel film structure provide a longer electrical breakdown path improving insulation electrical strength (Figure I.35) [115].

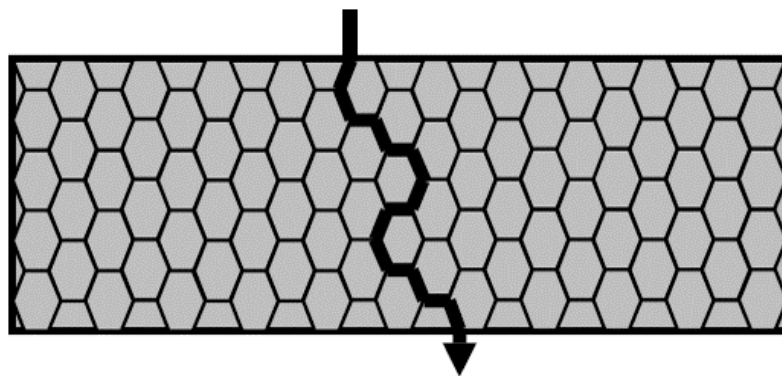


Figure I.35: Electrical breakdown path through inorganic filler spherical particles [115].

6 Conclusion

The present Chapter was devoted to an overview of factors affecting low voltage electrical machines fed by inverters. Firstly, different types of electrical machines which could be used in automotive and aeronautical applications are shortly discussed focusing on induction machines as commonly used and switched reluctance machines as promising competitive alternative to another electrical machines' types. For these machines construction and components of distributed and concentrated stator windings are given. It is shown, that the turn insulation composed of winding wire enamel insulation and impregnating material is the weakest element of winding insulation system. In this regard, the described technological parameters and operational stresses is presented in relation with their impact on the turn insulation.

The conducted literature survey reveals the negative influence of impulse supply voltage on winding insulation in electrical machines fed by inverters compared with sinusoidal voltage supplied machines. Arising overvoltage and uneven voltage distribution creates conditions for partial discharge ignition in winding insulation.

The implementation of wide bandgap power semiconductors as SiC in recent years

allows to create very powerful inverters with high switching speed and frequency enhancing electric drives efficiency and reducing their size and weight. However, resulting electrical stresses are severe for controlled motors: dV/dt with ns-level of rising and falling time, high switching frequency, raise of common mode currents and electromagnetic radiation. Due to this fact, partial discharges will occur with higher probability, and the winding insulation ageing and failure will be accelerated.

Thus, the aim of this work is to investigate the influence of voltage waveform on turn insulation ageing and destruction processes, highlighting the effect of high dV/dt and switching frequency. To achieve this objective, test benches allowing to perform insulation electro-thermal accelerated ageing tests were designed. These test benches make it possible to reproduce the stresses affecting the winding insulation of motors fed by inverters based on Silicon technology as well as inverters using high speed SiC switches.

Preceding the experimental study, a high frequency model of electric drive system composed by an inverter, a supply cable and a switched reluctance machine is proposed. The main goal is to study voltage transients and surges at motor terminals caused by high dV/dt and impedance mismatch between the cable and the motor fed by the SiC-based inverter.

References

References

- [1] Greg C. Stone, Ian Culbert, Edward A. Boulter, and Hussein Dhirani. *Electrical Insulation for Rotating Machines*. John Wiley & Sons, Inc., Hoboken, NJ, USA, jul 2014.
- [2] Stefan Grubic, J.M. Aller, Bin Lu, and T.G. Habetler. A Survey on Testing and Monitoring Methods for Stator Insulation Systems of Low-Voltage Induction Machines Focusing on Turn Insulation Problems. *IEEE Transactions on Industrial Electronics*, 55(12):4127–4136, dec 2008.
- [3] Vasile Mihaila. *Nouvelle Conception des bobinages statoriques des machines à courant alternatif pour réduire les effets négatifs des dV/dt* . PhD thesis, Université d’Artois, 2011.
- [4] Loucif Benmamas. *Méthodes d’évaluation du risque de décharges partielles dans le bobinage de machines électriques destinées à la traction automobile*. PhD thesis, Université Paris-Saclay, 2017.
- [5] Tomaz Munih and Damijan Miljavec. A method for accelerated ageing of electric machine insulation. In *Proceedings of the 16th International Conference on Mechatronics - Mechatronika 2014*, pages 65–70. IEEE, dec 2014.
- [6] Bin Lu, Yaoyu Li, Xin Wu, and Zhongzhou Yang. A review of recent advances in wind turbine condition monitoring and fault diagnosis. In *2009 IEEE Power Electronics and Machines in Wind Applications*, pages 1–7. IEEE, jun 2009.
- [7] Austin Bonnett and Chuck Yung. Increased Efficiency Versus Increased Reliability. *IEEE Industry Applications Magazine*, 14(1):29–36, jan 2008.
- [8] Subrata Karmakar, Surajit Chattopadhyay, Madhuchhanda Mitra, and Samarjit Sengupta. *Induction Motor Fault Diagnosis*. Power Systems. Springer Singapore, Singapore, 2016.
- [9] Horia Gavrila, Manescu (Paltanea) Veronica, Gheorghe Paltanea, Gheorghe Scutaru, and Ioan Peter. New Trends in Energy Efficient Electrical Machines. *Procedia Engineering*, 181:568–574, 2017.

-
- [10] C.C. Chan. The state of the art of electric and hybrid vehicles. *Proceedings of the IEEE*, 90(2):247–275, 2002.
- [11] David Dorrell, Leila Parsa, and Ion Boldea. Automotive Electric Motors, Generators, and Actuator Drive Systems With Reduced or No Permanent Magnets and Innovative Design Concepts. *IEEE Transactions on Industrial Electronics*, 61(10):5693–5695, oct 2014.
- [12] Arie Nawawi, Rejeki Simanjorang, Chandana Jayampathi Gajanayake, Amit K. Gupta, Chin Foong Tong, Shan Yin, Assel Sakanova, Yitao Liu, Yong Liu, Men Kai, Kye Yak See, and King-Jet Tseng. Design and Demonstration of High Power Density Inverter for Aircraft Applications. *IEEE Transactions on Industry Applications*, 53(2):1168–1176, mar 2017.
- [13] Walid Boughanmi. *Eco-Conception des motorisations électriques: application à la machine asynchrone*. PhD thesis, Université d’Artois, 2012.
- [14] M Olszewski. Final Report on Assessment of Motor Technologies for Traction Drives of Hybrid and Electric Vehicles. Technical report, 2011.
- [15] M. Fenger, S.R. Campbell, and J. Pedersen. Motor winding problems caused by inverter drives. *IEEE Industry Applications Magazine*, 9(4):22–31, jul 2003.
- [16] Peng Wang, Gian Carlo Montanari, and Andrea Cavallini. Partial Discharge Phenomenology and Induced Aging Behavior in Rotating Machines Controlled by Power Electronics. *IEEE Transactions on Industrial Electronics*, 61(12):7105–7112, dec 2014.
- [17] Gian Carlo Montanari and Fabio Ciani. Inverter design and partial discharge phenomenology in insulation systems of rotating machines. In *2017 IEEE International Electric Machines and Drives Conference (IEMDC)*, pages 1–5. IEEE, may 2017.
- [18] K. Kimura, S. Ushirone, T. Koyanagi, Y. Iiyama, S. Ohtsuka, and M. Hikita. Study of PD behaviors on a crossed sample of magnet-wire with repetitive bipolar impulses for inverter-fed motor coil insulation. In *CEIDP '05. 2005 Annual Report Conference on Electrical Insulation and Dielectric Phenomena, 2005.*, pages 393–396. IEEE, 2005.
- [19] Mateusz Szczepanski, David Malec, Pascal Maussion, Benoit Petitgas, and Philippe Manfe. Ozone concentration impact on the lifespan of enameled wires (conventional and corona-resistant) for low voltage rotating machines fed by inverters. In *2017 IEEE Electrical Insulation Conference (EIC)*, pages 443–446. IEEE, jun 2017.

- [20] Ahmed Elasser and T. Paul Chow. Silicon carbide benefits and advantages for power electronics circuits and systems. *Proceedings of the IEEE*, 90(6):969–986, jun 2002.
- [21] M. G. Hosseini Aghdam and T. Thiringer. Comparison of SiC and Si power semiconductor devices to be used in 2.5 kW DC/DC converter. In *2009 International Conference on Power Electronics and Drive Systems (PEDS)*, number December 2009, pages 1035–1040. IEEE, nov 2009.
- [22] M. Chinthavali, P. Otaduy, and B. Ozpineci. Comparison of Si and SiC inverters for IPM traction drive. In *2010 IEEE Energy Conversion Congress and Exposition*, pages 3360–3365. IEEE, sep 2010.
- [23] Shan Yin, King Jet Tseng, Rejeki Simanjorang, Yong Liu, and Josep Pou. A 50-kW High-Frequency and High-Efficiency SiC Voltage Source Inverter for More Electric Aircraft. *IEEE Transactions on Industrial Electronics*, 64(11):9124–9134, nov 2017.
- [24] Di Han, Silong Li, Yujiang Wu, Wooyoung Choi, and Bulent Sarlioglu. Comparative Analysis on Conducted CM EMI Emission of Motor Drives: WBG Versus Si Devices. *IEEE Transactions on Industrial Electronics*, 64(10):8353–8363, oct 2017.
- [25] Yuji Ando, Yasuhiro Shirahata, Takeo Oku, Taisuke Matsumoto, Yuya Ohishi, Masashi Yasuda, Akio Shimono, Yoshikazu Takeda, and Mikio Murozono. Comparison between SiC- and Si-Based Inverters for Photovoltaic Power Generation Systems. *Journal of Power and Energy Engineering*, 05(01):30–40, 2017.
- [26] Bulent Sarlioglu and Casey T. Morris. More Electric Aircraft: Review, Challenges, and Opportunities for Commercial Transport Aircraft. *IEEE Transactions on Transportation Electrification*, 1(1):54–64, jun 2015.
- [27] Balaji Narayanasamy, Arvind S Sathyanarayanan, Amol Deshpande, and Fang Luo. Analysis and mitigation of reflected wave voltages and currents in WBG devices based motor drives. In *2016 IEEE 4th Workshop on Wide Bandgap Power Devices and Applications (WiPDA)*, pages 297–301. IEEE, nov 2016.
- [28] Bouazza Taghia, Bernardo Cougo, Hubert Piquet, David Malec, Antoine Belinger, and Jean-Pierre Carayon. Overvoltage at motor terminals in SiC-based PWM drives. *Mathematics and Computers in Simulation*, 158:264–280, apr 2019.
- [29] F. Guastavino, E. Torello, D. Cordano, and L. Della Giovanna. Surface PD evolution of conventional and nanocomposite enamels. In *2016 IEEE International Conference on Dielectrics (ICD)*, volume 2, pages 760–763. IEEE, jul 2016.

- [30] F. Guastavino, D. Cordano, E. Torello, and L. Della Giovanna. PD evolution of conventional and corona resistant enamels. In *2016 IEEE Conference on Electrical Insulation and Dielectric Phenomena (CEIDP)*, pages 259–262. IEEE, oct 2016.
- [31] Barbara Florkowska, Marek Florkowski, Paweł Zydroń, and Józef Roehrich. Experimental evaluation of breakdown voltage and life time for models of the low voltage electrical motors windings. *PRZEGLĄD ELEKTROTECHNICZNY*, 1(10):23–27, oct 2016.
- [32] Francesco Guastavino, Alessandro Ratto, Eugenia Torello, and Giovanna Biondi. Aging Tests on Nanostructured Enamels for Winding Wire Insulation. *IEEE Transactions on Industrial Electronics*, 61(10):5550–5557, oct 2014.
- [33] Susanta Ray and Debangshu Dey. Characterization of stator turn to turn faults of induction motor using cross-correlation analysis based features. In *2016 International Conference on Intelligent Control Power and Instrumentation (ICICPI)*, pages 297–301. IEEE, oct 2016.
- [34] Pascal Maussion. Design of Experiments in electrical engineering: Applications in control and modeling. In *2017 IEEE Workshop on Electrical Machines Design, Control and Diagnosis (WEMDCD)*, pages 179–186. IEEE, apr 2017.
- [35] Farah Salameh, Antoine Picot, Marie Chabert, and Pascal Maussion. Parametric and Nonparametric Models for Lifespan Modeling of Insulation Systems in Electrical Machines. *IEEE Transactions on Industry Applications*, 53(3):3119–3128, may 2017.
- [36] Gabriel Velu, Stéphane Duchesne, Daniel Roger, Walid Boughamni, and Ewa Napieralska. Bobinage à faible impact environnemental. In *Symposium de Génie Électrique 2014*, pages 8–10, Cachan, 2014.
- [37] Vadim Iosif, Stéphane Duchesne, and Daniel Roger. Voltage stress predetermination for long-life design of windings for electric actuators in aircrafts. In *2015 IEEE Conference on Electrical Insulation and Dielectric Phenomena (CEIDP)*, pages 318–321. IEEE, oct 2015.
- [38] Liwei Wang, Carl Ngai-Man Ho, Francisco Canales, and Juri Jatskevich. High-Frequency Modeling of the Long-Cable-Fed Induction Motor Drive System Using TLM Approach for Predicting Overvoltage Transients. *IEEE Transactions on Power Electronics*, 25(10):2653–2664, oct 2010.
- [39] Christelle Saber. *Analysis and optimization of the conducted emissions of an on-board charger for electric vehicles*. PhD thesis, Université Paris-Saclay, 2017.

- [40] Oliver Deisser, Gerhard Kopp, Alexander Fridrich, and Jens Neubeck. Development and realization of an in-wheel suspension concept with an integrated electric drive. In *2018 Thirteenth International Conference on Ecological Vehicles and Renewable Energies (EVER)*, pages 1–8. IEEE, apr 2018.
- [41] Michele Trancossi and Jose C. Pascoa. Optimized Modular Design for Energy Efficiency: The Case of an Innovative Electric Hybrid Vehicle Design. In *ASME 2016 International Mechanical Engineering Congress and Exposition*, number Volume 12: Transportation Systems. American Society of Mechanical Engineers, nov 2016.
- [42] Martin März, Andreas Schletz, Bernd Eckardt, Sven Egelkraut, and Hubert Rauh. Power Electronics System Integration for Electric and Hybrid Vehicles. In *2010 6th International Conference on Integrated Power Electronics Systems*, pages 1–10, Nuremberg, 2010.
- [43] AgileSwitch LLC. Silicon Carbide Power Devices: Advanced Gate Driving Techniques, <https://www.poweramericainstitute.org/wp-content/uploads/2017/02/agileswitch-sic-overview-20170111.pdf>.
- [44] ROHM Semiconductor. ROHM supplies Full SiC Power Modules to Formula E racing team Venturi, dec 2017.
- [45] Ion Boldea, Lucian N Tutelea, Leila Parsa, and David Dorrell. Automotive Electric Propulsion Systems With Reduced or No Permanent Magnets: An Overview. *IEEE Transactions on Industrial Electronics*, 61(10):5696–5711, oct 2014.
- [46] Wenping Cao, Barrie C. Mecrow, G. J. Atkinson, John W. Bennett, and David J. Atkinson. Overview of Electric Motor Technologies Used for More Electric Aircraft (MEA). *IEEE Transactions on Industrial Electronics*, 59(9):3523–3531, sep 2012.
- [47] Mounir Zeraoulia, Mohamed El Hachemi Benbouzid, and Demba Diallo. Electric Motor Drive Selection Issues for HEV Propulsion Systems: A Comparative Study. *IEEE Transactions on Vehicular Technology*, 55(6):1756–1764, nov 2006.
- [48] Ion Boldea and Syed A. Nasar. *The Induction Machine Handbook*. CRC Press, Boca Raton, 1st editio edition, dec 2002.
- [49] Hussein Sarhan. Energy Efficient Control of Three-Phase Induction Motor Drive. *Energy and Power Engineering*, 03(02):107–112, 2011.
- [50] Abdullah Alwadie. A Concise Review of Control Techniques for Reliable and Efficient Control of Induction Motor. *International Journal of Power Electronics and Drive Systems (IJPEDS)*, 9:1124–1139, sep 2018.

-
- [51] Pierre Millithaler, Jean-Baptiste Dupont, Morvan Ouisse, Émeline Sadoulet-Reboul, and Nouredine Bouhaddi. Viscoelastic property tuning for reducing noise radiated by switched-reluctance machines. *Journal of Sound and Vibration*, 407:191–208, oct 2017.
- [52] Guang Jin Li, Xavier Ojeda, Sami Hlioui, Emmanuel Hoang, Mohamed Gabsi, and Cedric Balpe. Comparative study of Switched Reluctance Motors performances for two current distributions and excitation modes. In *2009 35th Annual Conference of IEEE Industrial Electronics*, pages 4047–4052. IEEE, nov 2009.
- [53] M. Rezik, M. Besbes, C. Marchand, B. Multon, S. Loudot, and D. Lhotellier. High-speed-range enhancement of switched reluctance motor with continuous mode for automotive applications. *European Transactions on Electrical Power*, 18(7):674–693, oct 2008.
- [54] Nidec Corporation. SR Drive® Technology, <http://www.srdrives.com/technology.shtml>.
- [55] Jan A Melkebeek. *Electrical Machines and Drives*. Power Systems. Springer International Publishing AG, Cham, 2018.
- [56] Z Q Zhu and David Howe. Electrical Machines and Drives for Electric, Hybrid, and Fuel Cell Vehicles. *Proceedings of the IEEE*, 95(4):746–765, apr 2007.
- [57] Yu Hasegawa, Kenji Nakamura, and Osamu Ichinokura. Optimization of a Switched Reluctance Motor Made of Permendur. *IEEE Transactions on Magnetics*, 46(6):1311–1314, jun 2010.
- [58] James D. Widmer, Richard Martin, and Mohammed Kimiabeigi. Electric vehicle traction motors without rare earth magnets. *Sustainable Materials and Technologies*, 3:7–13, apr 2015.
- [59] Pere Andrada. Switched Reluctance Drives for Electric Vehicle Applications. *Renewable Energy and Power Quality Journal*, 1(01):311–317, apr 2003.
- [60] B.A. Kalan, H.C. Lovatt, and G. Prout. Voltage control of switched reluctance machines for hybrid electric vehicles. In *2002 IEEE 33rd Annual IEEE Power Electronics Specialists Conference. Proceedings (Cat. No.02CH37289)*, volume 4, pages 1656–1660. IEEE, 2002.
- [61] Nadim Sakr, Alejandro Fernandez Sanchez, Daniel Sadarnac, and Alain Gascher. A combined switched reluctance motor drive and battery charger for electric vehicles. In *IECON 2015 - 41st Annual Conference of the IEEE Industrial Electronics Society*, pages 001770–001775. IEEE, nov 2015.

- [62] Nidec Corporation. Nidec SR Drive® motors power new Land Rover, <http://www.srdrives.com/land-rover.shtml>.
- [63] IEC 60034-18-41:2014. *Rotating electrical machines - Part 18-41: Partial discharge free electrical insulation systems (Type I) used in rotating electrical machines fed from voltage converters - Qualification and quality control tests*. Ts ed. 1.0 edition, 2014.
- [64] Electrical Apparatus Service Association. Failures in three-phase stator windings. Technical report, 2004.
- [65] A.M. EL-Refaie and T.M. Jahns. Optimal flux weakening in surface PM machines using concentrated windings. In *Conference Record of the 2004 IEEE Industry Applications Conference, 2004. 39th IAS Annual Meeting.*, volume 2, pages 1038–1047. IEEE, 2004.
- [66] Bulent Sarlioglu, Casey T. Morris, Di Han, and Silong Li. Driving Toward Accessibility: A Review of Technological Improvements for Electric Machines, Power Electronics, and Batteries for Electric and Hybrid Vehicles. *IEEE Industry Applications Magazine*, 23(1):14–25, jan 2017.
- [67] Jae-Hak Choi, Yon-Do Chun, Pil-Wan Han, Mi-Jung Kim, Dae-Hyun Koo, Ju Lee, and Jang-Sung Chun. Design of High Power Permanent Magnet Motor With Segment Rectangular Copper Wire and Closed Slot Opening on Electric Vehicles*. *IEEE Transactions on Magnetics*, 46(9):3701–3704, sep 2010.
- [68] M. Kimiabeigi and J. D. Widmer. On winding design of a high performance ferrite motor for traction application. In *2016 XXII International Conference on Electrical Machines (ICEM)*, pages 1949–1956. IEEE, sep 2016.
- [69] S. P. Tee, M. M. Ghazaly, S. H. Chong, and I. W. Jamaludin. Rotary switched reluctance actuator: A review on design optimization and its control methods. *International Journal of Power Electronics and Drive Systems*, 8(3):1087–1100, 2017.
- [70] IEC 60034-18-1:2010. *Rotating electrical machines – Part 18-1: Functional evaluation of insulation systems – General guidelines*. Ts ed. 2.0 edition, 2010.
- [71] Леонов, Андрей Петрович. Разработка методов оценки совместимости пропиточных составов и эмалированных обмоточных проводов. Канд. дисс., Томский политехнический университет, 2003.
- [72] Vlado Ostović. *The Art and Science of Rotating Field Machines Design: A Practical Approach*. Springer International Publishing, 2017.

- [73] Зеленецкий, Юрий Андреевич. Современные тенденции в производстве эмалированных проводов. Кабели и провода, 6 (295):6–9, 2005.
- [74] Андрианов, В.К. and Васильев, Е.Б. Состояние производства и научно-технические аспекты развития обмоточных проводов в России. Кабели и провода, 5 (348):3–6, 2014.
- [75] Fabrice Aymonino. *Contribution à l'étude du comportement des systèmes d'isolation des machines tournantes à courant alternatif fonctionnant sous très hautes températures (200-400°C)*. PhD thesis, l'Université Toulouse III - Paul Sabatier, 2008.
- [76] IEC 60317-0-1:2013. *Specifications for particular types of winding wires - Part 0-1: General requirements - Enameled round copper wire*. Ts ed. 4.0 edition, 2013.
- [77] IEC 60085:2007. *Electrical Insulation - Thermal evaluation and designation*. Ts ed. 4.0 edition, 2007.
- [78] Loucif Benmamas, Philippe Teste, Guillaume Krebs, Emmanuel Odic, Franck Vangraefschep, and Tahar Hamiti. Contribution to partial discharge analysis in inverter-fed motor windings for automotive application. In *2017 IEEE Electrical Insulation Conference (EIC)*, pages 348–351. IEEE, jun 2017.
- [79] Гольдберг, О.Д. Надежность электрических машин. М.: Издательский центр «Академия», 2010.
- [80] Суцуева, Аделя Сагынбековна. Снижение дефектности межвитковой изоляции обмоток низковольтных асинхронных электродвигателей. Канд. дисс., Национальный исследовательский Томский политехнический университет, 2016.
- [81] K. Tshiloz, A. C Smith, A. Mohammed, S. Djurovic, and T. Feehally. Real-time insulation lifetime monitoring for motor windings. In *2016 XXII International Conference on Electrical Machines (ICEM)*, pages 2335–2340. IEEE, sep 2016.
- [82] Thomas W Dakin. Electrical Insulation Deterioration Treated as a Chemical Rate Phenomenon. *Transactions of the American Institute of Electrical Engineers*, 67(1):113–122, jan 1948.
- [83] Thomas A. Lipo. *Introduction to AC Machine Design*. John Wiley & Sons, Inc., Hoboken, NJ, USA, aug 2017.
- [84] D. Fabiani, A. Cavallini, and G.C. Montanari. Aging investigation of motor winding insulation subjected to PWM-supply through PD measurements. In *CEIDP '05. 2005 Annual Report Conference on Electrical Insulation and Dielectric Phenomena, 2005.*, pages 434–437. IEEE, 2005.

- [85] Yue Liu, Ligu Wang, Han Gao, Haicong Zhang, and Dianguo Xu. Overvoltage mitigation of submersible motors with long cables of different lengths. In *2014 17th International Conference on Electrical Machines and Systems (ICEMS)*, pages 638–644. IEEE, oct 2014.
- [86] Peter Nussbaumer, Clemens Zoeller, Thomas M. Wolbank, and Markus A. Vogelsberger. Transient distribution of voltages in induction machine stator windings resulting from switching of power electronics. In *IECON 2013 - 39th Annual Conference of the IEEE Industrial Electronics Society*, pages 3189–3194. IEEE, nov 2013.
- [87] Martin Kaufhold, H. Aninger, Matthias Berth, Joachim Speck, and Martin Eberhardt. Electrical stress and failure mechanism of the winding insulation in PWM-inverter-fed low-voltage induction motors. *IEEE Transactions on Industrial Electronics*, 47(2):396–402, apr 2000.
- [88] M. Kaufhold, G. Borner, M. Eberhardt, and J. Speck. Failure mechanism of the interturn insulation of low voltage electric machines fed by pulse-controlled inverters. *IEEE Electrical Insulation Magazine*, 12(5):9–16, sep 1996.
- [89] Peng Wang and Andrea Cavallini. The influence of repetitive square wave voltage parameters on PD statistical features. In *2013 Annual Report Conference on Electrical Insulation and Dielectric Phenomena*, pages 1282–1285. IEEE, oct 2013.
- [90] Mike Melfi, A.M.J. Sung, Sidney Bell, and G.L. Skibinski. Effect of surge voltage rise-time on the insulation of low-voltage machines fed by PWM converters. *IEEE Transactions on Industry Applications*, 34(4):766–775, 1998.
- [91] *IEC TS 60034-25:2014. Rotating electrical machines - Part 25: AC electrical machines used in power drive systems - Application guide*. Ed. 3.0 edition, 2014.
- [92] *NEMA MG 1-2016 Part 31, Rev 3, Specification for Definite Purpose Inverter fed Motors*. 2016.
- [93] Davide Barater, Fabio Immovilli, Alessandro Soldati, Giampaolo Buticchi, Giovanni Franceschini, Christopher Gerada, and Michael Galea. Multistress Characterization of Fault Mechanisms in Aerospace Electric Actuators. *IEEE Transactions on Industry Applications*, 53(2):1106–1115, mar 2017.
- [94] Кучинский, Георгий Станиславович. Частичные разряды в высоковольтных конструкциях. Л.: Энергия. Ленинград, 1979.
- [95] Hitoshi Okubo, Naoki Hayakawa, and Gian Montanari. Technical Development on Partial Discharge Measurement and Electrical Insulation Techniques for Low Volt-

- age Motors Driven by Voltage Inverters. *IEEE Transactions on Dielectrics and Electrical Insulation*, 14(6):1516–1530, dec 2007.
- [96] Thibaut Billard, Cedric Abadie, and Bouazza Taghia. Non-Intrusive Partial Discharges Investigations on Aeronautic Motors. In *SAE 2016 Aerospace Systems and Technology Conference*, volume 1. SAE International, sep 2016.
- [97] Veronika Bolgova, Andrey Leonov, and Dmitry Charkov. Influence of VFD parameters on voltage stresses in low voltage windings. In *2016 57th International Scientific Conference on Power and Electrical Engineering of Riga Technical University (RTU-CON)*, pages 1–5. IEEE, oct 2016.
- [98] A. Cavallini, G. C. Montanari, D. Fabiani, and M. Tozzi. The influence of PWM voltage waveforms on induction motor insulation systems: Perspectives for the end user. In *8th IEEE Symposium on Diagnostics for Electrical Machines, Power Electronics & Drives*, pages 288–293. IEEE, sep 2011.
- [99] J.D. Kueck, H.D. Haynes, and R.H. Staunton. Stator insulation degradation test uses ASD switching frequency. *IEEE Power Engineering Review*, 22(1):7–11, 2002.
- [100] Veronika Bolgova, Stephane Lefebvre, Sami Hlioui, Nidhal Boucenna, Francois Costa, and Andrey Leonov. Development of testing methods for winding turn-to-turn insulation of low voltage motors fed by PWM converters. In *2017 19th European Conference on Power Electronics and Applications (EPE'17 ECCE Europe)*, pages P.1–P.10, Warsaw, sep 2017. IEEE.
- [101] Nadine Lahoud, Manh Quan Nguyen, Pascal Maussion, David Malec, and Dominique Mary. Lifetime model of the inverter-fed motors secondary insulation by using a design of experiments. *IEEE Transactions on Dielectrics and Electrical Insulation*, 22(6):3170–3176, dec 2015.
- [102] Daniel Roger, Sonia Ait-Amar, Ewa Napieralska, and Piotr Napieralski. A Proposition for Improving the Design of Motor Windings for low-Pressure Environment. In *2018 IEEE Transportation Electrification Conference and Expo (ITEC)*, pages 424–429. IEEE, jun 2018.
- [103] F. Koliatene, Th Lebey, J.P. Cambronne, and S. Dinculescu. Impact of the aeronautic environment on the Partial Discharges Ignition: A basic study. In *Conference Record of the 2008 IEEE International Symposium on Electrical Insulation*, pages 603–606. IEEE, jun 2008.
- [104] Peng Wang, Hongying Xu, Jian Wang, Andrea Cavallini, and Gian Carlo Montanari. Temperature effects on PD statistics and endurance of inverter-fed motor insula-

- tion under repetitive square wave voltages. In *2016 IEEE Electrical Insulation Conference (EIC)*, pages 202–205. IEEE, jun 2016.
- [105] M. M. Yaacob, M. A. Alsaedi, J. R. Rashed, A. M. Dakhil, and S. F. Atyah. Review on partial discharge detection techniques related to high voltage power equipment using different sensors. *Photonic Sensors*, 4(4):325–337, dec 2014.
- [106] Arsalan Hekmati. Proposed method of partial discharge allocation with acoustic emission sensors within power transformers. *Applied Acoustics*, 100:26–33, dec 2015.
- [107] B. Danouj, S.A. Tahan, and E. David. Using a new generation of piezoelectric sensors for partial discharge detection. *Measurement*, 46(1):660–666, jan 2013.
- [108] Othmane El Mountassir, Brian G. Stewart, Alistair J. Reid, and Scott G. McMeekin. Quantification of the performance of iterative and non-iterative computational methods of locating partial discharges using RF measurement techniques. *Electric Power Systems Research*, 143:110–120, feb 2017.
- [109] Tianlong Zhang, Xuezhong Liu, Shijin Tian, Guanfang Liu, and Pingzhen Lei. Research on current sensor adapted for partial discharge detection in inter-turn insulation of wind turbine generator. In *2016 International Conference on Condition Monitoring and Diagnosis (CMD)*, pages 858–861. IEEE, sep 2016.
- [110] Min Wu, Hong Cao, Jianneng Cao, Hai-Long Nguyen, Joao Bartolo Gomes, and Shonali Priyadarsini Krishnaswamy. An overview of state-of-the-art partial discharge analysis techniques for condition monitoring. *IEEE Electrical Insulation Magazine*, 31(6):22–35, nov 2015.
- [111] Daniel Siebler, Philipp Rohwetter, Roy Brusenbach, and Ronald Plath. Optical-only Detection of Partial Discharge with Fluorescent Polymer Optical Fiber Sensors. *Procedia Engineering*, 120:845–848, 2015.
- [112] Christophe Vermaelen. *Contribution à la modélisation et à la réduction des perturbations conduites dans les systèmes d'entraînement à vitesse variable*. PhD thesis, École normale supérieure de Cachan - ENS Cachan, 2003.
- [113] Gian Carlo Montanari, Fabrizio Negri, and Fabio Ciani. Partial Discharge and life behavior of rotating machine wire insulation under PWM waveforms: The influence of inverter characteristics. In *2017 IEEE Electrical Insulation Conference (EIC)*, pages 161–164. IEEE, jun 2017.
- [114] Xin Zhong, Akram Shakeel, Yan Yang, Guoqiang Gao, and Guangning Wu. Preparation and corona-resistance characteristics of double-layer polyimide/Al₂O₃

- nanocomposite film. In *2016 IEEE International Conference on High Voltage Engineering and Application (ICHVE)*, pages 1–4. IEEE, sep 2016.
- [115] Rudolf Brüttsch and Peter Weyl. A New Winding Wire for Inverter Driven Motors. In *9th INSUCON International Electrical Insulation Conference, Berlin*, Berlin, 2002.

Chapter II: High-frequency modelling of inverter-fed motor drive

Chapter II

High-frequency modelling of inverter-fed motor drive

Contents

1 Introduction	58
2 High frequency electrical machine modelling	58
2.1 High frequency motor models: literature review	58
2.2 Switched reluctance motor modelling	64
2.2.1 Proposed motor models	64
2.2.2 Motor impedance measurements	65
2.2.3 Model parameters identification	68
2.2.4 Comparison of measured and simulated motor impedances .	70
3 High frequency cable modelling	74
4 Simulation of transient overvoltage in inverter-fed motor drive	76
5 Conclusion	79
References	83

1 Introduction

With the objective to estimate the electrical stresses, arising in inverter-fed electric motor windings and causing their insulation degradation, the motor terminal transient overvoltage should be studied. The overvoltage at motor terminals is caused by impedance mismatch between the inverter, cable and the powered motor provoking propagation and reflexion phenomena along the cable [1], [2] and [3]. Overvoltage magnitude depends on the impedance of the machine, cable length and impulse voltage rise and fall times [1]. Hence, the use of fast switching WBG electronic devices leads to higher dV/dt and consequently to higher overvoltages [4], [5], giving rise to partial discharges and accelerating the insulation degradation.

To study and predict transient phenomena in PWM drives a High Frequency (HF) model-based approach is proposed in literature [4], [6], [7], [8], [9], [10] and [11]. The analysis of electric drive's high frequency behaviour includes a study of ElectroMagnetic Interference (EMI) considering the Common Mode (CM) and the Differential Mode (DM) for overvoltage transients.

In this regard, the present chapter is oriented toward the high frequency modelling of the electric drive system composed by inverter, supply cable and electric motor considering CM and DM parameters. This study is focused on the modelling of a three-phase SRM. The suggested HF equivalent circuit model of SRM is based on RLC-parameters extracted from CM and DM impedance measurements. In order to complement this model the power cable model proposed in [12] is used. Considering that in the present electric drive model the study of a single commutation effect is performed, the inverter is modelled by an ideal pulse generator.

2 High frequency electrical machine modelling

2.1 High frequency motor models: literature review

Since the transient overvoltage problems in variable frequency drives has been known in 1980 [1], many research works were dedicated to this phenomena. The analysis and prediction of overvoltage requires high frequency modelling, the maximum frequency of which depends on the rise time t_r . The frequency range is defined considering that the differential mode voltage spectrum contains a rise time frequency component determined as $f_r = 1/\pi t_r$ [3], or that the highest significant frequency of the spectrum corresponds to the inverse of the voltage rise time $f_{max} = 1/t_r$ [13]. Numerous HF motor models have been proposed for overvoltage and EMI analysis, as well as for EMI filters conception. The existing models have a similar topology but different calculation methods; some of them are presented below.

In paper [14], a HF model of three-phase AC motor's stator winding is proposed and analysed in frequency and time domains. The model of a random wound winding consists in a cascade connection of single-coil models (lumped equivalent circuits) and inductive couplings among the phases as shown Figure II.1.

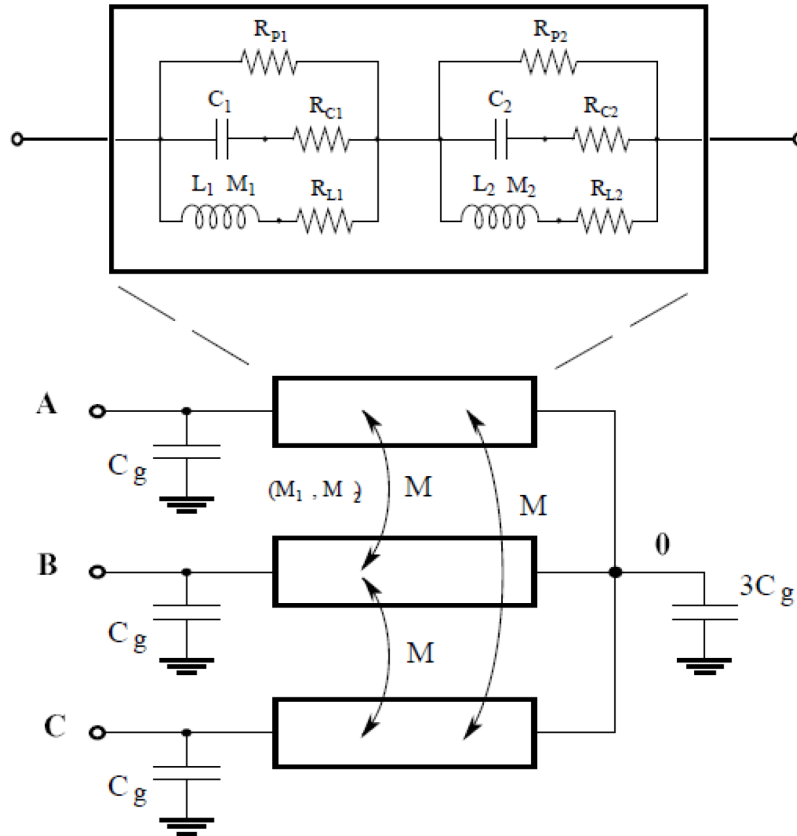


Figure II.1: HF equivalent circuit of a random wound coil [14].

The model parameters represent overall coil inductance, capacitance and losses (iron losses, losses caused by dissipative phenomena due to high frequency capacitive currents and dielectric losses), as well as capacitive and inductive coupling. Their identification was performed by “trial and error” method fitting the phase-to-phase and phase-to-ground impedance measurements in frequency range from 10 kHz to 1 MHz. The time-domain numerical analysis was carried out using PSpice and shows a good agreement between calculated and experimental results.

A high frequency model of induction motor based on lumped parameters approach is presented in [6]; the proposed equivalent circuit is given in Figure II.2a. The model parameters are evaluated basing on impedance measurements in the frequency range from 1 kHz to 1 MHz. Lately, authors have been refined this model by adding parameters considering the skin-effect as shown in Figure II.2b [15] and [16]. In order to obtain a global solution taking into account the high- and low-frequency phenomena of the inverter-motor system, the HF model is connected to the dq dynamic model [15]. The HF

model was extended in [16] to other types of AC motors such as synchronous reluctance (without interior permanent magnets), and brushless motors with acceptable accuracy using “trial and error” procedure for model parameters identification. Moreover, the integral HF model of AC PWM drive system for EMI analysis is discussed in paper [17] where a simplified motor model is used considering the predominant effect of the input capacitance due to the winding insulation and the motor frame resistance.

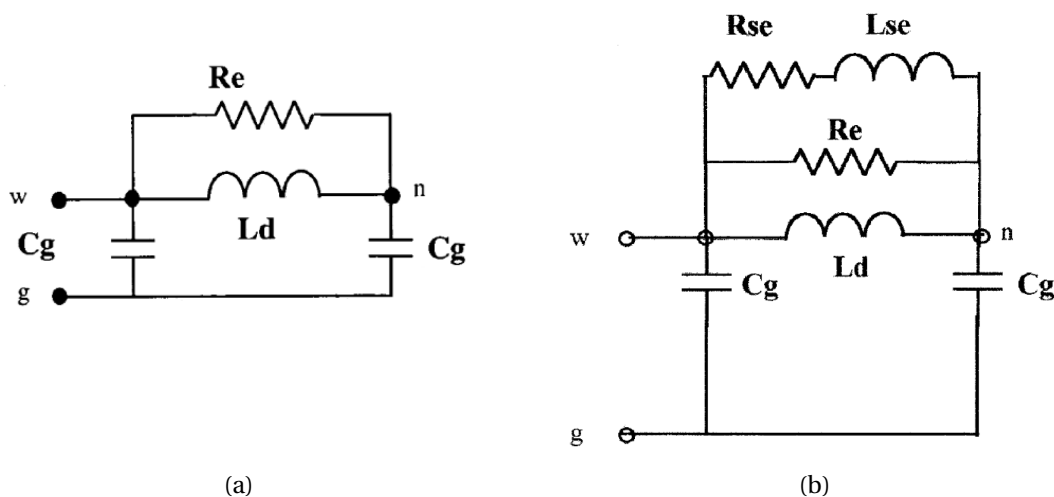


Figure II.2: Single-phase HF equivalent circuits:
 (a) model without the skin effect [6], (b) model taking into account the skin effect [15].

The authors of [9] have proposed a HF model of an induction motor providing simulation of both common and differential modes behaviour in frequency range from 10 kHz to 30 MHz. The proposed model composed of three electromagnetically coupled phase circuits as shown in Figure II.3. The paper details the procedure of CM and DM impedance measurements (star connected windings) and following model parameters identification from characteristic points and corresponded simplified circuits. The measurement setup is schematically represented in Figure II.4a and the obtained simulation results are given in Figure II.4b. A model extension was also proposed (additional capacitance and resistance in series resonance with the stray inductance) in order to increase the accuracy. The values of additional parameters are adjusted to better model fitting.

Basing on above described model, the improved HF motor model is proposed in [11]. A series R_t , L_t , C_t branch is introduced as shown in Figure II.5a, and analytical calculation of these parameters from the impedance measurements (delta-connected windings) is provided. The authors affirm that the three-phase HF model is valid independent of the stator windings connection (delta- or star-connection). Figure II.5b demonstrates the measured and fitted motor impedance for differential and common mode. This equivalent circuit model shows a good accuracy in the frequency range from 100 Hz to 10 MHz and keeps physical meaning of its parameters. Moreover, the induction motor drive system including the feeding cable is modelled in discrete time domain using

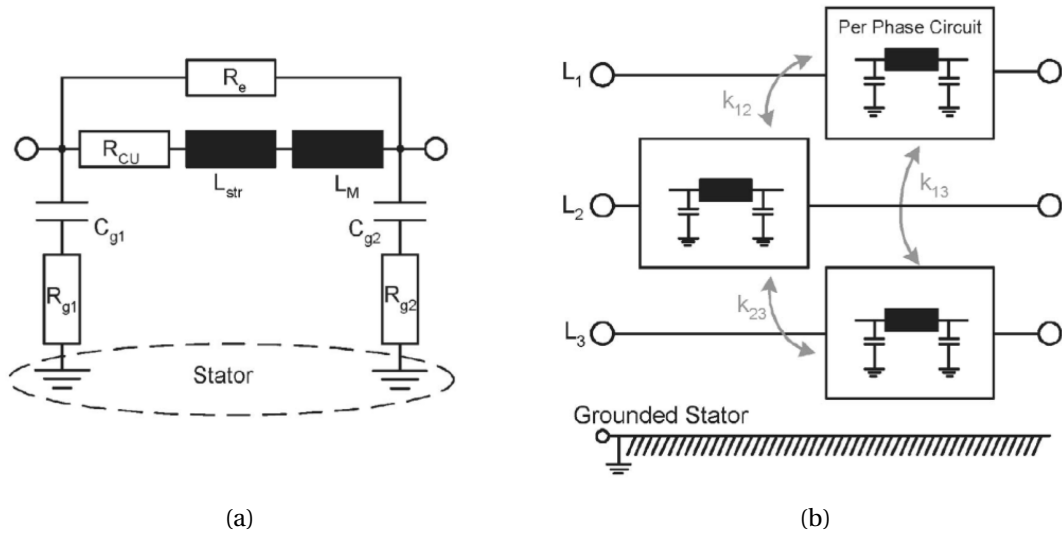


Figure II.3: Induction motor HF model: (a) per phase circuit, (b) three phase model [9].

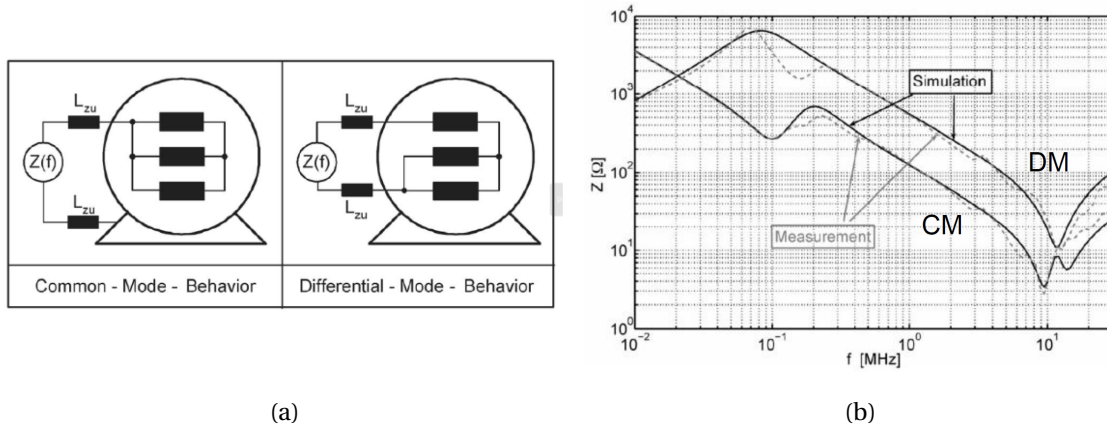


Figure II.4: HF model approach based on impedance measurements: (a) scheme of measurement setup, (b) comparison of measurement and simulation results [9].

transmission line modelling approach with the purpose to analyse transient overvoltage as shown in Figure II.6.

A high frequency lumped parameters model of induction motor similar to [16] and [9] was recently used to study overvoltage at motor terminals in SiC electric drives in [4]. The same impedance measurement technique in frequency range from 1 kHz to 100 MHz is used, but the model lumped parameters values are obtained from the Laplace domain transfer function formulas. A power cable HF model with lumped parameters is also provided that allows to model the overvoltage in the electric drive with different cable lengths. The evolution of overvoltage depending on the impulse voltage rise time and cable length is given in this paper and shown in Figure II.7. The fact that the overvoltage never reaches 2 times of DC bus voltage level is explained by losses presented in power cables. The similar results have been obtained by simulations in [5].

Other techniques and approaches for electric motor modelling can be found in

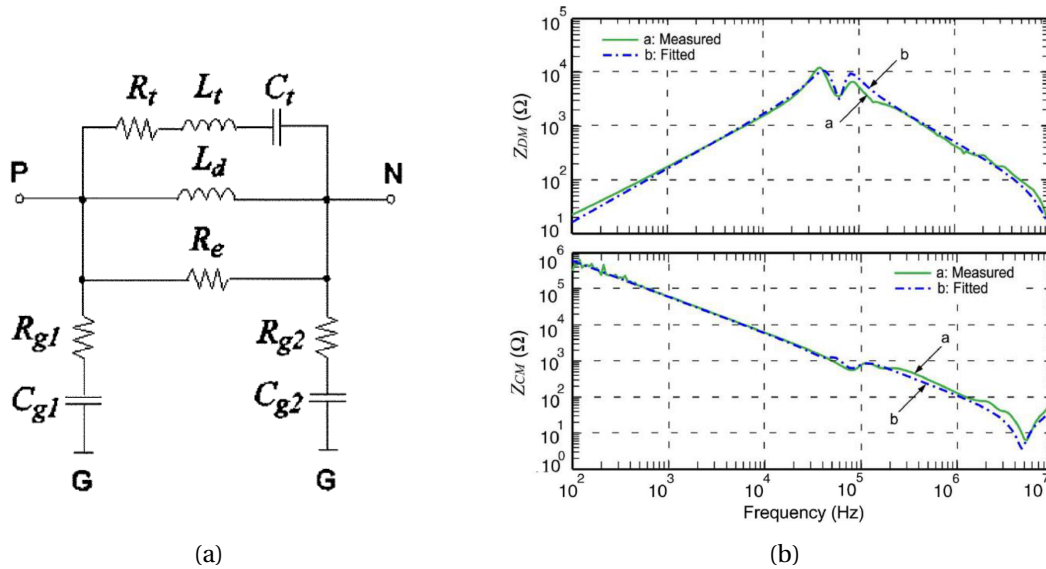


Figure II.5: Induction motor HF model: (a) HF per phase equivalent circuit, (b) measured and fitted impedances [11].

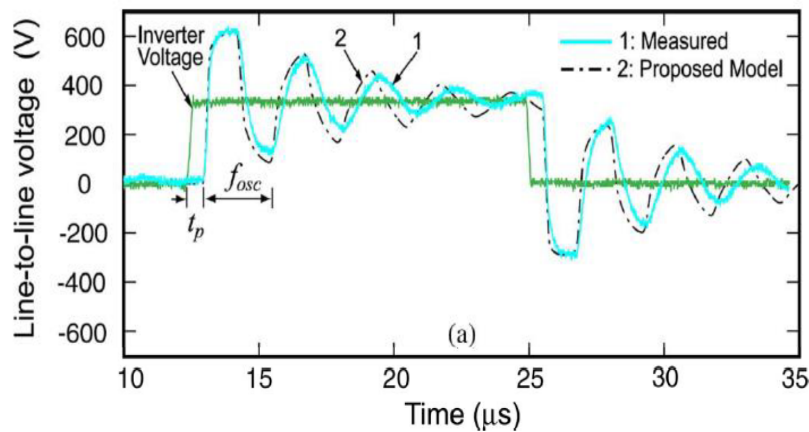


Figure II.6: Measured and simulated voltage waveforms at the motor terminals for 70-m cable [11].

literature. In paper [7] an analytical model of Adjustable-Speed Drive (ASD) motor was elaborated using a developed mathematical formula basing on Maxwell’s equations; the simulation was performed using Matlab Simulink software.

In [18], the HF model of synchronous machine is proposed. Parameters of the equivalent distributed circuit are derived from the measured voltage waveforms at the beginning and the end of the machine’s winding basing on the transmission line theory. The winding voltage is obtained by calculating the developed mathematical model.

A combined low and high frequency model of induction motor is developed in [12]. Impedance measurements to establish the equivalent circuits were performed. In order to determine the low frequency parameters, the tests were carried out at 50 Hz. The inductive effects as well as skin and proximity effects are observed up to 100 kHz, and capacitive couplings are defined accurately up to 100 kHz.

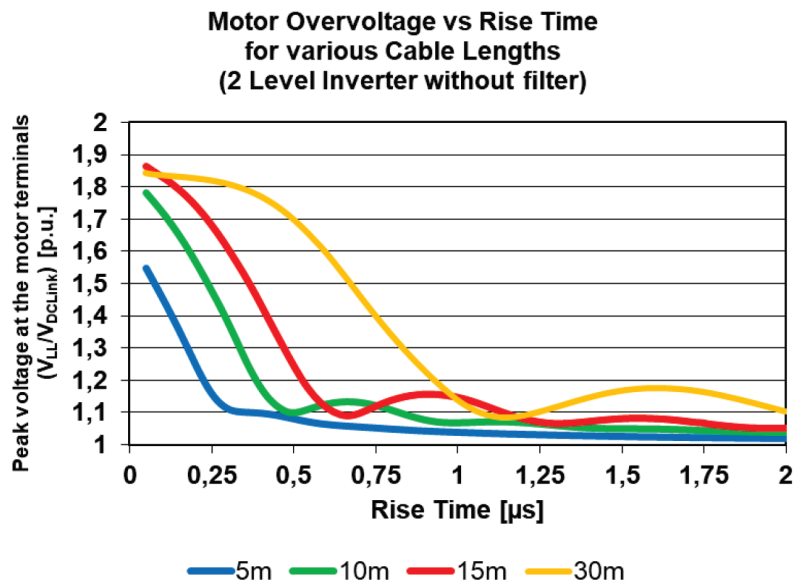


Figure II.7: Overvoltage evolution as function of the inverter's rise time for different cable lengths [4].

In theses [13], [19] and [20], the parameters of proposed electrical machine winding HF model are identified using Finite Element Method (FEM). The advantage of this method results in the possibility of predictive analysis of transient overvoltage and EMI propagation knowing the electrical machine geometry. On the other hand, the FEM analysis is often conducted on stator winding prototypes, and the model complexity for real-size electrical machine can be a limiting factor of this method.

The presented models allow to investigate machine behaviour in frequency and time domains. Typically, the models are developed for induction motors. The frequency depended parameters (caused by skin and proximity effect) can be represented by additional fixed values in the model circuit in order to provide the time-domain analysis. Motor winding impedance has distributed parameters, but the utilization of distributed parameters is avoided in HF modelling because it increases significantly the calculation time. Instead, a number of cells or equivalent circuit per winding phase with lumped parameters is often used. The model frequency range and accuracy depends on the number of circuit parameters. Equivalent circuit of electric motor and associated parameters can be established from the motor impedance characteristic measurements and/or its geometry. In this work, the HF motor modelling is based on methods described in [9] and [11], where the equivalent circuit parameters are extracted from CM and DM impedance measurements.

2.2 Switched reluctance motor modelling

As it was shown in Chapter I, the switched reluctance machine is a promising and attractive electrical machine which may be used in many industrial and transport applications. The main advantages of this machine are its simple construction, robust structure, and its reliability. In contrast with the induction machine having distributed (random wound) stator winding, the conventional switched reluctance machine has concentrated stator windings made with round or rectangular wires. The concentrated windings offer the possibility to make fault-tolerant multiphase electrical machine: the larger the number of phases, the greater the reliability and the lower torque pulsations. In turn, the large number of phases requires high operating frequency and accurate control of switches. The fact that the rotor does not contain windings or magnets makes SRM suitable for very high speeds that also necessitates high switching frequency [21], [22]. On the other hand, the literature review shows the absence of high frequency model proposed for this machine's type that makes it a relevant task.

2.2.1 Proposed motor models

The high frequency models proposed for SRM modelling correspond to the equivalent circuit models described in [9] and [11]. Two types of per phase circuits having relatively simple structure as shown in Figures II.8a and II.8b are studied. In these schemes, the parameters have physical meaning. Thus, the parasitic capacitance and resistance between the motor frame and stator winding phase are modelled by C_{g1} and R_{g1} . The parasitic capacitance and resistance between the motor frame and stator neutral are modelled by C_{g2} and R_{g2} . The inductance of the electrical machine stator winding L_d can be represented by the mutually coupled stray inductance L_{str} and main inductance L_M , where $L_d = L_{str} + L_M$. The copper losses are represented by resistance R_{cu} (neglected in [11]) and iron losses are represented by R_e . The series branch R_t , L_t and C_t introduced in [11] is intended to improve the model fitting to the measured motor impedance simulating a second resonance in this characteristic. These parameters may be associated with inter-turn effects and skin effect.

Common mode and differential mode impedance frequency responses were measured for model parameters identification.

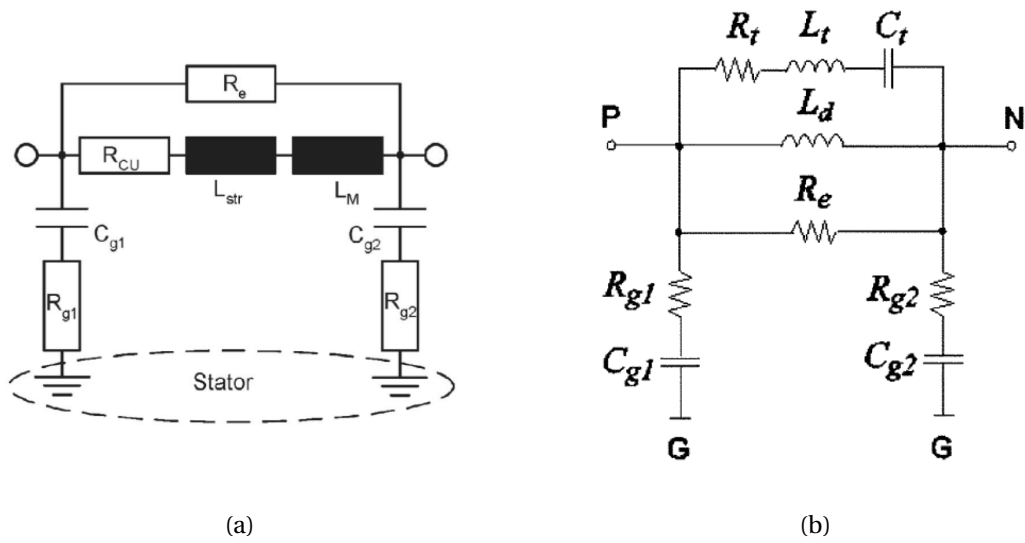


Figure II.8: High frequency per phase equivalent circuits:
 (a) simplified model defined in [9], (b) extended model defined in [11].

2.2.2 Motor impedance measurements

The studied electrical machine is a three-phase switched reluctance motor having six slots, four poles and concentrated winding made with rectangular wires. Figure II.9a provides the front-view of this motor demonstrating a simple access to stator winding coils terminals. During the impedance measurements, the winding is star-connected.

Figure II.9 shows the measurement setup equipped with the network analyzer Agilent Technologies E5061B having a frequency range from 5 Hz to 30 MHz of gain-phase test port. In order to minimize the influence of external parasitic inductances during measurements, the shortest cable connections were used. These cables were installed before the analyzer calibration procedure.

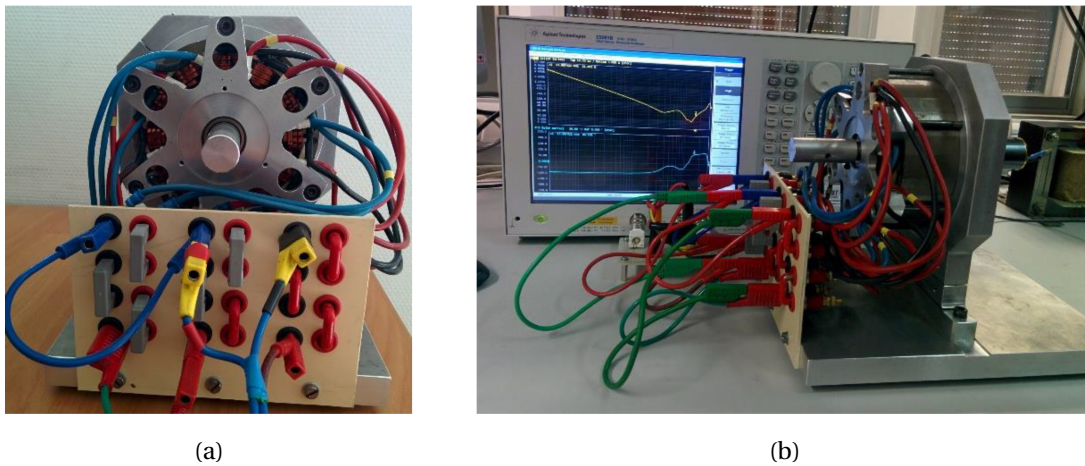


Figure II.9: Studied switched reluctance motor: (a) front-view, (b) setup for impedance measurement.

The SRM impedances were measured in frequency range from 30 kHz to 30 MHz. Firstly, the common mode impedance was measured as schematically represented by Figure II.10. The cables connections were placed between the phase A and the motor frame, three per phase circuits are connected in parallel, the winding neutral is not grounded. Secondly, the differential mode impedance was measured in accordance with connections scheme given in Figure II.11. Two per phase circuits B and C were connected in parallel, the both were connected in series with the phase A. The impedance was measured between these phases.

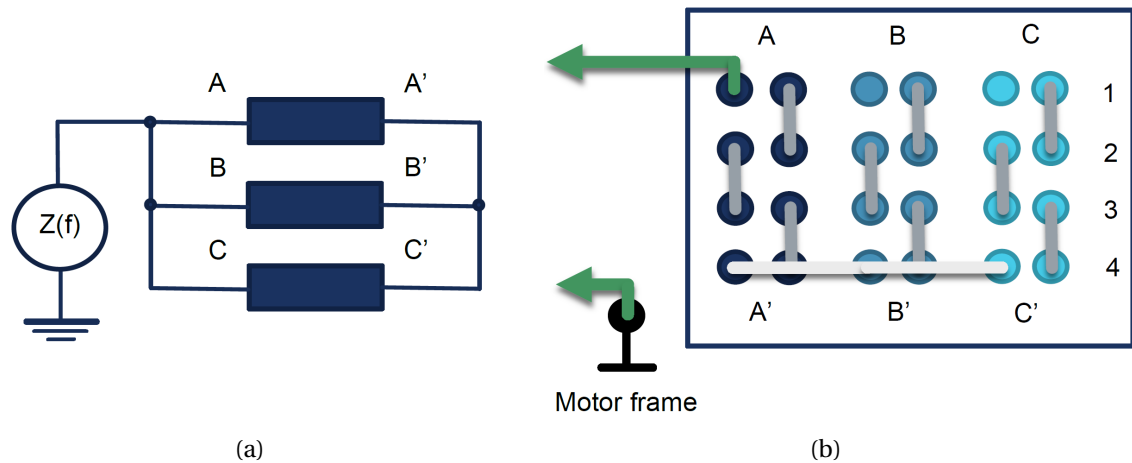


Figure II.10: Common mode impedance measurement: (a) per phase circuit connections, (b) winding coils connections.

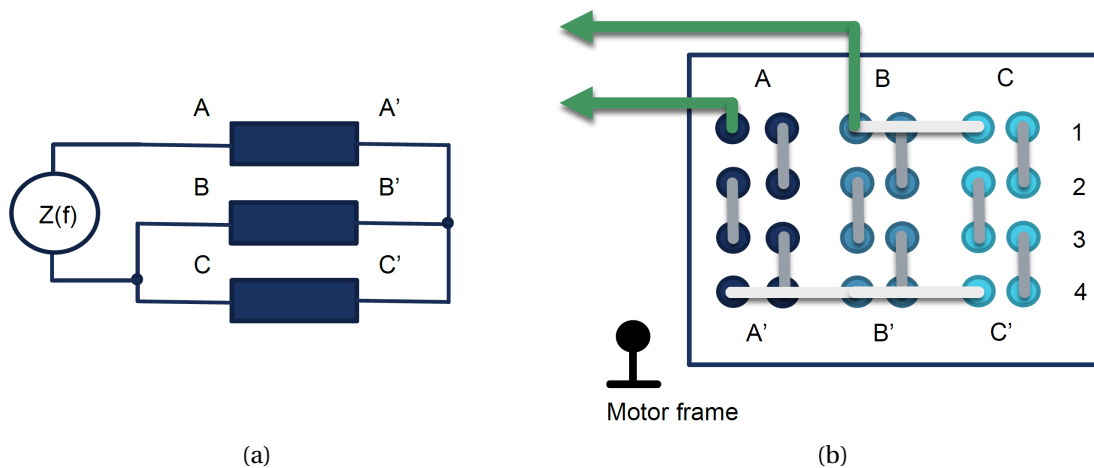


Figure II.11: Differential mode impedance measurement: (a) per phase circuit connections, (b) winding coils connections.

The tests were performed connecting the impedance analyzer to different phases, and it was observed that the three phases have almost the same frequency response. Measurements performed at different rotor positions shown that it slightly affects the CM impedance. On the other hand, the changing in DM impedance magnitude and phase (keeping the similar curves shapes) was observed in frequency range from 30 kHz to 5 MHz which is related to the SRM construction and operation. The motor's inductance depends on rotor position: maximum inductance when rotor poles are aligned with the stator poles, and minimum inductance at the unaligned position [23].

In the present study this changing is not considered and the model parameters are extracted from the motor impedances measured when rotor was stationary and its poles were aligned with the stator poles. The obtained impedances are provided in Figures II.12 and II.13. The characteristic points used for model parameters calculation described in the following section are shown in these figures.

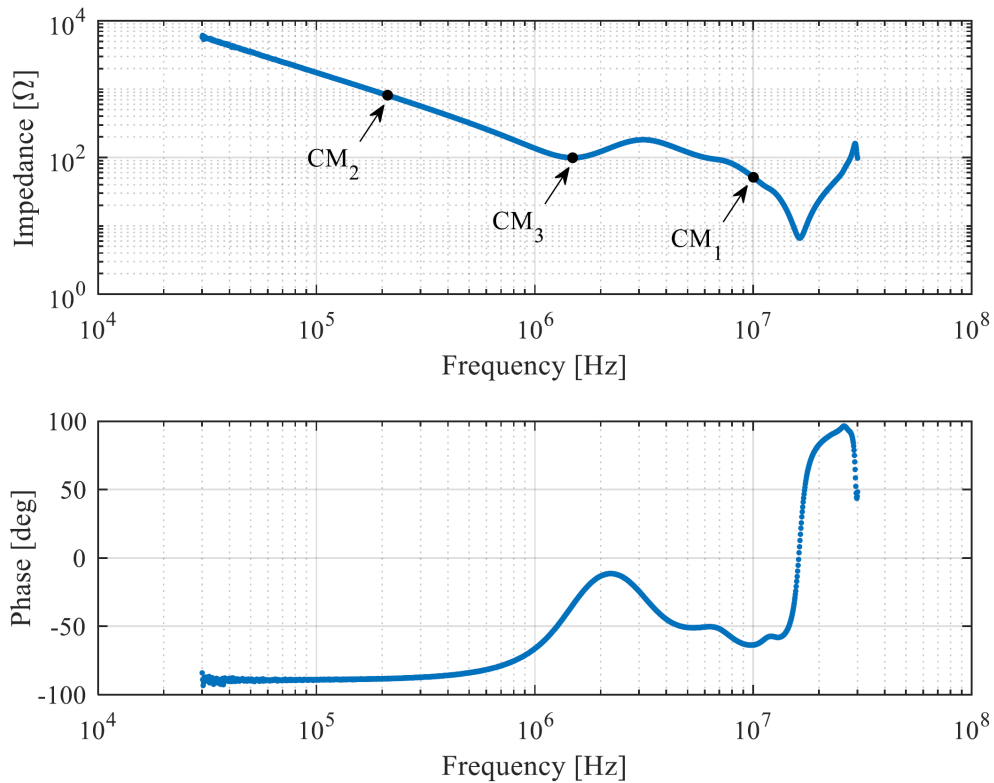


Figure II.12: Measured CM impedance of SRM.

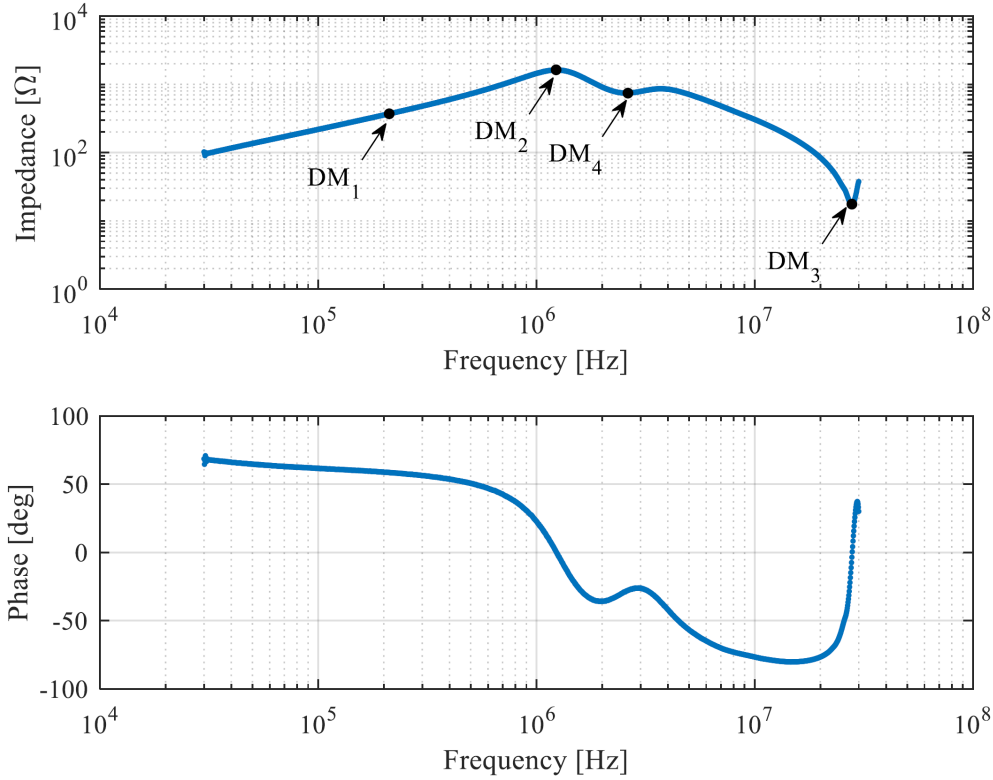


Figure II.13: Measured DM impedance of SRM.

2.2.3 Model parameters identification

The parameters of switched reluctance motor model are identified using the characteristic points from CM and DM impedance measurements. As for induction machines studied in [9] and [11], the SRM impedance is mainly capacitive in common mode. The point CM₃ corresponding to the first series resonance indicates an influence of CM inductance of studied motor, and the last series resonance is mainly due to the effect of measuring cable connections and motor internal feed lines stray inductance.

Coming now to the measured differential mode impedance. At low frequencies and up to the parallel resonance (point DM₂), the DM impedance of the studied SRM is mainly inductive. Then, the series resonance at point DM₄, which may be associated with winding inter-turn effects, is observed. After that, the DM impedance becomes mainly capacitive until the last series resonance (point DM₃) due to the effect of stray inductance.

According to the calculation methods described in [9] and [11], the model parameters discussed in Section 2.2.1 are derived as follows.

Basing on the equation $C = \frac{1}{2\pi fZ}$, the low- and high frequency CM capacitances C_{total} (point CM₂) and C_{HF} (point CM₁) are derived from the measured CM impedance. Then, the resonance frequency f_{res1} and corresponded impedance magnitude Z_{min1} (point CM₃) are identified. Using the obtained values, the following model parameters are calculated:

$$C_{g1} = \frac{1}{3} C_{HF} \quad (II.1)$$

$$C_{g2} = \frac{1}{3} (C_{total} - C_{HF}) \quad (II.2)$$

The CM inductance L_{CM} required for further calculations is determined from the resonance at point CM₃:

$$L_{CM} = \frac{1}{12\pi^2 C_{g2} f_{res1}^2} \quad (II.3)$$

Using the measured DM impedance and basing on the equation $L = \frac{Z}{2\pi f}$, the DM inductance L_{DM} (point DM₁) is calculated. The impedance magnitude Z_{max} is identified on the global maximum (point DM₂). Moreover, the impedance magnitudes Z_{min2} and Z_{min3} on global minima (points DM₃ and DM₄), the respective resonance frequencies f_{res2} and f_{res3} , as well as the phase θ_{Z3} at point DM₄, are extracted from the DM impedance.

The copper losses R_{cu} according to [9] can be estimated by a value less than 5 Ω for this model. The iron losses R_e are estimated by II.4. The equation II.5 gives the stray inductance of measuring cable connections and motor internal feed lines L_{zu} and the equation II.6 gives the parasitic resistance R_{g1} .

$$R_e \approx \frac{2}{3} Z_{max} \quad (II.4)$$

$$L_{zu} = \frac{3}{16\pi^2 C_{g1} f_{res2}^2} \quad (II.5)$$

$$R_{g1} = \frac{2}{3} Z_{min2} \quad (II.6)$$

Using the common mode and differential mode inductances L_{CM} and L_{DM} , the inductance L_d can be calculated.

$$L_d = L_{CM} + \frac{4}{9} L_{DM} \quad (II.7)$$

The parasitic resistance R_{g2} can be approximately calculated by II.8 or more accurately – by II.9. In the present study, the second equation is used.

$$R_{g2} \approx \frac{1}{3} Z_{min1} \quad (II.8)$$

$$R_{g2} = 3Z_{min1} - \frac{9R_e(2\pi f_{res1}L_{CM})^2}{R_e^2 + 36\pi^2 f_{res1}^2 L_{CM}^2} \quad (II.9)$$

Finally, with the purpose to catch the resonance at point DM₄, according to [11] the parameters R_t , L_t and C_t are calculated as follows.

$$R_t = Z_{min3} \cos \theta_{Z3} \quad (II.10)$$

$$C_t \approx \frac{1}{6} (C_{g1} + C_{g2}) \quad (II.11)$$

$$L_t = \frac{1}{4\pi^2 C_t f_{res3}^2} \quad (II.12)$$

The Table II.1 summarize the obtained model parameters values, which are used in further simulations.

Table II.1: Calculated parameters of switched reluctance motor HF model.

Model parameter	Value	Model parameter	Value
C_{g1} , pF	103.43	R_e , kΩ	1.087
C_{g2} , pF	204.18	L_d , μH	142.58
R_{g1} , Ω	11.702	L_{zu} , nH	236.01
R_{g2} , Ω	89.55	C_t , pF	51.268
R_{cu} , Ω	4	R_t , Ω	656.88
		L_t , μH	71.577

2.2.4 Comparison of measured and simulated motor impedances

With the objective to test the effectiveness of the chosen models for the studied switched reluctance motor modelling as well as the model parameters identification method, the measured and simulated motor impedances are compared. To this purpose, the frequency-domain numerical analysis was performed using LTSpice powered by Matlab software.

Firstly, the switched reluctance motor is modelled by the simplified equivalent circuit proposed in [9]. Figure II.14 shows the studied per phase circuit. The three-phase equivalent circuit model is obtained assuming a star-connection of three per phase circuits as during the impedance measurements. Figure II.15 provides the obtained simulation results in common and differential modes superimposed with the measurements.

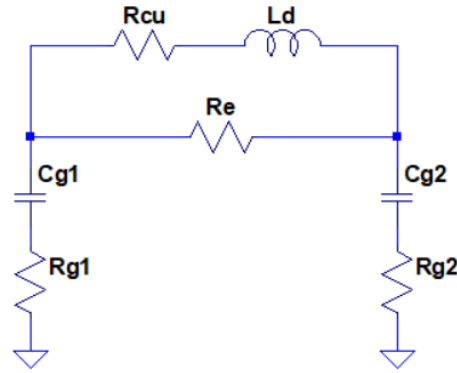


Figure II.14: Simplified HF per phase circuit motor model basing on [9].

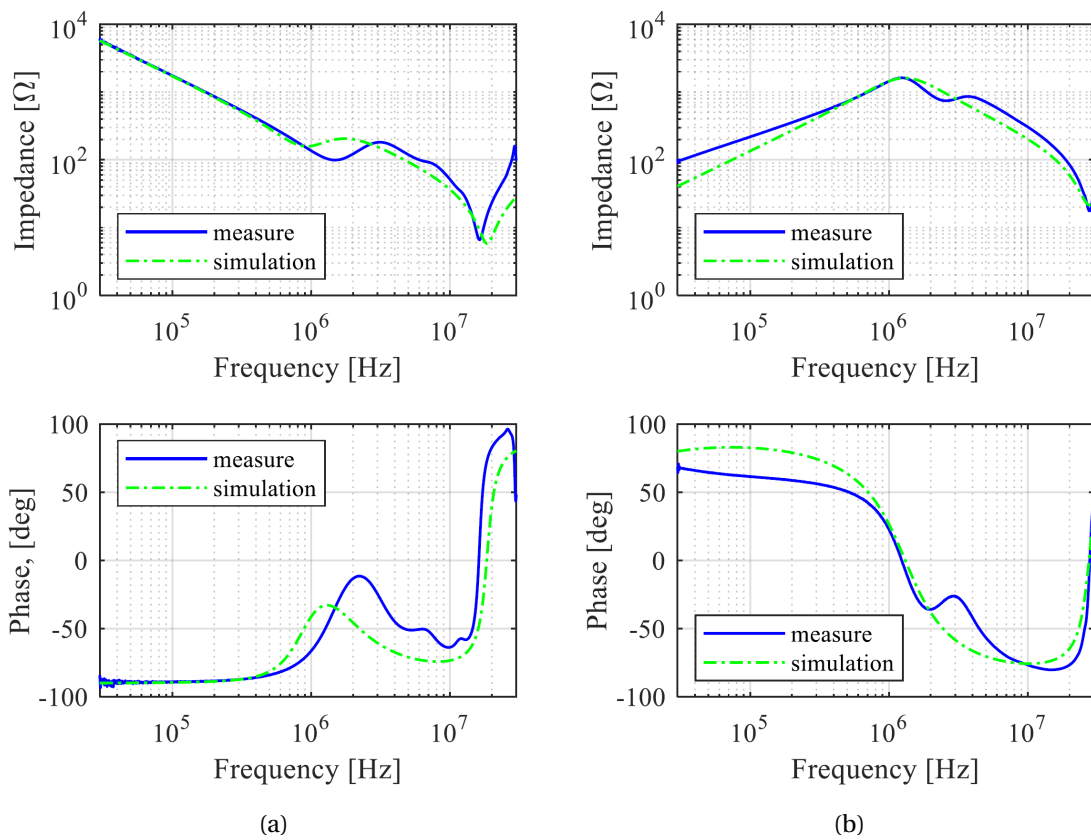


Figure II.15: Comparison of measured and simulated by simplified HF model motor impedances: (a) CM and (b) DM.

The simulation results of the model having previously calculated parameters show the similar trend of the impedance magnitude and phase angle. However, the resonances of simulated CM impedance are shifted in frequency. The low frequency slope of simulated DM impedance unfits the measured one. Moreover, the resonance at point DM₄ cannot be reproduced by this simplified circuit.

With the purpose to improve the model accuracy, the extended model from [11] is tested for our switched reluctance motor. The equivalent per phase circuit is given in Figure II.16. The model parameters provided in Table II.1 are used in the simulation. Figure II.17 demonstrates the obtained results.

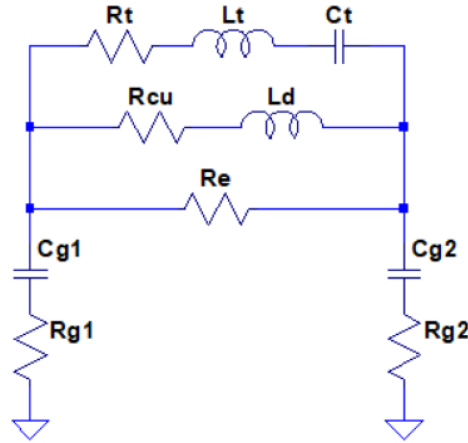


Figure II.16: Extended HF per phase circuit motor model basing on [11].

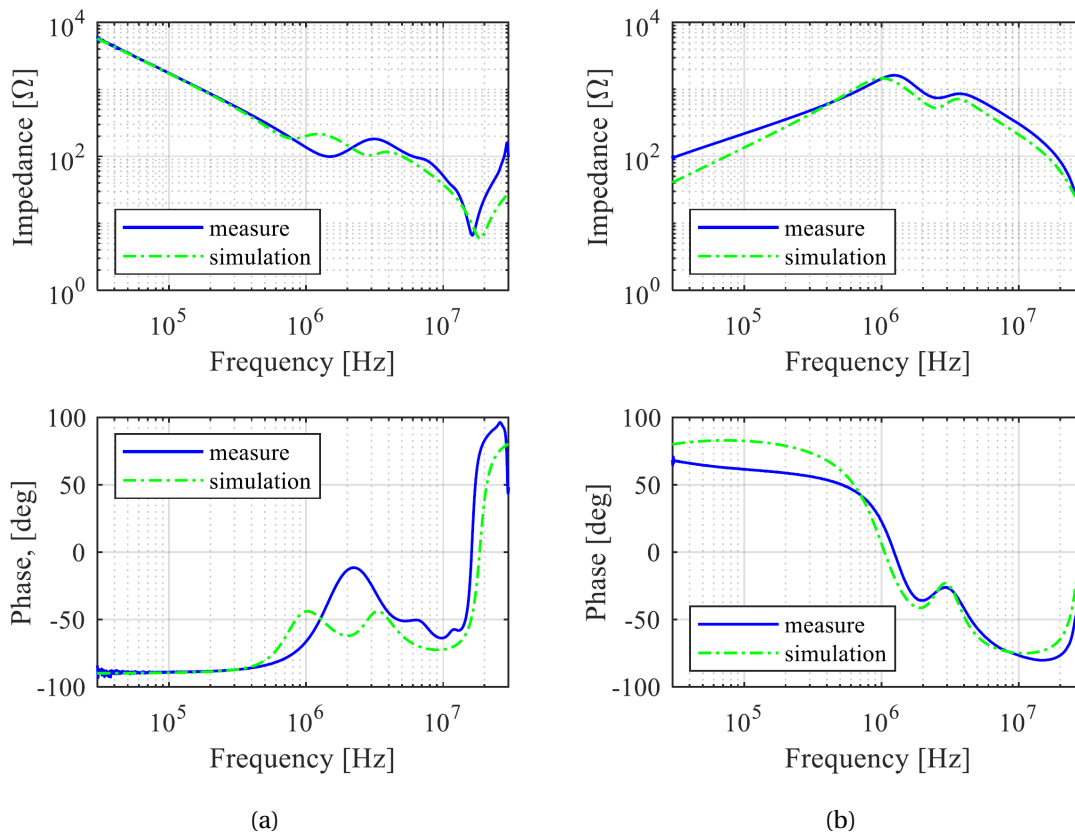


Figure II.17: Comparison of measured and simulated by extended HF model motor impedances: (a) CM and (b) DM.

By adding the series R_t , L_t , C_t branch, we reproduce the second resonance in differential mode improving the model accuracy. The extended model shows a better corre-

lation. In spite of this, an adjustment of model parameters is still needed to fit the simulation results to the measured ones considering the fact, that the choice of certain characteristic points and parameters' values is arbitrary. In this regard, the "trial-and-error" method or optimization algorithms are often used in literature, e.g. in [14], [16] and [9], in order to increase the model efficiency.

Table II.2 demonstrates the model parameters influence on the simulated impedance curves basing on the performed simulations.

Table II.2: Influence of model parameters on the CM and DM impedance magnitude curves.

Model parameter	Effect
C_{g1}	CM: modify the low-frequency slope (having point CM_2), resonance at point CM_3 , high-frequency slope (having point CM_1), and shift the frequency of the last resonance
	DM: shift the resonance frequency at point DM_2 , high-frequency slope, and shift the frequency of the last resonance
C_{g2}	CM: modify the low-frequency slope (having point CM_2) and the shape near to point CM_3
	DM: no effect
R_{g1}	CM: modify the last resonance amplitude
	DM: modify the last resonance amplitude
R_{g2}	CM: modify the shape near to point CM_3
	DM: no effect
R_{cu}	CM: no effect
	DM: slightly modify the low-frequency slope (having point DM_1)
R_e	CM: modify the shape near to point CM_3
	DM: modify the amplitude of resonance at point DM_2
L_d	CM: modify the shape near to point CM_3
	DM: modify the low-frequency slope (having point DM_1) and the resonance at point DM_2
L_{zu}	CM: modify the last resonance amplitude and frequency
	DM: modify the last resonance amplitude and frequency
C_t, R_t, L_t	CM: modify the resonance at point CM_3
	DM: modify the resonances at points DM_2 and DM_4

These observations correlate with [4] where the equivalent circuit model similar with [9] is studied. It should be noted that the changing in the model parameters values affects both common and differential modes. However, it is observed that improving in simulation accuracy of one mode results in decorrelation of another mode.

The parameters representing the skin and proximity effects should be frequency-dependent for better HF model accuracy, but it complicates the time-domain analysis. Moreover, specific features of SRM concerning its winding construction and consequent minimum magnetic coupling between phases, as well dependence of the machine reluctance on its rotor position [22] are not considered in the studied models. At the same time, it is noted that differences observed at last impedance resonance can be neglected considering the significant influence of measuring cable connections.

Although the mentioned above imperfections, the conducted study in frequency-domain shows that the extended HF equivalent circuit model may be used for modelling switched reluctance motors. Therefore, this motor model is retained for further time-domain modelling.

3 High frequency cable modelling

In the order to predict the overvoltage at inverter-fed motor terminals, an accurate high frequency model of the feeding cable is also required. As for the electric motor, the cable impedance behaviour over the frequency range should be reproduced. Different approaches to model cables for electric drives exist in literature. Cable models having distributed [5], [10] and [24] or lumped parameters [4], [8], [11], [12], [25] and [26] are proposed for time-domain analysis. In order to provide a good accuracy of lumped-parameter model considering the distributed parameters effect, an adequate number of cells or segments corresponding to elementary cable length should be used. The model parameters values can be extracted from differential mode impedance measurements (open circuit and short circuit impedances) [4], [12] or calculated using the finite-element method [5], [10], [24], transmission-line modelling technique [11] and modal transformation method [26], or evaluated by applying evolutionary algorithms [25]. By analogy with the HF motor model, the validation of proposed cable model is performed through the HF simulated and measured impedances comparison. The models taking into account skin and proximity effects as well as dielectric losses show the best accuracy.

With the purpose to perform the transient overvoltage analysis, the HF cable model proposed in [12], which provides a good compromise between model complexity and efficiency, is chosen. This model represents a cascade of cells (equivalent circuits) with lumped parameters and is compatible with the described above equivalent circuit model of switched reluctance motor. In this model, the lumped parameters R-L are cascaded in order to reproduce the skin and proximity effects. The dielectric losses are neglected. Figure II.18 provides the equivalent circuit (or cell) modelling the cable having two symmetrical cores (phases) and metal shield.

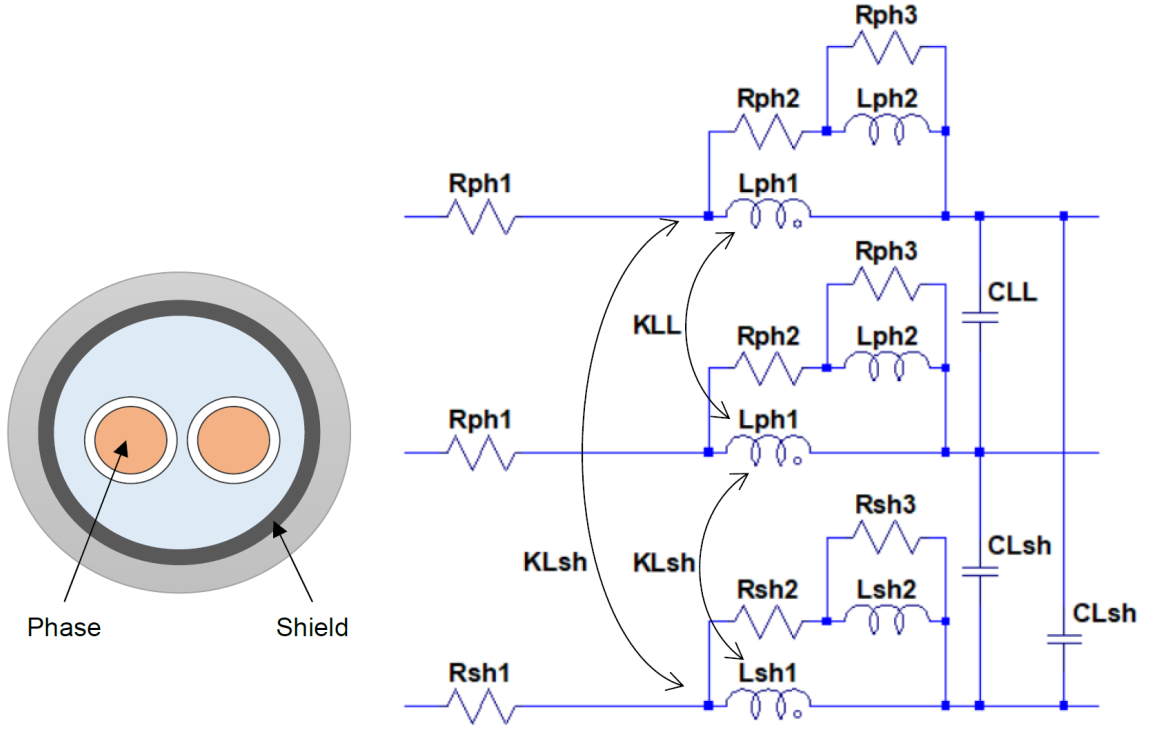


Figure II.18: Two-wire shielded cable: (a) cable's structure, (b) HF equivalent circuit model basing on [12].

In order to approximate the distributed parameters effects along the cable, a multi-cell model should be used for a long cable modelling. In this case, one cell or equivalent circuit should correspond to electrically short cable length l at the maximum signal frequency f_{max} . According to [27] $l = \frac{1}{10}\lambda$, where λ is the wavelength which in cable line is defined by (II.13).

$$\lambda = v \frac{1}{f_{max}} \quad (\text{II.13})$$

The signal propagation velocity v depends on the surrounding medium. Electromagnetic waves in cable line can be expressed in terms of the cable insulation permittivity ϵ_r :

$$v = \frac{c}{\sqrt{\epsilon_r}} \quad (\text{II.14})$$

where c is the speed of electromagnetic propagation in free space. The permittivity of polyethylene is equal to 2.3, thus the propagation velocity $v \cong 2 \times 10^8 \text{ m/s}$.

Thus, for the frequency of 30 MHz, the minimal cable length adequately represented by its equivalent circuit should not exceed 0.67 m. In case of impulse voltage having very short rise time, *e.g.* $t_r = 10 \text{ ns}$, the induced waveform should have significant spectral content up to around $1/10 \text{ ns} = 100 \text{ MHz}$ [27]. Therefore, the corresponded cable length modelled by the equivalent circuit model should be no more than 0.2 m.

In this Chapter, we focus on the motor modelling, therefore the cable parameters used in our simulations are based on values obtained by C. Vermaelen in [12]. In his work RLC-parameters of the proposed equivalent circuit correspond to 1 m of cable length for the frequency range up to 10 MHz. As discussed above, in order to investigate the effect of very short rise time, the minimal cable length should not exceed 0.2 m. Thus, the HF model corresponding to cable of one meter length is composed by five equivalent circuits and the RLC-parameters values are divided by 5. Table II.3 provides the parameters values of the equivalent circuit.

Table II.3: HF cable model parameters basing on [12].

Model parameter		Value
Phase resistance	R_{ph1}, Ω	0.012
	R_{ph2}, Ω	1.8
	R_{ph3}, Ω	200
Shield resistance	R_{sh1}, Ω	0.012
	R_{sh2}, Ω	0.6
	R_{sh3}, Ω	60
Phase inductance	$L_{ph1}, \mu\text{H}$	0.1018
	$L_{ph2}, \mu\text{H}$	0.4
Phase inductance	$L_{sh1}, \mu\text{H}$	0.14
	$L_{sh2}, \mu\text{H}$	0.28
Capacitance between phases	C_{LL}, pF	20
Capacitance between phase and shield	C_{Lsh}, pF	40
Coefficient of inductive coupling between phases	K_{LL}	0.65
Coefficient of inductive coupling between phase and shield	K_{Lsh}	0.83

4 Simulation of transient overvoltage in inverter-fed motor drive

In order to analyse the overvoltage phenomena at inverter-fed motor terminals the numerical study is performed. The system, consisting of a pulse voltage source, the equivalent circuit of feeding cable and the motor equivalent circuit, is simulated in time-domain using LTSpice software. The inverter voltage is approximated as trapezoidal pulses (the inverter internal impedances are neglected) with specified rise and fall times as in [8], [17] and [5]. Moreover, considering the particularity of switched reluctance motor supply-

ing when its phases are energized independently, a single-phase study may be sufficient. To study the effects of a single commutation the inverter can be modelled by an ideal pulse generator.

Firstly, the voltages applied to motor winding (the phase is energized) are simulated using simplified and extended motor models based on [9] and [11] respectively. The obtained waveforms are shown in Figure II.19. Taking into account the rated voltage of the studied SRM, the voltage of the ideal pulse generator is set at 300V, the pulse rise time is equal to $t_R = 30$ ns, and the single phase cable model corresponds to cable length $L = 1$ m. The similar results are obtained using the simplified and the extended models. The extended motor model is retained for the further simulations.

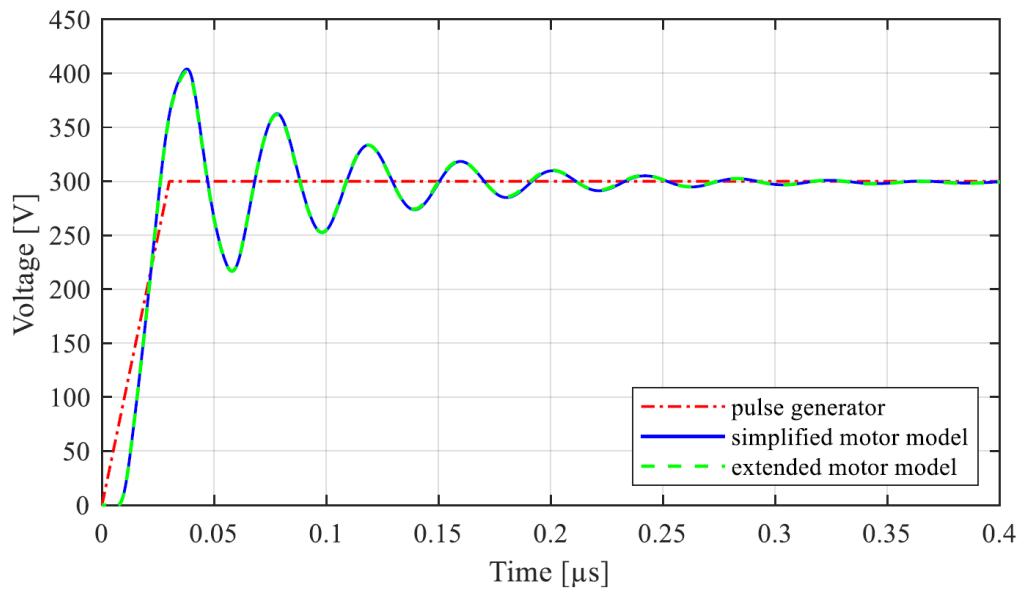


Figure II.19: Voltage waveforms for pulse generator voltage rise time $t_R = 30$ ns (10 kV/ μ s) and cable length $L = 1$ m simulated with two proposed motor models.

Secondly, the effect of impulse voltage rise time on motor overvoltage is studied at two cable lengths. Figure II.20 reports the simulation results for different rise times when the length of cable is equal to one meter. The shorter is the rise time, the higher is the overvoltage. On the other hand, increasing in power cable length influences the transient overvoltage and ringing reducing the variation between waveforms obtained at different rise times.

Then, the rise time is set at 30 ns (10 kV/ μ s) and the voltages at motor phase winding when supplying through the cable lengths of five and ten meters are simulated and shown in Figure II.21. As it was shown above, increasing in cable length intensifies the transient overvoltage and affects the oscillating frequency making the transients longer. In the current simulations, the overvoltage doesn't reach two times of pulse generator's voltage. It may be explained by cable losses considering in this model. Moreover, the used cable model can be not fully adapted to high cable length combined with very low

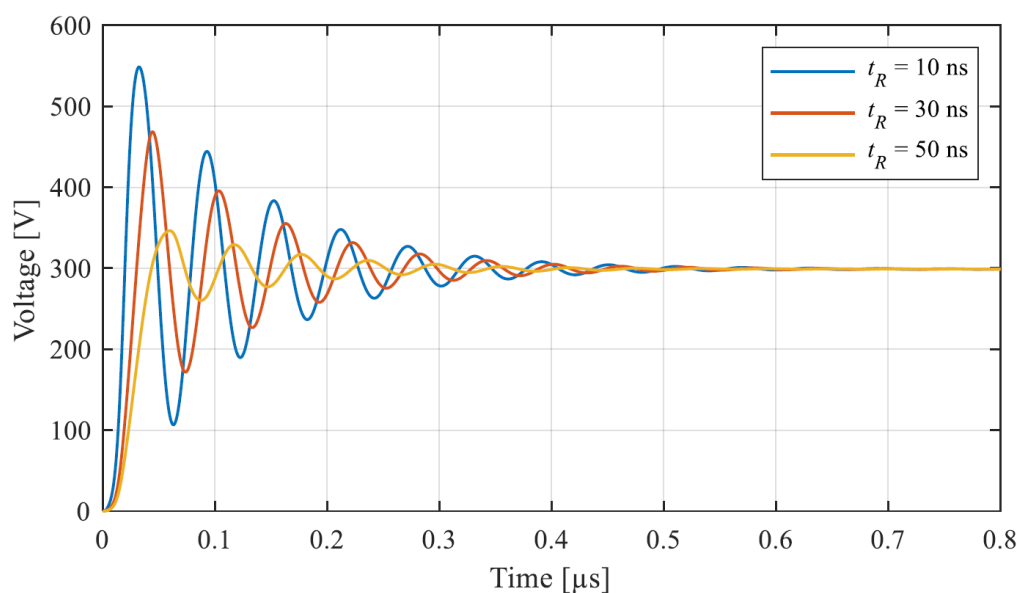


Figure II.20: Voltage waveforms for different pulse generator voltage rise times simulated with the extended motor model $L = 1$ m

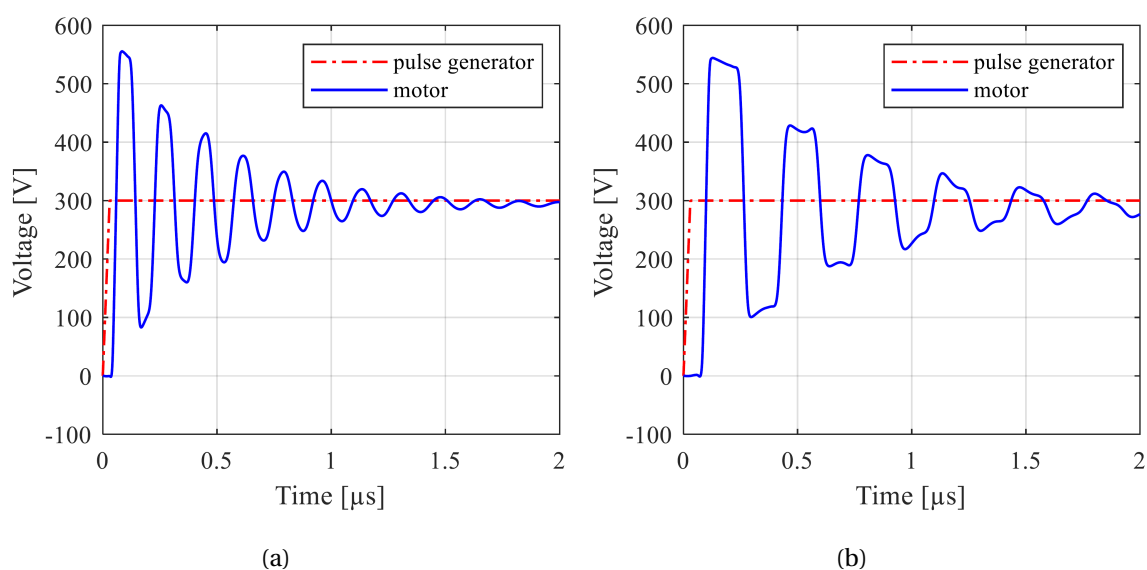


Figure II.21: Voltage waveforms at the motor terminals for pulse generator voltage rise time $t_R = 30$ ns and different cable lengths: (a) $L = 5$ m and (b) $L = 10$ m.

pulse rising time requiring multiple cells. As it was noted in [12], the model is limited in frequency and number of cells. In spite of that, performed simulations show that in case of high dV/dt impulse voltage even the short cable connections will lead to important transient overvoltage at motor terminals.

5 Conclusion

In the present Chapter, the high frequency model of the electric drive for overvoltage analysis at motor terminals is proposed. Considering the high frequency oscillations in inverter-fed motor winding, the prediction of overvoltage requires high frequency modelling in the range of the rise time. In this regard, the lumped parameters HF model for the switched reluctance motor is suggested for a first time, basing on the models developed for induction motors. The RLC-parameters of equivalent circuit model are derived from the motor winding impedance measurements in common and differential modes. The model is validated in frequency-domain comparing the measured and simulated impedance frequency responses. Additional study may be performed to improve the model accuracy. Nevertheless, the present model can be used to estimate the overvoltage occurring at motor terminals.

Taking into account the influence of feeding cable on motor overvoltage due to the propagation and reflexion phenomena, the proposed in literature HF cable model having cascaded lumped parameters is used in this study. The single inverter commutation simulation is performed using the ideal pulse generator producing trapezoidal pulses with regulated rising time. The effect of impulse voltage rise time and length of feeding cable is studied. The shorter is the rise time, the smaller will be the critical cable length causing the considerable overvoltage.

The performed numerical study described in this Chapter is completed in follow-up the previously discussed literature survey of factors affecting low voltage electrical machines. The objective was to put into evidence the effect of high dV/dt on overvoltage at inverter-fed motor terminals, especially in case of WBG-based electronic devices. The arising overvoltage in inverter-fed motor winding can lead to partial discharges inception accelerating winding insulation degradation. The use of high speed switching electronic devices will increase the risk of transient overvoltage even for short cable connections and, consequently, the risk of partial discharges occurrence.

References

References

- [1] Mike Melfi, A.M.J. Sung, Sidney Bell, and G.L. Skibinski. Effect of surge voltage rise-time on the insulation of low-voltage machines fed by PWM converters. *IEEE Transactions on Industry Applications*, 34(4):766–775, 1998.
- [2] M. Fenger, S.R. Campbell, and J. Pedersen. Motor winding problems caused by inverter drives. *IEEE Industry Applications Magazine*, 9(4):22–31, jul 2003.
- [3] G.L. Skibinski, R.J. Kerkman, and Dave Schlegel. EMI emissions of modern PWM AC drives. *IEEE Industry Applications Magazine*, 5(6):47–80, nov 1999.
- [4] Francesco Pulsinelli, Luca Solero, Davide Chiola, Klaus Sobe, and Fabio Brucchi. Overvoltages at Motor Terminals in SiC Electric Drives. In *2018 International Symposium on Power Electronics, Electrical Drives, Automation and Motion (SPEEDAM)*, pages 513–518. IEEE, jun 2018.
- [5] Bouazza Taghia, Bernardo Cougo, Hubert Piquet, David Malec, Antoine Belinger, and Jean-Pierre Carayon. Overvoltage at motor terminals in SiC-based PWM drives. *Mathematics and Computers in Simulation*, 158:264–280, apr 2018.
- [6] A. Boglietti and E. Carpaneto. Induction motor high frequency model. In *Conference Record of the 1999 IEEE Industry Applications Conference. Thirty-Forth IAS Annual Meeting (Cat. No.99CH36370)*, volume 3, pages 1551–1558. IEEE, 1999.
- [7] A. Said and Kamal Al-Haddad. A new approach to analyze the overvoltages due to the cable lengths and EMI on adjustable speed drive motors. In *2004 IEEE 35th Annual Power Electronics Specialists Conference (IEEE Cat. No.04CH37551)*, volume 5, pages 3964–3970. IEEE, 2004.
- [8] H. De Paula, M.L.R. Chaves, D.A. Andrade, J.L. Domingos, and M.A.A. Freitas. A new strategy for differential overvoltages and common-mode currents determination in PWM induction motor drives. In *IEEE International Conference on Electric Machines and Drives, 2005.*, pages 1075–1081. IEEE, 2005.
- [9] M. Schinkel, S. Weber, S. Guttowski, W. John, and H. Reichl. Efficient HF Modeling and Model Parameterization of Induction Machines for Time and Frequency Do-

- main Simulations. In *Twenty-First Annual IEEE Applied Power Electronics Conference and Exposition, 2006. APEC '06.*, volume 2006, pages 1181–1186. IEEE, 2006.
- [10] Gary Skibinski, Rangarajan Tallam, Robert Reese, Brian Buchholz, and Richard Lukaszewski. Common Mode and Differential Mode Analysis of Three Phase Cables for PWM AC Drives. In *Conference Record of the 2006 IEEE Industry Applications Conference Forty-First IAS Annual Meeting*, volume 2, pages 880–888. IEEE, oct 2006.
- [11] Liwei Wang, Carl Ngai-Man Ho, Francisco Canales, and Juri Jatskevich. High-Frequency Modeling of the Long-Cable-Fed Induction Motor Drive System Using TLM Approach for Predicting Overvoltage Transients. *IEEE Transactions on Power Electronics*, 25(10):2653–2664, oct 2010.
- [12] Christophe Vermaelen. *Contribution à la modélisation et à la réduction des perturbations conduites dans les systèmes d'entraînement à vitesse variable*. PhD thesis, École normale supérieure de Cachan - ENS Cachan, 2003.
- [13] Loucif Benmamas. *Méthodes d'évaluation du risque de décharges partielles dans le bobinage de machines électriques destinées à la traction automobile*. PhD thesis, Université Paris-Saclay, 2017.
- [14] G. Grandi, D Casadei, and A. Massarini. High Frequency Lumped Parameter Model for AC Motor Windings. In *European Conference on Power Electronics and Applications*, volume 2, 1997.
- [15] E. Carpaneto, A. Boglietti. An Accurate Induction Motor High-Frequency Model for Electromagnetic Compatibility Analysis. *Electric Power Components and Systems*, 29(3):191–209, mar 2001.
- [16] Aldo Boglietti, Andrea Cavagnino, and Mario Lazzari. Experimental High-Frequency Parameter Identification of AC Electrical Motors. *IEEE Transactions on Industry Applications*, 43(1):23–29, 2007.
- [17] A. Boglietti and E. Carpaneto. An accurate high frequency model of AC PWM drive systems for EMC analysis. In *Conference Record of the 2001 IEEE Industry Applications Conference. 36th IAS Annual Meeting (Cat. No.01CH37248)*, volume 2, pages 1111–1117. IEEE, 2001.
- [18] Sara Mahdavi and Kay Hameyer. High frequency equivalent circuit model of the stator winding in electrical machines. In *2012 XXth International Conference on Electrical Machines*, pages 1706–1711. IEEE, sep 2012.

- [19] Vasile Mihaila. *Nouvelle Conception des bobinages statoriques des machines à courant alternatif pour réduire les effets négatifs des dV/dt* . PhD thesis, Université d'Artois, 2011.
- [20] Nidhal Boucenna. *Contribution à la modélisation en compatibilité électromagnétique des machines électriques triphasées*. PhD thesis, École normale supérieure de Cachan - ENS Cachan, 2014.
- [21] Jan A Melkebeek. *Electrical Machines and Drives*. Power Systems. Springer International Publishing AG, Cham, 2018.
- [22] Guang Jin Li, Xavier Ojeda, Sami Hlioui, Emmanuel Hoang, Mohamed Gabsi, and Cedric Balpe. Comparative study of Switched Reluctance Motors performances for two current distributions and excitation modes. In *2009 35th Annual Conference of IEEE Industrial Electronics*, pages 4047–4052. IEEE, nov 2009.
- [23] Amissa Arifin, Ibrahim Al-Bahadly, and Subhas Chandra Mukhopadhyay. State of the Art of Switched Reluctance Generator. *Energy and Power Engineering*, 04(06):447–458, 2012.
- [24] Y. Weens, N. Idir, R. Bausiere, and J.J. Franchaud. Modeling and simulation of unshielded and shielded energy cables in frequency and time domains. *IEEE Transactions on Magnetics*, 42(7):1876–1882, jul 2006.
- [25] S. Bogarra, J.-R. Riba, V. Sala-Caselles, and A. Garcia. Optimal fitting of high-frequency cable model parameters by applying evolutionary algorithms. *International Journal of Electrical Power & Energy Systems*, 87:16–26, may 2017.
- [26] Abdullah Hoshmeh. A three-phase cable model based on lumped parameters for transient calculations in the time domain. In *2016 IEEE Innovative Smart Grid Technologies - Asia (ISGT-Asia)*, pages 580–585. IEEE, nov 2016.
- [27] Clayton R Paul. *Analysis of Multiconductor Transmission Lines*. Wiley-IEEE Press, 2nd ed. edition, 2008.

Chapter III : Endurance testing methods for turn insulation of motors fed by inverters

Chapter III

Endurance testing methods for turn insulation of motors fed by inverters

Contents

1 Introduction	90
2 Review of methods for testing the inverter-fed motors winding insulation .	90
3 Testing methodology	94
3.1 Test objects: winding wires	94
3.2 Specimens preparation	96
3.3 Breakdown voltage tests	98
3.4 Endurance tests	99
3.4.1 Endurance test under sinusoidal voltage	100
3.4.2 Endurance test under low dV/dt PWM impulse voltage: μ s - level rise time	103
3.4.3 Endurance test under high dV/dt impulse voltage: ns - level rise time	109
A Half-bridge inverter topology	109
B H-bridge inverter topology	112
3.5 Partial discharges detection tests	116
3.5.1 Optical method	117
3.5.2 Electromagnetic method	119
3.5.3 Chemical method	121
4 Conclusion	123
References	127

1 Introduction

This chapter details methods and experimental benches for testing winding insulation of low voltage electric motors fed by inverters. Firstly, a brief review of methods proposed in literature is given. Following sections detail a testing methodology including test objects' specifications, specimens' constructions, standard and novel experimental test techniques utilized in this study. The obtained experimental results, their analysis, and the main observations conducted during the endurance testing are provided in Chapter IV.

The preliminary test under AC sinusoidal voltage is conducted. It provides the initial information about testing winding wires allowing to compare their electrical endurance under sinusoidal voltage before performing impulse voltage tests. The impulse voltage waveforms are used to study the effect of electrical stresses on motor winding insulation engendering by conventional Si and modern SiC high-speed switches. For this purpose, original test benches have been developed. During the experiment the specimens are exposed to variable thermal and electrical stresses provoking electric discharges. The insulation accelerated ageing is engendered. The mean time to breakdown is used as the end-point criteria for the insulation endurance evaluation.

2 Review of methods for testing the inverter-fed motors winding insulation

Various testing methods are proposed to investigate the effect of impulse voltage generated by PWM based inverters on electrical machines insulation. These tests focus on winding insulation owing to the fact that it is the weakest point of electrical machine. The experimental studies are carried out both on electric motors [1], [2], [3], [4], [5], [6], [7], [8] and on different winding wires' specimens. With the objective to test phase-to-phase and phase-to-ground insulation, motorettes fabricated using winding wires and intertape are used in [8] (see Figure III.1) and [9]. For qualification of hairpin motors insulation having bar windings, formettes and coupled bars (shown in Figure III.2) are proposed in [10] to test phase-to phase and turn-to-turn insulation respectively. The turn-to-turn insulation is identified as the weakest part of winding insulating system in [10] and [11].

Turn insulation tests are mainly conducted on twisted pairs which are standardized specimens for round section enamelled wires [9], [12], [13], [14], [15], [16], [17], [18], [19], [20], [21], [22], [23], [24], [25], [26], [27] and [28]. These specimens should be prepared in accordance with the standard IEC 60851-5 [29] (see Figure III.3). Otherwise, in works [20], [30], [31], [32], [33], [34], [35], [36] and [37] specimens represent two enamelled wires having one contact point where partial discharges are generated (Figure III.4), what allows to investigate partial discharges phenomenon.

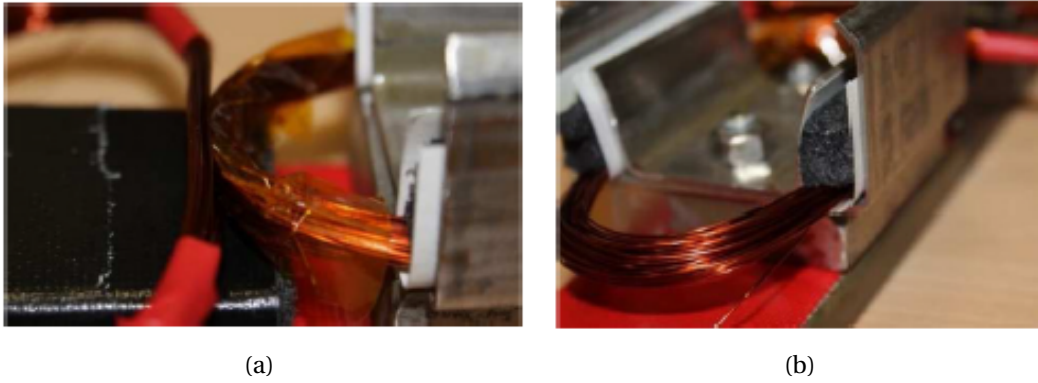


Figure III.1: Examples of motorette test setup configurations: (a) phase-to-phase motorette setup and (b) phase-to-ground motorette setup [8].

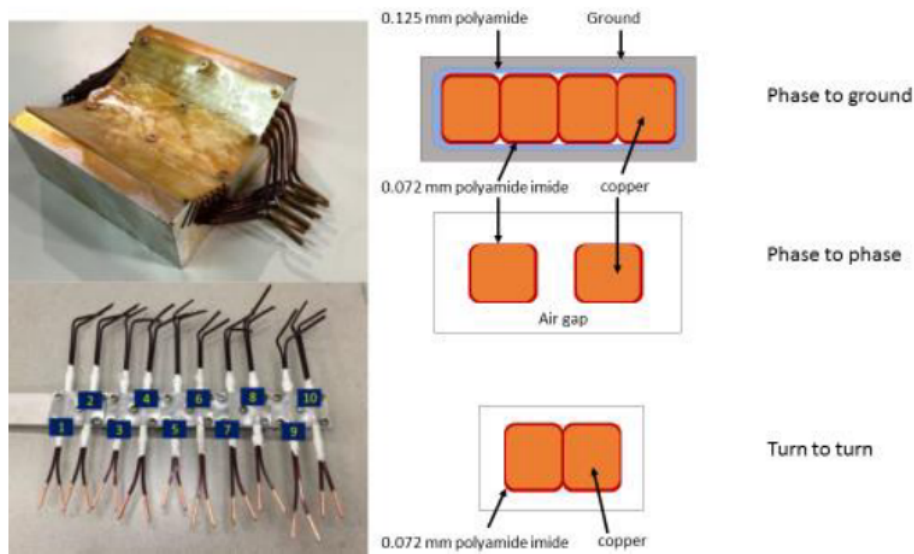


Figure III.2: Samples for hairpin motors insulation qualification tests [10].

The mentioned studies are related to PDs and insulation failure mechanism investigation in low voltage electrical machines fed by inverters for various applications including automotive [10], [19] and aeronautical ones [3], [6], [7], [8], [9], [13] and [22].

In [5], [20], [23], [30], [38], [39] and [40] partial discharges characteristics, inception conditions, and the influence of PDs activity on the insulation lifetime are investigated. The effects of testing voltage waveform parameters on PDs features and winding wires endurance are shown in [8], [21], [31], [32], [33], [34], [35] and [37]. These works show that the higher is the PDIV, the longer will be the insulation service life in PWM drive environment. The PDs patterns and inception voltage under repetitive impulse voltage changes significantly comparing to the sinusoidal voltage. It was observed, that the very short impulse voltage rise time, *e.g.*, 20 ns in [39], may lead to higher PDIV. At the same time, the faster rise time and higher frequencies shorten the insulation lifetime due to the increased PDs repetition rate and PDs magnitude. It is also noted, that the endurance of turn insulation can be increased using the wires with thicker enamel layer.

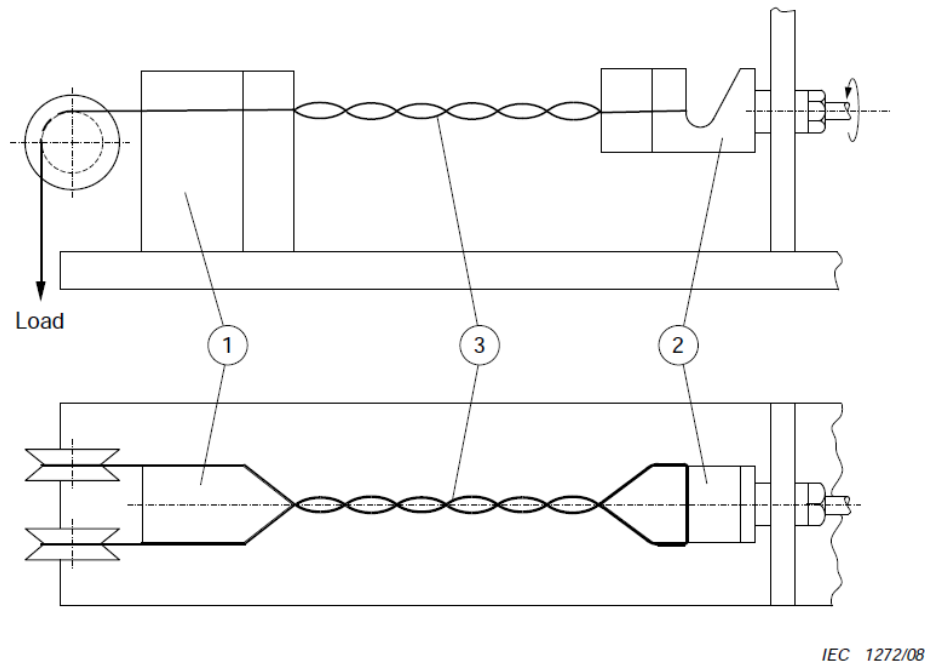


Figure III.3: Device for twisting the specimen for breakdown voltage test: 1 – spacer; 2 – rotary hook; 3 – specimen [29].

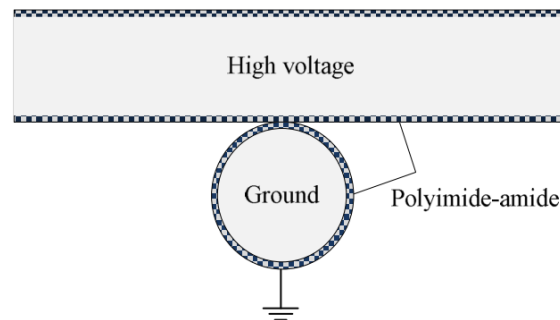


Figure III.4: Two crossed enamelled wires creating one-point contact specimen [30].

In [15], [16], [17] and [21] the endurance of conventional and corona resistant (nano-filled) enamelled winding wires are compared. The corona resistant wires demonstrate the better endurance under partial discharges and they are recommended to use in inverter-fed motors. In [26] the impact of ozone generated by PDs activity as a factor accelerating the insulation ageing is analysed. Insulation lifetime models depending on the applied stresses (voltage amplitude, frequency and temperature) and their interaction are described in [25], [41] and [42]. The design of experiments and response surface methods are used to establish the lifetime models. The effect of the initial conditions of winding wires is studied in [25], where the lifetime of mechanically damaged wires (light, medium and heavy manually wound wires) is evaluated. It is shown that the heavy wound dramatically affects the insulation lifetime, and a bi-modal lifetime distribution is observed in this case. Mechanical, thermal and electrical stresses effects on turn insulation were studied

in [27]. In this paper different types of enamels and impregnating compositions are compared in terms of breakdown voltage and PDIV. A novel fabrication method of enamelled wire using the enamel extrusion and the following polymerization by an ultraviolet lamp is proposed. The works [9], [12], [13], [22], [45] and [46] are intended to the investigation of temperature, humidity and pressure effects on PDIV in motor winding insulation. These studies show that the humidity has lower impact on partial discharges inception than the pressure and the temperature. A technique to improve winding insulation design and, consequently, to reduce partial discharge activity in inverter-fed motors is proposed in [13] and [28]. The proposal consists in adding a thin silver conducting paint on enamelled wire outer surface. This solution provides the increasing in the the partial discharge inception voltage. In works [8], [19], [43], [44] methods for determination of voltage distribution and overvoltage in motor windings are given. This type of study is conducted in order to predict the partial discharges occurrence determining the potential overvoltage in motor winding, or to prevent their ignition improving the voltage distribution within the winding.

The use of wide bandgap power electronics in motor drives requires new approaches to study PDs effects on motor winding insulation. SiC-based inverters may intensify electrical stresses on driven motors' winding insulation because of their higher switching speeds and switching frequencies comparing with silicon electronic components. Due to this fact, PDs will occur with higher probability, and the motor insulation ageing and failure will be accelerated. In reference [6], the experimental study is conducted on the electric motor using SiC-based inverter and thermal vacuum chamber reproducing environmental and operational conditions. Nevertheless, the fact that the tests are carried out on the complex motor drive system makes them relatively expensive and difficult to use in order to study the physical processes of dielectric ageing. Therefore, ageing and deterioration process in insulation subjected to PWM voltage waveform, in particular impulse voltage with high dV/dt and high switching frequency, are not thoroughly investigated. Moreover, taking into account influence of thermal stresses affecting the insulation during motor operation, the simultaneous effect of these factors and the process of electro-thermal ageing need to be considered.

Thus, the aim of this experimental work is to investigate the influence of voltage waveform on enamel insulation endurance, highlighting the effect of high dV/dt and switching frequency, as well as the effect of rise in ambient temperature. To achieve these objectives, experimental benches allowing to perform insulation endurance tests have been designed. The test benches make it possible to reproduce the stresses affecting the winding insulation of motors fed by inverters, generating repetitive impulse voltage with μ s- and ns-level of rise/fall time, that corresponds to conventional Si and modern SiC-based inverters respectively.

3 Testing methodology

3.1 Test objects: winding wires

In standard IEC TS 60034-18-41 [47] two types of winding insulation are defined. Type I and Type II are distinguished according to their rated voltage level, partial discharges withstanding capability, used dielectric materials and winding constructions. The insulation of Type I is generally used in machines rated at 700 V RMS or less (low voltage electric machines) and should not be subjected to PDs contrary to the Type II insulation which is generally used above 700 V RMS. However, the previous studies mentioned in the present work show that partial discharges may occur in low voltage machine's winding when supplying by PWM converters. Partial discharges activity and insulation destruction depend on operation conditions (humidity, pressure) and thermal, electrical and mechanical stresses. PDs appearance can also be a symptom of the insulation degradation process, which can lead to a final failure.

In the present research the winding insulation of Type I is studied. As previously mentioned, the weakest element of winding insulation system is the turn insulation, consisting of enamelled winding wire and impregnating compound. Basing on consideration that partial discharges can occur in defects of winding impregnation such as voids and cracks, the enamel insulation resistance to partial discharges determines the turn insulation endurance. In this regard, the endurance tests are mostly conducted on unimpregnated enamelled winding wires presented below.

The commercially available conventional wires and one corona resistant wire are tested. The specific composition of the corona resistant nano-filled wire makes possible a better resistance to degradation caused by PDs, providing improvement in terms of chemical erosion by partial discharges, electrical breakdown and endurance behaviour, as well as space charge mitigation, comparing to conventional enamelled wires [15], [17], [48] and [49].

For this study, enamelled winding wires manufactured by JSC "Sibkabel" (part of "Cable Alliance Holding", Russia) of brands PETD2-K-180 (corona resistant wire) and PETD-180 (conventional wire) are chosen. Furthermore, two wires, named herein APX-1 and APX-2, issued by the cable supplier APX (France) are tested. The studied wires have similar applications: electrical machines, apparatus and appliances production. The wire APX-2 has a rectangular section; other wires have round section. Rectangular enamelled wires can be used in motors with concentrated or coil stator windings (*e.g.*, switched reluctance machines), and round section wires are usually used for distributed windings (*e.g.*, induction machines). For more details on studied wires, please refer to Appendix III-A.

The insulation thickness of tested wires is determined experimentally using a micrometer MK-25 0.01 SHAN 123738 having accuracy class 1. The obtained results are given in Table III.1 and Table III.2.

Table III.1: The enamel insulation thickness measurement results for round section wires.

		PETD2-K-180		PETD-180		APX-1	
		D, mm	d, mm	D, mm	d, mm	D, mm	d, mm
Specimens	#1	1.21	1.13	1.13	1.06	1.08	1.01
	#2	1.19	1.11	1.14	1.06	1.09	1.03
	#3	1.19	1.12	1.13	1.08	1.08	1.04
	#4	1.19	1.12	1.13	1.06	1.08	1.02
	#5	1.19	1.11	1.13	1.07	1.08	1.02
	#6	1.20	1.12	1.13	1.06	1.09	1.02
	#7	1.19	1.13	1.13	1.11	1.09	1.03
	#8	1.19	1.12	1.13	1.09	1.08	1.02
	#9	1.21	1.11	1.13	1.06	1.08	1.03
	#10	1.21	1.11	1.13	1.06	1.08	1.02
\bar{D} and \bar{d} , mm		1.1970	1.1180	1.1310	1.0710	1.0830	1.0240
σ , mm		0.0095	0.0079	0.0032	0.0173	0.0048	0.0084
δ_{rad} , mm		0.0395		0.0300		0.0295	

In Table III.1, D is the insulated wire's diameter, d is the conductor's diameter, \bar{D} and \bar{d} are the diameters' mean values, σ is the diameters' standard deviations and δ_{rad} is the insulation radial thickness (see Figure III.5a), calculated as follows:

$$\delta_{rad} = \frac{\bar{D} - \bar{d}}{2} \quad (III.1)$$

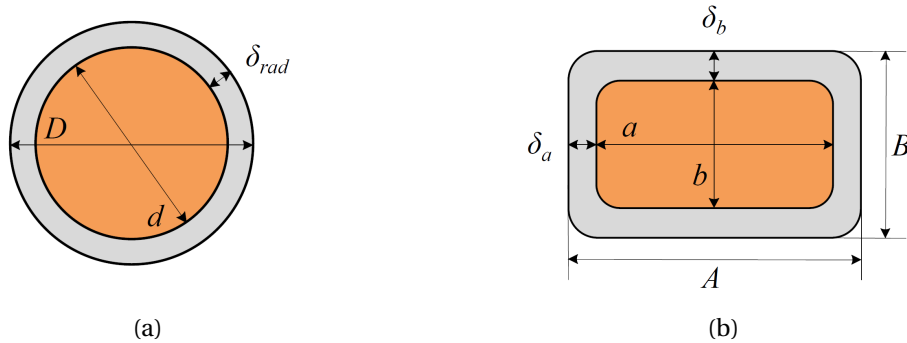


Figure III.5: Geometry of winding wire: (a) round section wire and (b) rectangular section wire.

Table III.2: The enamel insulation thickness measurement results for rectangular section wire.

		APX-2			
		A, mm	a, mm	B, mm	b, mm
Specimens	#1	2.96	2.82	1.15	1.05
	#2	2.94	2.83	1.16	1.06
	#3	2.95	2.82	1.15	1.06
	#4	2.94	2.82	1.16	1.05
	#5	2.95	2.80	1.15	1.03
	#6	2.96	2.80	1.15	1.03
	#7	2.95	2.81	1.15	1.06
	#8	2.96	2.82	1.16	1.03
	#9	2.96	2.82	1.16	1.03
	#10	2.96	2.82	1.15	1.05
Mean, mm		2.9530	2.8160	1.1540	1.0450
Standard deviation, mm		0.0082	0.0097	0.0052	0.0135
δ_a , mm		0.0685		-	
δ_b , mm		-		0.0545	

In Table III.2, A is the insulated wire's width, a is the conductor's width, B is the insulated wire's thickness, b is the conductor's thickness, δ_a and δ_b are the insulation thickness on wide and narrow wire's sides respectively (see Figure III.5b). The insulation thickness is find by analogy with (III.1).

3.2 Specimens preparation

Firstly, the breakdown voltage tests are conducted on bent wire specimens shown in Figure III.6 according to the standard IEC TS 60851-5 [29]. The experimental setup and testing procedure will be given hereinafter. Specimens are made of straight pieces of round and rectangular sections wires of 200 mm length, where tested area is equal to 125 mm.

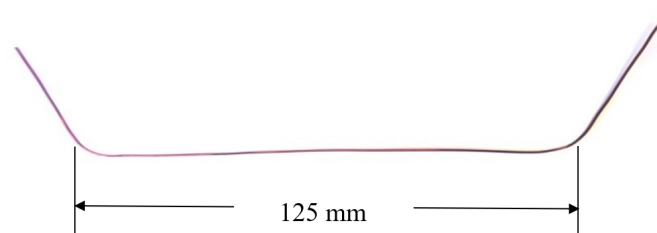


Figure III.6: Bent wire specimen for breakdown voltage tests.

For the experimental study of wires' insulation endurance, specimens in form of twisted pair are used to test the winding wires having round section. Twisted pairs are manufactured in compliance with [29] in a repeatable manner keeping the same tested area of 125 mm length and the same number of twists (7 twists) for all of specimens. The specimen's construction is shown in Figures III.7a, III.7b and III.7c.

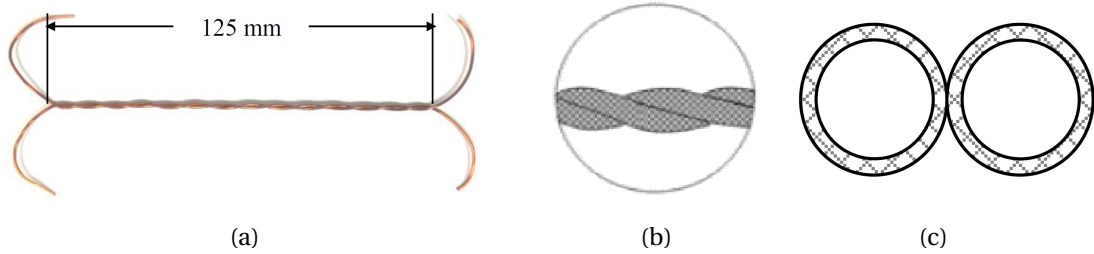


Figure III.7: Twisted pair specimen: (a) general view, (b) schematic view and (c) cross-section at the contact point.

To test the rectangular enamelled wire, the specimens in form of coupled bars held together with insulating material are made for the first attempt. The general and schematic views are represented in Figures III.8a and III.8b. Specimens are tested in two configurations: wide sides contact and narrow sides contact as depicted in Figures III.8c and III.8d respectively. The coupled bar specimens had a limitation consisting in non-uniformity of contact area where partial discharges occur. It leads to different enamel degradation along specimens' length and considerable deviation in time to breakdown. In this regard, this specimen type wasn't chosen for further tests.

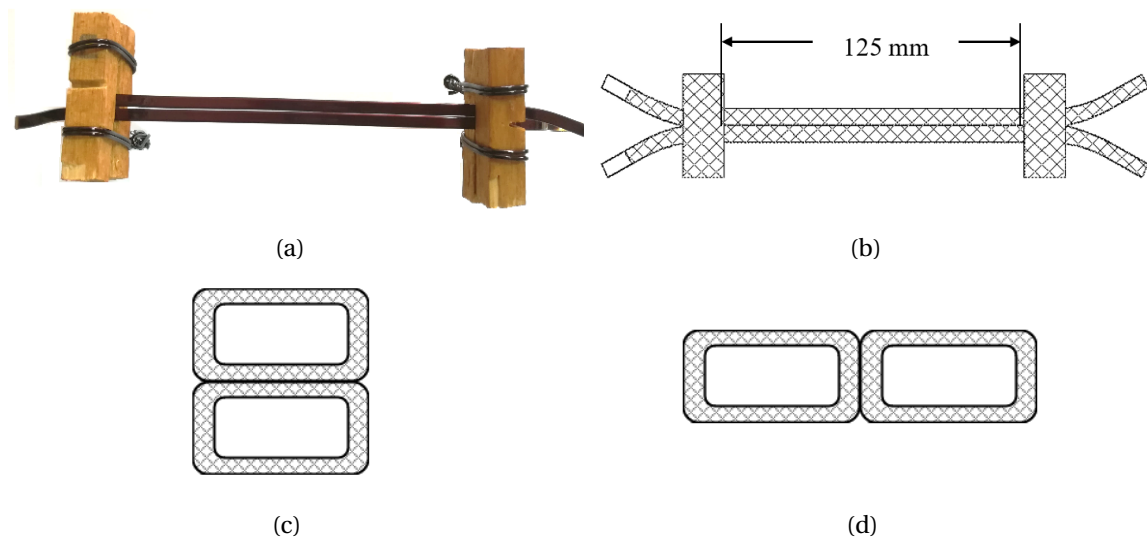


Figure III.8: Coupled bar specimen: (a) general view, (b) schematic view, (c) and (d) cross-sections at the contact area.

The other specimens for testing insulation of rectangular winding wires are designed; the specimens' photographs and their cross-sections at the contact areas are depicted in Figure III.9. The first specimen's configuration called single coil is shown in

Figures III.9a and III.9b. It represents a small coil made of two rectangular wire's pieces wound in parallel in a repeatable manner. The equivalent tested area of 125 mm length corresponding to the wound part and the number of turns in coils (4 turns for the studied rectangular wire) are kept the same for all of specimens. A metal tube having 130 mm diameter is used to wound the coils. The tested wire's dimensions provide a sufficient rigidity, while the wires with smaller sections should be placed on dielectric tube for keeping coil's shape during testing.

The second configuration depicted in Figures III.9c and III.9d is called double coil. As differentiated from the single coil, two pieces of wire are superimposed while winding. It creates a contact on wires' wide sides. In the both described configurations the wires' ends should be kept separated or insulated in order to avoid a flashover during the test.

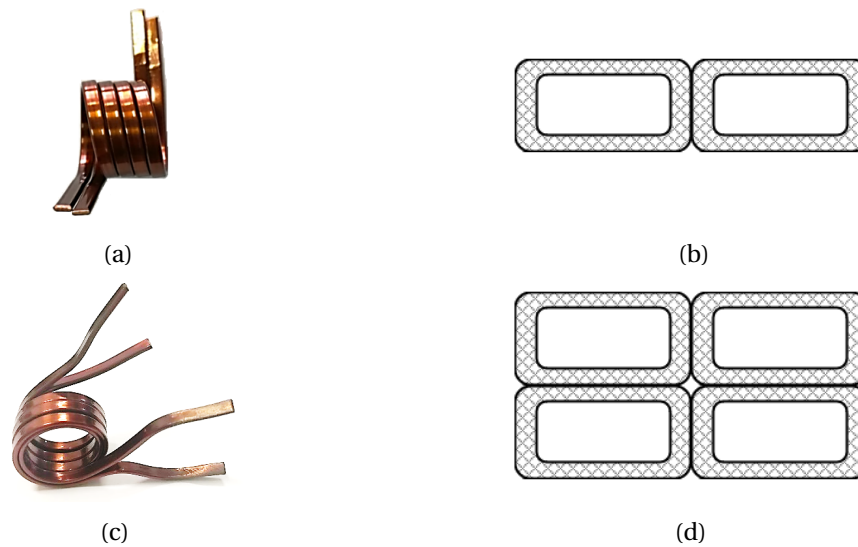


Figure III.9: Coil specimen: (a) single layer coil general view and (b) single layer coil cross-section at the contact area, (c) double layer coil general view and (d) double layer coil cross-section at the contact area.

The proposed coil's shape specimen has no analogues and it allows to model the turn insulation in concentrated winding configuration made of rectangular section wire.

3.3 Breakdown voltage tests

The breakdown voltage value (given in kV or V/ μm) is usually provided in enamelled winding wires' specifications in order to characterize the insulation electrical properties. With the objective to complete the specifications data by experimental results, AC sinusoidal voltage is applied to studied wires. This experiment allows to compare wires breakdown voltages under sinusoidal waveform before conducting endurance tests at impulse voltage.

To obtain experimental breakdown voltage values, bent wires specimens (see Figure III.6) are exposed to AC sinusoidal voltage of 50 Hz nominal frequency at normal am-

bient temperature (approximately 25 °C) and atmospheric pressure. The test voltage is applied at zero and increased at a uniform rate until reaching insulation breakdown voltage level. The experimental bench contains a step up transformer, a variable autotransformer providing sinusoidal voltage level adjustment, a fault detection circuit, and a voltmeter (RMS breakdown voltage is measured).

According to [29] test voltage can be applied between the wire's conductor and the metal shot. Therefore, the tested specimen is placed in a bath made of dielectric material (Plexiglas©) filled by a stainless steel shot as shown in Figure III.10. The tests carried out in the metal shot are hereinafter referred to as "wire – shot" tests.

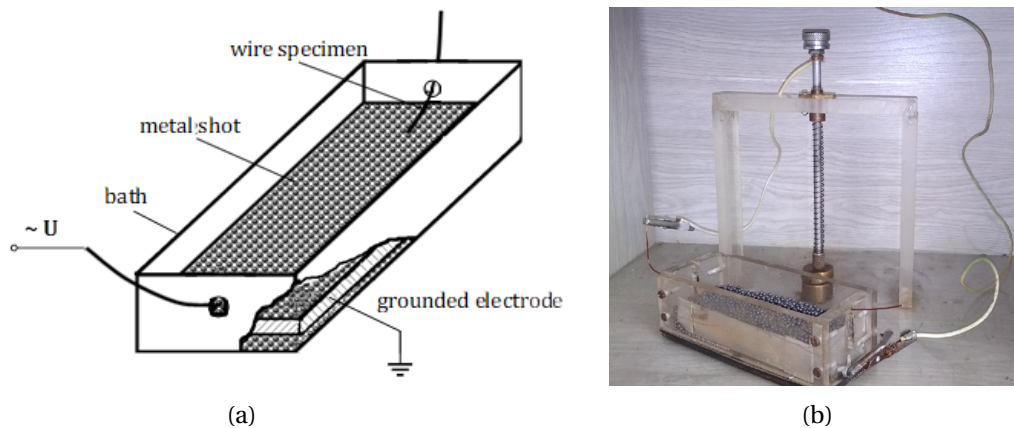


Figure III.10: Sketch (a) and photograph (b) of the specimen placed in "wire – shot" test.
Developed and installed in TPU, Russia

To place a wire specimen two cuts are made on the bath's opposite sides at a distance of at least 10 mm from the shot level to prevent it's spilling out. The cuts' width should be in 1.5-2.5 larger of the tested wire's diameter. The specimen in the bath is covered by the shot. The shot's diameter is no more than double the wire's diameter. It ensures a close contact between the shot and specimen's surface. Grounded metal electrodes can be placed parallel to the bath's bottom or on its long sides. The sinusoidal voltage is applied to the wire specimen at the one end while the other end is not connected (in the air). The bath's dimensions are sufficient to fully submerge the tested specimen into the shot. It is important to note, that the specimen ends should be sufficiently long in order to avoid a flashover. In this regard, the rectangular wire specimen's length is increased up to 300 mm and the wire's end in the air is additionally insulated by a fluoroplastic band.

3.4 Endurance tests

The proposed methodology is based on insulation endurance tests, in which the test object is exposed to one or more ageing factors related to service conditions. It gives an opportunity to study processes of dielectric materials degradation and failure mechanism, to find out the impact of applied stresses and to conduct the withstand capabil-

ity comparative analysis of tested winding wires. This experimental study focuses on enamel insulation ageing investigation incorporating both voltage and temperature effects as they are significant ageing factors in inverter fed motors according to [11], [50], [51] and [52]. The tests are conducted on above described wires' specimens for the purpose to assess the enamel insulation endurance to partial discharges.

To provoke the electrical ageing of enamel insulation, sinusoidal or impulse voltages are applied to wires' specimens using different electrical benches. The voltage amplitude is set higher than the PDIV level determined by preliminary tests when partial discharges activity has been detected. The partial discharges detection methods and utilized equipment are detailed in Section 3.5. The electrical ageing of insulation is done at ambient temperature equal to 25 °C. Furthermore, combined stresses (electrical and thermal), are applied simultaneously with the purpose to enlarge the study considering the interaction of temperature and impulse voltage effects. In this case, the temperature in the thermal chamber is set at 180 °C. It corresponds to wires' insulation thermal class H. In the context of the electrical machine operation, it indicates the peak temperature into a stator winding which winding wire can tolerate.

The endurance tests have been performed under PDs activity until enamel insulation breakdown occurred. Thus, the times to breakdown are measured for a number of test specimens conforming to IEC standards [53] and [54]. The tests parameters sequences (ageing factors levels) are randomized to avoid false trends due to possible interactions with uncontrollable environmental factors.

The tests are carried out with the following goals:

- to evaluate the influence of voltage waveform parameters on insulation ageing and life time by comparing the obtained mean times to breakdown;
- to estimate and compare the ability of different winding wires to withstand partial discharges activity depending on applied stresses;
- to study the effect of high temperature accelerating insulation ageing and breakdown when combined with electrical stresses.

The experimental results and their analysis will be discussed in Chapter IV.

3.4.1 Endurance test under sinusoidal voltage

The experimental bench similar to described in Section 3.3 can be used to conduct the wires insulation endurance tests. The “wire – shot” tests are performed in accordance with the method proposed in [55] and [56], where the resistance of enamelled wires to corona (surface) discharges is estimated. Sinusoidal voltage is applied as shown in Figure III.11a. Electrical discharges are observed on the insulation surface contacting with the metal shot when voltage level exceeds the ionization voltage in this system of electrodes. The methods used to detect electrical discharges are described in Section 3.5. The

chosen test sinusoidal voltage levels are higher than discharge inception voltage but lower than immediate insulation breakdown threshold. Thus, the enamel insulation is gradually aged and degraded by electrical discharges up to the final breakdown. The mean time to breakdown, obtained by calculating the arithmetical mean of at least five tested winding wire specimens, is used as the endurance criterion for further comparative analysis.

Furthermore, endurance test under sinusoidal voltage are carried out on twisted pairs and coils specimens (see Section 3.2). In this case, one wire of the tested twisted pair or coil is connected to the ground and to the other wire the sinusoidal voltage is applied as shown in Figures III.11b, III.11c and III.11d. The wires' ends are in the air. To study the electro-thermal stresses effect, the test bench is equipped by a thermal chamber: oven with air-forced circulation, maximum temperature 200 °C, deviation ± 5 °C. Partial discharges endurance tests are performed at two temperature levels: 25 and 180 °C.

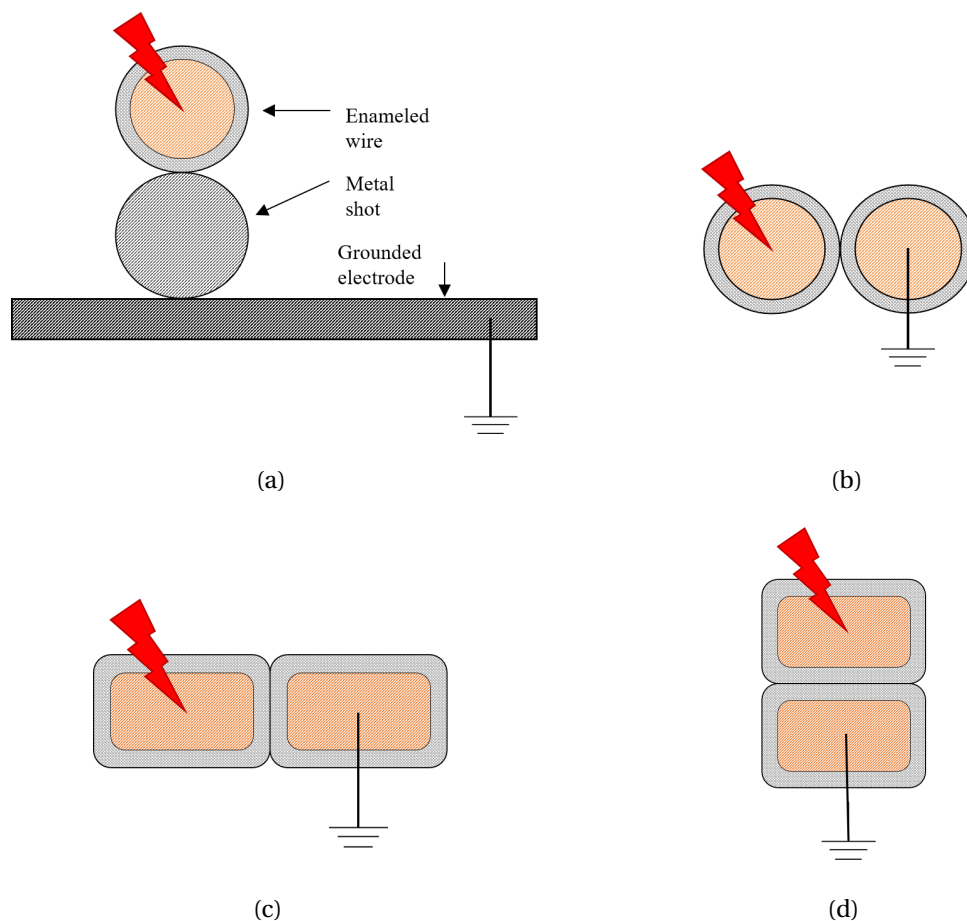


Figure III.11: Voltage on specimens while insulation endurance testing: (a) in “wire – shot” test, (b) twisted pair test, (c) single coil test and (d) double coil test.

The experimental setup sketch is given in Figure III.12a. This sketch depicts schematically the main components of the setup, the tested specimen's placement and the electrical connections in the thermal chamber. The Figures III.12b and III.12c give a general view of experimental setup and demonstrates the specimens while testing. The testing voltage is controlled using electrostatic kilovoltmeter and measured by means of the oscilloscope Tektronix TDS 2014C 200 MHz and the high voltage probe Tektronix P6015A 1000X 75 MHz 20 kV.

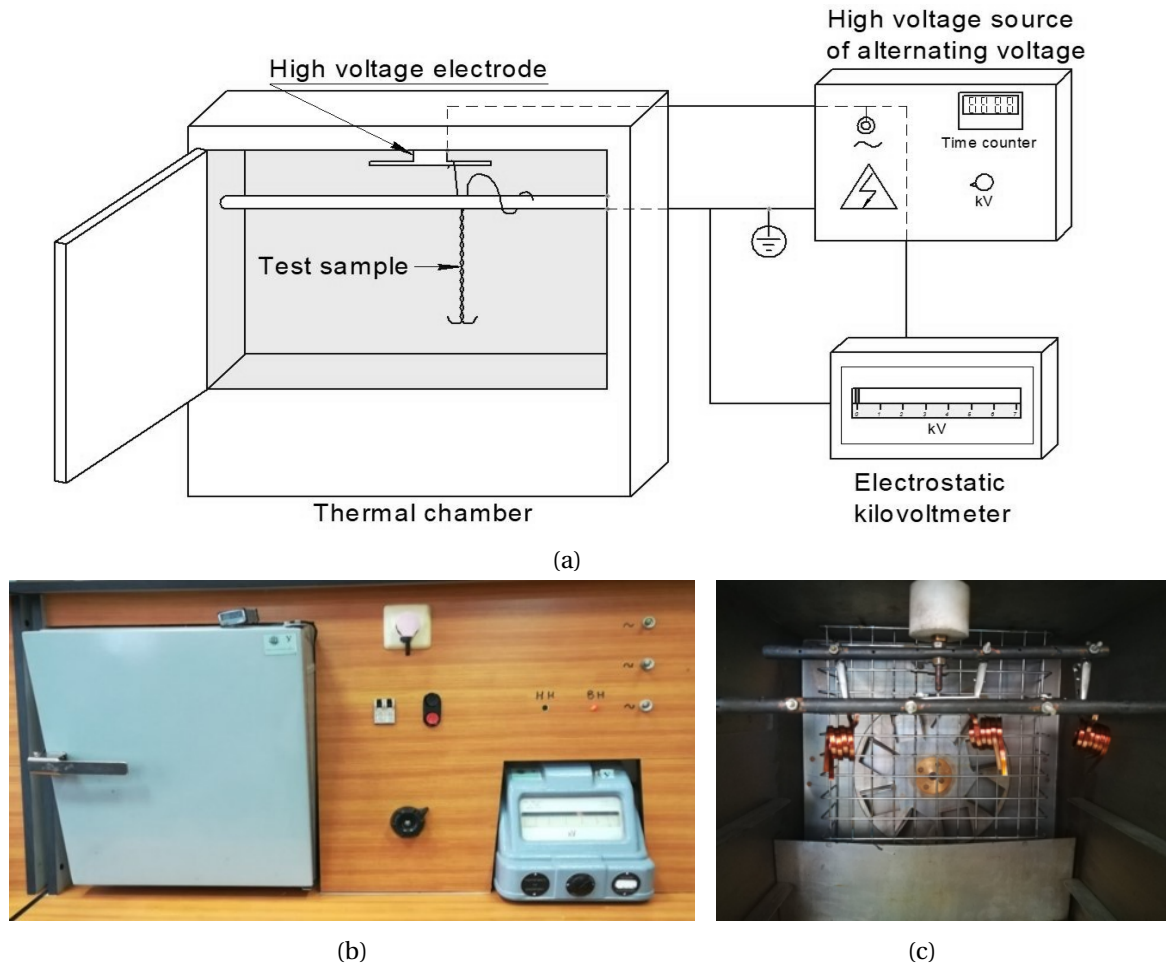


Figure III.12: Experimental setup for sinusoidal voltage tests: (a) sketch, (b) general view and (c) tested specimens in the thermal chamber.
Developed and installed at TPU, Russia

The simplified electric scheme of experimental bench and voltage waveform measured by means of the high voltage probe on the tested specimen are shown in Figures III.13a and III.13b respectively. The twisted pairs or the rectangular wire's coils can be installed for insulation endurance testing.

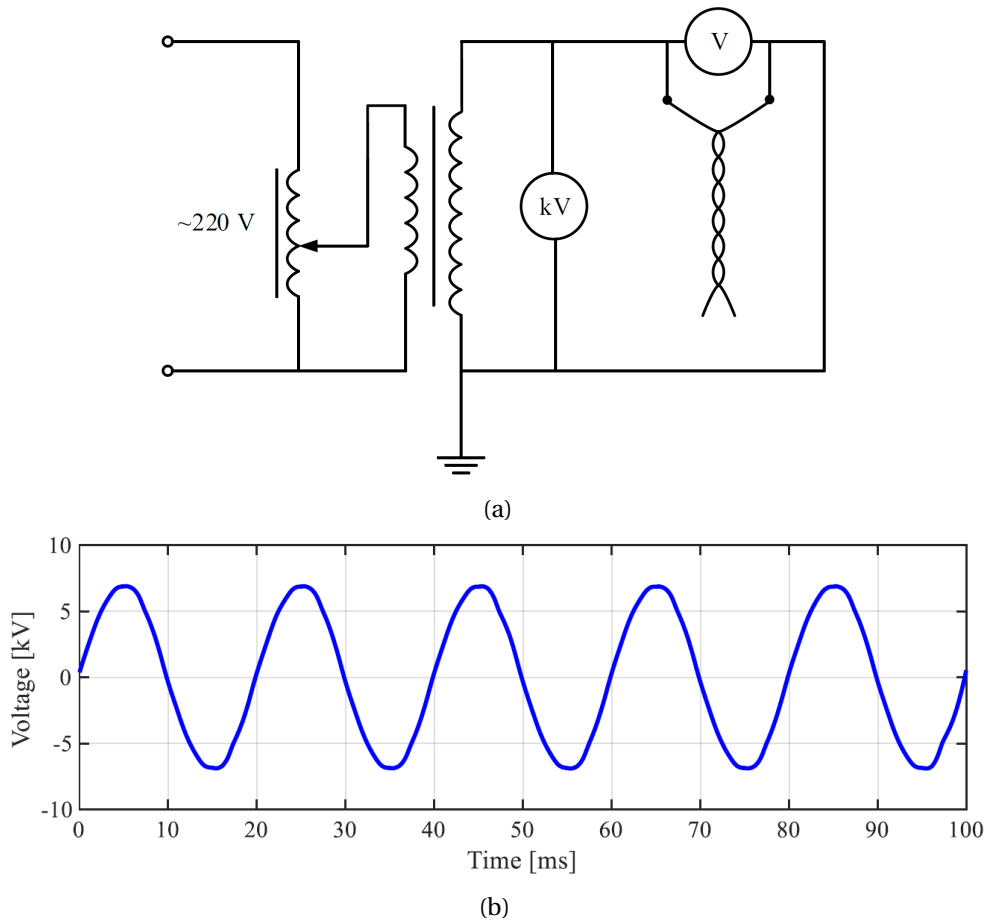


Figure III.13: Simplified electric scheme and voltage waveform measured on the tested specimen, $V_{rms} = 5 \text{ kV}$, $f = 50 \text{ Hz}$

3.4.2 Endurance test under low dV/dt PWM impulse voltage: μs - level rise time

The turn insulation endurance tests performed under sinusoidal voltage exceeded PDIV allow to evaluate insulation withstand capability while damaged by partial discharges. However, the partial discharges' features and insulation destruction process depend on voltage waveform parameters and inverter realization. Thus, to qualify and evaluate insulation system of inverter-fed motors impulse voltage testing is recommended in [47].

The presented in this section electrical bench has been designed in the interest of reproducing a voltage waveform generating by conventional inverter based on Silicon semiconductor technology. The main component of this setup is a pulse generator having a single-phase half-bridge inverter topology. This inverter is built using 600 V Si IGBT (IRGP6630DPBF) transistors which are controlled by ACPL-333J gate drivers. The

schematic structure of the pulse generator is detailed in Figure III.14. The inverter provides low voltage bipolar impulses which are increased using a step-up transformer MII2000HM (primary windings $w_1 = w_2 = 105$ wire turns, secondary winding $w_3 = 2800$ wire turns). Thus, the obtained bipolar PWM-like voltage waveform having μs -level rise time is applied on enamelled wires' specimens. A time counter is used for recording a time to samples' insulation breakdown. This test bench is designed and installed in TPU laboratory (Tomsk, Russia); to have more details on test bench conception, please refer to [57].

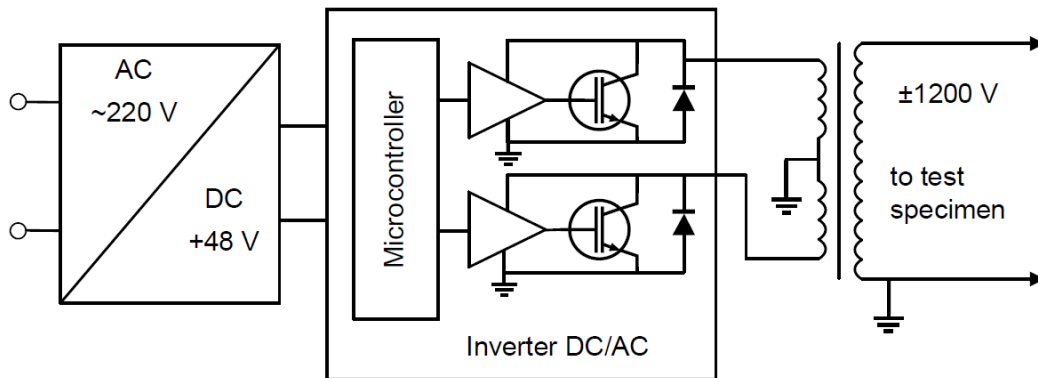


Figure III.14: Scheme of the low dV/dt pulse generator: Si IGBT inverter.

The Figure III.15 details the experimental setup configuration and specimen installation: one wire of the twisted pair is connected to the ground and the impulse voltage is applied to the other wire like in the preceding endurance tests (see Figures III.11b, III.11c and III.11d). The wires' ends are not connected. Measuring instruments are also shown in this sketch. The experimental bench photographs are given in Figure III.16.

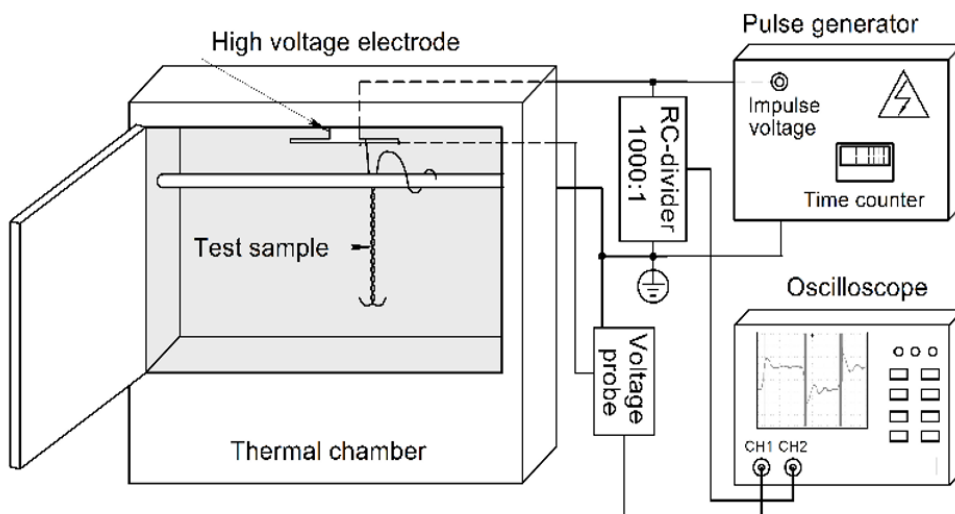


Figure III.15: Sketch of the low dV/dt experimental bench.



(a)



(b)



(c)

Figure III.16: Low dV/dt experimental bench photographs: (a) general view, (b) testing twisted pairs' installation and visible effect of PDs (purple light on the twists), (c) pulse generator view.
Developed and installed at TPU, Russia

In the present study the generated bipolar impulse voltage waveform is determined basing on NEMA MG1 Part 30.1 standard definitions and study [39] by the following parameters (see Figure III.17):

- V_a – steady state impulse voltage amplitude (ultimate value), that corresponds to DC bus voltage V_{dc} when the machine is fed by inverter, $V_a = V_{dc}$;
- V_{os} – overshoot voltage, defined as the amplitude of the peak voltage in excess of the steady state impulse voltage;
- $V_{pk/pk}$ – peak to peak voltage;
- V_{pk} – peak voltage; for bipolar voltage impulses, it is half the peak to peak voltage;
- t_r – rise time of impulse voltage defined as time required to rise from 10% to 90% of the steady state voltage; from 10% to 90% of $2V_a$ for bipolar impulse.

The rate of voltage change dV/dt is defined here as the voltage rise from 10% and 90% $2V_a$ over the time t_r at the start of the impulse.

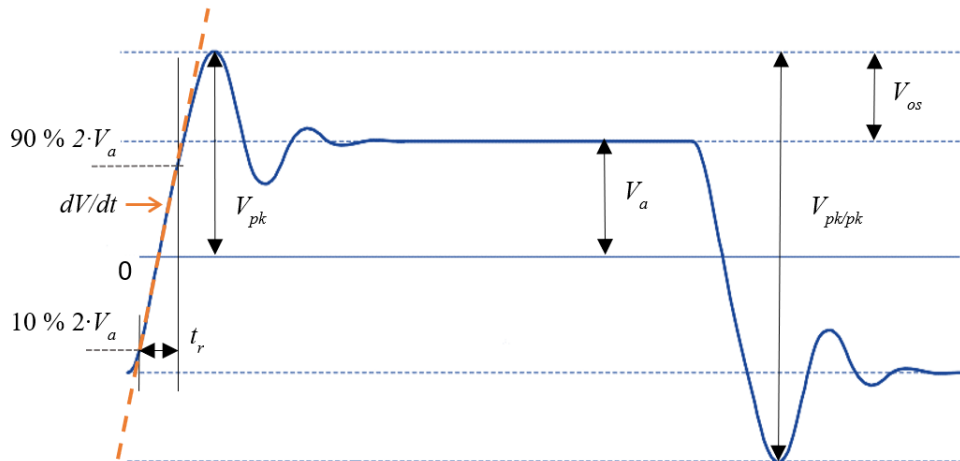


Figure III.17: Bipolar impulse voltage waveform parameters.

The voltage applied to specimen is measured using a RC-divider with a ratio of 1000:1 (see Figure III.18) placed between the pulse generator output and specimen' connection points, connected to the oscilloscope Tektronix TDS 2014C via coaxial cable 50 Ω . The voltage probe PPE5KV 100:1 400 MHz 5 kV is used to measure the voltage on specimen's connection points. Measured voltage is shown Figure III.19a.

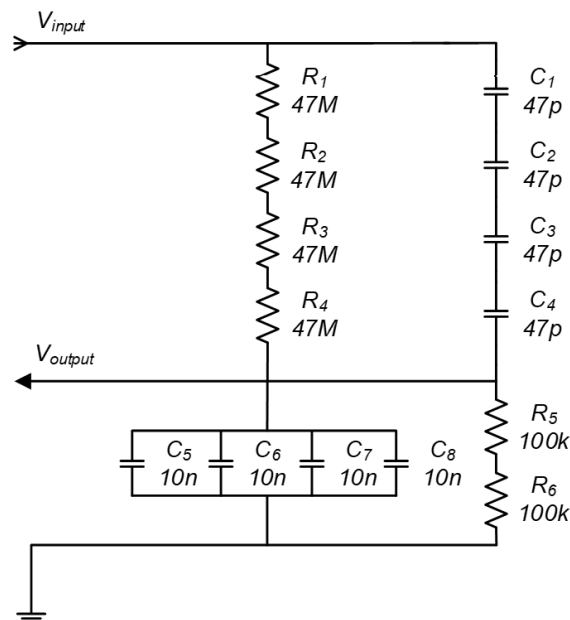


Figure III.18: Electrical scheme of the high-frequency RC-divider 1000:1.

The surges and “ringing” observed on voltage waveform in Figure III.19a are caused by use of step-up transformer and connections inductance. This effect was desired because this test bench was designed with the objective to simulate a voltage waveform in inverter-fed motor supplied by a long cable line. The enlarged plot in Figure III.20 details voltage waveform parameters, as steady state voltage V_a , rise time t_r and dV/dt .

The transient overvoltage can be decreased using a metal oxide varistor connected in parallel to the pulse generator output that also smooths the dV/dt (as presented in Figure III.19b). Thus, the influence of presence or absence of repetitive surges on enamel insulation can also be studied comparing experimental results obtained for two voltage waveforms. During endurance tests of studied winding wires, the impulse voltage with surges is mainly applied.

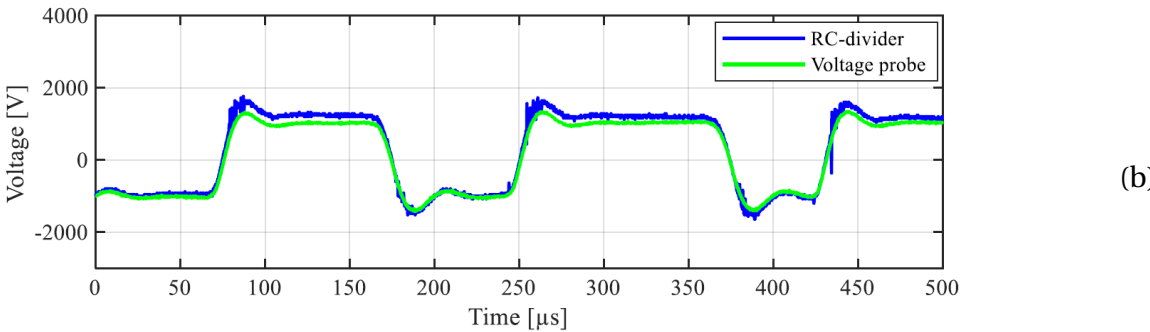
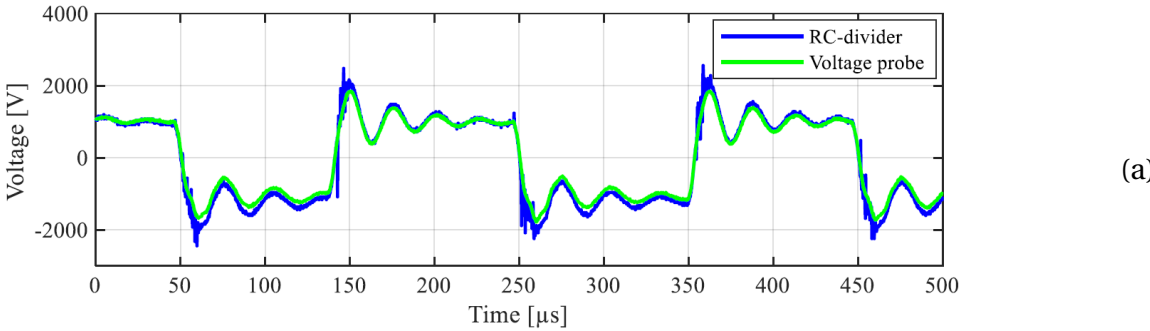


Figure III.19: Low dV/dt PWM impulse voltage scopes: (a) with surges and “ringing” effect, (b) surges and “ringing” effect are limited.

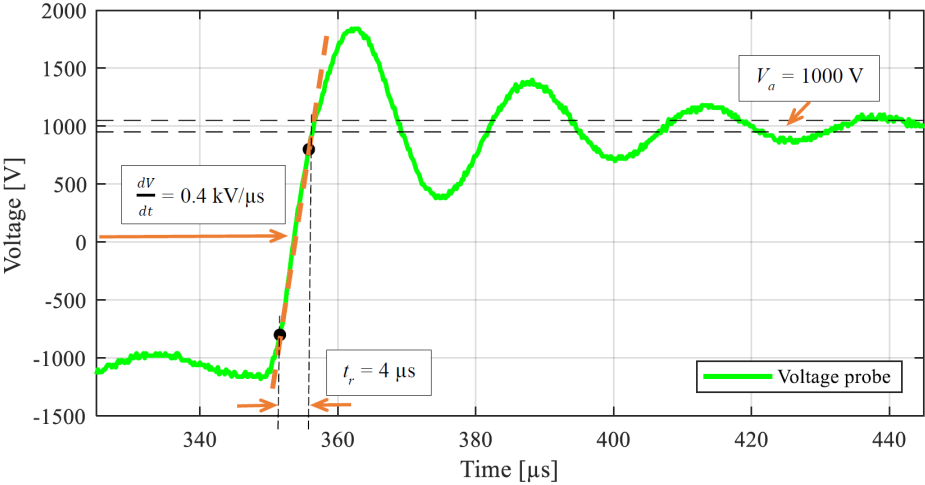


Figure III.20: Enlarged plot showing impulse voltage parameters.

The presence of high frequency components is observed on voltage waveforms measured by RC-divider. Comparing two signals measured without any load (Figure III.21a) and with the twisted pair (Figure III.21b), it can be noticed that the disturbance of the voltage signal measured by RC-divider is caused by both transistor commutations and partial discharges activity on the tested specimen.

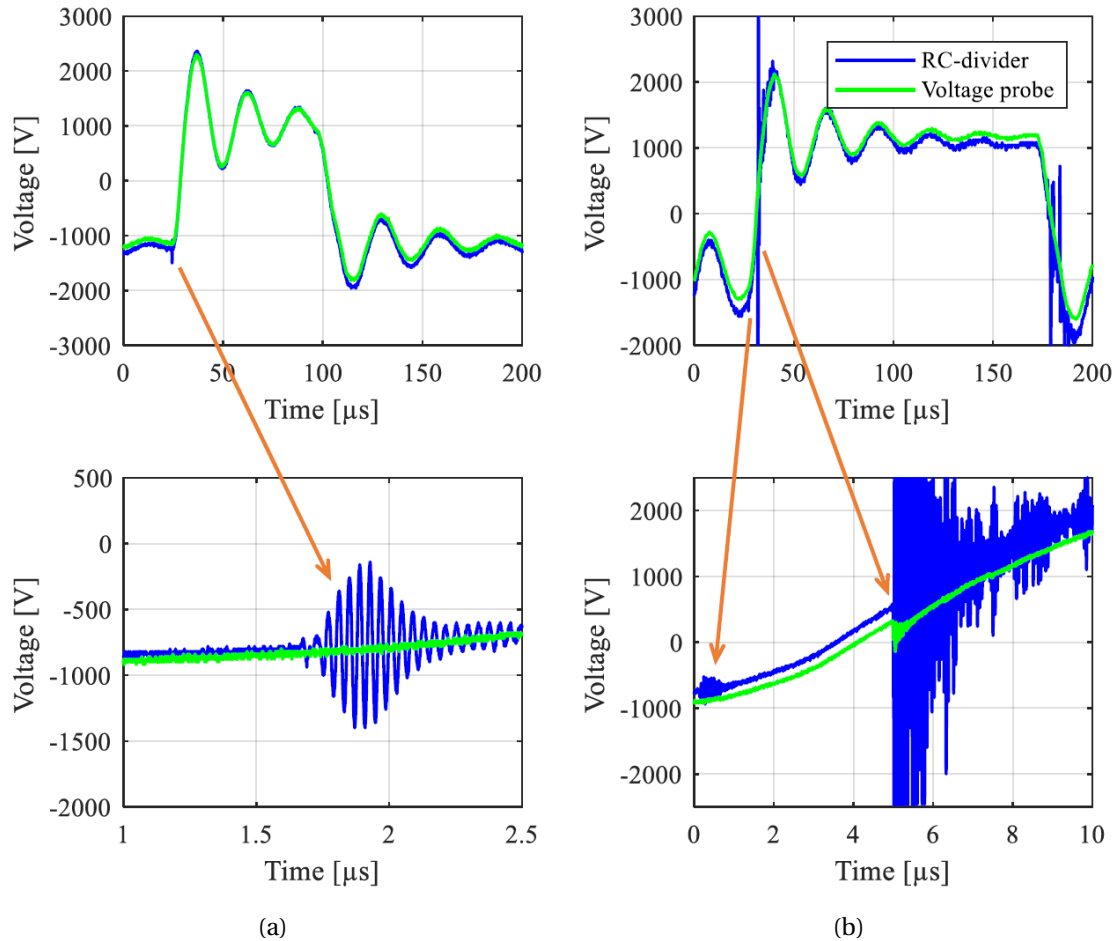


Figure III.21: Voltage measured at the pulse generator output without specimen (a), voltage measured on the tested specimen (b).

The present pulse generator produces PWM voltage having the modulation frequency $f_m = 400$ Hz and the carrier frequency $f_c = 5$ kHz. In this test bench impulse voltage waveform parameters are not adjustable.

3.4.3 Endurance test under high dV/dt impulse voltage: ns - level rise time

A Half-bridge inverter topology

The experimental bench described in the previous section allows the adequate reproducing of stresses typical for inverter-fed motors with electronic devices based on Silicon technology. With the objective to study the electrical stresses effect on motor winding insulation engendering by SiC high-speed switches, another test bench has been designed and tested at SATIE laboratory. The general view of the high dV/dt experimental bench and the designed SiC inverter view are given in Figure III.22.

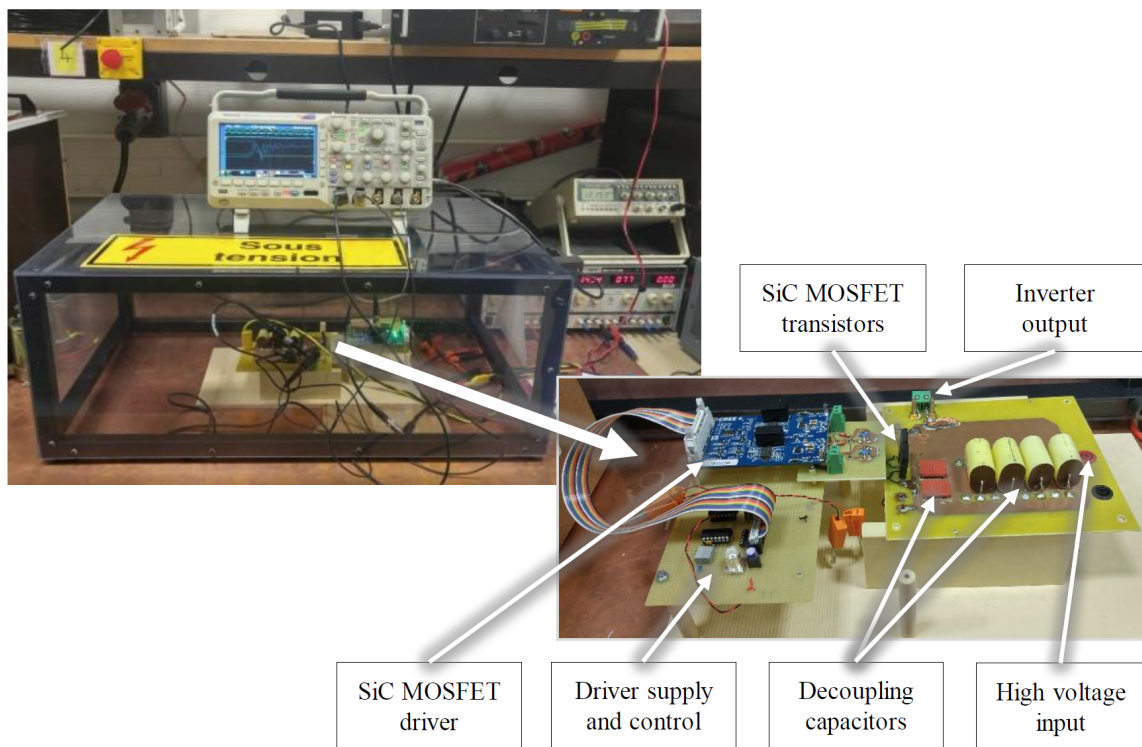


Figure III.22: General view of the high dV/dt experimental bench and SiC inverter.
 Developed and installed at SATIE, France

The pulse generator proposed to use in insulation endurance tests has a half-bridge inverter topology; its scheme is depicted in Figure III.23. This scheme presents a pulse generator based on SiC MOSFET switches: $V_{DS} = 1200\text{ V}$, $R_{DS(on)} = 280\text{ m}\Omega$ at $25\text{ }^\circ\text{C}$, ref. Cree®C2M0280120D [58]. They are controlled by the Dual Channel SiC MOSFET driver for industrial applications, ref. Cree®CGD15HB62P1 [59]. A low output capacitance transistor (and thus the high on-state resistance) has been selected to maximize dV/dt at the output of the inverter. The power electronic components used in this test bench allow to generate voltage pulses having ns-level rise time with the maximum amplitude up to 1200 V and the switching frequency up to 64 kHz (limitation of the driver). The voltage changing rate dV_{DS}/dt can be adjusted modifying the gate resistances R_{G1} , R_{G2} . The driver

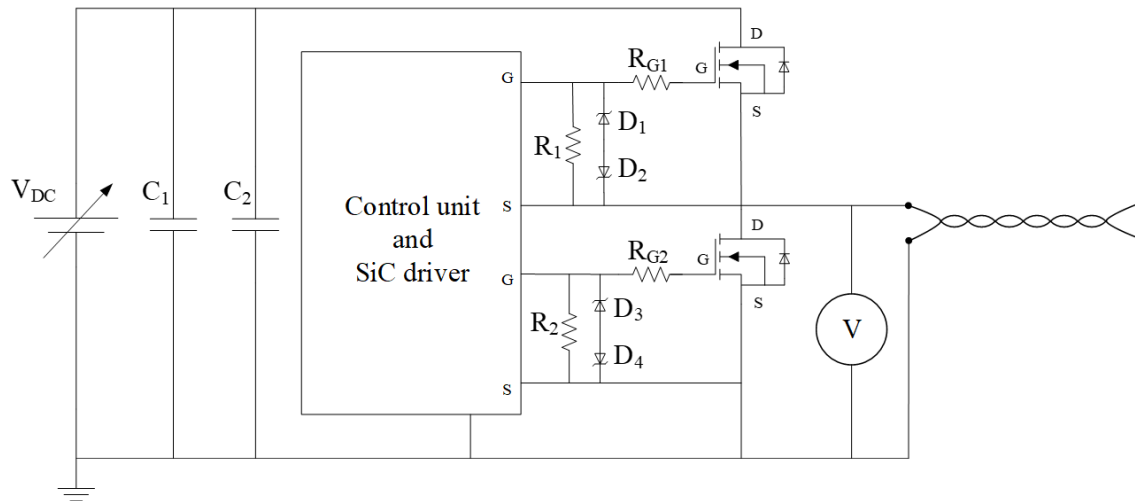


Figure III.23: Scheme of pulse generator for high dV/dt tests: SiC half-bridge inverter.

supply and control plate provides a dead time adjusting, voltage source and function generator connections. Resistors R_1 , R_2 and diodes D_1 , D_2 are placed to protect the transistors from Gate-Source overvoltage.

This experimental setup was designed in such a way as to minimize parasitic inductances and to generate very high dV/dt . As in the test bench described in the preceding paragraph, one wire of the tested twisted pair is connected to the ground and to the other wire the voltage waves generated by the half-bridge inverter are applied (inverter output). The wires' ends are in the air. To measure the voltage on the tested specimen, the oscilloscope Tektronix DPO4034 and the high voltage differential probe Tektronix THDP0100 having a bandwidth of 100 MHz (shown as voltmeter in Figure III.23) are used. The measured voltage waveforms at the twisted pair terminals during turn-on and turn-off switching at 100 V, 200 V and 300 V and corresponding dV/dt are shown in Figure III.24.

This setup already allowed us to apply very steep voltage rates, which can affect the partial discharges' properties and served as a first prototype of high dV/dt test bench. Whereas the previous studies [33] and [60] show that bipolar pulses can have a greater effect on insulation lifetime than unipolar pulses, so another pulse generator assembly was designed and used for winding wires insulation endurance tests. This experimental bench is described in the following section.

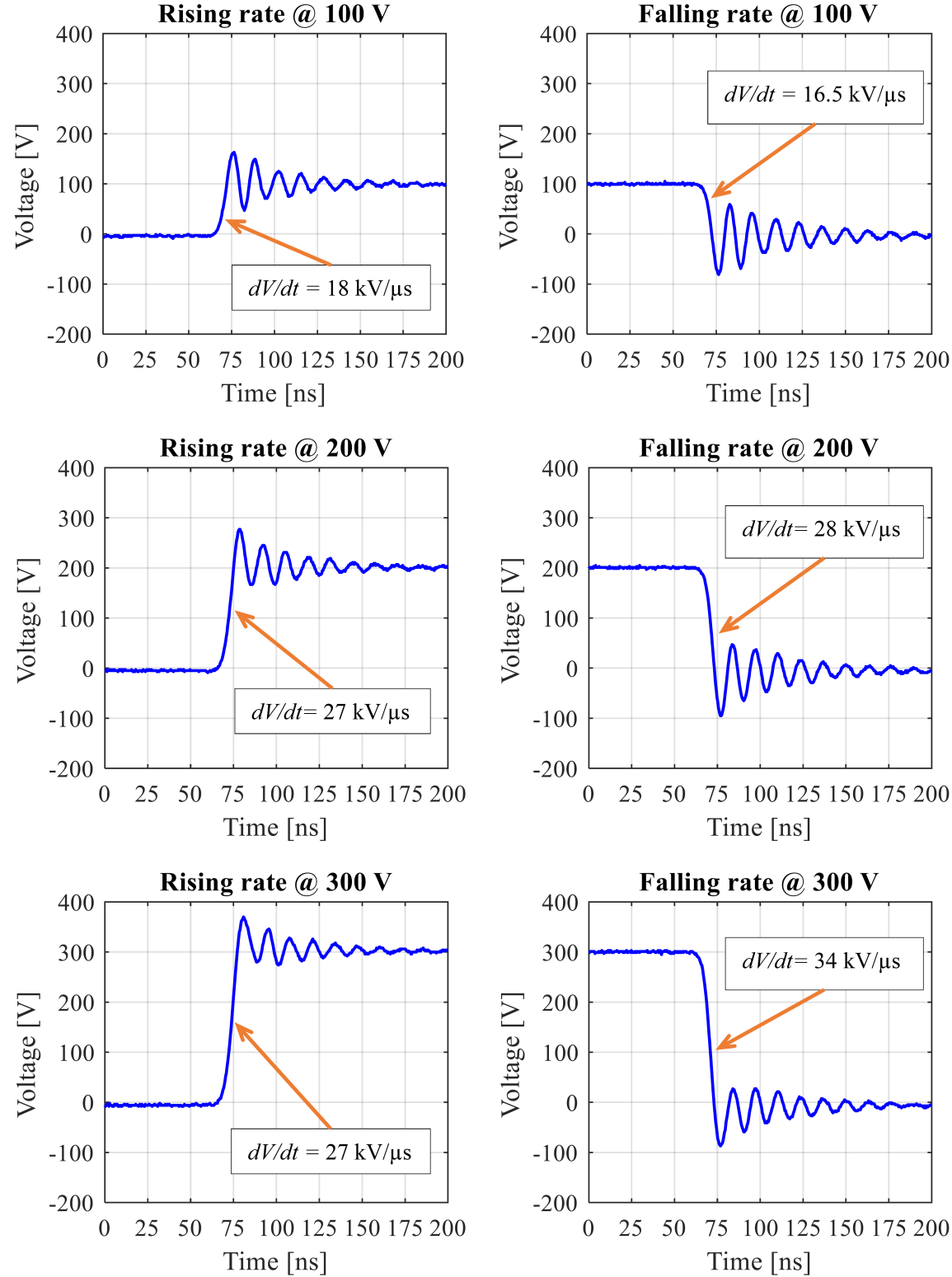


Figure III.24: High dV/dt impulse voltage scopes: half-bridge inverter topology.

B H-bridge inverter topology

The designed electrical test bench acts like a pulse generator assembled with a measurement unit and a thermal chamber where tested specimens are installed. The main components of this setup are shown in Figure III.25 and detailed in Table III.3.

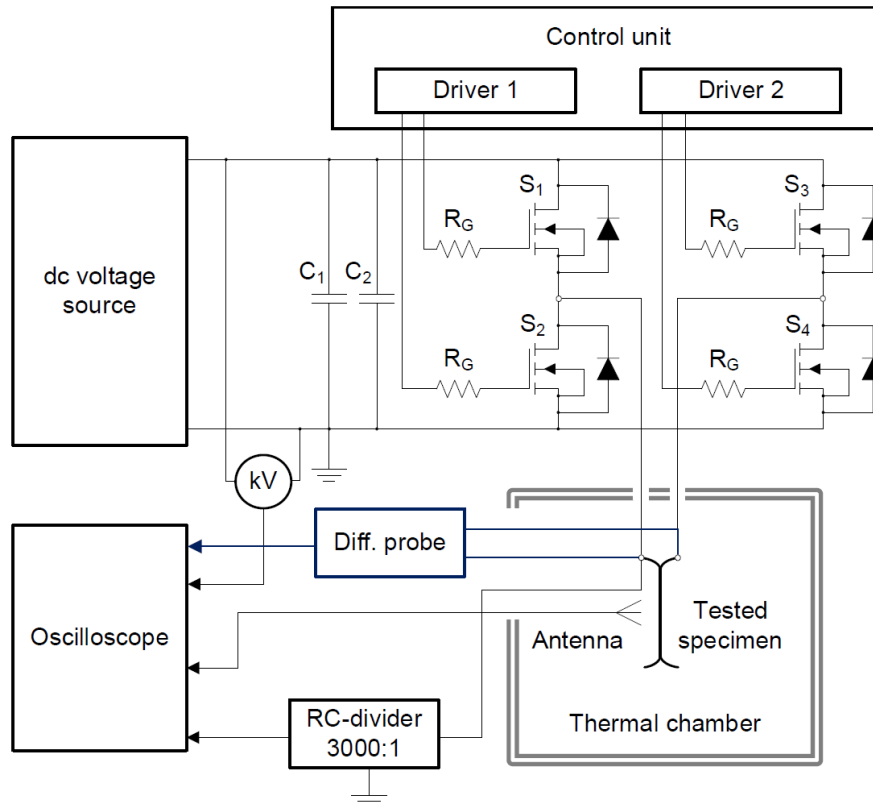


Figure III.25: Scheme of experimental setup for high dV/dt tests: SiC full bridge inverter.

The inverter plate made from double-sided Printed Circuit Board (PCB) have been designed and fabricated at SATIE laboratory. The experimental bench is installed in TPU laboratory where the winding wires insulation endurance tests are carried out. The photographs of the experimental setup general view, the SiC H-bridge inverter and the specimen installation are demonstrated in Figure III.26.

The inverter realization allows to utilize it as a full bridge inverter applying bipolar impulse voltage on the tested specimen, and also as a half-bridge inverter generating unipolar impulse voltage. Performed with modern SiC MOSFET 1700 V transistors, the test bench can generate adjustable impulse voltage waveforms with steep rising and falling rates. Selected transistors allow to reach high voltage levels with high dV/dt due to low output capacitance with a maximum switching frequency up to 125 kHz (limitation of gate drivers). The inverter electrical circuit design is similar to the first prototype (half-bridge inverter) specified in Section 3.4.3 A.

Table III.3: Main components of high dV/dt experimental bench with pulse generator having H-bridge topology.

Component	Characteristics
SiC inverter	
Switches, $S_1 - S_4$	MOSFET SiC Wolfspeed transistors with built-in SiC body diode, ref. C2M1000170D, $V_{DS} = 1700$ V, $R_{DS(on)} = 1 \Omega$ at 25°C
Decoupling capacitance, C_1 and C_2	TDK DC Link Film Capacitors, ref. B32776G, $8 \mu\text{F}$, and Multilayer Ceramic Capacitors MLCC – SMD, 100 nF
Gate resistance, R_G	3.5Ω
Drivers	Dual 1700 V SiC MOSFET Driver, ref. PT62SCMD17
Measuring tools	
Oscilloscope	Keysight Technologies DSOX2014A 100 MHz, Tektronix MDO3024 200 MHz
Kilovoltmeter	AC/DC, 0 - 120 kV, precision 0.25%
Divider	RC voltage divider, $3000:1$
Antenna	150Ω coaxial radio frequency cable PK 150-7-11
Differential probe	Tektronix THDP0100, 100 MHz, up to 6000 V differential
Test chamber	
Thermal chamber	Maximum temperature 200°C , deviation $\pm 5^\circ\text{C}$

The required voltage waveform is generated by means of a function generator connected to drivers' inputs. Comparing to the experimental bench described in Section 3.4.2, the advantage of this setup is in the possibility to vary voltage waveform parameters, such as the amplitude, the switching frequency, the duty cycle and dV/dt . It makes possible to examine their specific effects on the partial discharges and insulation degradation.

Tested specimen connection points are shown in Figure III.25 and Figure III.26: two wires of tested twisted pair or coil are connected via cables to midpoints of the inverter. This connection allows to apply the impulse voltage to the both of twisted wires alternately as differentiated from previous test benches where only one of tested wires is under voltage.

In the present setup tested specimens are installed in the thermal chamber that provides a temperature control and serves as a grounded metal screen protecting the inverter from electromagnetic interferences issued from partial discharges. To improve this protection, the inverter is put in the grounded aluminium cage (Faraday cage).

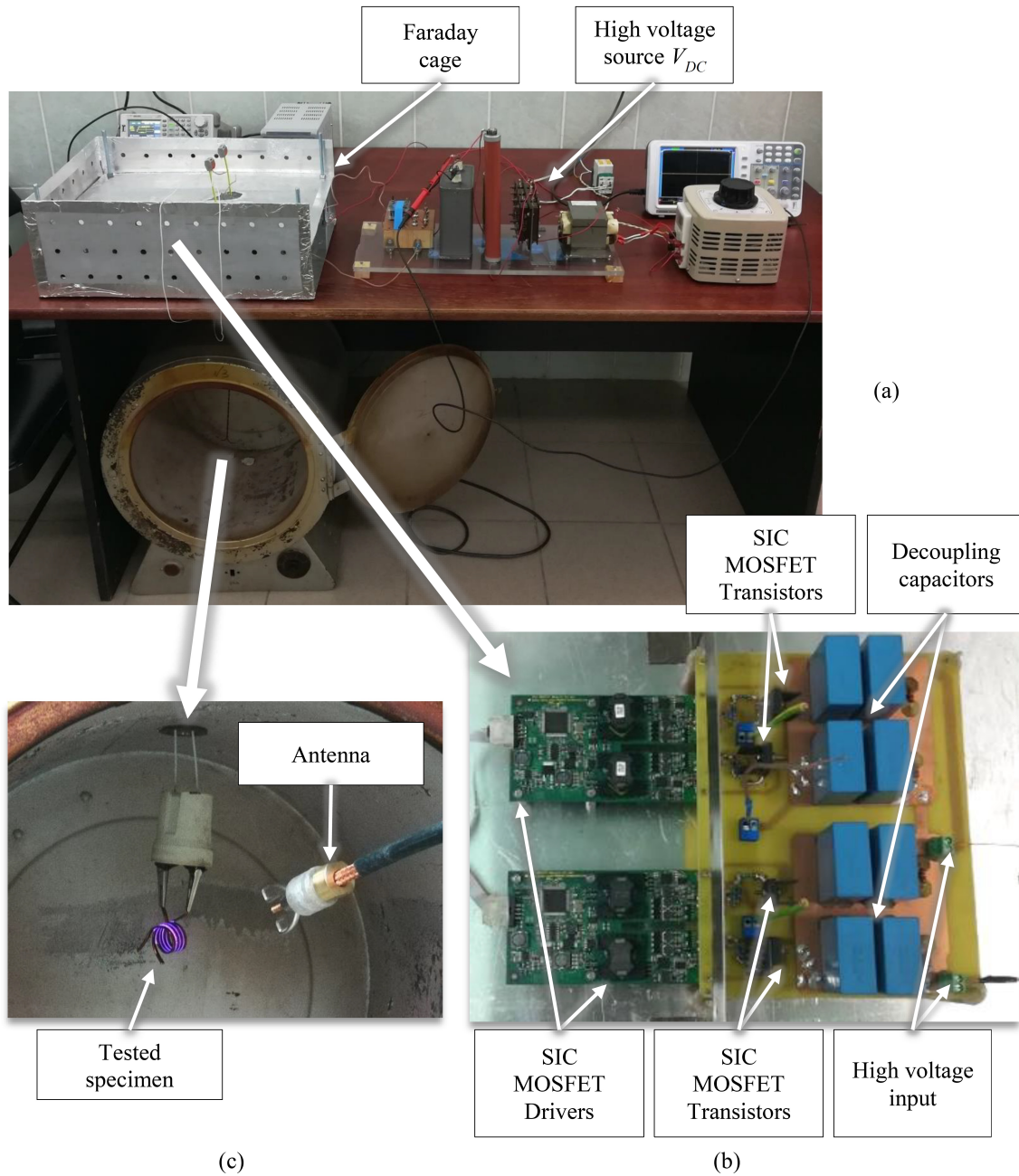


Figure III.26: General view of the high dv/dt experimental bench (a), SiC inverter (b) and tested specimen installation (c).

The SiC inverter is developed at SATIE, France, and experimental assembly is developed and installed at TPU, Russia.

The effect of cable length on the transient overvoltage when applying impulse voltage with short rise time as shown in Chapter II should be considered. In this regard, the electrical connections between the inverter's PCB and the tested specimen is made using a 1 m length cable. For this purpose, the cable insulated by polytetrafluoroethylene enabling operation at high temperatures was chosen.

Initially, measurements were carried out using a RC-divider connected at one of the specimen's connection point in the thermal chamber and the ground. There was no specimen connected in order to avoid the signal disturbances issued from partial discharges while the voltage is measured. Figure III.27 gives the measured waveform corresponding to pulse generator output voltage for a 1 kV DC bus voltage level. The obtained voltage waveform represents the RC-divider response to the signal generated by the pulse generator with high frequency oscillations during the first few hundred nanoseconds after switching. Characteristics of the used RC-divider are detailed in Appendix III-B.

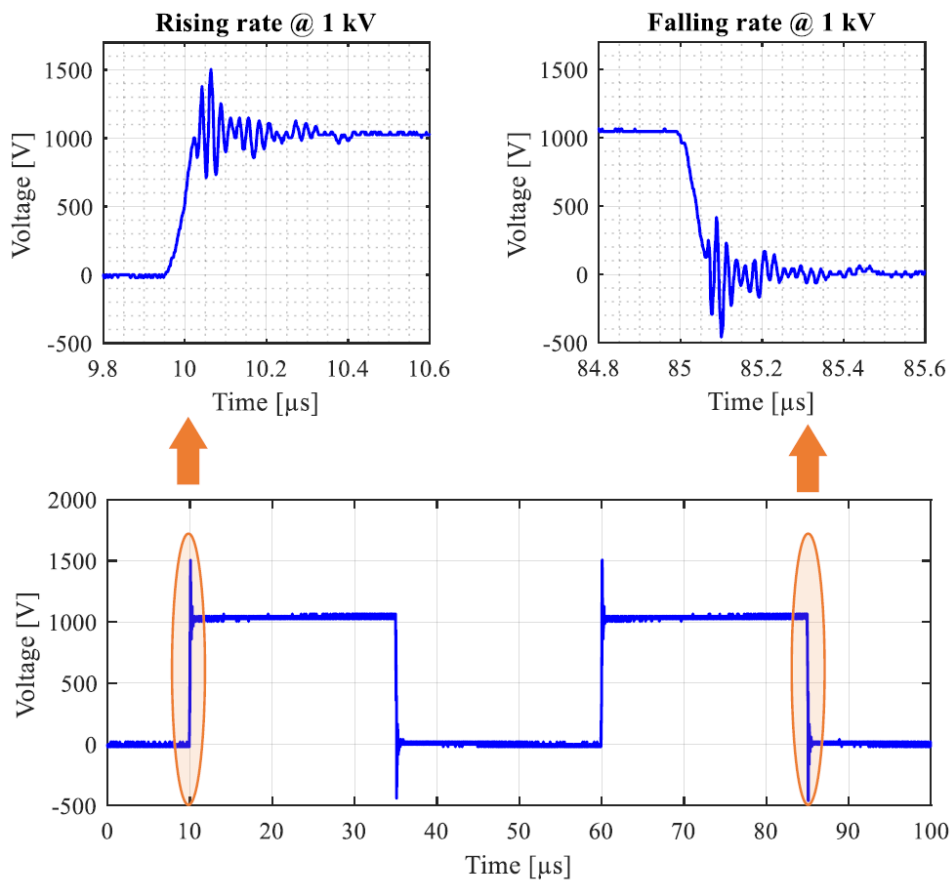


Figure III.27: High dv/dt impulse voltage scopes.

The voltage waveform applied to the specimen was also measured with the differential probe Tektronix THDP0100 as shown in Figure III.25. It provides the better demonstration of the high dv/dt bipolar voltage impulse produced by the SiC-based pulse generator. Figures III.28 shows the rising and falling rates of the impulse voltage measured at the specimen's connection points in the thermal chamber when there is no specimen connected (no PDs activity) and when the twisted pair is connected (with PDs), $V_{DC} = 1$ kV.

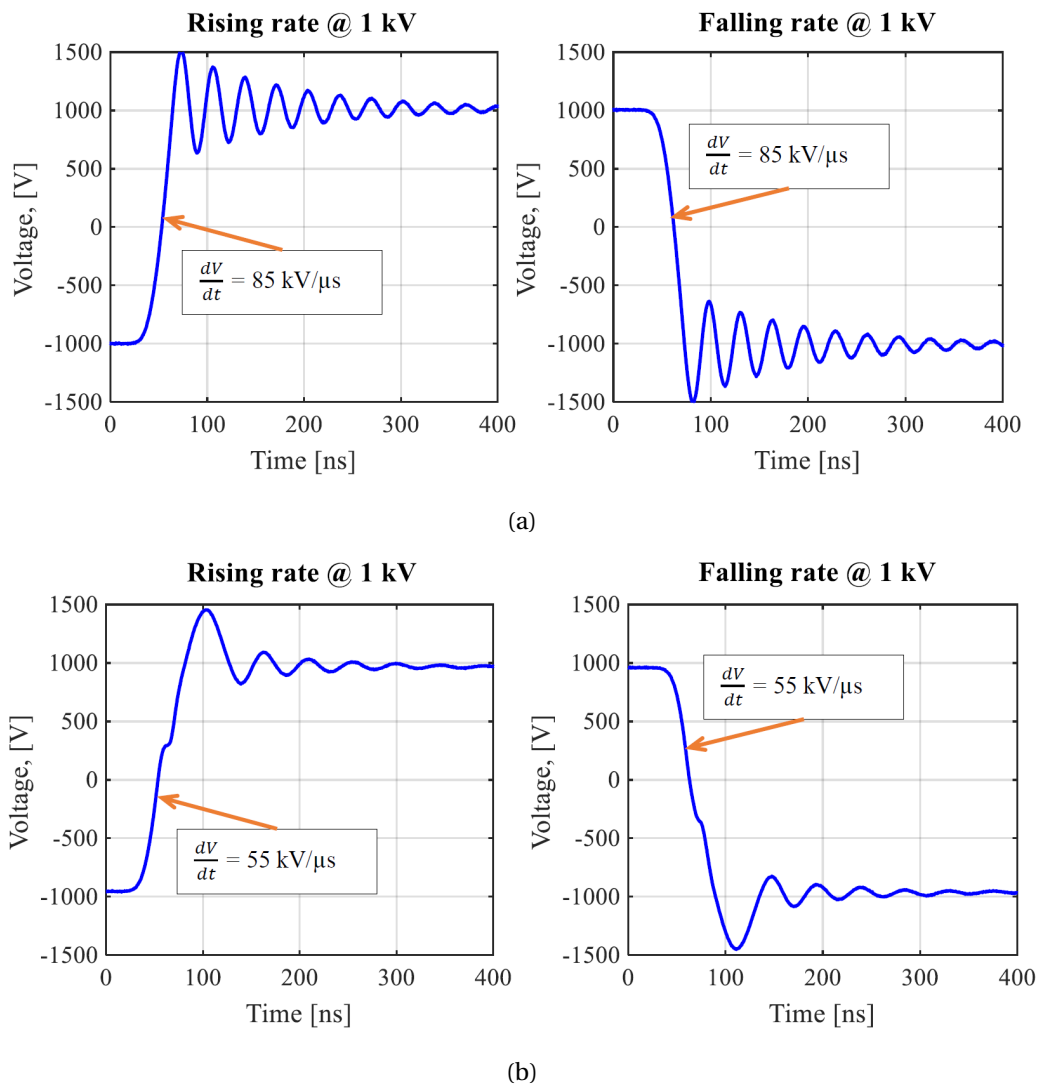


Figure III.28: Voltage measured at the pulse generator output without specimen (a), voltage measured on the tested specimen in the thermal chamber (b).

Waveforms obtained using the antenna shown in Figure III.25 and Figure III.26 will be discussed in the following section.

3.5 Partial discharges detection tests

The endurance tests of winding wires' enamel insulation were carried out on the described experimental benches. The main ageing factor was the sinusoidal or repetitive impulse voltage. Furthermore, the electrical stresses were combined with the thermal ones that accelerates the insulation ageing. The applied voltage activates the ionization processes in the insulation engendering partial discharges in air gaps between turns of enamelled wires. In this study, partial discharges signal measurements have been performed with the aim to demonstrate the presence of PDs activity during the endurance tests. The optical, electromagnetic and chemical PD detection methods are used.

3.5.1 Optical method

The optical method is based on detection of radiation emitted as a result of dielectric ionization, excitation and recombination occurring during the electrical discharges activity. The radiation associated with electrical discharges appears in the Ultraviolet (UV) spectrum, the visible light and the infrared region. Depending on dielectric materials, surface condition and discharge type, different optical detectors or sensors can be used: photomultipliers, optical fiber sensors, UV cameras [61], [62], [63] and [64].

In this work the optical detection of partial discharges is carried out using an electron–optical defectoscope Filin-7 [64] shown in Figure III.29. This device allows to record the electromagnetic radiation in the UV spectrum band if surface partial discharge and corona discharges appear. This monitoring procedure is often used for detecting defects and failures in high voltage electrical equipment (power transmission lines, insulators).



Figure III.29: Electron-optical defectoscope Filin-7.

In our experiments, it allows to detect the PD inception when discharges are weakly luminous. The brightness of UV emission increases proportionally to PDs intensity and can be visible without using a special equipment. The specimens' installation photographs, as well as photographs and optical images of observed partial discharges are given in Figures III.30, III.31, III.32 and III.33 for used experimental benches.

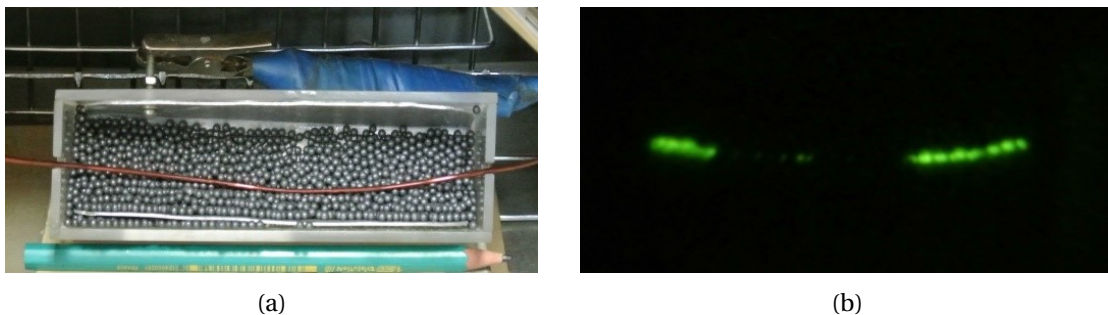


Figure III.30: “Wire-shot” test under sinusoidal voltage $V_{rms} = 5 \text{ kV}$, $f = 50 \text{ Hz}$: specimen's photograph (a) and PDs optical image (b).

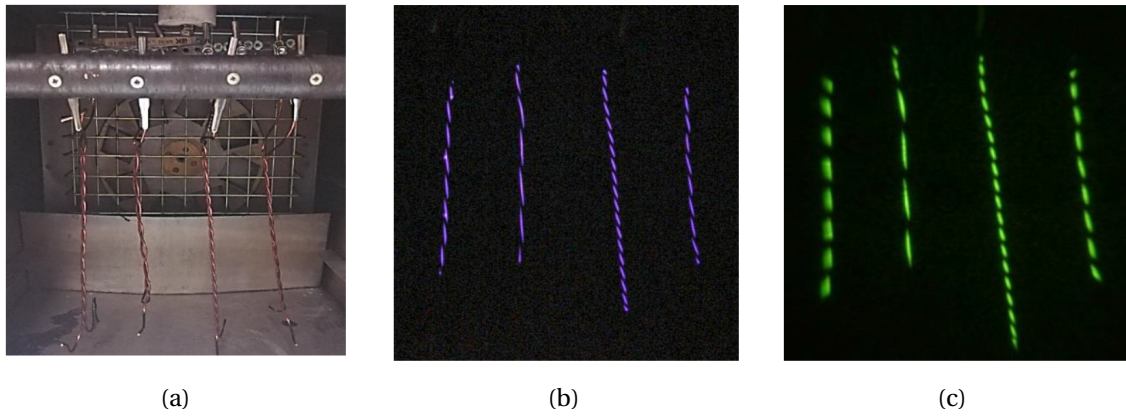


Figure III.31: Test under low dV/dt PWM impulse voltage $V_a = 1.2$ kV, $f_c = 5$ kHz: twisted pairs' installation (a), PDs photograph (b) and PDs optical image (c).

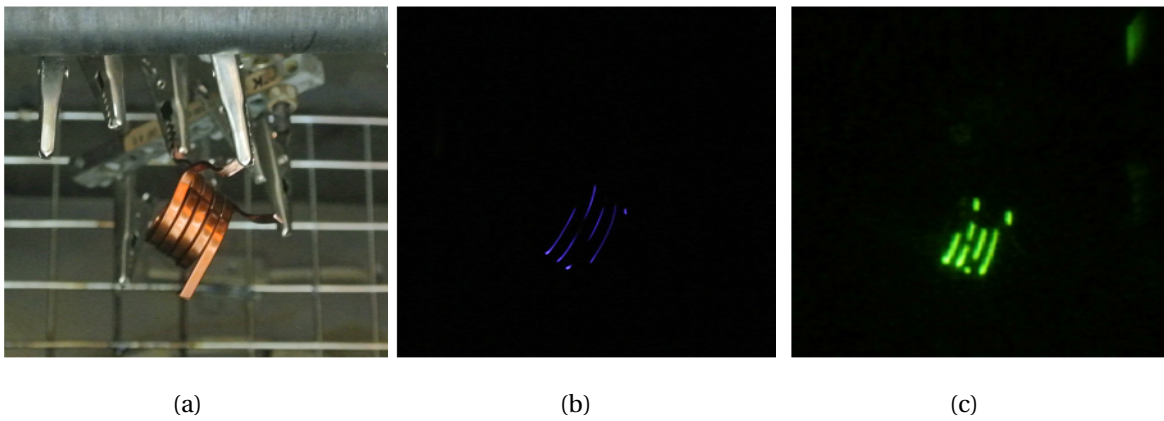


Figure III.32: Test under low dV/dt PWM impulse voltage $V_a = 1.2$ kV, $f_c = 5$ kHz: coil's installation (a), PDs photograph (b) and PDs optical image (c).

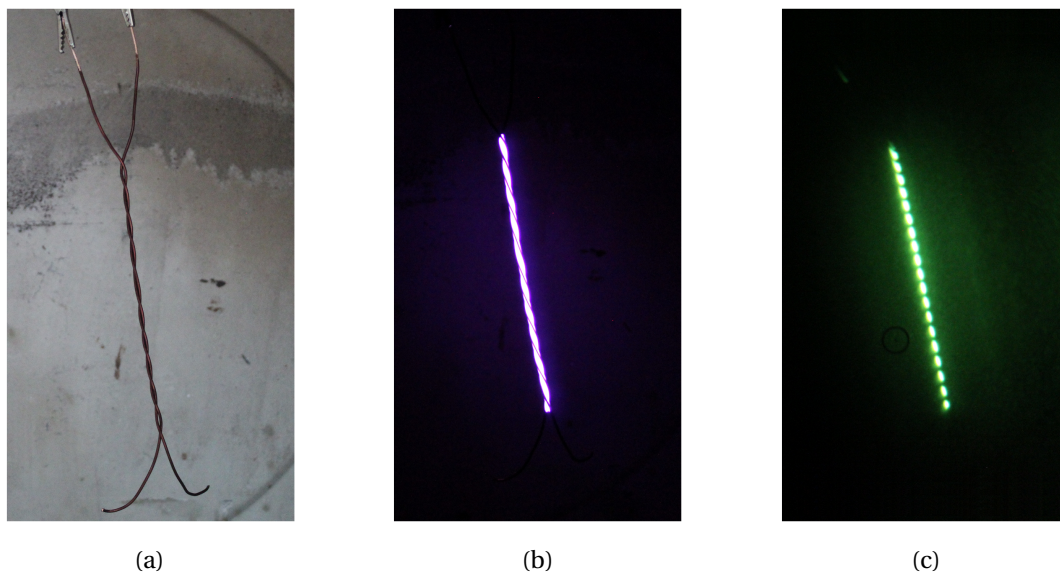


Figure III.33: Test under high dV/dt impulse voltage $V_{dc} = 1.4$ kV, $f = 50$ kHz: twisted pair's installation (a), PDs photograph (b) and PDs optical image (c).

The partial discharges on specimens under sinusoidal voltage varying from 2 to 5 kV RMS have the weakest radiation level. The most luminous discharges are observed during the test on the high dV/dt experimental bench (see Figure III.33). This effect can be associated with voltage changing rate and high frequency of impulse voltage resulting in high energy discharges.

3.5.2 Electromagnetic method

The detection of PDs is also performed using an antenna considering that partial discharges activity has an impact on the electromagnetic field in very high frequency (30-300 MHz) and ultra-high frequency (300-3000 MHz) ranges [65], [19], [61] and [66]. The antenna is made with a 150 Ω coaxial cable PK 150-7-11 (Russia) for radio frequency signal transmission of 6 m length. It's electrical parameters are given in Table III.4. The cable type and length is chosen in order to minimize its attenuation factor. The cable high impedance allows to increase antenna sensitivity. The cable terminations are connected to impedance matching resistors: $R_1 = R_2 = 150 \Omega$. The antenna is fixed at a distance of 10 cm from the specimen as shown in Figure III.34 in order to keep its position and the setup geometry during the measurements. When PD occur near the antenna, the displacement current created by the PD is received by the antenna and observed on the oscilloscope.

Table III.4: Parameters of radio frequency cable PK 150-7-11.

Parameter	Value
cable impedance	$150 \pm 10 \Omega$
attenuation factor at frequency 0.045 GHz	$\leq 0.08 \text{ dB/m}$
attenuation factor at frequency 3 GHz	$\leq 1.2 \text{ dB/m}$
electrical capacitance	29 pF



Figure III.34: Photograph of antenna detecting PD on the coil tested under high dV/dt impulse voltage $V_{dc} = 1.4 \text{ kV}$, $f = 50 \text{ kHz}$.

The voltage waveforms shown in Figures III.35a and III.35b have been measured below and above the PDIV level. The remarkable difference in amplitude of electromagnetic radiation can be observed on the signals measured by antenna when the bipolar impulse voltage applying to the specimen has crossed the discharge inception voltage threshold.

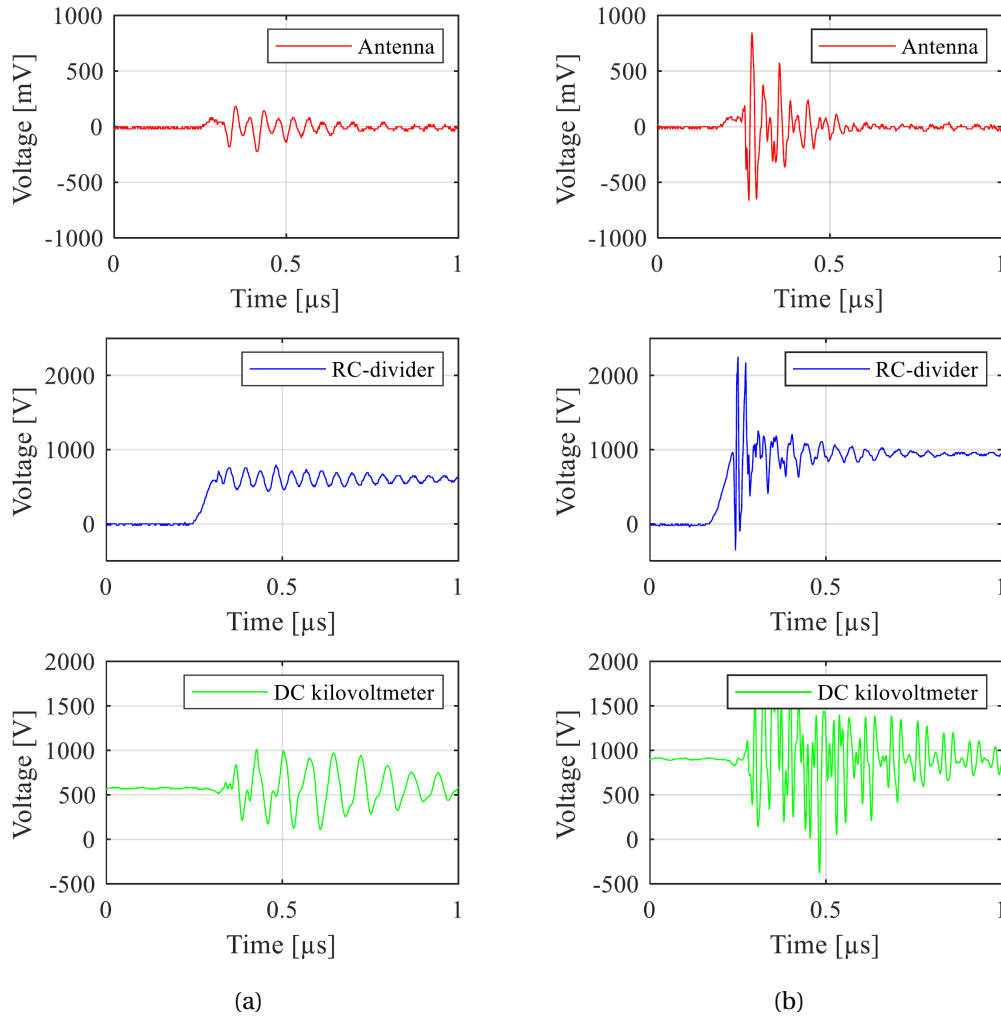


Figure III.35: Voltage waveforms measured at high dV/dt test bench: (a) below the PDIV $V_{dc} = 600$ V, (b) above the PDIV $V_{dc} = 900$ V.

The scopes in Figure III.35 also depict high frequency perturbations on the DC bus (DC kilovoltmeter) and at the inverter output (RC-divider). The observed perturbations are caused by fast commutations of transistors and, at the same time, are induced by the partial discharges occurring on rising and falling voltage rates (see Figure III.36). In fact, when the impulse voltage rise time is estimated to be 50 ns, and the PDs pulses' duration coming up to 10-30 ns, these two signals cause overlaps in the time domain. This phenomenon complicates the analysis of PDs when impulse voltage has high dV/dt .

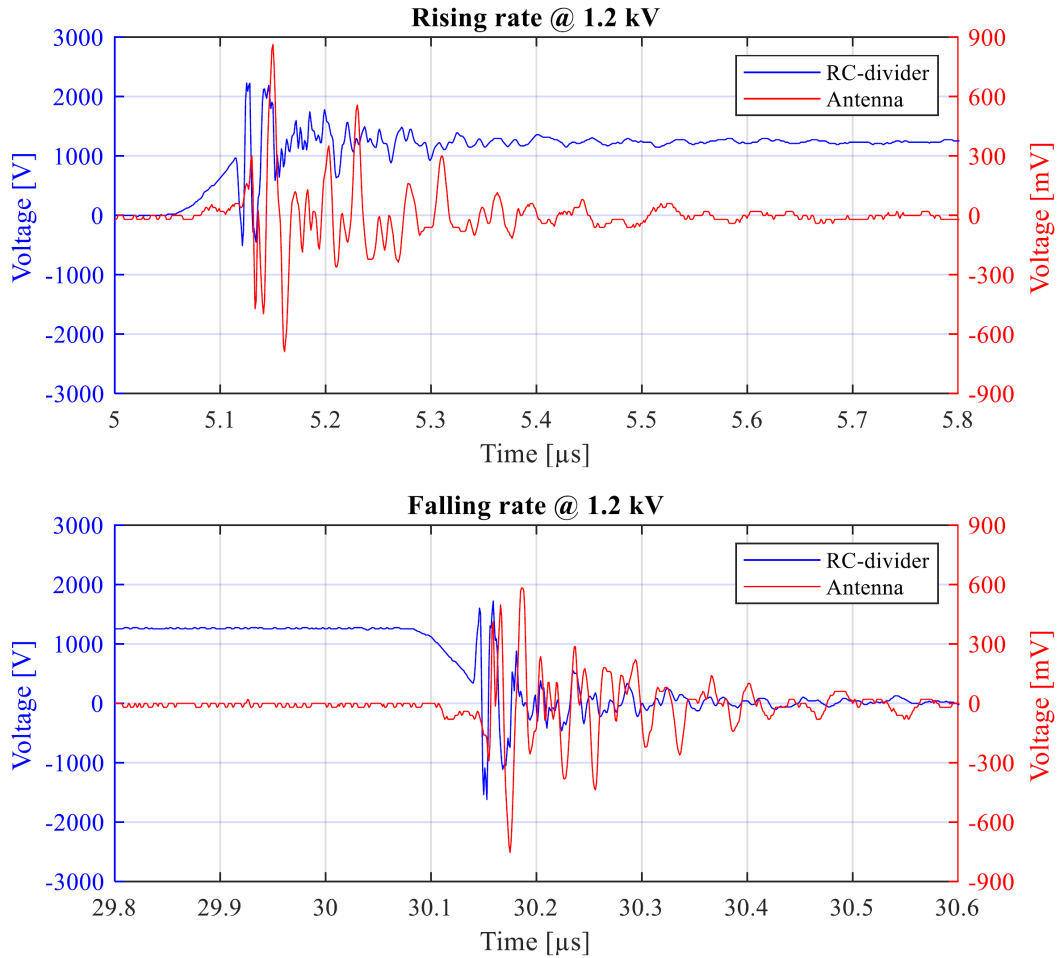


Figure III.36: Voltage waveforms measured at high dV/dt test bench above the PDIV: rising and falling rates at $V_{dc} = 1200$ V.

3.5.3 Chemical method

It is widely known that partial discharges generate ozone and other chemically active species. Ozone is highly corrosive gas, its effect leads to insulating material oxidation, breaking of organic polymers' C-C bonds, and facilitate dielectric breakdown [26] and [67].

Ozone concentration measurements are proposed in [68] and [69] as an insulation fault diagnostic method based on the detection of air derivatives such as ozone and Oxides of Nitrogen (NO_x), inside hydro-generator stator cores or transformers.

In described experimental benches two wires of twisted pair or coil present two electrodes covered by enamel insulation and have small air gaps between turns. When the high potential difference is applied between these electrodes the test bench acts like a plasma reactor generating ozone from the ambient air. The development of such plasma reactor intended for ozone generation is reported by [70] and [71].

In this regard, the experimental setup is implemented for detecting ozone generated by partial discharges on tested specimen as demonstrated in Figure III.37.

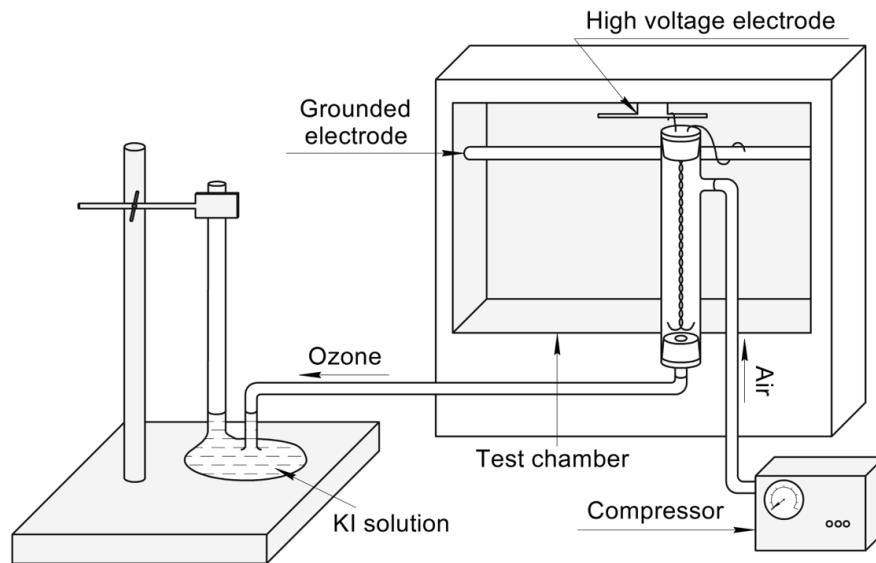
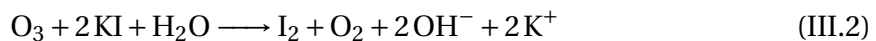


Figure III.37: Experimental setup for ozone detection.

In the purpose to prove the ozone formation during the test, the classic iodometric determination of ozone is used [72]. Using the compressor as shown in Figure III.37, a portion of a gas from the hermetical glass tube containing the specimen under high voltage is directed to the gas bubbler. This gas bubbler is partially filled with Potassium Iodide (KI) solution. Ozone produced by partial discharges reacts with the KI solution to form the iodine:



As a result of this reaction, the solution changes its color from transparent to yellow due to formed iodine (see Figure III.38). As it is known, that the iodine has a dark-blue appearance in the presence of starch, its water solution is used as an indicator (see Figure III.39). Using this iodometric method the ozone produced by PD on the tested twisted pair is detected under sinusoidal and impulse voltage with low and high dV/dt .

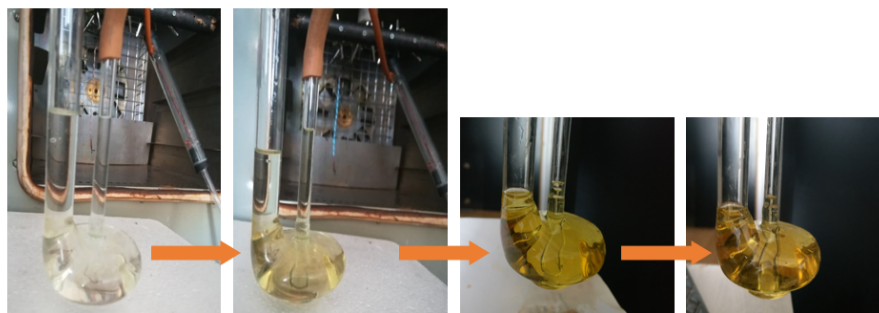


Figure III.38: Photographs of chemical reactions resulting from PDs on tested specimen: changing of solution color with the start of partial discharges.

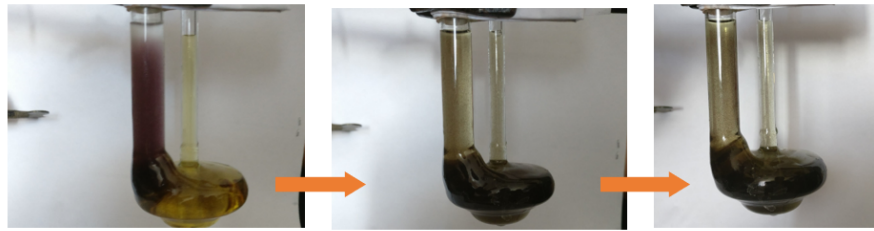


Figure III.39: Photographs of chemical reactions of iodine and starch solution.

4 Conclusion

With regard to minimize the risk of unexpected motor failures it is indispensable to analyse comprehensively voltage parameters influence, such rising and falling times, dV/dt and frequency, combined with thermal stresses. In this regard, it is essential to design experimental equipment to reproduce the constraints imposed by converters controlling electrical machines.

The presented there experimental benches allow to evaluate the endurance of insulating materials considering the changing in the process of ageing and the mechanism of enamel insulation destruction due to changes in controlling power electronics. The relevance of new testing methods and test benches is well found by remarkable modern advances in semiconductors technology.

Testing methods for low voltage motors winding wires insulation proposed in this work permit to evaluate the withstand capability of insulation materials applying firstly classic sinusoidal voltage of 50 Hz; secondly, the PWM signals representative for traditional Silicone-based converters supplying (μ s-level of impulse rise/fall times); and finally, the voltage waveforms with steep dV/dt , very fast rise and fall times (ns-level of impulse rise/fall times) and high switching frequency, engendered by new semiconductor devices based on wide bandgap materials. Furthermore, the proposed test benches make possible an insulation ageing investigation incorporating both electrical and thermal stresses as they are significant ageing factors in inverter fed motors. Thus, voltage parameters of designed pulse generator based on SiC inverter, as well as temperature levels in the thermal chamber, can be varied.

In this chapter the testing methodology and experimental benches are detailed and the following chapter gathers the obtained experimental data and analysis.

References

References

- [1] D. Fabiani, A. Cavallini, and G.C. Montanari. Aging investigation of motor winding insulation subjected to PWM-supply through PD measurements. In *CEIDP '05. 2005 Annual Report Conference on Electrical Insulation and Dielectric Phenomena, 2005.*, pages 434–437. IEEE, 2005.
- [2] F. Guastavino, D. Cordano, E. Torello, and L.Della Giovanna. Aging tests on type I insulating systems applying pulsed waveform. In *2016 IEEE International Conference on Dielectrics (ICD)*, volume 1, pages 556–560. IEEE, jul 2016.
- [3] Thibaut Billard, Cedric Abadie, and Thierry Lebey. Recent advances in on-line PDs'detection in power conversion chains used in aeronautics. In *2017 IEEE Workshop on Electrical Machines Design, Control and Diagnosis (WEMDCD)*, pages 281–289. IEEE, apr 2017.
- [4] Walid Boughamni, Jean-Paul Manata, Sonia Ait-Amar, and Daniel Roger. Electrical machines insulation: Towards low environmental impact solutions. In *2013 IEEE International Conference on Solid Dielectrics (ICSD)*, pages 557–560. IEEE, jun 2013.
- [5] Dennis Bogh, Jeff Coffee, Greg Stone, and Jim Custodio. Partial-discharge-inception testing on low-voltage motors. *IEEE Transactions on Industry Applications*, 42(1):148–154, jan 2006.
- [6] Davide Barater, Fabio Immovilli, Alessandro Soldati, Giampaolo Buticchi, Giovanni Franceschini, Christopher Gerada, and Michael Galea. Multistress Characterization of Fault Mechanisms in Aerospace Electric Actuators. *IEEE Transactions on Industry Applications*, 53(2):1106–1115, mar 2017.
- [7] Thibaut BILLARD, Cedric Abadie, and Bouazza Taghia. Advanced Partial Discharge Testing of 540V Aeronautic Motors Fed by SiC Inverter under Altitude Conditions. In *SAE Technical Paper Series*, volume 1, sep 2017.
- [8] Thibaut Billard, Cedric Abadie, and Bouazza Taghia. Non-Intrusive Partial Discharges Investigations on Aeronautic Motors. In *SAE 2016 Aerospace Systems and Technology Conference*, volume 1. SAE International, sep 2016.

-
- [9] Richard Gardner, Ian Cotton, and Mario Kohler. Comparison of power frequency and impulse based Partial Discharge measurements on a variety of aerospace components at 1000 and 116 mbar. In *2015 IEEE Electrical Insulation Conference (EIC)*, number June, pages 430–433. IEEE, aug 2015.
- [10] Paolo Mancinelli, Simone Stagnitta, and Andrea Cavallini. Qualification of Hairpin Motors Insulation for Automotive Applications. *IEEE Transactions on Industry Applications*, 53(3):3110–3118, may 2017.
- [11] Stefan Grubic, J.M. Aller, Bin Lu, and T.G. Habetler. A Survey on Testing and Monitoring Methods for Stator Insulation Systems of Low-Voltage Induction Machines Focusing on Turn Insulation Problems. *IEEE Transactions on Industrial Electronics*, 55(12):4127–4136, dec 2008.
- [12] Peng Wang, Hongying Xu, Jian Wang, Andrea Cavallini, and Gian Carlo Montanari. Temperature effects on PD statistics and endurance of inverter-fed motor insulation under repetitive square wave voltages. In *2016 IEEE Electrical Insulation Conference (EIC)*, pages 202–205. IEEE, jun 2016.
- [13] Daniel Roger, Sonia Ait-Amar, Ewa Napieralska, and Piotr Napieralski. A Proposition for Improving the Design of Motor Windings for low-Pressure Environment. In *2018 IEEE Transportation Electrification Conference and Expo (ITEC)*, pages 424–429. IEEE, jun 2018.
- [14] M. Fenger, S.R. Campbell, and J. Pedersen. Motor winding problems caused by inverter drives. *IEEE Industry Applications Magazine*, 9(4):22–31, jul 2003.
- [15] Francesco Guastavino, Alessandro Ratto, Eugenia Torello, and Giovanna Biondi. Aging Tests on Nanostructured Enamels for Winding Wire Insulation. *IEEE Transactions on Industrial Electronics*, 61(10):5550–5557, oct 2014.
- [16] F. Guastavino, D. Cordano, E. Torello, and L. Della Giovanna. PD evolution of conventional and corona resistant enamels. In *2016 IEEE Conference on Electrical Insulation and Dielectric Phenomena (CEIDP)*, pages 259–262. IEEE, oct 2016.
- [17] F. Guastavino, E. Torello, D. Cordano, and L. Della Giovanna. Surface PD evolution of conventional and nanocomposite enamels. In *2016 IEEE International Conference on Dielectrics (ICD)*, volume 2, pages 760–763. IEEE, jul 2016.
- [18] Andreas Ruf, Jorg Paustenbach, David Franck, and Kay Hameyer. A methodology to identify electrical ageing of winding insulation systems. In *2017 IEEE International Electric Machines and Drives Conference (IEMDC)*, pages 1–7. IEEE, may 2017.

- [19] Loucif Benmamas, Philippe Teste, Guillaume Krebs, Emmanuel Odic, Franck Vangraefscheppe, and Tahar Hamiti. Contribution to partial discharge analysis in inverter-fed motor windings for automotive application. In *2017 IEEE Electrical Insulation Conference (EIC)*, pages 348–351. IEEE, jun 2017.
- [20] K. Kimura, S. Ushirone, T. Koyanagi, Y. Iiyama, S. Ohtsuka, and M. Hikita. Study of PD behaviors on a crossed sample of magnet-wire with repetitive bipolar impulses for inverter-fed motor coil insulation. In *CEIDP '05. 2005 Annual Report Conference on Electrical Insulation and Dielectric Phenomena, 2005.*, pages 393–396. IEEE, 2005.
- [21] Barbara FLORKOWSKA, Marek FLORKOWSKI, Paweł ZYDRON, and Józef ROEHRICH. Experimental evaluation of breakdown voltage and life time for models of the low voltage electrical motors windings. *PRZEGLĄD ELEKTROTECHNICZNY*, 1(10):21–25, oct 2016.
- [22] Luca Lusuardi and Andrea Cavallini. The Problem of Altitude When Qualifying the Insulating System of Actuators for More Electrical Aircraft. In *2018 IEEE International Conference on Electrical Systems for Aircraft, Railway, Ship Propulsion and Road Vehicles & International Transportation Electrification Conference (ESARS-ITEC)*, pages 1–4. IEEE, nov 2018.
- [23] Gian Carlo Montanari and Fabio Ciani. Inverter design and partial discharge phenomenology in insulation systems of rotating machines. In *2017 IEEE International Electric Machines and Drives Conference (IEMDC)*, pages 1–5. IEEE, may 2017.
- [24] Gian Carlo Montanari, Fabrizio Negri, and Fabio Ciani. Partial Discharge and life behavior of rotating machine wire insulation under PWM waveforms: The influence of inverter characteristics. In *2017 IEEE Electrical Insulation Conference (EIC)*, pages 161–164. IEEE, jun 2017.
- [25] Farah Salameh, Antoine Picot, Marie Chabert, and Pascal Maussion. Parametric and Nonparametric Models for Lifespan Modeling of Insulation Systems in Electrical Machines. *IEEE Transactions on Industry Applications*, 53(3):3119–3128, may 2017.
- [26] Mateusz Szczepanski, David Malec, Pascal Maussion, Benoit Petitgas, and Philippe Manfe. Ozone concentration impact on the lifespan of enameled wires (conventional and corona-resistant) for low voltage rotating machines fed by inverters. In *2017 IEEE Electrical Insulation Conference (EIC)*, pages 443–446. IEEE, jun 2017.
- [27] Gabriel Velu, Stéphane Duchesne, Daniel Roger, Walid Boughamni, and Ewa Napieralska. Bobinage à faible impact environnemental. In *Symposium de Génie Électrique 2014*, pages 8–10, Cachan, 2014.

-
- [28] Daniel Roger, Sonia Ait-Amar, and Ewa Napieralska. A method to reduce partial discharges in motor windings fed by PWM inverter. *Open Physics*, 16(1):599–604, oct 2018.
- [29] *IEC 60851-5:2008. Winding wires - Test methods - Part 5: Electrical properties*. Ed. 4.0 edition, 2008.
- [30] Peng Wang, Gian Carlo Montanari, and Andrea Cavallini. Partial Discharge Phenomenology and Induced Aging Behavior in Rotating Machines Controlled by Power Electronics. *IEEE Transactions on Industrial Electronics*, 61(12):7105–7112, dec 2014.
- [31] Peng Wang, Andrea Cavallini, and Gian Carlo Montanari. The effect of impulsive voltage rise time on insulation endurance of inverter-fed motors. In *2015 IEEE 11th International Conference on the Properties and Applications of Dielectric Materials (ICPADM)*, volume 2015-Octob, pages 84–87. IEEE, jul 2015.
- [32] Peng Wang, Hongying Xu, Jian Wang, Andrea Cavallini, and Gian Carlo Montanari. The effects of asymmetry repetitive square wave voltages on PD statistics and endurance. In *2016 IEEE International Conference on Dielectrics (ICD)*, volume 2, pages 693–696. IEEE, jul 2016.
- [33] Peng Wang, Andrea Cavallini, and Gian Montanari. The influence of repetitive square wave voltage parameters on enameled wire endurance. *IEEE Transactions on Dielectrics and Electrical Insulation*, 21(3):1276–1284, jun 2014.
- [34] Peng Wang and Andrea Cavallini. The influence of repetitive square wave voltage parameters on PD statistical features. In *2013 Annual Report Conference on Electrical Insulation and Dielectric Phenomena*, pages 1282–1285. IEEE, oct 2013.
- [35] Peng Wang, Andrea Cavallini, and Gian Carlo Montanari. The influence of square wave voltage duty cycle on PD behavior. In *2015 IEEE Conference on Electrical Insulation and Dielectric Phenomena (CEIDP)*, volume 2015-Decem, pages 338–341. IEEE, oct 2015.
- [36] Vadim Iosif, Daniel Roger, Stéphane Duchesne, and David Malec. Assessment and improvements of inorganic insulation for high temperature low voltage motors. *IEEE Transactions on Dielectrics and Electrical Insulation*, 23(5):2534–2542, oct 2016.
- [37] Peng Wang, Andrea Cavallini, G. C. Montanari, and Guangning Wu. Effect of rise time on PD pulse features under repetitive square wave voltages. *IEEE Transactions on Dielectrics and Electrical Insulation*, 20(1):245–254, feb 2013.

- [38] M. Kaufhold, G. Borner, M. Eberhardt, and J. Speck. Failure mechanism of the interturn insulation of low voltage electric machines fed by pulse-controlled inverters. *IEEE Electrical Insulation Magazine*, 12(5):9–16, sep 1996.
- [39] Peng Wang, Hongying Xu, Jian Wang, Wanya Zhou, and Andrea Cavallini. The influence of repetitive square wave voltage rise time on partial discharge inception voltage. In *2016 IEEE Conference on Electrical Insulation and Dielectric Phenomena (CEIDP)*, pages 759–762. IEEE, oct 2016.
- [40] A Madonia, P Romano, T. Hammarstrom, S M Gubanski, F Viola, and A Imburgia. PD characteristics at square shaped voltages applying two different detecting techniques. In *2016 IEEE Conference on Electrical Insulation and Dielectric Phenomena (CEIDP)*, pages 247–250. IEEE, oct 2016.
- [41] Nadine Lahoud, Jerome Faucher, David Malec, and Pascal Maussion. Electrical Aging of the Insulation of Low-Voltage Machines: Model Definition and Test With the Design of Experiments. *IEEE Transactions on Industrial Electronics*, 60(9):4147–4155, sep 2013.
- [42] Nadine Lahoud, Manh Quan Nguyen, Pascal Maussion, David Malec, and Dominique Mary. Lifetime model of the inverter-fed motors secondary insulation by using a design of experiments. *IEEE Transactions on Dielectrics and Electrical Insulation*, 22(6):3170–3176, dec 2015.
- [43] Vadim Iosif, Stephane Duchesne, and Daniel Roger. Voltage stress predetermination for long-life design of windings for electric actuators in aircrafts. In *2015 IEEE Conference on Electrical Insulation and Dielectric Phenomena (CEIDP)*, pages 318–321. IEEE, oct 2015.
- [44] Bouazza Taghia, Bernardo Cougo, Hubert Piquet, David Malec, Antoine Belinger, and Jean-Pierre Carayon. Overvoltage at motor terminals in SiC-based PWM drives. *Mathematics and Computers in Simulation*, 158:264–280, apr 2019.
- [45] Hitoshi Okubo, Naoki Hayakawa, and Gian Montanari. Technical Development on Partial Discharge Measurement and Electrical Insulation Techniques for Low Voltage Motors Driven by Voltage Inverters. *IEEE Transactions on Dielectrics and Electrical Insulation*, 14(6):1516–1530, dec 2007.
- [46] X. Wang, N. Taylor, and H. Edin. Effect of humidity on partial discharge in a metal-dielectric air gap on machine insulation at trapezoidal testing voltages. *Journal of Electrostatics*, 83:88–96, oct 2016.

- [47] IEC 60034-18-41:2014. *Rotating electrical machines - Part 18-41: Partial discharge free electrical insulation systems (Type I) used in rotating electrical machines fed from voltage converters - Qualification and quality control tests*. Ts ed. 1.0 edition, 2014.
- [48] Xin Zhong, Akram Shakeel, Yan Yang, Guoqiang Gao, and Guangning Wu. Preparation and corona-resistance characteristics of double-layer polyimide/Al₂O₃ nanocomposite film. In *2016 IEEE International Conference on High Voltage Engineering and Application (ICHVE)*, pages 1–4. IEEE, sep 2016.
- [49] Rudolf Brüttsch and Peter Weyl. A New Winding Wire for Inverter Driven Motors. In *9th INSUCON International Electrical Insulation Conference, Berlin*, Berlin, 2002.
- [50] Greg C. Stone, Ian Culbert, Edward A. Boulter, and Hussein Dhirani. *Electrical Insulation for Rotating Machines*. John Wiley & Sons, Inc., Hoboken, NJ, USA, jul 2014.
- [51] Subrata Karmakar, Surajit Chattopadhyay, Madhuchhanda Mitra, and Samarjit Sen-gupta. *Induction Motor Fault Diagnosis*. Power Systems. Springer Singapore, Singa-pore, 2016.
- [52] K. Tshiloz, A. C Smith, A. Mohammed, S. Djurovic, and T. Feehally. Real-time insula-tion lifetime monitoring for motor windings. In *2016 XXII International Conference on Electrical Machines (ICEM)*, pages 2335–2340. IEEE, sep 2016.
- [53] IEC 60034-18-1:2010. *Rotating electrical machines – Part 18-1: Functional evaluation of insulation systems – General guidelines*. Ts ed. 2.0 edition, 2010.
- [54] IEC 62539:2007. *Guide for the statistical analysis of electrical insulation breakdown data*. Ed. 1.0 edition, 2007.
- [55] A.P. Leonov, A.A. Korobtsov, and A.S. Supueva. Method for determining enameled wires insulation resistance to surface discharges. RU patent № 2491565, 2012.
- [56] A. Leonov, V Red’ko, and E. Soldatenko. Estimation of winding insulation resistance to the corona discharges. *IOP Conference Series: Materials Science and Engineering*, 66(1):012004, oct 2014.
- [57] A. P. Leonov, V V Red’ko, L A Red’ko, and E. Y. Soldatenko. Determination of enamel insulation corona resistance by high- frequency modulated pulses. *IOP Conference Series: Materials Science and Engineering*, 81(1):012094, apr 2015.
- [58] C2M0280120D Silicon Carbide Power MOSFET C2M TM MOSFET Technology N-Channel Enhancement Mode Technology. Product data sheet.
- [59] Dual Channel SiC MOSFET Driver Gate Driver for 1200V, 62mm SiC MOSFET Power Module. Product data sheet.

- [60] Jian Wang, Peng Wang, Wei Wang, Kai Zhou, Qun Zhou, Yong Lei, and Andrea Cavallini. Novel repetitive square wave voltage generator used for the insulation evaluation of rotating machines driven by power electronics. *IEEE Transactions on Dielectrics and Electrical Insulation*, 24(4):2041–2049, 2017.
- [61] M. M. Yaacob, M. A. Alsaedi, J. R. Rashed, A. M. Dakhil, and S. F. Atyah. Review on partial discharge detection techniques related to high voltage power equipment using different sensors. *Photonic Sensors*, 4(4):325–337, dec 2014.
- [62] Daniel Siebler, Philipp Rohwetter, Roy Brusenbach, and Ronald Plath. Optical-only Detection of Partial Discharge with Fluorescent Polymer Optical Fiber Sensors. *Procedia Engineering*, 120:845–848, 2015.
- [63] Michael Muhr and Robert Schwarz. Experience with Optical Partial Discharge Detection. In *APTADM*, pages 26–29. ., 2007.
- [64] N. V. Krupenin and V. I. Zavidai. Methods for remote monitoring and defectoscopy systems for electrical machine high-voltage insulation by using an optical radiation. *Russian Electrical Engineering*, 82(9):460–463, sep 2011.
- [65] G C Stone, C Chan, and H G Sedding. Relative ability of UHF antenna and VHF capacitor methods to detect partial discharge in turbine generator stator windings. *IEEE Transactions on Dielectrics and Electrical Insulation*, 22(6):3069–3078, dec 2015.
- [66] Fakhru Rozi and Umar Khayam. Development of Loop Antennas for Partial Discharge Detection. *International Journal on Electrical Engineering and Informatics*, 7(1):29–41, mar 2015.
- [67] Jean-Pierre Habas, Jean-Marie Arrouy, and Fabrice Perrot. Effects of electric partial discharges on the rheological and chemical properties of polymers used in HV composite insulators after railway service. *IEEE Transactions on Dielectrics and Electrical Insulation*, 16(5):1444–1454, oct 2009.
- [68] C. Millet, D. N. Nguyen, L. Lepine, M. Belec, D. Lessard-Deziel, and C. Guddemi. Case study - high ozone concentration in hydro generators. In *2009 IEEE Electrical Insulation Conference*, pages 178–182. IEEE, may 2009.
- [69] Kang Li, Hassan Javed, and Guoqiang Zhang. Experimental Study on Ozone Production under 50Hz Corona Discharge Used for Faults Diagnostic. In *Proceedings of the 2015 2nd International Conference on Machinery, Materials Engineering, Chemical Engineering and Biotechnology*, number Mmceeb 2015, pages 456–460, Paris, France, 2016. Atlantis Press.

- [70] N. Mericam-Bourdet, M.J. Kirkpatrick, F. Tuvache, D. Frochot, and E. Odic. Effect of voltage waveform on dielectric barrier discharge ozone production efficiency. *The European Physical Journal Applied Physics*, 57(3):30801, mar 2012.
- [71] Xuming Zhang, Bok Jik Lee, Hong G. Im, and Min Suk Cha. Ozone Production With Dielectric Barrier Discharge: Effects of Power Source and Humidity. *IEEE Transactions on Plasma Science*, 44(10):2288–2296, oct 2016.
- [72] David A Reckhow. Laboratory Ozonation. UMass Environmental Engineering Program. Standard Operating Procedures. Technical report, University of Massachusetts, Amherst, 2012.

Chapter IV : Analysis of turn insulation endurance experimental results

Chapter IV

Analysis of turn insulation endurance experimental results

Contents

1 Introduction	138
2 Breakdown voltage tests	138
3 Endurance tests	142
3.1 Endurance tests under sinusoidal voltage	142
3.2 Endurance tests under PWM impulse voltage: low dV/dt	148
3.2.1 Tests on unimpregnated specimens	148
3.2.2 Influence of defects on turn insulation endurance	154
3.3 Endurance tests under rectangular impulse voltage: high dV/dt	159
4 Thermal imaging study	167
5 Conclusion	169
References	173

1 Introduction

This Chapter gathers the experimental protocols and results of tests conducted on previously described benches followed by statistical analysis and main observations. Firstly, the results of breakdown voltage tests carried out under sinusoidal voltage are given. Then, the results of endurance tests conducted on studied winding wires under sinusoidal voltage, PWM impulse voltage (μm -level of rise time) and rectangular impulse voltage (ns-level of rise time) are presented. The influence of voltage waveforms on turn insulation ageing and endurance, as well as the effect of thermal stresses are discussed.

2 Breakdown voltage tests

The experimental characterization of electrical insulation materials may be performed using progressive stress tests in which breakdown voltage values are measured, and constant stress tests in which times to breakdown are observed. Data obtained for a number of identical specimens for given test conditions may be represented by a statistical distribution [1].

Firstly, the breakdown voltage tests are conducted on all studied winding wires under AC sinusoidal voltage of 50 Hz nominal frequency at normal ambient temperature (approximately 25 °C) and atmospheric pressure. The tests are performed in “wire-shot” test configuration in accordance with the method described in Chapter III Section 3.3. The broken down specimens exhibit insulation punctures as shown in Figure IV.1. The experimental results constituting of measured breakdown voltages are given in Table IV.1. In tables and figures herein after, the following abbreviations are used to indicate the type of tested winding wires: corona resistant (CR) wire, and conventional (CV) wires.



Figure IV.1: Photograph of a broken specimen made of APX-1 (CV).

Table IV.1: Breakdown voltage under progressive voltage stress on winding wires.

Test (repetition)	Breakdown voltage V_{BD} , kV			
	PETD2-K-180 (CR)	PETD-180 (CV)	APX-1 (CV)	APX-2 ¹ (CV)
#1	7.0	6.0	5.5	9.0
#2	7.0	6.0	5.8	10.5
#3	7.5	6.0	6.1	11.0
#4	8.0	6.0	6.5	12.0
#5	8.5	6.0	6.7	12.0
#6	8.5	6.7	6.7	-
#7	8.5	7.0	6.8	-
#8	9.0	7.5	6.9	-
#9	9.0	8.3	7.1	-
#10	10.0	8.5	7.3	-

All the tested specimens are broken down in this test, so the data is referred to as complete. In order to identify the statistical distribution which best fits the recorded breakdown voltage data, probability distribution plots are compared (see Figure IV.2). Adequacy tests of Weibull, Normal, lognormal and exponential distributions are performed with 95% confidence interval using the MATLAB Distribution Fitting Tool. Based on Probability Distribution Function (PDF) [2] plots, the Normal, lognormal and Weibull distributions seem appropriate for fitting the breakdown voltage data distribution. The hypothesis of the exponential distribution is rejected for all wires tested under sinusoidal voltage, even under the weaker conditions induced by the rounding and the estimation of the parameter of the exponential distribution.

The Normal (or Gaussian) distribution is probably the best known distribution which often gives a good approximation of breakdown voltage of solid dielectrics [1] and [3]. The Normal distribution is described in terms of the mean μ and standard deviation σ measuring the dispersion of the data points relative to the mean. A continuous random variable X (e.g., breakdown voltage data) with probability density function

$$f(x) = \frac{1}{\sqrt{2\pi}\sigma} e^{-\frac{(x-\mu)^2}{2\sigma^2}} \quad -\infty < \mu < \infty \quad (IV.1)$$

is a normal random variable with parameters μ , where $-\infty < \mu < \infty$ and $\sigma > 0$. The value of the random variable measured with n repetitions is denoted by x .

¹The tested specimens' number is reduced to five for rectangular section wire APX-2 by the reason of difficulty to avoid flashovers between wires ends and the grounded metal shot.

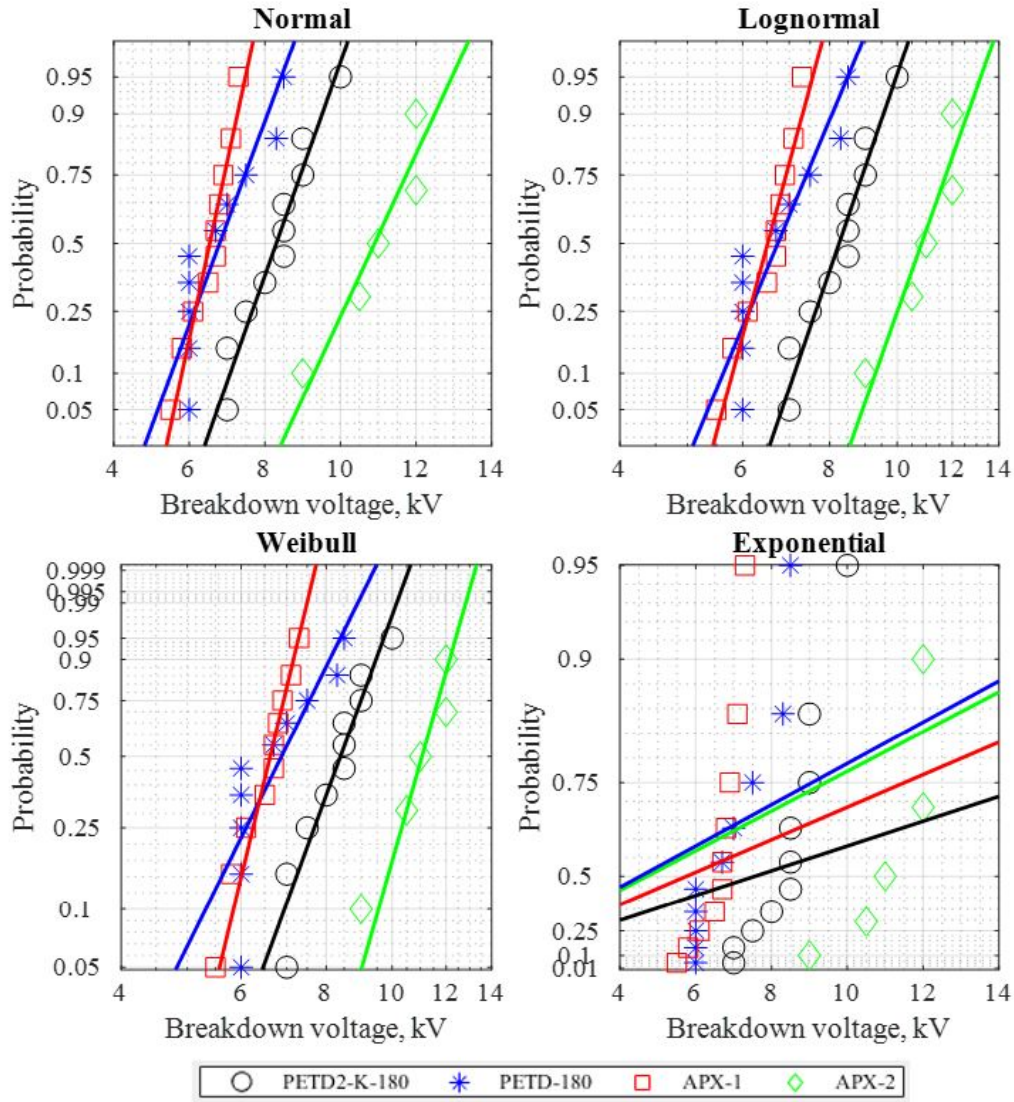


Figure IV.2: Comparison among different PDF plots of breakdown voltage data.

Also, the expected value $E(X)$ and the variance $V(X)$ figured by (IV.2) and (IV.3) , the standard deviation $\sigma = \sqrt{\sigma^2}$ and the notation $N(\mu, \sigma^2)$ is used to denote the distribution [2]. The estimated parameters $\hat{\mu}$ and $\hat{\sigma}$ are given in Table IV.2.

$$\mu = E(x) \quad \hat{\mu} = \frac{1}{n} \sum_{i=1}^n x_i \quad (IV.2)$$

$$V(x) = \sigma^2 \quad \hat{\sigma}^2 = \frac{1}{n-1} \sum_{i=1}^n (x_i - \hat{\mu})^2 \quad (IV.3)$$

Table IV.2: Normal distribution parameters of breakdown voltage data.

Parameter	PETD2-K-180 (CR)	PETD-180 (CV)	APX-1 (CV)	APX-2 (CV)
Mean $\hat{\mu}$, kV	8.30	6.80	6.54	10.90
Standard deviation $\hat{\sigma}$, kV	0.949	0.993	0.574	1.245

In order to estimate the effect of winding wire's type (insulation material) on the obtained breakdown voltage, a one-way analysis of variance (ANOVA) has been performed. It shown that the experimental data do not go against the equivalence between PETD-180 and APX-1 with regard to breakdown voltage. At the same time, these wires shows significant difference from the other (PETD2-K-180 and APX-2).

Figure IV.3 sums up experimental mean breakdown voltages and breakdown voltage values given in wires' specifications. For wires APX-1 and APX-2 the values of dielectric strength E_{spec} (kV/mm) are given in the specifications. To compare with other winding wires the breakdown voltage V_{spec} is calculated by IV.4 using averaged measured insulation thickness δ : δ_{rad} for the round section wire, δ_a and δ_b for the rectangular section wire [see Chapter III Section 3.1].

$$V_{spec} = E_{spec} \cdot \delta \quad (IV.4)$$

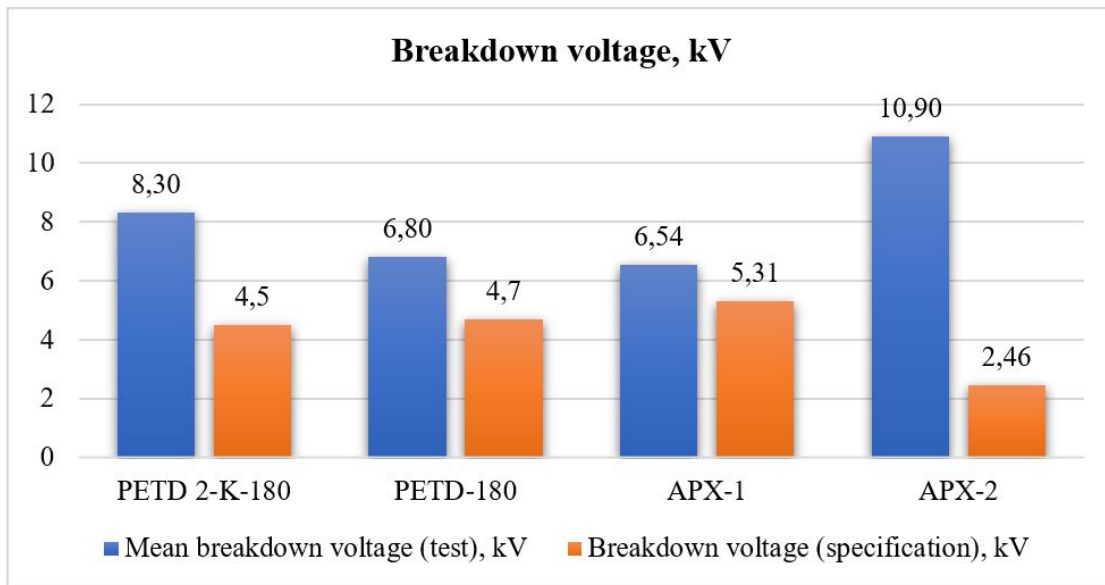


Figure IV.3: Histogram of mean breakdown voltages issued from tests and breakdown voltage given in wires' specifications.

The values of breakdown voltage given in specifications are lower because it may be multiplied by reduction factor with regard to provide the minimal guaranteed limits of insulation electrical strength taking into account possible defects. Furthermore, the value of dielectric strength E_{spec} given in specification also depends on measurement method, test equipment and environmental conditions. The dielectric strength of an enamel could be tested on enamel coated steel plates and not on wires. It should be noted, that higher electric strength of rectangular section wire APX-2 comparing to other winding wires for given test conditions might be explained by higher insulation layer thickness.

Basing on measured breakdown voltages of winding wires, the voltage values for further lifetime tests under sinusoidal voltage are then chosen.

3 Endurance tests

In the present work, the insulation endurance tests are conducted under constant stress choosing as factors voltage waveforms parameters and temperature levels. These tests are also called accelerated life tests; times to breakdown are measured in specified test conditions accelerating the insulation ageing and failure. At least five repetitions (winding wire specimens tested in the same conditions) are made for the sake of statistical analysis of experimental variability.

3.1 Endurance tests under sinusoidal voltage

Experimental protocol

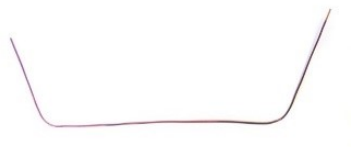


The endurance tests are started by applying AC sinusoidal voltage (50 Hz). Both electrodes systems are used: (i) “shot-wire” test system and (ii) two wires connection (twisted pairs for round section wires and coils for rectangular section wires). The test are performed on unimpregnated specimens. Table IV.3 recaps the specimen’s types and experimental conditions (voltage and temperature levels). The tests have been conducted at normal atmospheric pressure and humidity $\phi = [15 \div 30]\%$. These environmental conditions have not been controlled and may have slightly varied during testing.

Experimental results and analysis

Lifetime data obtained corresponding to the experimental protocol and estimated parameters $\hat{\mu}$ (IV.2) and $\hat{\sigma}$ (IV.3) are reported in Appendix IV-A, and graphically shown in figures below. In order to provide a clear visual insight, boxplots are used to present the experimental data. The time to breakdown is given in logarithmic scale.

Figure IV.4 gives a boxplot of times to breakdown for bent wires. The 25th and 75th percentiles are displayed by the edges of the box; the red line in the box is the median, and the minimum and maximum are plotted using the whiskers. The symbol inside the box corresponds to the estimated mean value $\hat{\mu}$. The data values that lie too far from the bulk of data are referred to as outliers (shown by red X markers).

Table IV.3: Normal distribution parameters of breakdown voltage data.

		
Specimens		
bent wires	twisted pairs	coils
Winding wires		
PETD 2-K-180 (CR) PETD-180 (CV)	PETD-180 (CV) APX-1 (CV)	APX-2 (CV)
Voltage (RMS)		
4.0 kV 4.5 kV 5.0 kV	5.0 kV	5.0 kV
Temperature		
180 °C	25 °C 180 °C	25 °C 180 °C

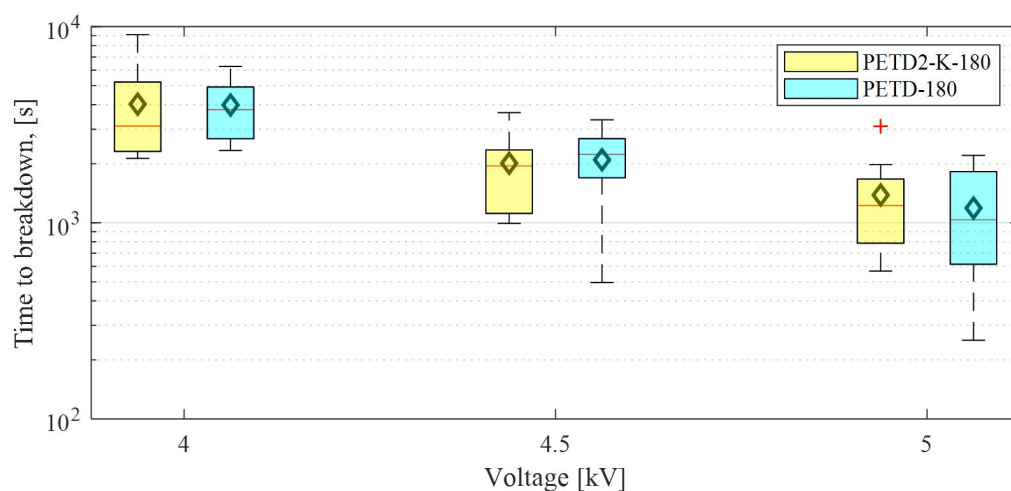


Figure IV.4: Time to breakdown of bent wires specimens tested in “wire-shot” electrode system: voltage amplitude effect, $T = 180\text{ }^{\circ}\text{C}$.

Figure IV.5 gives a graphical comparison of probability distribution plots. Analysis of probability plots shows that the lognormal and Weibull distributions may be appropriate for fitting the time to breakdown distribution. It correlates with recommendations of IEC standard [1], where these distributions are used to represent electrical breakdown. According to the performed Shapiro-Wilk test, not all the experimental data follow the Normal distribution. Moreover, as in the case of the breakdown voltage data, the hypothesis of the exponential distribution is rejected.

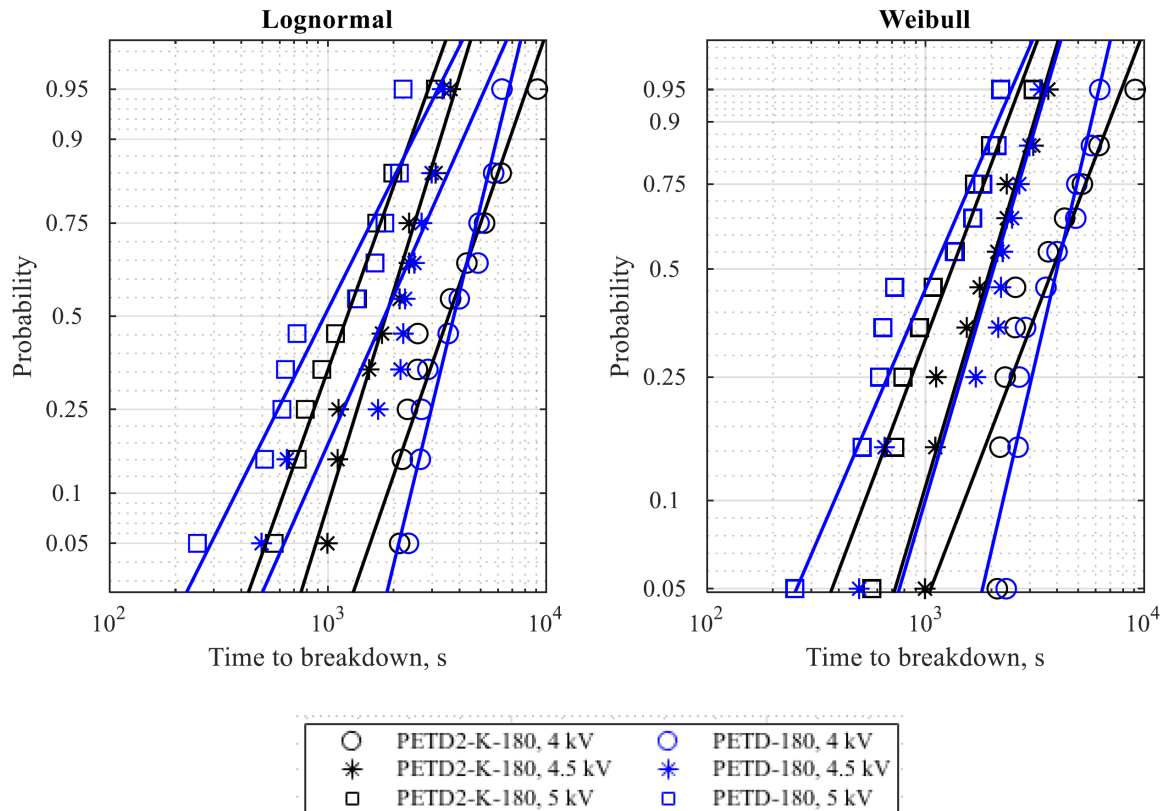


Figure IV.5: Comparison among different probability distribution plots of time to breakdown data of PETD2-K-180 and PETD-180

The experimental results analysis does not show a perceptible difference between corona resistant and conventional wires in these given test conditions. Considering the lognormal distribution, a two-way ANOVA has been performed on logarithms of experimental data. This test show that the effect of winding wire' type is not significant. On the other hand, the time to breakdown logarithmic means are significantly different when changing the voltage level. Indeed, the rise in voltage shorten the wires' lifetime.

This observation correlates with the results of Weibull distribution analysis. The expression for the probability density function of the two-parameter Weibull distribution according to [4] is given by IV.6:

$$f(t) = \beta \frac{t^{\beta-1}}{\eta^\beta} e^{-\left(\frac{t}{\eta}\right)^\beta} \quad (IV.5)$$

where t is the measured variable (time to breakdown in our case); η is the scale parameter or characteristic life, $\eta > 0$, and β is the shape parameter, $\beta > 0$. The scale parameter η represents the time for which the failure probability is 0.632, and the shape parameter β is a measure of the range of the failure times. The larger shape parameter is, the smaller is the failure time range. The shape parameter has three ranges of values: for $\beta < 1$ the failure rate decreases with time, for $\beta = 1$ the failure rate is constant (consistent with the exponential distribution), and for $\beta > 1$ the failure rate increases with time. Experimental results analysis shows that the estimated scale parameter $\hat{\eta}$ decreases with the increasing of voltage applied to tested specimens and the shape parameter $\hat{\beta} \geq 2$.

A ratio of mean time to breakdown K is also used as an indicator for estimating the effect of test conditions (voltage, temperature, type of specimen) as suggested in [5]. For the described above endurance tests under sinusoidal voltage, the ratio K_{RMSsin} is calculated using mean times to breakdown t_{4sin} and t_{5sin} of two wires tested at 4 and 5 kV RMS respectively.

$$K_{RMSsin} = \frac{t_{4sin}}{t_{5sin}} \quad (IV.6)$$

For the studied winding wires the ratios are the following:

$K_{RMSsin}(\text{PETD2} - \text{K} - 180) = 2.91$ and $K_{RMSsin}(\text{PETD} - 180) = 3.35$. It shows the influence of higher voltage level accelerating the insulation breakdown.

During the "wire-shot" tests low partial discharge intensity, low ozone production and UV emissions resulted from surface electrical activities were observed. The broken specimens had local punctures similar to previously shown in Figure IV.1.

Figures IV.6a and IV.6b show boxplots of times to breakdown for twisted pairs and coils tested under sinusoidal voltage at 5 kV RMS at two temperature levels: 25 and 180 °C. The corona resistant wire PETD2-K-180 is not displayed on this chart. Without heating (lifetime tests at 25 °C) the applied voltage had insufficient capability to break down the specimens made of corona resistant wire during a day. The specimens made of rectangular wire APX-2 also shown very high endurance at 25 °C, which decreased significantly when heated at 180 °C as can be seen from Figure IV.6b).

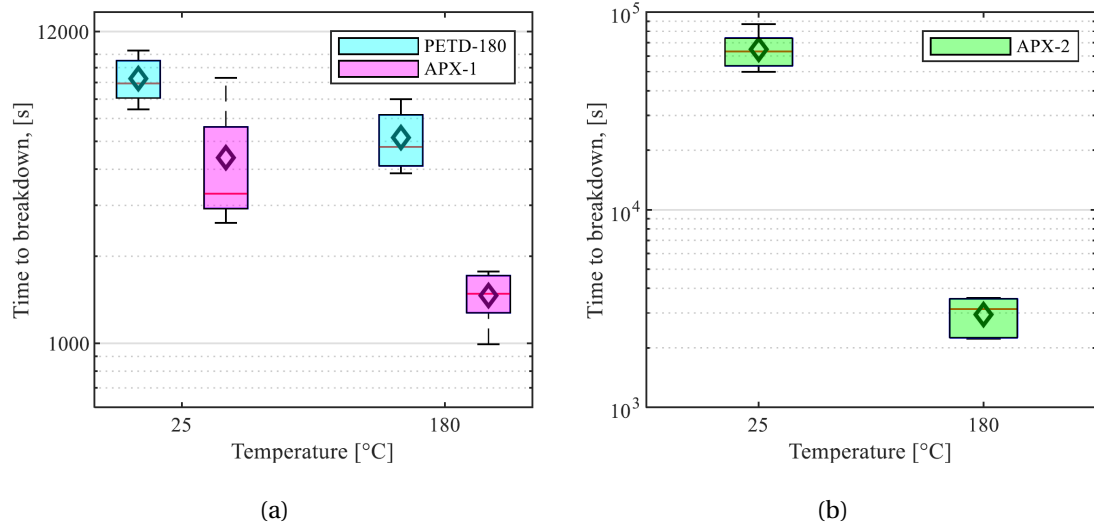


Figure IV.6: Time to breakdown of twisted pairs (a) and coils (b) under sinusoidal voltage: temperature effect.

The probability distribution was analysed by plotting probability distribution functions as previously shown. The lognormal and Weibull distributions seem appropriate for fitting the time to breakdown data distribution. The two-way ANOVA conducted on logarithms of times to breakdown shows the significance of temperature effect and difference in response between three tested winding wires.

The analysis of the Weibull distribution parameters show that increase in the heating of specimens accelerates the insulation deterioration, *e.g.*, the estimated shape parameter for the wire APX-1: $\hat{\beta} = 2.27$ at 25 °C and $\hat{\beta} = 6.74$ at 180 °C.

Moreover, the mean time to breakdown ratio K_{Tsin} is calculated for the twisted pairs and coils tested under sinusoidal voltage at two temperature levels (t_{25sin} at 25 °C and t_{180sin} at 180 °C):

$$K_{Tsin} = \frac{t_{25sin}}{t_{180sin}} \quad (IV.7)$$

Respectively to studied winding wires the ratios are the following:

$K_{Tsin}(\text{PETD} - 180) = 1.60$, $K_{Tsin}(\text{APX} - 1) = 3.00$ and $K_{Tsin}(\text{APX} - 2) = 22.01$. These ratios highlight the temperature effect, especially significant for the rectangular wire APX-2.

Long duration tests (especially in case of rectangular wire) at 25 °C provoked an ozone accumulation in the enclosed test chamber. Visible light blue deposits (products of decomposition of solid dielectric) called “frost-effect” in [6] and [7] have appeared on the enamel surface resulted from chemical reactions between the insulation and the aggressive ionized substances (ozone O_3 and nitrous oxide NO_x gases) produced by the discharges. This effect is shown in Figure IV.7. The longer was the test duration, the more marked was the “frost-effect”. In this case, the insulation deterioration may be caused by mainly two mechanisms: chemical reactions and direct physical attack by ion and elec-

tron bombardment provoking C-H bond scissions in the dielectric material.

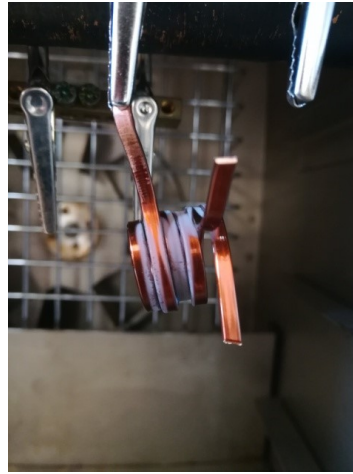


Figure IV.7: Photograph of the coil specimen after being tested at 5 kV RMS, $T = 25\text{ }^{\circ}\text{C}$.

The simultaneous heating in the thermal chamber at $180\text{ }^{\circ}\text{C}$ during endurance tests may cause ozone decomposition, weakening its impact on the insulation destruction. The “frost-effect” is less marked on the insulation surface. The impact of chemical attack could be less important in this case. Moreover, as reported in [8], increasing in temperature decreases the total energy of partial discharges weakening their effect. On the other hand, the rise in temperature leads to thermal ageing of insulation materials. According to Zhurkov’s thermo fluctuational theory [9], the breaking of chemical bonds in material occurs due to the energy of thermal fluctuations of atoms creating these bonds. Electrical and thermal stresses decrease the potential barrier and facilitate the bonds scissions.

As it can be seen from previous charts, both bent wires and twisted pairs of wire PETD-180 have been tested under sinusoidal voltage at 5 kV RMS while heating at $180\text{ }^{\circ}\text{C}$. That allows to compare the breakdown data as shown in Figure IV.8.

The mean time to breakdown ratio between two types of round sections wires’ specimens under sinusoidal voltage K_{SR} demonstrating their difference is equal to:

$$K_{SR} = \frac{t_{twist}}{t_{bent}} = 4.33 \quad (\text{IV.8})$$

where t_{twist} and t_{bent} are the mean times to breakdown of twisted pairs and bent specimens respectively. The time to breakdown of bent specimens is lower than the time demonstrated by twisted pairs. In the electrode system “wire-shot” the partial discharges occur between the enamel insulation layer and the grounded metal shot, whereas in twisted pair two enamel layers separate copper conductors slowing the destruction process. The twisted pair specimen’s type is kept for further tests.

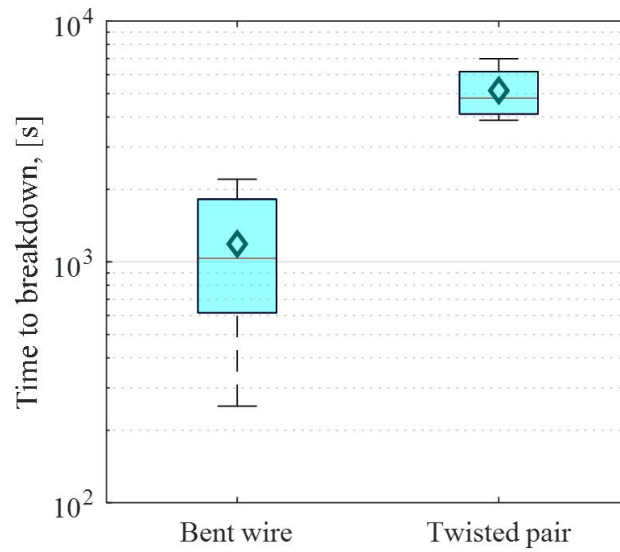


Figure IV.8: Time to breakdown of two specimens' types made of PETD-180 tested at 5 kV RMS, 180 °C.

3.2 Endurance tests under PWM impulse voltage: low dV/dt

First of all, this section presents endurance test results obtained on unimpregnated specimens (twisted pairs and coils) made of four studied winding wires. The effect of impregnating varnish was neglected as in previously described tests. The influence of thermal stresses and impulse voltage waveform is investigated. Then, we compare times to breakdown of two constructions of rectangular section winding wire specimens proposed in Chapter III.




The second part of this section gives an analysis of a “healing” of defects in the winding wires insulation by the impregnation. The time to breakdown is measured on different tested insulation systems “winding wire – impregnating varnish”. In this experiment, twisted pairs made of corona resistant wire having artificial defects impregnated by different compositions are exposed to PWM impulse voltage and thermal stress. The study is intended to reveal the effect of dielectric materials compatibility in the insulation system (turn insulation of electrical machine winding).

3.2.1 Tests on unimpregnated specimens

Experimental protocol

By analogy with previous tests performed under sinusoidal voltage, the endurance tests of winding wires subjected to electro-thermal stresses have been carried out under impulse PWM voltage. Table IV.4 gives the specimen's types and details experimental conditions. Please refer to Chapter III Section 3.4.2 for the description of voltage waveform parameters given in Table IV.4. The tests are conducted at normal atmospheric pressure and humidity $\phi = [15 \div 30]\%$ slightly varies during tests.

Table IV.4: Experimental protocol of endurance tests under PWM voltage with low dV/dt .

			
Specimens			
twisted pairs		coils	double coils
Winding wires			
PETD 2-K-180 (CR)	PETD-180 (CV)	APX-2 (CV)	APX-2 (CV)
PETD-180 (CV)	PETD-180 (CV)		
APX-1 (CV)	APX-1 (CV)		
Voltage waveform parameters			
<ul style="list-style-type: none"> · steady-state amplitude $V_a = 1.2$ kV · modulation frequency $f_m = 400$ Hz · carrier frequency $f_c = 5$ kHz 			
<ul style="list-style-type: none"> · overshoot voltage 			
$V_{os} = 900$ V	$V_{os} = 300$ V	$V_{os} = 900$ V	
<ul style="list-style-type: none"> · voltage edge 			
$dV/dt = 0.40$ kV/ μ s	$dV/dt = 0.18$ kV/ μ s	$dV/dt = 0.40$ kV/ μ s	
Temperature			
25 °C		25 °C	
100 °C			
180 °C	180 °C		180 °C
190 °C		180 °C	
200 °C			

With the objective to study the effect of repetitive surges on enamel insulation endurance, two impulse voltage waveforms (as described in Chapter III Section 3.4.2) are applied. Figure IV.9 provides both voltage waveforms.

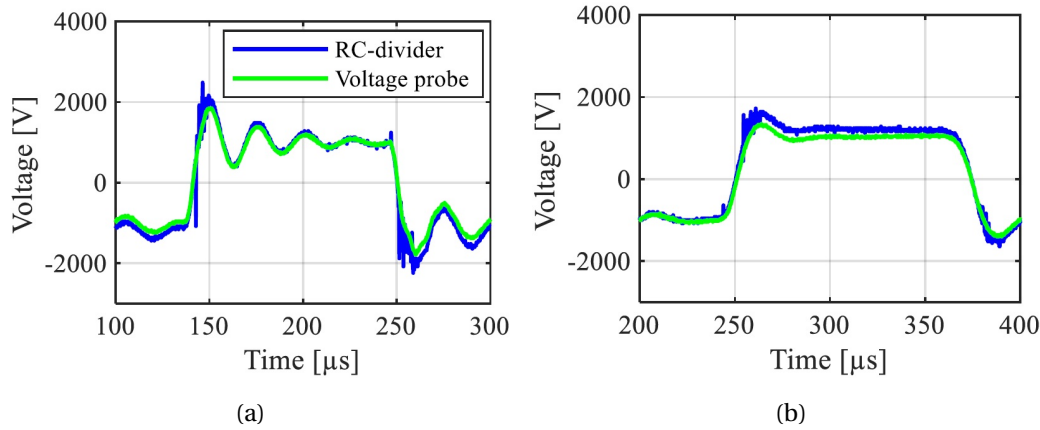


Figure IV.9: PWM impulse voltage waveform:
 (a) with surges $V_{os} = 900\text{V}$, (b) surges are limited $V_{os} = 300\text{V}$.

Experimental results and analysis

Experimental results corresponding to the experimental protocol given above are reported in Appendix IV-B and graphically shown in figures below.

Figure IV.10 gives the lifetime boxplot of four wires tested under impulse voltage with repetitive surges at five levels of temperature (five test repetitions). The corona resistant wire demonstrated outstanding endurance at 25 °C; tests were continued during several days. Thereby, only three repetitions were effectuated at this temperature level on the corona resistant winding wire.

According to the probability distribution functions analysis, the lognormal and Weibull distributions seem appropriate for fitting the time to breakdown data distribution. The two-way ANOVA conducted on logarithms of times to breakdown shows the significance of temperature effect. In these experimental conditions, two conventional winding wires PETD-180 and APX-2, demonstrate the insignificant difference in times to breakdown.

The analysis of the Weibull distribution parameters show that increase in the heating of specimens accelerates the insulation deterioration. It should be noticed that the values of time to breakdown are lower and shape parameters are higher for wires tested under the PWM impulse voltage compared to the results of endurance tests under sinusoidal voltage. The estimated shape parameter for and the wire APX-1: $\hat{\beta} = 13.91$ at 25 °C, and $\hat{\beta} = 12.00$ at 180 °C.

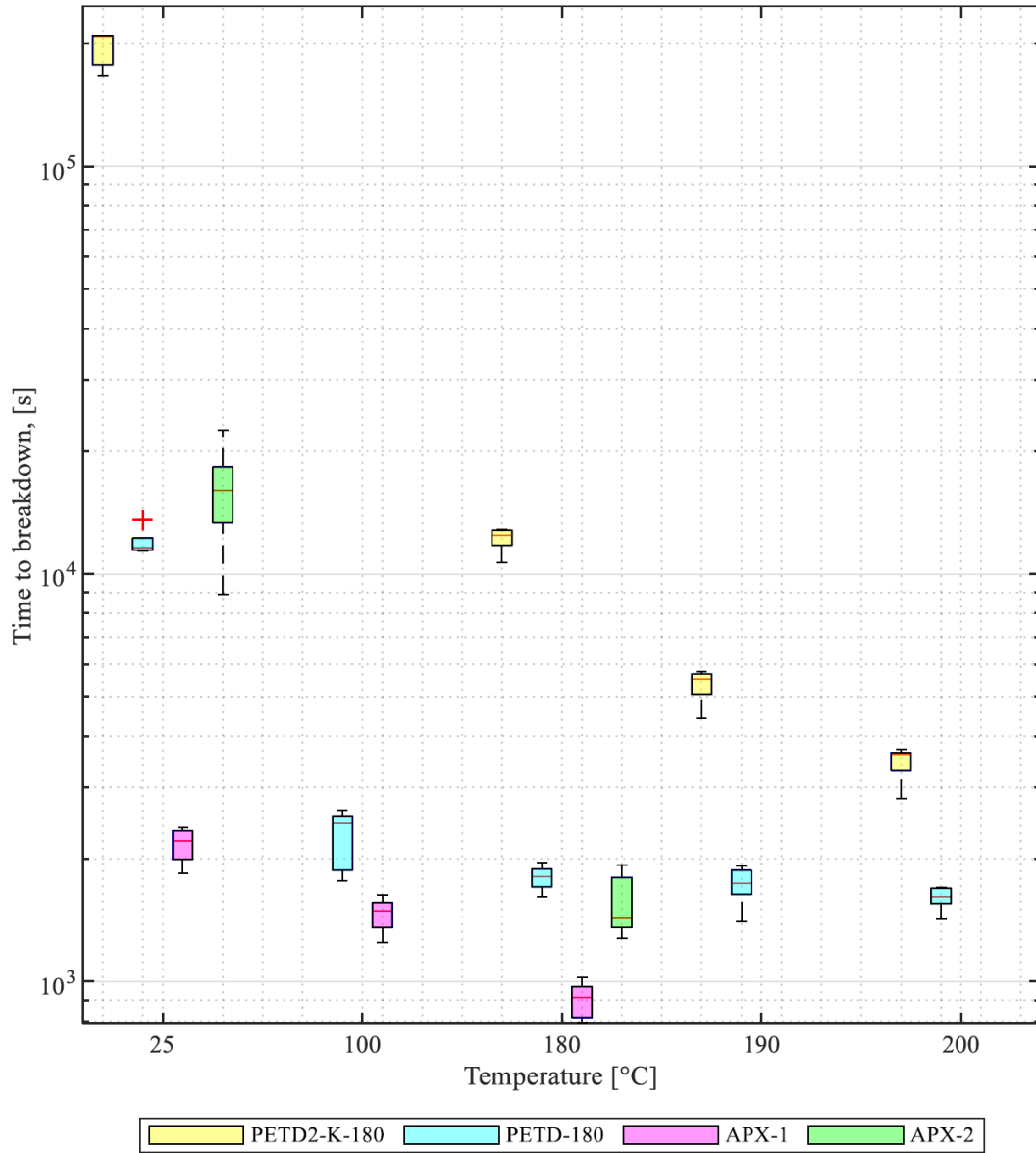


Figure IV.10: Time to breakdown of twisted pairs and coils under PWM impulse voltage with surges $V_{os} = 900$ V, $V_a = 1.2$ kV, $f_m = 400$ Hz, $f_c = 5$ kHz: temperature effect.

Thus, as in previous tests, we observe the decrease in lifetime with increasing temperature. The mean time to breakdown ratio $K_{T_{\mu s}}$ of twisted pairs and coils tested under impulse voltage with μs – level rise time at two temperature levels (at 25 °C $t_{25\mu s}$ and at 180 °C $t_{180\mu s}$) is equal to:

$$K_{T_{\mu s}} = \frac{t_{25\mu s}}{t_{180\mu s}} \quad (IV.9)$$

Respectively to studied winding wires the ratios are the following: $K_{T_{\mu s}}(\text{PETD2-K-180}) = 15.99$, $K_{T_{\mu s}}(\text{PETD-180}) = 6.66$, $K_{T_{\mu s}}(\text{APX-1}) = 2.40$, and $K_{T_{\mu s}}(\text{APX-2}) = 10.18$. As can be seen from the boxplot and the calculated ratios, the temperature effect is stronger marked for wires having better endurance comparing to others. The in-

Insulation with good resistance to electrical stresses and partial discharges will be less performant at increasing environmental temperature; the thermal ageing might be a critical factor accelerating the final insulation breakdown.

Figure IV.11 shows the lifetime box charts of wires tested under impulse voltage having overshoot and voltage edge $V_{os} = 900$ V, $dV/dt = 0.40$ kV/ μ s, compared to the same wires subjected to impulse voltage with lower parameters $V_{os} = 300$ V, $dV/dt = 0.18$ kV/ μ s. In order to accelerate the endurance tests, two conventional winding wires, PETD-180 and APX-1, have been subjected to the electro-thermal stresses, the temperature in the thermal chamber was set to 180 °C.

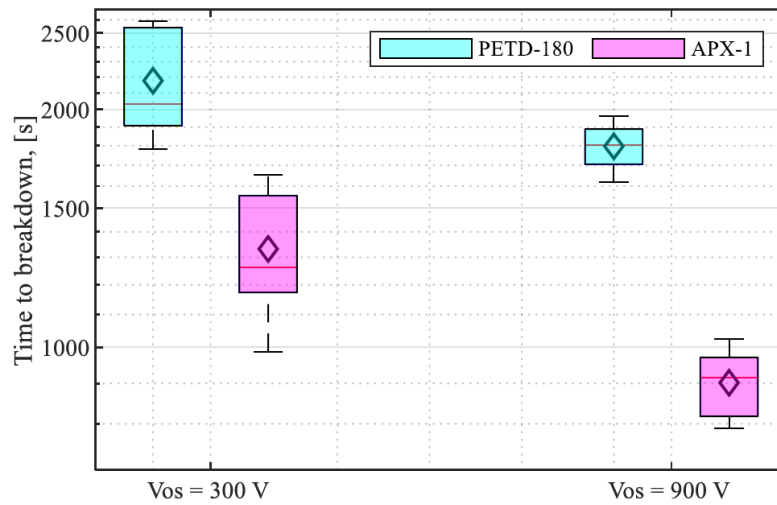


Figure IV.11: Time to breakdown of twisted pairs under PWM impulse voltage $V_a = 1.2$ kV, $f_m = 400$ Hz, $f_c = 5$ kHz with surges $V_{os} = 900$ V and when surges are limited $V_{os} = 300$ V: surge effect, $T = 180$ °C.

As expected, the decrease in the overvoltage and dV/dt increase the insulation lifetime; this factor causes the significant difference in times to breakdown according to ANOVA results. The mean time to breakdown ratio $K_{os\mu s}$ is equal to:

$$K_{os\mu s} = \frac{t_{300\mu s}}{t_{900\mu s}}, \quad (IV.10)$$

where $t_{300\mu s}$ and $t_{900\mu s}$ correspond to mean time to breakdown at lower overshoot ($V_{os} = 300$ V) and at higher overshoot ($V_{os} = 900$ V) respectively. The ratios are the following: $K_{os\mu s}(\text{PETD} - 180) = 1.21$ and $K_{os\mu s}(\text{APX} - 1) = 1.48$.

As described in Chapter III Section 3.2, two specimen's types are proposed for testing the rectangular section wire. The first specimen's configuration called single coil (or simply "coil"), represents a small coil made of two rectangular wire's pieces wound in parallel. In the second configuration called double coil, two pieces of wire are superimposed while winding creating contact on wires' wide sides. Figure IV.12 reports the lifetime box-plot of two specimens' configurations tested under PWM impulse voltage with surges and simultaneous heating at 180 °C.

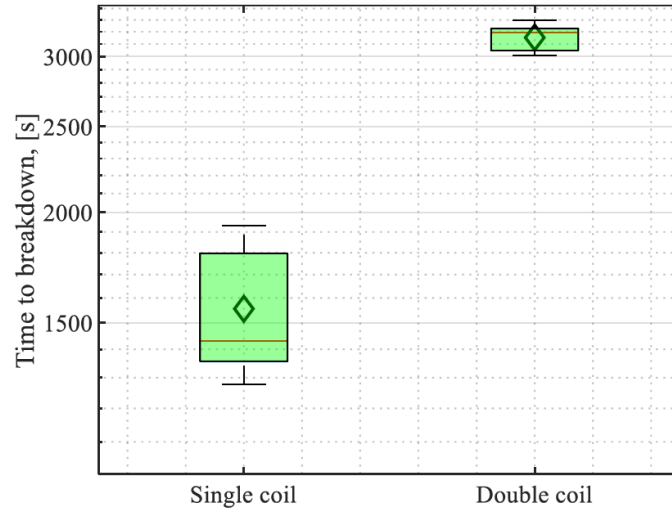


Figure IV.12: Time to breakdown of two specimens' types made of rectangular wire APX-2 under PWM impulse voltage with surges $V_{os} = 900$ V, $V_a = 1.2$ kV, $f_m = 400$ Hz, $f_c = 5$ kHz, $T = 180$ °C.

The mean time to breakdown ratio between two types of rectangular section wire's specimens K_{SC} is:

$$K_{SC\mu s} = \frac{t_{double}}{t_{single}} = 2.03, \quad (IV.11)$$

where t_{double} and t_{single} are the mean times to breakdown of twisted pairs and bent specimens respectively. The double coil specimens demonstrated higher endurance compared to single coils, that confirms by ANOVA results. In the double coil the contact areas (PDs activity zone) are larger, the electric field distribution is more uniform, that decreases the electric stress effect. Depending on a winding turns arrangement of studied electrical machine, the corresponding specimen type may be used to test the turn insulation. In this work, the single coil specimen type is selected for endurance tests.

Figure IV.13 gives photographs and microscopic images (taken through an optical microscope) of corona resistant wire's and conventional rectangular section wire's specimens. The "frost-effect" was observed on the enamel insulation surface after being tested under impulse voltage.

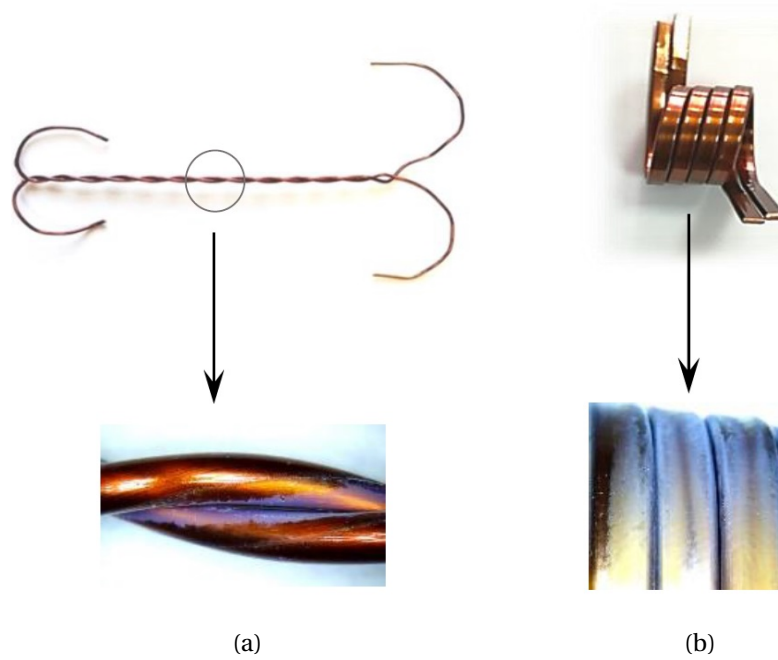


Figure IV.13: Views of specimens made of corona resistant wire PETD2-K-180 (a) and conventional wire APX-2 (b) after being tested under PWM impulse voltage with surges $V_{os} = 900 \text{ V}$, $V_a = 1.2 \text{ kV}$, $f_m = 400 \text{ Hz}$, $f_c = 5 \text{ kHz}$, $T = 180 \text{ }^\circ\text{C}$.

3.2.2 Influence of defects on turn insulation endurance

As shown in Chapter I, electrical machines failures generally occur because of winding insulation damages. One of the failure criterion may be the presence of defects within the insulation, such as impurities, voids and cuts reducing the insulation performance and service life. All things being equal, the greater the number of existing defects (“weakest-links”), the higher the probability of insulation failure. If there is a weak point (defect), which cannot carry the applied electric field, a complete breakdown will be initiated.

The term defectiveness λ (1/mm) is commonly used for a quantitative assessment of the insulation damage [10]. This characteristic defines the number of defects per unit of the winding wire length. These defects can exist in winding wires insulation in the delivered condition (defects in the delivered condition λ_D), occur during the production technology process (technology process defects λ_{TP}) and electrical machines operation (operational defects λ_{OP}) [10]. The total defectiveness for the entire period of the electrical machine service life can be determined as the sum:

$$\lambda = \lambda_D + \lambda_{TP} + \lambda_{OP} \quad (\text{IV.12})$$

Defects existing in the delivery condition and appearing during the windings manufacturing process may be “healed” due to the high quality impregnation of machine’s winding, *e.g.* VPI. In this case, the dielectric strength of the insulation’s damaged parts

recovers and provides the required endurance under operational factors. It is therefore very important to provide the most complete “healing” of such defects by impregnation. A relevant question is how effective is the defects “healing” by the impregnation when stressed by impulse voltage?

To answer this question, first of all, notion of turn insulation’s defects should be given more in detail. The defects “healing” quality depends on their type (point, ring, extended cut) and their location in the winding. Two types of defects, dependent and independent, are distinguished in turn insulation [11]. Dependent defects penetrating simultaneously in the structure “enamel insulation - impregnating varnish - enamel insulation” are considered as critical defects (see Figure IV.14).

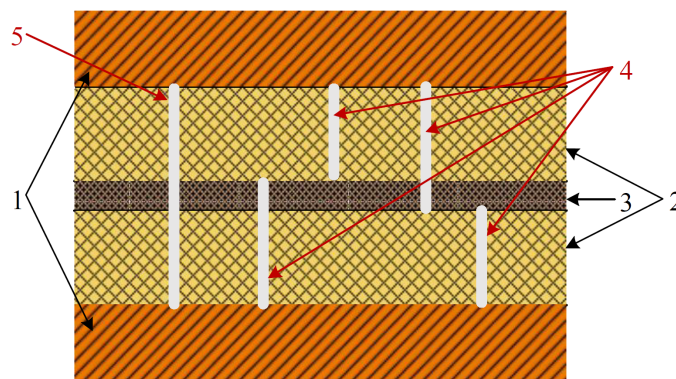


Figure IV.14: Possible defects in turn insulation system:
1 - copper conductors, 2 - enamel insulation, 3 - impregnating varnish,
4 - independent defects, 5 – dependent defect.

As shown in Figure IV.14, independent defects are the defects within insulation of one of conductors in contact. It may also be defects penetrating into the structure “enamel - impregnating varnish” during the insulation ageing. Such defects usually do not lead to a premature winding failure because the breakdown voltage of even aged low-voltage insulation exceeds the operating voltage and eventual surges in electrical machines operating at AC sinusoidal voltage of 50 Hz.

Closely located defects within adjacent winding turns may be also critical for insulation system endurance. In this case, a short circuit associated with the effect of spark discharges in defective areas during switching operations (electrical machine’s run and stop) may probably occur due to switching overvoltage pulses. These spark discharges and insulation impurities in defective areas provoke an increase in leakage current and local overheating. As a result, the insulation flashover voltage decreases in the defective areas. Finally, it leads to a sustainable spark discharge appearing under operating voltage, *i.e.*, the insulation system failure.

The described failure mechanism is characteristic for sinusoidal supply voltage. The endurance tests have been performed with the objective to examine the failure mech-

anism and the effectiveness of defects “healing” by the impregnation when stressed by impulse voltage.

Experimental protocol

The experimental procedure includes a particular specimens’ preparation. Specimens with artificial defects were made of corona resistant wire PETD2-K-180. The enamel insulation was damaged by an independent ring defect on one of the turns (ring cutting of enamel insulation until reaching a conductor) as shown in Figure IV.15.

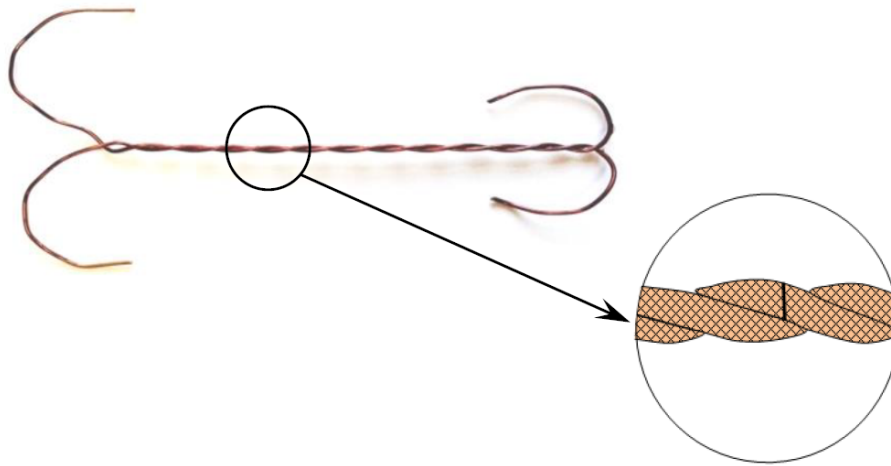


Figure IV.15: Twisted pair having a ring defect on the one turn.

The prepared twisted pairs were impregnated by dipping into the varnish (or compound), in particular, the organic-silicone varnish (KO-916K), the polyether compound modified by organic-silicone resins (KP-55-5), and the compound based on oligo-ether-acrylates (KP-50). The specimens were dipped into a bath contained impregnating varnish during 20 seconds and drained for a certain time at room temperature. Then the specimens were subjected to a two-stage curing process. Firstly, curing was carried out in a convection oven at the temperature of a varnish solvent evaporation ($110 \pm 5^\circ\text{C}$) during one hour, and, secondly, at the temperature of a varnish solid base polymerization ($200 \pm 5^\circ\text{C}$) during 12 hours.

Then, the specimens are stressed under PWM impulse voltage with surges at 180°C till the breakdown. The partial discharge activity is observed during the tests.

Experimental results and analysis

Figure IV.16 shows the lifetime boxplot of defective specimens impregnated by different varnishes compared to non-defective specimens of corona resistant wire tested before. The time to breakdown data is also given in Appendix IV-C. The presence of defects in the enamel insulation, even on one turn (independent defect), leads to the endurance reduction (Figure IV.16 B and C).

The mean time to breakdown ratio showing the influence of defects on insulation lifetime $K_{def\mu s}$ is equal to:

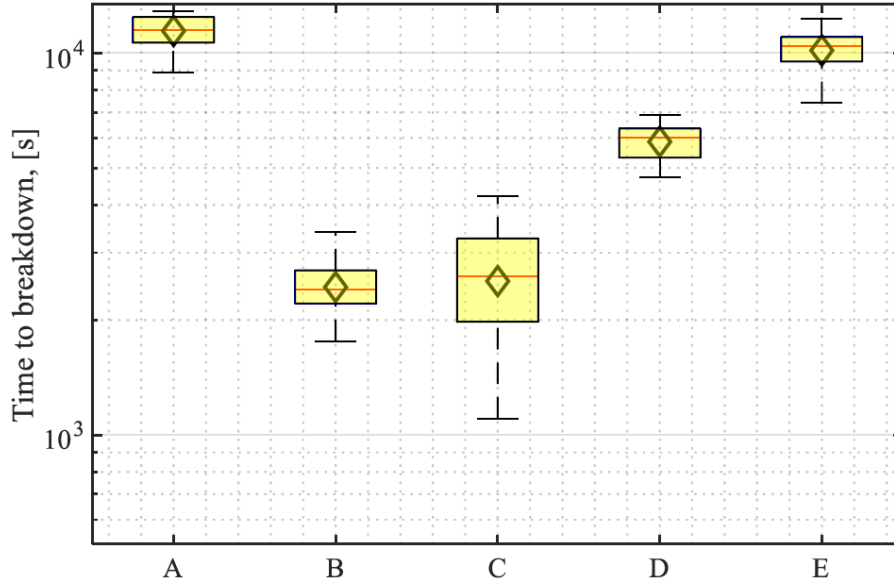


Figure IV.16: Time to breakdown of twisted pairs made of CR wire tested under PWM impulse voltage with surges $V_{os} = 900$ V, $V_a = 1.2$ kV, $f_m = 400$ Hz, $f_c = 5$ kHz, $T = 180$ °C:

- A – non-defective unimpregnated specimens, B – defective unimpregnated specimens,
- C – defective specimens impregnated by organic-silicone varnish,
- D – defective specimens impregnated by polyether compound modified by organic-silicone resins;
- E – defective specimens impregnated by compound based on oligo-ether-acrylates.

$$K_{def\mu s} = \frac{t_{nondef\mu s}}{t_{def\mu s}} = 4.68, \quad (IV.13)$$

$t_{nondef\mu s}$ and $t_{def\mu s}$ are the mean times to breakdown of non-defective unimpregnated specimens and unimpregnated specimens having independent defects respectively. This ratio shows that the presence of defects within the enamel insulation considerably decreases its endurance when subjected to impulse voltage.

Insulation breakdown occurs in insulation defective area at almost all tested specimens as shown in Figure IV.17. On the basis of the obtained results it should be noted, that when applying the impulse voltage, partial discharges incepted in local independent defects lead to accelerated destruction of undamaged enamel insulation on the second turn. The model of destruction mechanism is proposed in Figure IV.18.

In order to evaluate the effect of defects “healing” the mean time to breakdown ratio for studied impregnating composition $K_{heal\mu s}$ is calculated:

$$K_{heal\mu s} = \frac{t_{impr\mu s}}{t_{def\mu s}}, \quad (IV.14)$$

$t_{impr\mu s}$ is the mean time to breakdown of defective specimens impregnated by different compositions. The ratios are the following: $K_{heal\mu s}(KO - 916) = 1.04$, $K_{heal\mu s}(KP - 55 - 5) = 2.40$ and $K_{heal\mu s}(KP - 50) = 4.16$.

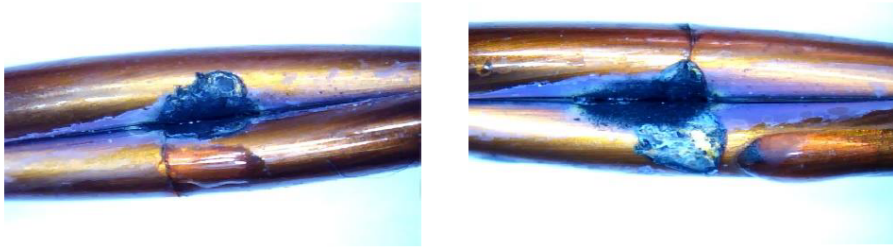


Figure IV.17: Views of twisted pairs' insulation breakdown in defective area.

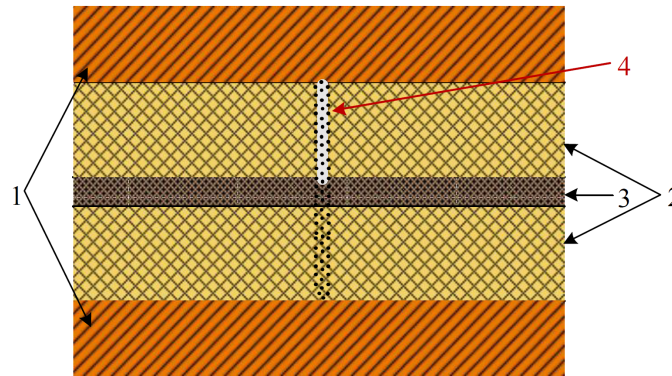


Figure IV.18: Model of turn insulation destruction mechanism in presence of partial discharges: 1 - copper conductors, 2 - enamel insulation, 3 - impregnating varnish, 4 - PDs in defective area .

Figure IV.16 as well as calculated $K_{def\mu s}$ and $K_{heal\mu s}$ show that in most cases, the mean time to breakdown of non-defective specimens was higher than if the specimen had a defect despite the impregnation. The utilization of the organic-silicone varnish does not provide sufficient defects “healing”; the lifetime almost does not change compared to unimpregnated defective specimens (Figure IV.16 C). According to ANOVA results, the two groups of specimens B and C shown in Figure IV.16 have not significant difference in times to breakdown. Thus the winding impregnation may not provide sufficient “healing” of defects when insulation subjected to electro-thermal stresses, typical for inverter-fed motors.

On the other hand, a significant lifetime raise is provided by the impregnation using compounds (Figure IV.16 D and E). Therefore, among the investigated impregnating compositions, the “healing” effect of defects within enamel insulation may be provided by the impregnating compound based on oligomers. The groups of specimens A and E shown in Figure IV.16 have not significant difference in times to breakdown. The solidified compound’s film has lower shrinkage and greater thickness compared to varnishes that provide better resistance to electro-thermal stresses, increasing the insulation system lifetime. Taking into account that the endurance tests have been performed at $T = 180^{\circ}\text{C}$, it can be noted that this compound may provide a good impregnating quality with thermal ageing.

As discussed in Chapter I Section 4.3, the compatibility of impregnating compositions and winding wires enamel insulation plays an important role in insulation system reliability. In this regard, the quality of defects “healing” will also depend on the compatibility of insulating materials.

To sum up, it should be noted that even mismatched (independent) defects of winding wires critically affect the turn insulation lifetime in inverter-fed motors. The defects within the insulation create weak spots facilitating the PDs inception which is detrimental to low voltage insulation. The winding wires having low defectiveness as well as impregnating compositions having compatible chemical and physico-mechanical properties, should be used in order to obtain the insulation system with minimum defects.

3.3 Endurance tests under rectangular impulse voltage: high dV/dt

With the objective to investigate the effect of high dV/dt impulse voltage, winding wires endurance tests have been carried out using the designed SiC-based pulse generator. The full bridge inverter configuration is used to apply bipolar impulse voltage on the tested specimens. As it was noted in Chapter III, the parameters of the generated voltage pulses such as the impulse amplitude, the switching frequency and the duty cycle are adjustable. Therefore, the effects of impulse voltage amplitude and frequency on the insulation lifetime are studied in present endurance tests. Moreover, the winding wires were also subjected to thermal stresses simultaneously with the electrical stresses.

Experimental protocol

Table IV.5 gives the tested specimen’s types and details experimental conditions. The tests are conducted at normal atmospheric pressure and humidity $\phi = [15 \div 30]\%$ slightly varies during tests. Figure IV.19 recalls the voltage waveform applied to the specimens (measured on the twisted pair put into the thermal chamber). The use of cable between inverter output and specimen input creates surges up to 500 V.

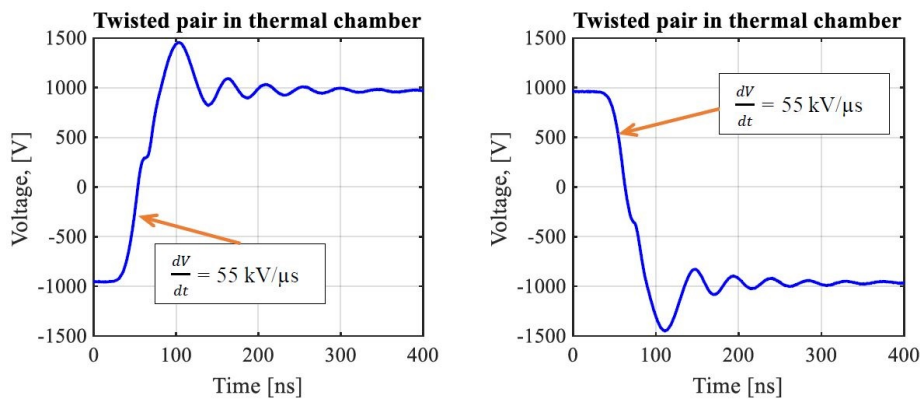




Figure IV.19: Rectangular impulse voltage waveform having high dV/dt .

Table IV.5: Experimental protocol of endurance tests under rectangular impulse voltage with high dV/dt .

					
Specimens					
twisted pairs			coils		
Winding wires					
PETD 2-K-180 (CR)		PETD-180 (CV) APX-1 (CV)		APX-2 (CV)	
Voltage waveform parameters					
<ul style="list-style-type: none"> · DC bus voltage $V_{dc} = [1.0; 1.2; 1.4]$ kV · overshoot voltage $V_{os} = 500$ V <ul style="list-style-type: none"> · duty cycle $\alpha = 50\%$ · voltage edge $dV/dt \geq 55$ kV/μs · switching frequency 					
$f_s = 20$ kHz	$f_s = 50$ kHz	$f_s = 20$ kHz	$f_s = 50$ kHz	$f_s = 20$ kHz	$f_s = 50$ kHz
Temperature					
25 °C	25 °C	25 °C		25 °C	25 °C
		100 °C		100 °C	
180 °C		180 °C	180 °C	180 °C	180 °C

Experimental results and analysis

The time to breakdown data of studied winding wires obtained in different combinations of electrical and thermal stresses are reported in Appendix IV-D and shown by box charts below.

Figure IV.20 shows the effect of simultaneous heating of specimens lifetime tested under impulse voltage with high dV/dt , DC bus voltage $V_{dc} = 1.2$ kV and switching frequency $f_s = 20$ kHz at three levels of temperature.

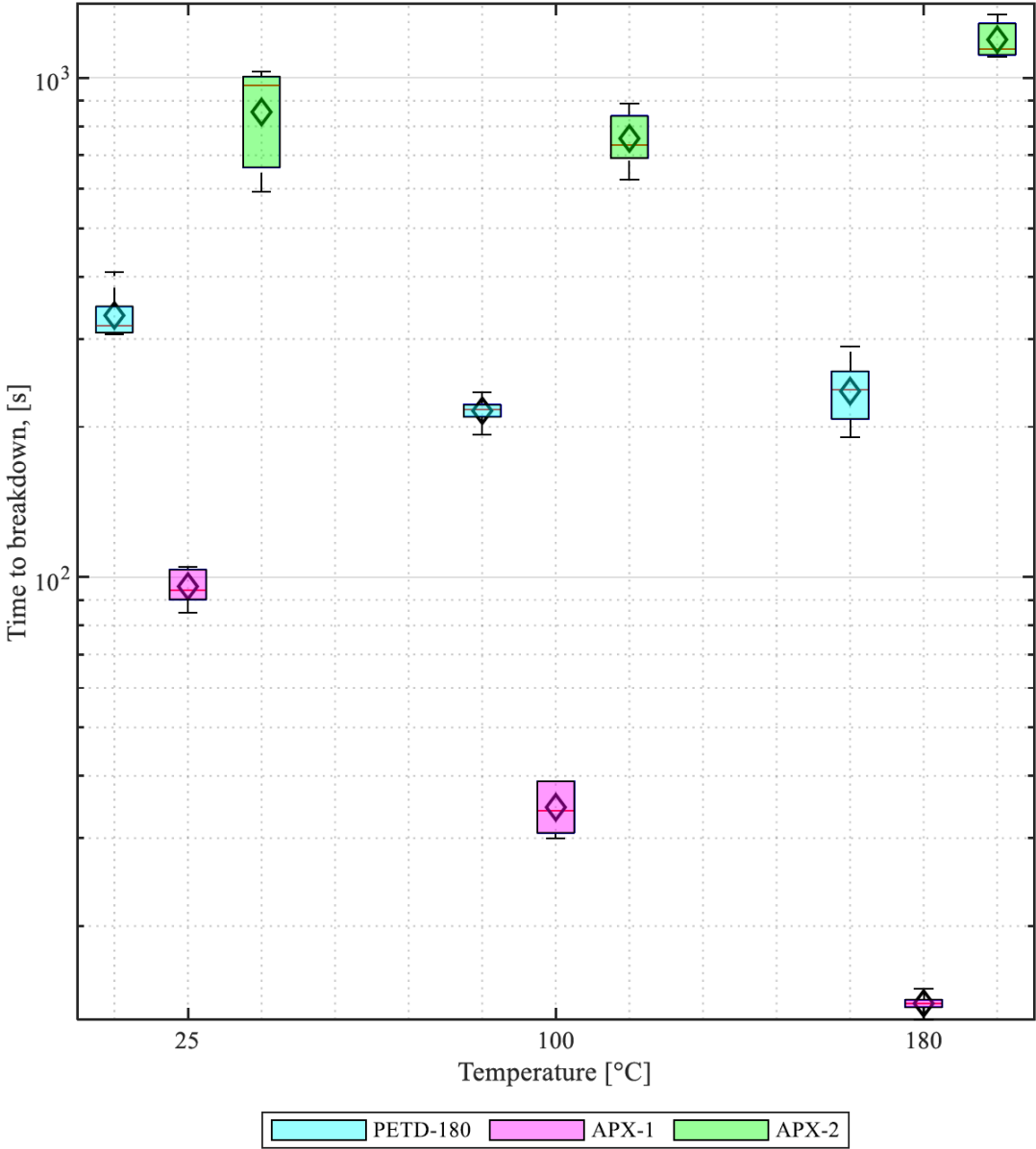


Figure IV.20: Time to breakdown of twisted pairs and coils under impulse voltage with high dV/dt , $V_{dc} = 1.2$ kV, $f_s = 20$ kHz: effect of temperature.

For better understanding of acquired data, the time to breakdown ratios were calculated by analogy with the previous tests. The mean time to breakdown ratio K_{Tns} of twisted pairs and coils tested under impulse voltage with ns – level rise time ($V_{dc} = 1.2$ kV, $f_s = 20$ kHz) at two temperature levels: at 25 °C t_{25ns} and at 180 °C t_{180ns}) is equal to:

$$K_{Tns} = \frac{t_{25ns}}{t_{180ns}} \quad (IV.15)$$

Respectively to studied winding wires the ratios are the following:

$$K_{Tns}(\text{PETD} - 180) = 1.42, K_{Tns}(\text{APX} - 1) = 6.84, \text{ and } K_{Tns}(\text{APX} - 2) = 0.72.$$

The conventional wire APX-1 demonstrated the decrease of lifetime with the temperature increasing that is in line with expectations. However, the other conventional wires, PETD-180 and APX-1, did not followed the same trend showing the mean time to breakdown at 100 °C lower than at 180 °C. In case of wires having better endurance and thermal stability, the environmental temperature may be not the determining factor limited the insulation lifetime when subjected to high dV/dt impulse voltage. Electrical stresses and partial discharges become the detrimental factors. The breakdown time data of corona resistant wire had not been acquired in these conditions because the time span required to have a complete data set exceeded the day duration.

Figures IV.21, IV.22, IV.23 and IV.24 report the lifetime of each studied winding wire tested at different combinations of electrical and thermal stresses. These combinations are obtained by varying the following parameters: three levels of DC bus voltage V_{dc} , two levels of switching frequency f_s , and two levels of temperature T . The time to breakdown ratios of studied wires showing effects of voltage K_{Vns} , temperature K_{Tns} and switching frequency K_{fsns} , are calculated according to (IV.15, IV.16 and IV.17) and reported in Table IV.6.

$$K_{Vns} = \frac{t_{1.0ns}}{t_{1.4ns}} \quad (IV.16)$$

$$K_{fsns} = \frac{t_{20ns}}{t_{50ns}} \quad (IV.17)$$

Where $t_{1.0ns}$ and $t_{1.4ns}$ are mean times to breakdown corresponding to DC bus voltage of 1.0 and 1.4 kV; t_{20ns} and t_{50ns} are mean times to breakdown corresponding to switching frequencies of 20 and 50 kHz respectively. The test conditions are detailed in Table IV.6.

Among tested winding wires, the corona resistant one shown the best endurance with the highest times to breakdown, especially at lower voltage amplitude. However, the performance of this wire is limited and decreases remarkably when the voltage amplitude and the switching frequency increase.

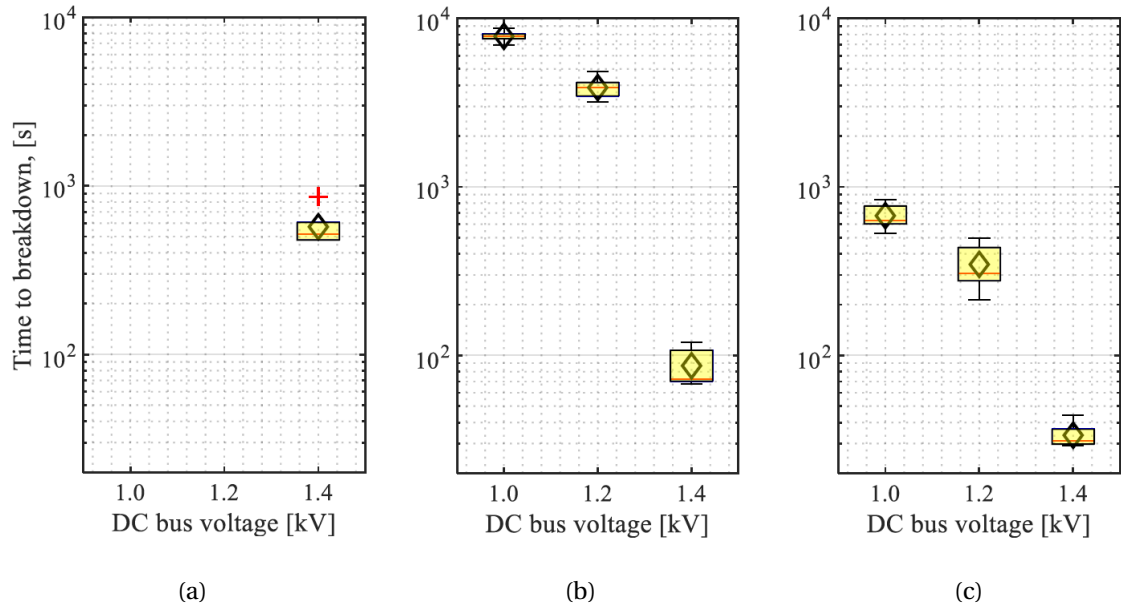


Figure IV.21: Time to breakdown of twisted pairs made of PETD2-K-180 (CR) under impulse voltage with high dV/dt :
 (a) $f_s = 20$ kHz, $T = 25$ °C; (b) $f_s = 20$ kHz, $T = 180$ °C; (c) $f_s = 50$ kHz, $T = 25$ °C.

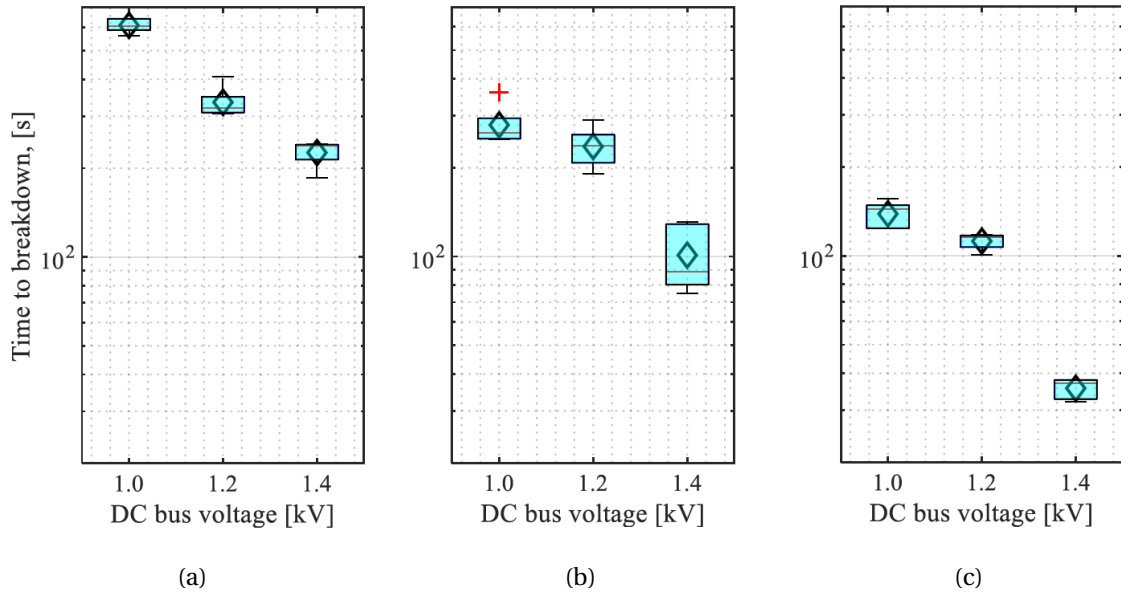


Figure IV.22: Time to breakdown of twisted pairs made of PETD-180 (CV) under impulse voltage with high dV/dt :
 (a) $f_s = 20$ kHz, $T = 25$ °C; (b) $f_s = 20$ kHz, $T = 180$ °C; (c) $f_s = 50$ kHz, $T = 25$ °C.

The rectangular winding wire APX-2 demonstrates a good endurance comparing to other conventional wires, especially when the stresses are increased. As to the conventional wire APX-1, its lifetime is very low under high dV/dt impulse voltage, that complicates the analysis of factors effect, but it also means that this wire (insulation composition) should not be used for electrical machines operating in such conditions. In general, the box plot charts and the time to breakdown ratios highlight the significance of impulse

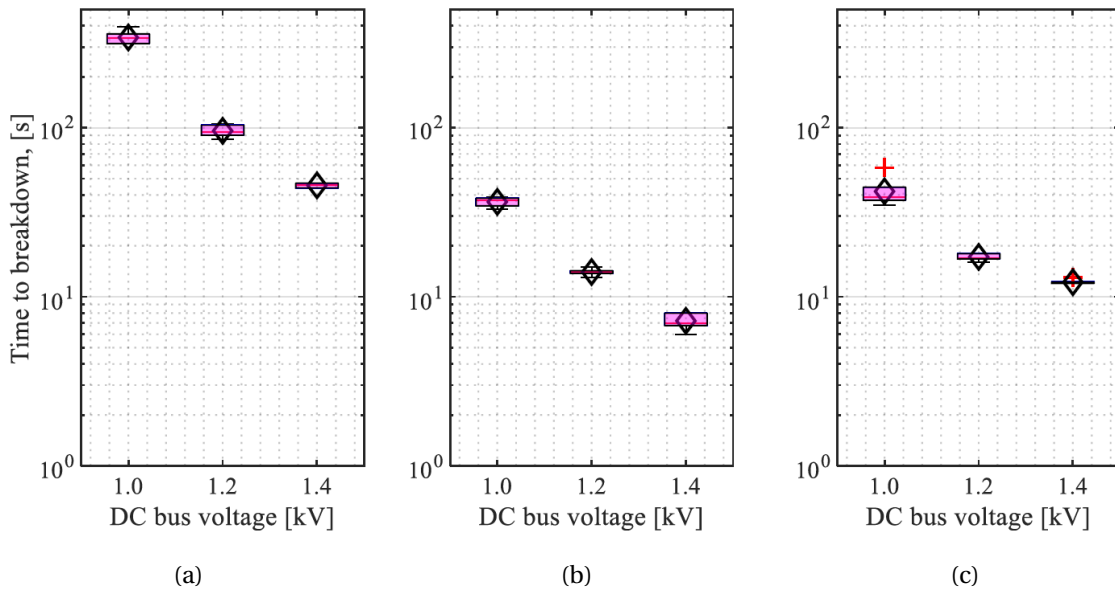


Figure IV.23: Time to breakdown of twisted pairs made of APX-1 (CV) under impulse voltage with high dV/dt :

(a) $f_s = 20$ kHz, $T = 25$ °C; (b) $f_s = 20$ kHz, $T = 180$ °C; (c) $f_s = 50$ kHz, $T = 25$ °C.

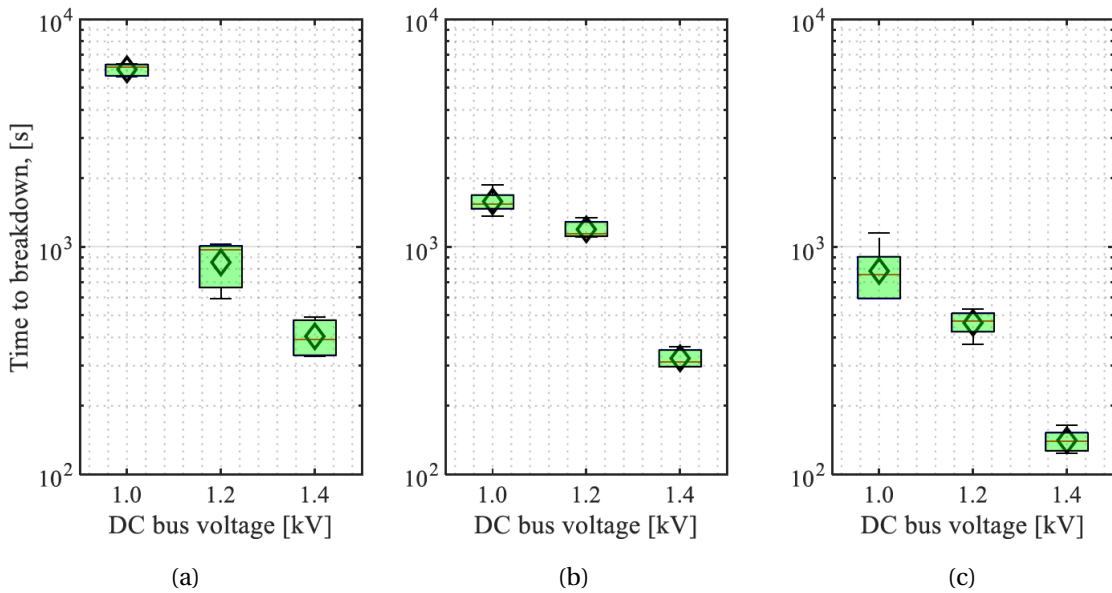


Figure IV.24: Time to breakdown of coils made of APX-2 (CV) under impulse voltage with high dV/dt :

(a) $f_s = 20$ kHz, $T = 25$ °C; (b) $f_s = 20$ kHz, $T = 180$ °C; (c) $f_s = 50$ kHz, $T = 25$ °C.

voltage parameters variation, dominating the thermal stresses created by heating in the thermal chamber.

The analysis of probability plots shows that the lognormal and Weibull distributions may be appropriate for fitting the time to breakdown distribution for all tested wires and experimental conditions. The estimated shape parameter $\hat{\beta} > 1$ for all factors combinations, that means that the failure rate increases with time. The analysis of variance

Table IV.6: Time to breakdown ratios of studied wires depending on test conditions.

Winding wires	Test conditions			Time to breakdown ratio
	V_{dc} , kV	f_s , kHz	T , °C	
PETD2-K-180 (CR)	1.0 and 1.4	20	180	90.05
	1.4	20	25 and 180	6.58
	1.4	20 and 50	25	16.99
PETD-180 (CV)	1.0 and 1.4	20	180	2.76
	1.4	20	25 and 180	2.24
	1.4	20 and 50	25	6.34
APX-1 (CV)	1.0 and 1.4	20	180	5.06
	1.4	20	25 and 180	6.33
	1.4	20 and 50	25	3.74
APX-2 (CV)	1.0 and 1.4	20	180	4.89
	1.4	20	25 and 180	1.25
	1.4	20 and 50	25	2.87

reveals the significance of all the factors. More tests with greater test repetition number should be done in order to determine which of these factors has the most significant effect on ageing acceleration. This analysis is complicated by the electrical and thermal stresses interaction.

Microscopic images of broken specimens in Figures IV.25, IV.26 and IV.27 show the impact of thermal and electrical stresses on enamel insulation degradation depending on test conditions. The “frost effect” can be observed on the enamel surface at lower voltage amplitude ($V_{dc} = 1.0$ kV and $V_{dc} = 1.2$ kV, $f_s = 50$ kHz). However, when electrical stress reached critical values ($V_{dc} = 1.4$ kV, $f_s = 50$ kHz), the enamel insulation was severely damaged, effects of carbonization and sticking of turns is observed. This destruction process in most cases was very fast and lasted 30-50 s before the breakdown occurred. As noted below, the damage is more severe in the central part of the broken specimen (Figure IV.25) and it has a thermal breakdown nature. The insulation thermal run away issued not from external heating but under high frequency pulses. The insulation destruction process will be discussed more in details in Chapter V. It should be noted, that in this case, the insulation defects might not play such an important role in insulation breakdown as during the tests under low dV/dt impulse voltage.

Considering the drastic destruction in such short terms, dielectrics ageing might be caused by both the partial discharges and the fast rising of dielectric losses. The high ozone concentration, high visible and UV range radiation have been observed during the endurance tests indicating a high level of PD activity. As far as, the effect of significant temperature increase of tested specimens has been revealed in these conditions, the temperature measurements were performed.

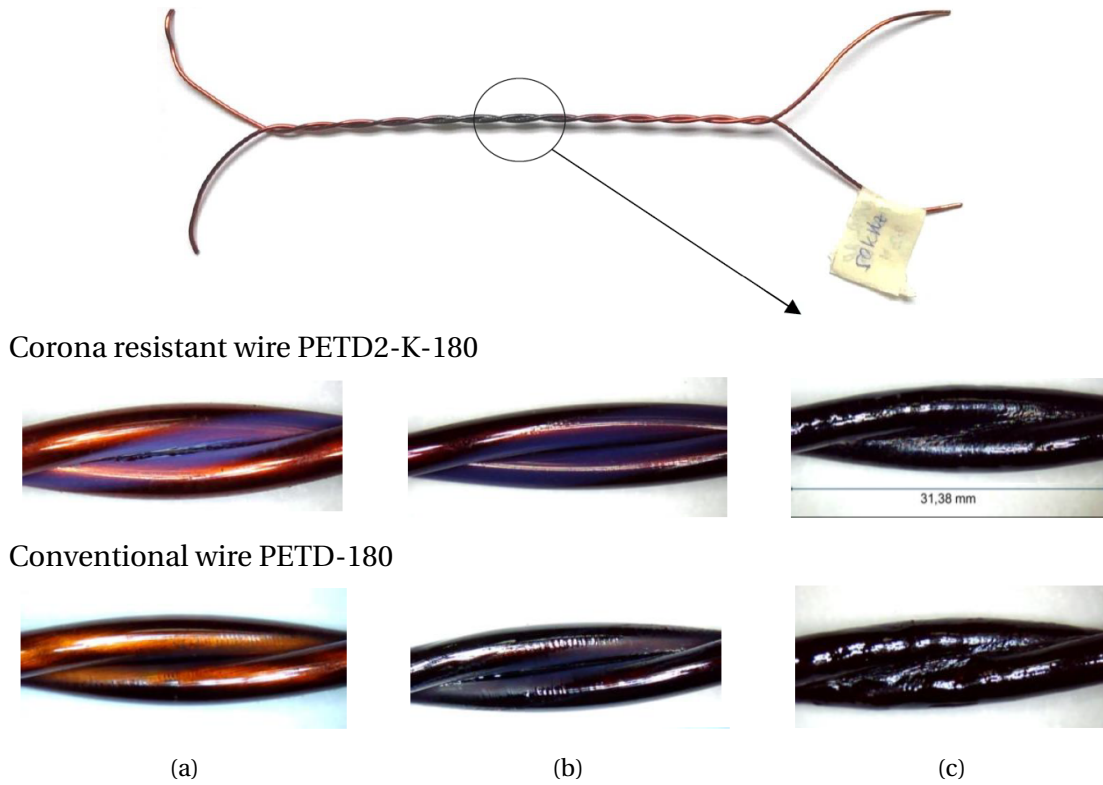


Figure IV.25: Winding wires' photograph and microscopic images after testing under high dV/dt impulse voltage, $T=25^{\circ}\text{C}$, $f_s = 50\text{ kHz}$: (a) $V_{dc} = 1\text{ kV}$; (b) $V_{dc} = 1.2\text{ kV}$ and (c) $V_{dc} = 1.4\text{ kV}$.

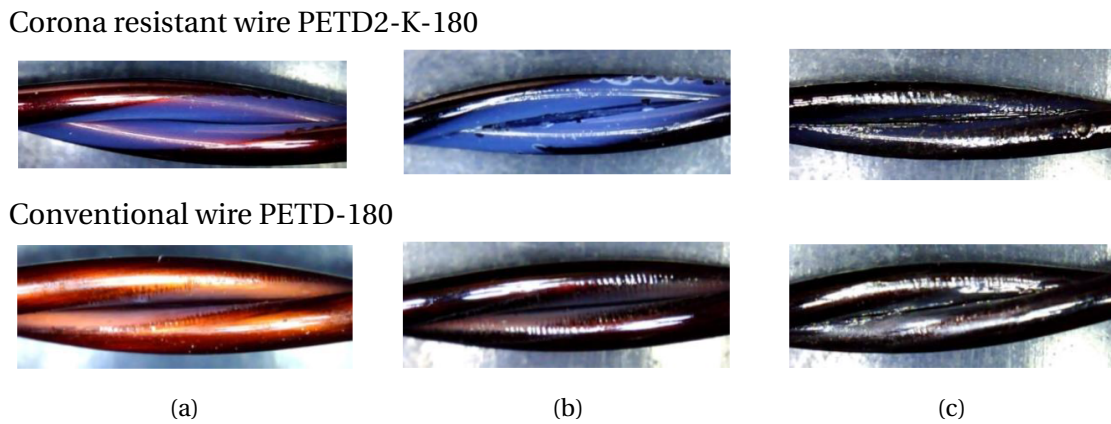


Figure IV.26: Winding wires' microscopic images after testing under high dV/dt impulse voltage, $T=180^{\circ}\text{C}$, $f_s = 20\text{ kHz}$: (a) $V_{dc} = 1\text{ kV}$; (b) $V_{dc} = 1.2\text{ kV}$ and (c) $V_{dc} = 1.4\text{ kV}$.



Figure IV.27: Microscopic images of rectangular winding wire after testing under high dV/dt impulse voltage, $T=180^{\circ}\text{C}$, $f_s = 20\text{ kHz}$, $V_{dc} = 1.2\text{ kV}$.

4 Thermal imaging study

The thermal imaging method can be used as PD sensing method showing local heating (hot spots) of electrical equipment resulted from partial discharges currents [12]. However, this method has a limitation due to relatively low temperatures of PDs. In the present study an infrared camera is used with the objective to compare the thermal radiation of specimens subjected to sinusoidal and impulse voltage.

The specimens' temperature in presence of partial discharges is evaluated by means of the infrared camera FLIR E50 having two temperature ranges $[-20\text{ }^{\circ}\text{C}$ to $120\text{ }^{\circ}\text{C}$] and $[0\text{ }^{\circ}\text{C}$ to $650\text{ }^{\circ}\text{C}]$, and an accuracy of $\pm 2\text{ }^{\circ}\text{C}$. The measurements of hot spots have been carried out at the distance of one meter, ambient temperature was generally of $25\text{ }^{\circ}\text{C}$. The PDs activity has been detected by means of electron-optical defectoscope and antenna [see Chapter III Section 3.5]. As a result of measurements performed on specimens made of corona resistant wire and conventional rectangular wire, combined thermal images and photographs have been obtained as shown in Figure IV.28 and Figure IV.29. The results of temperature measurements (five repetitions), the mean value and standard deviation of the hot spots on the surface of tested twisted pairs and coils are given in Appendix IV-E and mean values are shown in Figure IV.30.

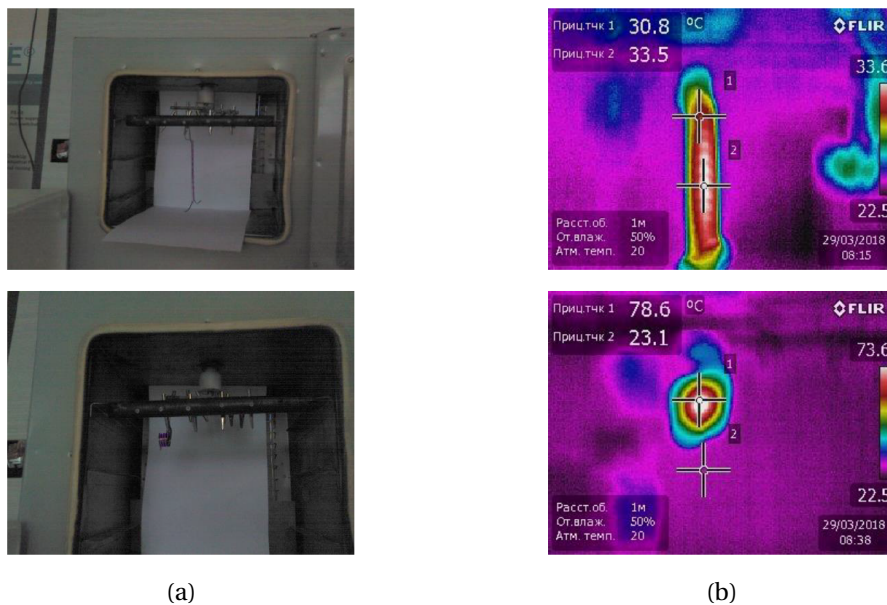


Figure IV.28: Photographs (a) and thermal images (b) of twisted pair and coil tested under PWM-like low dV/dt impulse voltage at $V_a = 1.2\text{ kV}$ and $f_c = 5\text{ kHz}$

At the voltage value below the PDIV, the specimen's temperature practically does not change. When the voltage is increased, the inception of partial discharges results in local shunts between adjacent turns in twisted pairs and in coils; the insulation is heated by PDs. During the experiment, the electrical stresses were applied during a few minutes until the temperature level remained almost unchanged and it was taken as a result. At

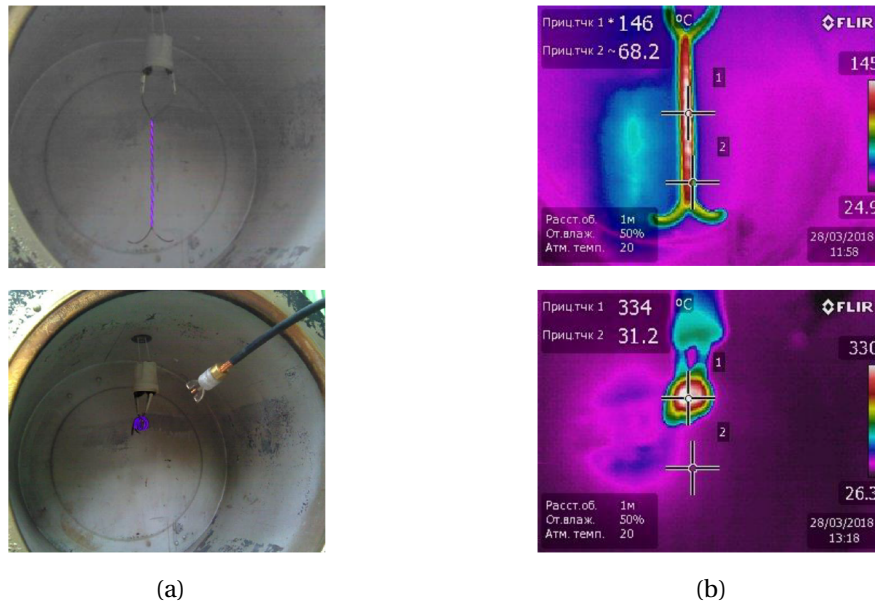


Figure IV.29: Photographs (a) and thermal images (b) of twisted pair and coil tested under high dV/dt impulse voltage at $V_{dc} = 1.4$ kV and $f_s = 50$ kHz

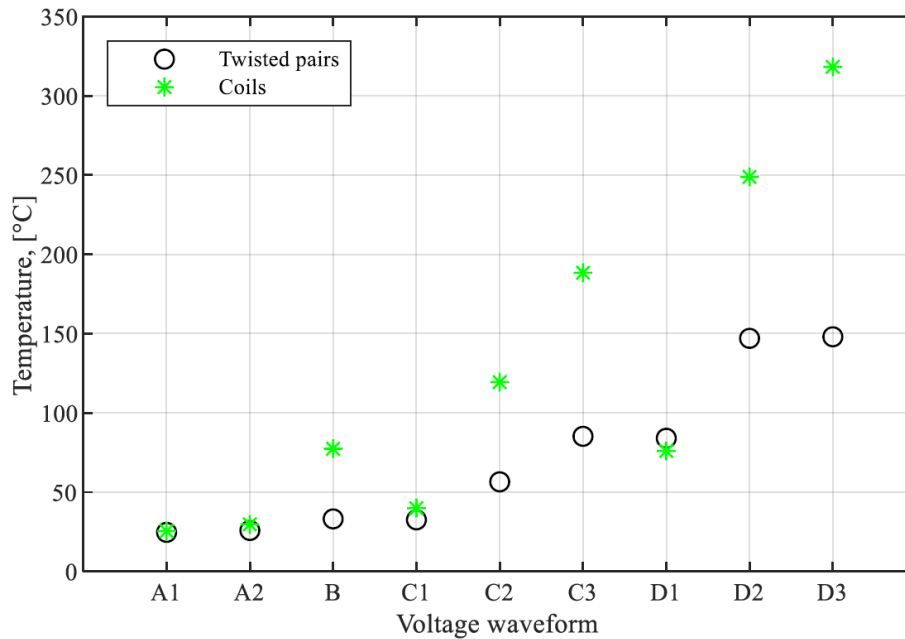


Figure IV.30: Temperature of twisted pairs and coils tested under different voltage waveforms:
 A1 – sinusoidal voltage, 50 Hz, 3 kV RMS; A2 - sinusoidal voltage, 50 Hz, 5 kV RMS;
 B – low dV/dt impulse voltage, 5 kHz 1.2 kV; C1 – high dV/dt impulse voltage 20 kHz, 1.0 kV;
 C2 – high dV/dt impulse voltage 20 kHz, 1.2 kV; C3 – high dV/dt impulse voltage 20 kHz, 1.4 kV;
 D1 – high dV/dt impulse voltage 50 kHz, 1.0 kV; D2 – high dV/dt impulse voltage 50 kHz, 1.2 kV;
 D3 – high dV/dt impulse voltage 50 kHz, 1.4 kV.

high electrical stress levels, the measurements correspond to the temperature immediately prior to the specimens' insulation breakdown. It should be noted that the partial discharges activity was detected immediately after application of voltage.

A slight temperature rise of twisted pairs and coils was observed during the tests at sinusoidal voltage, despite the partial discharge activity. While the impulse voltage test shows the more significant increase in temperature. It is particularly remarkable for rectangular wire specimens, where discharges are concentrated in a small volume and heat transfer is worse than in twisted pairs. In high dV/dt tests, the rise in voltage amplitude and especially in switching frequency had a significant effect on the tested specimens' rapid heating. The increase in frequency leads to an increase in the number of partial discharge repetition rate, and the total energy thereof is increased. The time to enamel insulation breakdown is also significantly reduced.

In this experiment, dielectric heating occurs as a result of PDs activity and depends on their intensity and energy, which in turn is determined by the applied voltage parameters. Moreover, partial discharges lead to the increase of leakage currents and the dielectric losses provoking an extra heating. Thus, the interaction and mutual intensification of both electrical and thermal stresses accelerate the insulation ageing and destruction, leading to a thermal runaway and thermal insulation breakdown.

5 Conclusion

With the objective to investigate winding wires endurance, tests have been conducted on standard twisted pairs and proposed coil-type specimens under electro-thermal stresses till an enamel insulation breakdown. Most of the time, tests have been performed on unimpregnated wires' specimens in order to evaluate their endurance to partial discharges in motor winding. It is based on consideration that partial discharges can occur in voids and cracks of winding impregnation. Testing winding wires with different enamel composition allows to investigate enamel insulation failure mechanisms and to choose the optimal insulation type for motors fed by inverters.

The endurance tests conducted on impregnated wires allowed to study the impregnation "healing" effect and failure mechanism in presence of insulation defects. It was shown, that even independent defect leads to insulation weakening that accelerates the destruction. The experimental results highlight the important role of impregnating compositions and enamel insulation compatibility.

Among studied wires, the tested corona resistant round section wire and rectangular section wire demonstrate the best endurance having the highest time to breakdown. The better endurance of rectangular winding wire comparing to other conventional wires may be related to its enamel composition and thicker insulation, as well as the better thermal stability – its thermal index is 200 °C. However, the time to breakdown decreased significantly when heated at 180 °C or with the rise of voltage amplitude and switching frequency.

Endurance tests results and insulation destruction analysis confirm the significant influence of voltage and temperature interaction on insulation deterioration. Higher temperature accelerates the electrical ageing, leading to electro-thermal failure mechanism. PD would be the main factor causing the final breakdown at low temperatures due to mechanical and chemical erosion. At higher temperatures, thermal ageing becomes more and more important.

The results of endurance tests conducted at PWM-like pulses with low voltage edge shown that breakdown mainly occurred at defective area forming weak point for partial discharges. The additional thermal stress reduces the lifetime. The tests performed under high dV/dt impulse voltage with high switching frequency show that damages (rapid irreversible deterioration, enamel melting, burning) tend to be more significant at the central part of the specimens indicating a thermal failure nature. At higher frequency the increasing of ultraviolet radiation was observed that indicates the rise of PDs currents and intensity. The rapid dielectric destruction is a result of ionization in gaps between wires' turns, photoionization, high ozone concentration and local temperature raise. Therefore, it can be assumed that electro-thermal ageing and the related deterioration of the dielectric's physico-chemical properties due to PDs will eventually lead to a thermal failure of dielectric, lowering the threshold breakdown voltage.

Thus, the fast-rising impulse voltage combined with high switching frequency can be a limiting factor that determines the applicability of insulating materials in inverter fed motors. Conducting insulation endurance tests on winding wires' specimens gives an opportunity, at machine design stage, to estimate and compare the insulation materials ability to tolerate applied stresses and thus, to minimize the risk of unexpected machine's failure. The analysis of breakdown data acquired on wire's specimens cannot be straightforwardly used for machine's winding design or life time prognosis. Nevertheless, based on this experiment the following recommendations may be given for improving winding reliability:

- using corona resistant wires;
- improving temperature stability by using winding wires with higher operating temperature and short-time permissible temperature considering the electro-thermal failure mechanism;
- ensure the manufacturing quality of winding wire and impregnation (defects free insulation, dielectric material compatibility, impregnation quality);
- limiting voltage surges and dV/dt .

References

References

- [1] IEC 62539:2007. *Guide for the statistical analysis of electrical insulation breakdown data*. Ed. 1.0 edition, 2007.
- [2] Douglas C Montgomery and George C Runger. *Applied Statistics and Probability for Engineers*. John Wiley & Sons, 3rd ed. edition, 2003.
- [3] Койков, С. Н. and Цикин, А. Н. Электрическое старение твердых диэлектриков. Энергия. Ленингр. отд-ние, – Л., 1968.
- [4] IEC 61649:2008. *Weibull analysis*. Ed. 2.0 edition, 2008.
- [5] Barbara FLORKOWSKA, Marek Florkowski, Paweł ZYDROŃ, and Józef ROEHRICH. Experimental evaluation of breakdown voltage and life time for models of the low voltage electrical motors windings. *PRZEGLĄD ELEKTROTECHNICZNY*, 1(10):21–25, oct 2016.
- [6] F.-R. Bohm, Klaus Nagel, and Heinz Schindler. A new generation of wire enamel for the production of magnet wires with outstanding corona resistance. In *Proceedings: Electrical Insulation Conference and Electrical Manufacturing and Coil Winding Technology Conference (Cat. No.03CH37480)*, pages 109–113. IEEE, 2003.
- [7] R.J. Beeckman, J.J. Harber, and S.J. Wentz. Studies on magnet wire degradation with inverter driven motors. In *Proceedings: Electrical Insulation Conference and Electrical Manufacturing and Coil Winding Conference*, pages 383–387. IEEE, 1997.
- [8] Peng Wang, Hongying Xu, Jian Wang, Andrea Cavallini, and Gian Carlo Montanari. Temperature effects on PD statistics and endurance of inverter-fed motor insulation under repetitive square wave voltages. In *2016 IEEE Electrical Insulation Conference (EIC)*, pages 202–205. IEEE, jun 2016.
- [9] Бартнев, Г.М. Прочность и механизм разрушения полимеров. Химия, Москва, 1984.
- [10] V. V. Pykhtin. A method for experimental determination of defectiveness in the insulation system of induction motor windings taking into account different mecha-

- nisms of the production of defects. *Russian Electrical Engineering*, 78(7):335–340, jul 2007.
- [11] Супуева, Аделя Сагынбековна. Снижение дефектности межвитковой изоляции обмоток низковольтных асинхронных электродвигателей. Канд. дисс., Национальный исследовательский Томский политехнический университет, 2016.
- [12] R W Meggs and K Daffey. Partial Discharge Monitoring in Marine HV Systems. In *Proc. IMarEST*, 2011.

**Chapter V: Deterioration of turn
insulation under partial discharges at
high dV/dt impulse voltage**

Chapter V

Deterioration of turn insulation under partial discharges at high dV/dt impulse voltage

Contents

1 Introduction	178
2 Characterization and modelling of twisted pair	179
2.1 Evaluation of overvoltage at twisted pair resulting from high dV/dt and cable connections	179
2.2 Barrier discharges in the twisted pair and in the turn insulation	187
2.3 Modelling of dielectric barriers in twisted pair	188
2.4 Current-voltage characteristics of twisted pair	191
2.4.1 Theoretical current-voltage characteristics	191
2.4.2 Empirical current-voltage characteristics	194
3 Study of turn insulation deterioration	198
3.1 Experimental study	199
3.2 Finite element modelling	205
4 Synthetic experimental setup for turn insulation testing	208
5 Conclusion	211
References	215

1 Introduction

Reliability of electrical machine depends on reliability of electric insulation system. The winding turn insulation is the weakest element in this system. The literature review and the performed endurance tests put into evidence the detrimental effect of partial discharges on turn insulation of inverter-fed motors. In this regard, the phenomenological investigation of turn insulation deterioration when subjected to high dV/dt impulse voltages and high switching frequency is a relevant task. Thus, Chapter V is devoted to study of enamel insulation destruction mechanisms using numerical simulations and experimental failure analysis methods.

Firstly, the twisted pair is modelled as a part of electric circuit with RLC-parameters. It allows to simulate and evaluate overvoltage caused by cable connections between the twisted pair and the SiC inverter generating high dV/dt impulse voltage.

Secondly, the dielectric barriers composed by enamel film and air voids between turns of twisted pair are modelled by corresponded capacitances. A variable resistance is used in order to take into account the changing of electric circuit parameters due to PD inception. This model is used to analyse current-voltage characteristic of twisted pair and partial discharges comparing it with experimental observations.

Experiments are conducted on twisted pairs under different impulse voltage amplitude and switching frequencies using previously described test benches. Specimens' temperatures, discharge currents and light emission spectra are measured. The discharge filamentary structure and periodical traces of erosion on twisted pair's turns have been observed by optical microscopy.

With the objective to supplement these observations, a FEM modelling is performed to calculate the electric field distribution in the twisted pair in order to correlate areas of high electric field and damaged insulation areas.

Furthermore, a synthetic test bench equipped with two different voltage sources and a vacuum pump is proposed. This synthetic test bench allows to control experimental conditions as temperature, pressure, and gas media of tested specimen in the absence of climate chamber. Finally, a brief study of low pressure effect is conducted. In the absence of vacuum chamber, the twisted pair is placed in a hermetical glass tube where the pressure is lowed using the vacuum pump. Consequently, a method to detect defects in the insulation under low pressure and partial discharge activity is proposed.

2 Characterization and modelling of twisted pair

In order to investigate the deterioration of turn insulation under partial discharges we have used unimpregnated twisted pair specimens. The twisted pair represents a physical model of turn insulation for low voltage electrical machines having random wound winding. This is the specimen recommended by international standards for testing and qualifying winding wires insulation in terms of electrical [1], thermal [2], chemical [3] and mechanical properties [4]. Thermal life evaluation of winding wire [5], dielectric breakdown at rated temperatures, and retained dielectric after refrigerant conditioning [6] tests are also conducted on twisted pairs. Moreover, as mentioned in Chapter III, twisted pairs are often used in studies focused on partial discharges in inverter-fed motors. Authors of papers [7], [8], [9], [10], [11], [12], [13] and [14] investigate lifetime of insulation subjected to partial discharges, and PD statistical features as PDIV, PD magnitude and repetition rate. Thus, the twisted pair can serve as physical model and instrument to investigate the phenomenon of electrical discharges occurred in air gaps between two twisted wires as well as to examine the insulation material degradation under these discharges. The twisted pair can be characterized by its geometrical factors such as wire's diameter, insulation thickness, length, and electrical properties such as relative permittivity ϵ_r and RLC-parameters.

2.1 Evaluation of overvoltage at twisted pair resulting from high dV/dt and cable connections

Considering that the designed SiC-inverter described in Chapter III Section 3.4.3. A generates very high dV/dt , even short cable connections cause overvoltage at tested twisted pair. This effect can be observed in voltage waveforms shown in Figure V.1. Voltage has been measured with and without connected twisted pair at two different points: at the nearest accessible point from the inverter output, a distance from inverter's PCB is equal to 0.15 m), and at electric contacts in the thermal chamber, a distance from inverter's PCB is equal to 1 m that comprises the total length of cable connections with distance between cables approximatively equal to 50 mm as shown in Figure V.2. In order to exclude PD effect during these measurements, a voltage below PDIV ($V_{DC} = 600$ V) was applied.

The high-voltage differential probe Tektronix THDP0100 100 MHz and the Oscilloscope Tektronix MDO3024 are used. These measurements demonstrate the effect of cable connections and twisted pair on voltage surges and oscillations. To study this effect, we have modelled our test setup by a pulse generator with limited dV/dt and RLC circuit as shown in Figure V.3, where R_d is the damping resistor, L_{cable} and C_{cable} are the cable inductance and capacitance, L_{twist} and C_{twist} are the inductance and capacitance of the tested twisted pair.

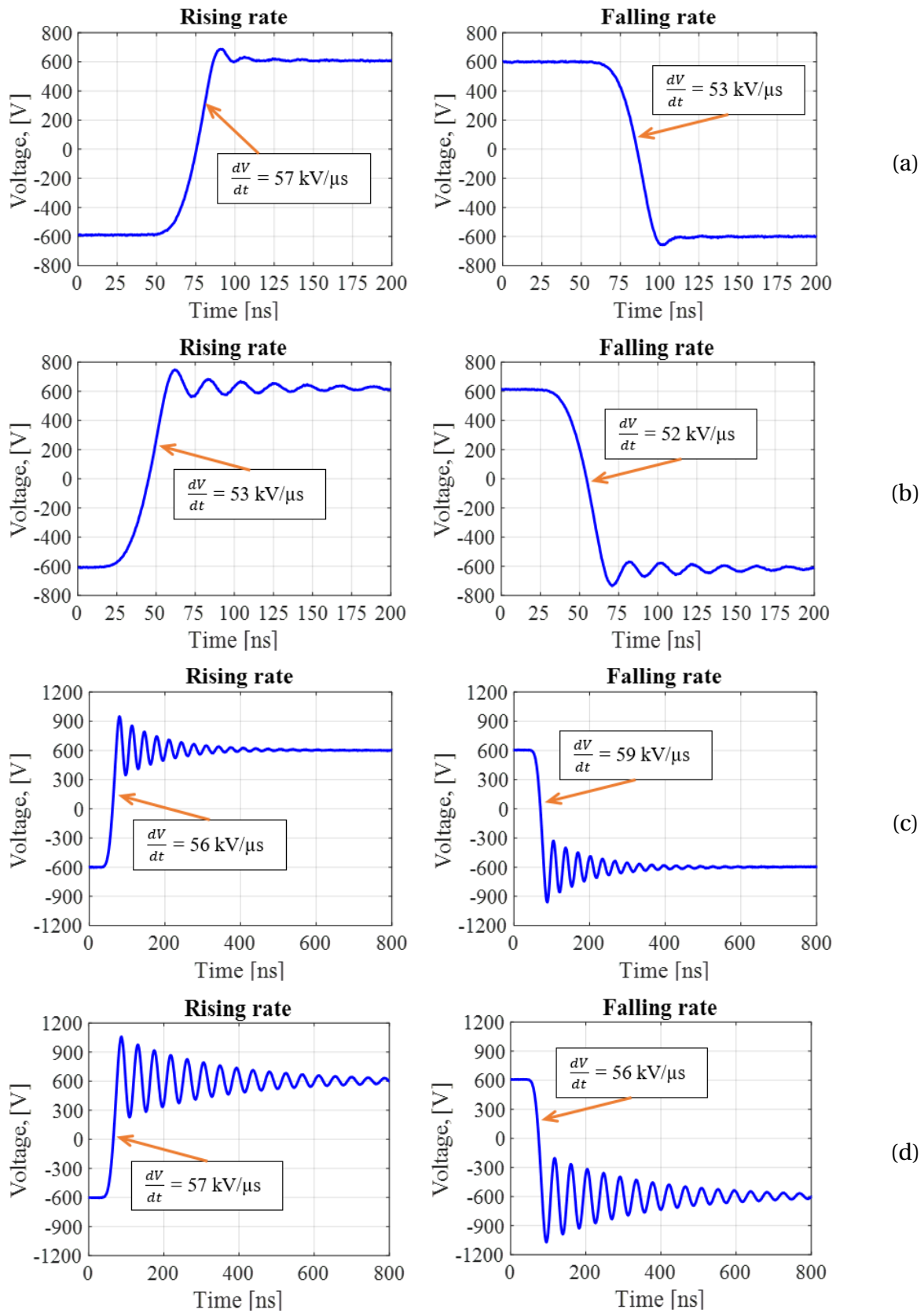


Figure V.1: Inverter's voltage waveforms measured at different contact points: at the inverter output (no load) (a), at the inverter output (twisted pair connected) (b); at contacts in the thermal chamber (no load) (c); at contacts in the thermal chamber (twisted pair connected).

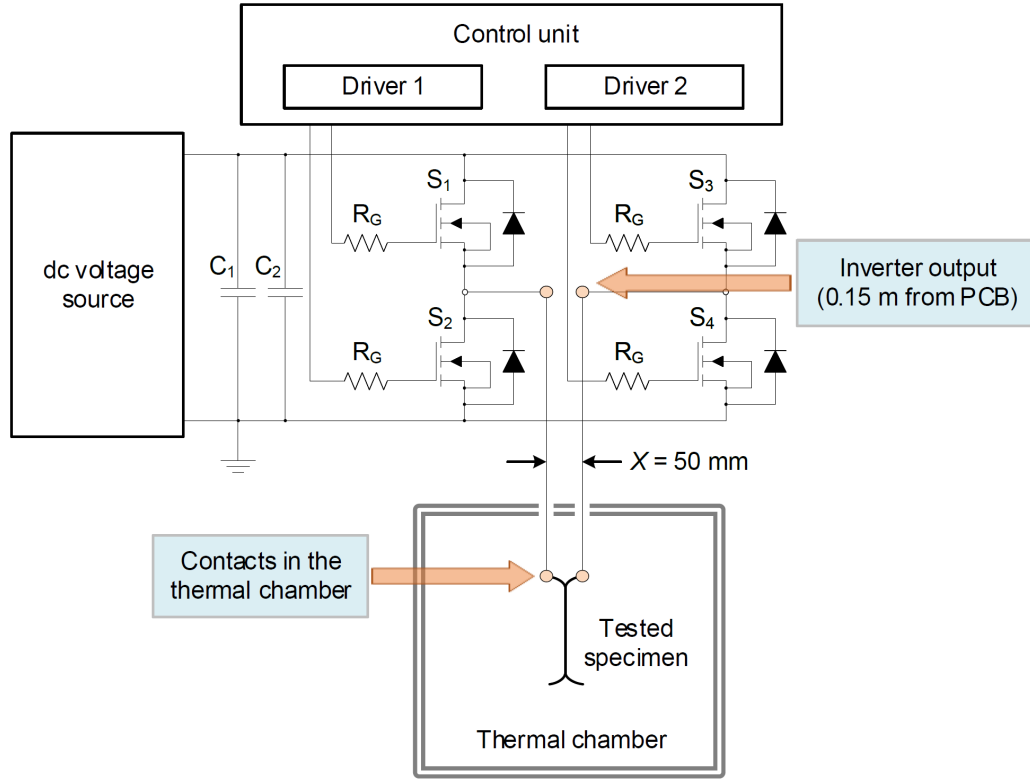


Figure V.2: Scheme of experimental setup presented measurement points.

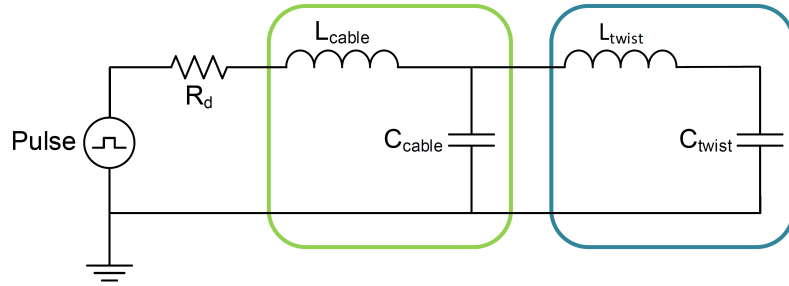


Figure V.3: Test setup modelled by an equivalent circuit.

The model parameters calculation is based on the electromagnetic approach and low-loss transmission line equations from [15]. Then an enamelled wire is energized, its conductor and polarized outer insulation layer form a coaxial structure as shown in Figure V.4a and can be considered as cylindrical capacitor. The expression (V.1) gives a capacitance per unit length C_l for this case.

$$C_l = \frac{2\pi\epsilon_0\epsilon_r}{\ln\left(\frac{R_{out}}{R_{in}}\right)} \quad (V.1)$$

In V.1, $\epsilon_0 = 8.854 \times 10^{-12}$ is the vacuum permittivity, $R_{out} = D_{out}/2$ is the external radius and $R_{in} = D_{in}/2$ is the internal radius (see Figure V.4). The diameters D_{out} and D_{in} of cable and enamel wire were measured using a micrometer having a $1 \mu\text{m}$ scale division.

Relative permittivity ϵ_r values are determined using references [16] and [17] for cable and enamelled wire respectively. Electrical and geometrical parameters are given in Table V.1. For enamelled wire, the value $\epsilon_r = 3$ is used in calculations.

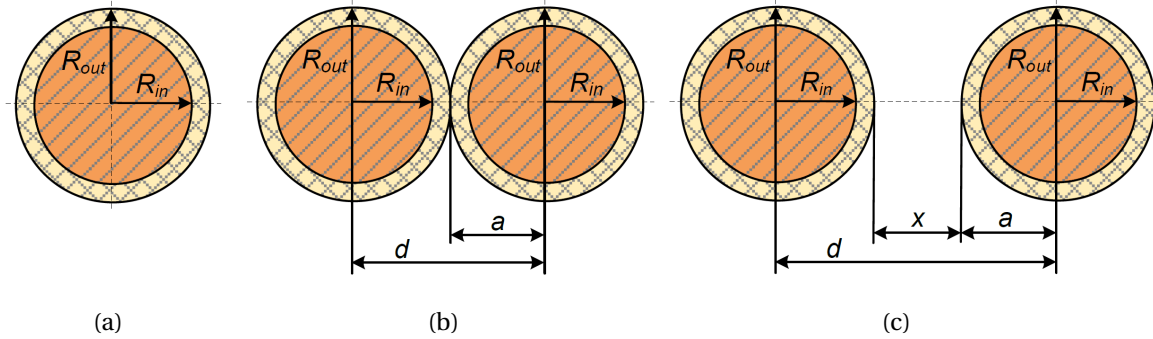


Figure V.4: Coaxial strictures corresponding to enamelled wires and cables configurations:
(a) single wire or cable; (b) twisted pair; (c) two cables .

Table V.1: Electrical and geometrical parameters of cable connections and tested winding wire.

Type	Insulation	ϵ_r	D_{out} , mm	D_{in} , mm	l , m
unshielded cable MGTF	tetrafluoroethylene (TFE)	2.1	1.090	0.730	1.000
conventional enamelled wire PETD-180	polyesterimide (PEI) and polyamide-imide (PAI)	2.9 - 4.3	0.885	0.800	0.125

The transmission line's low-loss approximation makes it possible to express the phase velocity V_p as follows:

$$V_l \approx \frac{1}{\sqrt{L_l C_l}} = \frac{1}{\sqrt{\mu_0 \epsilon_0 \epsilon_r}} \quad (V.2)$$

Therefore, the self inductance per unit length L_l can be written as

$$L_l = \frac{\mu_0}{2\pi} \ln \left(\frac{R_{out}}{R_{in}} \right) \quad (V.3)$$

Then, the capacitance and inductance of enamelled wire and cable can be calculated by multiplying C_l and L_l by their length l given in Table V.1.

With regard to twisted pair construction, it can be approximatively represented by two parallel coaxial cylinders having geometrical parameters as shown in Figure V.4b. In this case, the mutual capacitance and inductance of twisted pair are given by (V.4) and (V.5).

$$C = \frac{\pi \epsilon_0 \epsilon_r l}{\ln \left(\frac{d}{a} \right)} \quad (V.4)$$

$$L = \frac{\mu_0}{\pi} \ln\left(\frac{d}{a}\right) l \quad (V.5)$$

where $a = R_{out}$ and $d = 2R_{out}$.

Two cables connecting the inverter output and twisted pair are placed at the distance x from each other as shown in Figure V.4c. Thus, the capacitance and the inductance of two parallel cables are given by (V.6) and (V.7) respectively.

$$C = \frac{\pi \epsilon_0 \epsilon'_r l}{\ln\left(\frac{d-a}{a}\right)} \quad (V.6)$$

$$L = \frac{\mu_0}{\pi} \ln\left(\frac{d-a}{a}\right) l \quad (V.7)$$

where $a = R_{out}$, $d = 2R_{out} + x$ and ϵ'_r is the complex dielectric permittivity of composed dielectric media (cable insulation and air), also known as effective relative permittivity. To estimate ϵ'_r of two-component mixture different mixing rules can be used.

The proposed by Lichtenecker logarithmic mixing rule [18] and [19] is

$$\log(\epsilon'_r) = \sum_{i=1}^m y_i \sqrt[3]{\epsilon_i} \quad (V.8)$$

The equation of Landau-Lifshitz to calculate the effective relative permittivity of mixed components [18] is

$$\sqrt[3]{\epsilon'_r} = \sum_{i=1}^m y_i \sqrt[3]{\epsilon_i} \quad (V.9)$$

The proposed by Beer mixing rule [18] is

$$\sqrt{\epsilon'_r} = \sum_{i=1}^m y_i \sqrt{\epsilon_i} \quad (V.10)$$

In equations (V.8), (V.9) and (V.10) m is the number of mixture's components, y_i designates the volume concentrations of these components and ϵ_i corresponds to relative permittivities of mixed dielectrics.

Volume concentrations can be determined considering the distance x between the two cables and the cable insulation thickness δ (calculated using equation III.1). For the distance $x = 50$ mm and the insulation thickness $\delta = 0.18$ mm, the volume concentrations of dielectrics are the following:

- air: $y_{air} = 99.64\%$,
- TFE: $y_{TFE} = 0.36\%$.

In this case, the effective relative permittivity calculated using (V.8), (V.9) and (V.10) is equal to 1.0033, 1.0036 and 1.0038 respectively. Figure V.5 demonstrates the variation of

effective relative permittivity with distance between two cables calculated using the three mixing rules. This plot shows that the used mixing rules give similar results and ϵ'_r value tends to be equal to ϵ_{air} with increase in distance between the cables. Therefore, then $x \gg \delta$, the effective relative permittivity can be defined as $\epsilon'_r \approx \epsilon_{air} = 1.0006$. Consequently, the capacitance of cable connections will decrease with distance increasing.

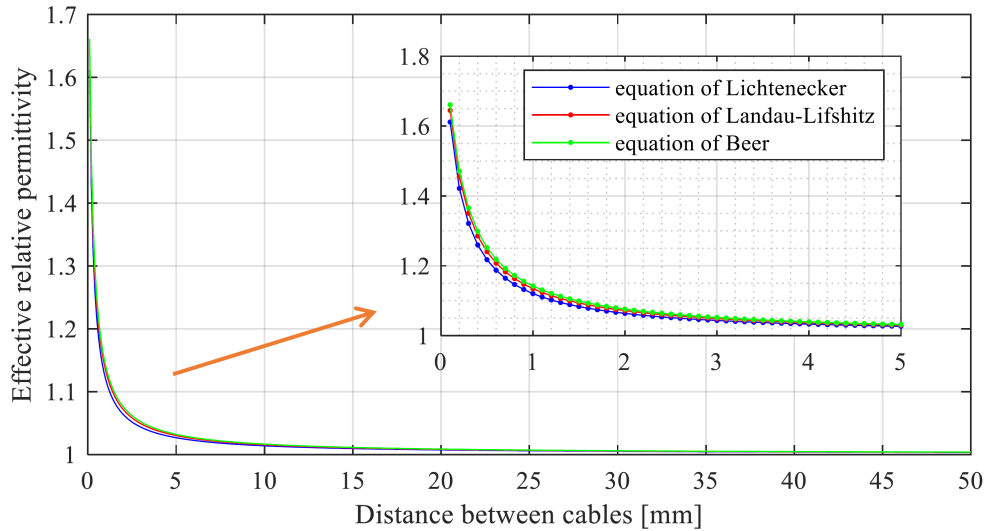


Figure V.5: Variation of effective relative permittivity with distance between two cables.

Since $x = 50$ mm, $a \ll d$, thus Eq. V.4 and Eq. V.5 can be used to calculate the capacitance and inductance of cable connections.

The obtained capacitance and inductance for use in electrical circuit simulations are given in Table V.2.

Table V.2: Calculated electrical parameters for electrical circuit simulations
(twisted pair length $l = 0.125$ m and cable length $l = 1$ m).

Type	C_l , pF/m	L_l , nH/m	C , pF	L , nH
Twisted pair	120.388	277.259	15.049	34.657
Cable connections	6.130	1816.223	6.130	1816.223

Additionally, using the low-loss approximation the propagation delay t_d is estimated for the twisted pair and cable connections according to (V.11).

$$t_d = \sqrt{L_l C_l} \quad (V.11)$$

Thus, the propagation delay t_d of 1 m of cable connections is equal to 3.34 ns, t_d of 1 m of twisted pair is equal to 5.78 ns and t_d of 0.125 m of twisted pair is equal to 0.72 ns. Rise time of the impulse voltage produced by SiC pulse generator is about $t_r = 25 \sim 30$ ns, so $t_d < t_r$ and the proposed equivalent circuit model given in Figure V.3 can be used for high dV/dt pulses.

The high frequency of voltage and current oscillations caused by steep impulse voltage rate lead to increasing of cable and twisted pair resistance due to skin effect. In consequence of increased resistance, the damping characteristic of the overvoltage transient is affected. The skin depth δ is defined in accordance with (V.12) [20].

$$\delta = \frac{1}{\sqrt{\pi f \mu \sigma}} \quad (\text{V.12})$$

where f is the frequency of voltage oscillations estimated at 23 MHz basing on the voltage waveform shown in Figure V.1d; μ and σ are the copper permeability and conductivity. Thus the effective resistance of cable and twisted pair are simply calculated according to (V.13) and are equal to 0.5484Ω and 0.0624Ω respectively:

$$R = \frac{\rho l}{\pi(2r - \delta)\delta} \quad (\text{V.13})$$

where ρ is the copper resistivity.

Therefore, the test bench is modelled using LTSpice (SPICE simulation software) and MATLAB software to control the simulations and to analyse the obtained results. Simulated and measured voltages are superimposed in Figure V.6. The simulated voltage source generates bipolar voltage $V = \pm 600 \text{ V}$ and rise and fall times are set equal to 27 ns. The electrical circuit parameters such as an inverter output impedance (parasitic resistance and capacitance contributing to the inverter ringing), a proximity effect and additional losses were not defined here. Therefore, the damping resistor $R_d = 12 \Omega$ is adjusted to limit oscillations in the LC-circuit and match the damping time to the experimental one, that allows to obtain the good fitting of simulation results to measurements.

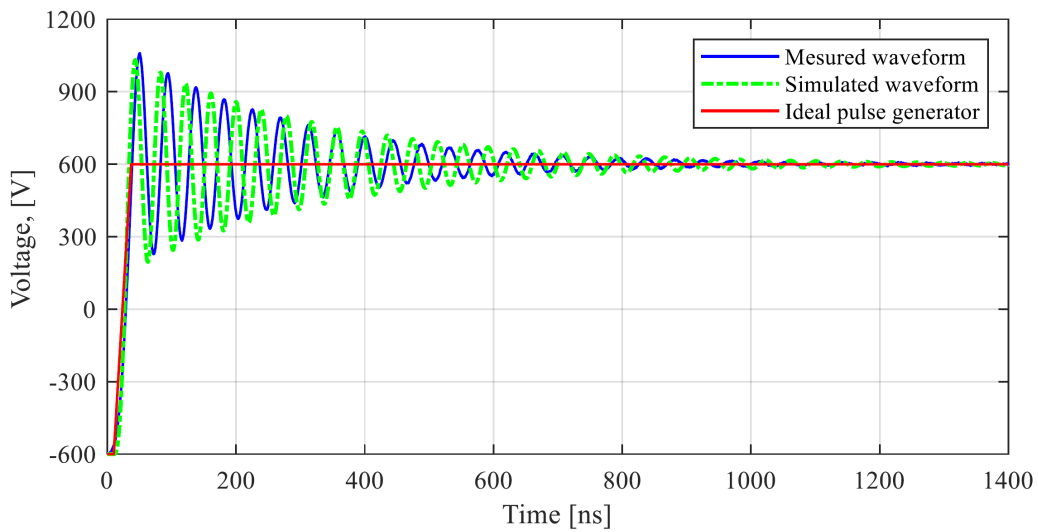


Figure V.6: Inverter's voltage waveforms measured at contacts in the thermal chamber (twisted pair connected) and simulated by equivalent RLC-circuit using LTSpice.

The obtained equivalent circuit allows to reproduce the test setup making it possible to conduct an analysis of voltage transients depending on model parameters. Therefore, the influence of cable length and impulse voltage rise time on voltage oscillations and surges can be investigated. Firstly, the cable length is kept equal to 1 m and the pulse rise time t_R is taken as variable. Voltage waveforms obtained at three t_R levels are given in Figure V.7. In line with the expectations, the transient overvoltage and ringing are strongly depend on pulse rise time. It should be noticed, that even short cable line connecting high dV/dt pulse generator and its load leads to increasing of maximum voltage at the load. Therefore, the higher dV/dt will give rise to higher overvoltage and stronger electric field, which will increase the probability of partial discharge ignition in inverter-fed motor.

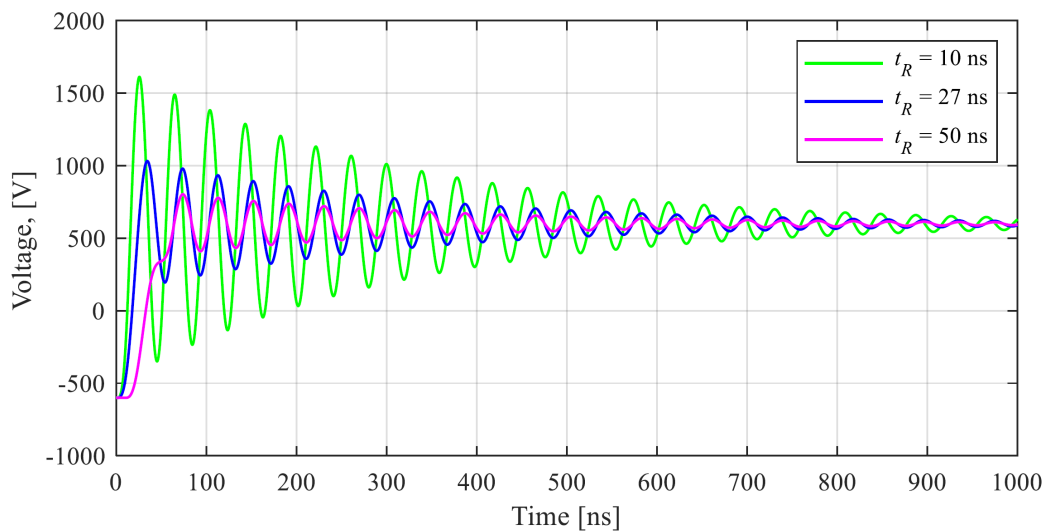


Figure V.7: Simulated voltage waveforms for different pulse rise times, $l = 1$ m.

Secondly, the effect of cable connections length is studied. For this purpose, the scheme shown in Figure V.3 is modified by adding a number of series LC-sections where one section correspond to 1 m length cable connections (green circuit in Figure V.3). The impulse voltage rise time is set $t_R = 27$ ns. Figure V.8 gives simulation results for cable connections length of 1 and 2 meters. Increasing in the length intensifies the maximum voltage but slows down the voltage edge rate.

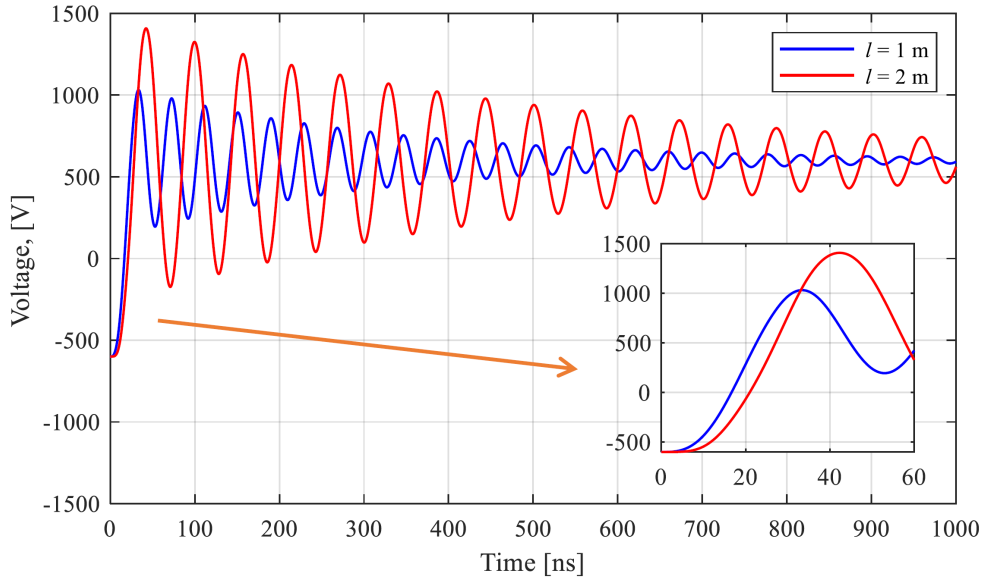


Figure V.8: Simulated voltage waveforms for two cable lengths, $t_R = 27$ ns.

This proposed equivalent circuit gives an approximate model of the laboratory designed SiC-inverter with the output cable used to connect the twisted pairs. It allows to analyse the voltage transients resulted from very fast transistors switching. We have observed the importance to minimize the cable line length when the voltages oscillations and surges should be limited. This objective can be achieved using a low inductive damping resistor. On the hand, it will decrease output voltage edge rate that can be also seen from the proposed model.

2.2 Barrier discharges in the twisted pair and in the turn insulation

For better understanding of physical processes in turn insulation under PD activity, the type of partial discharges should be defined. In earlier researches *e.g.*, in [21] and [22], the partial discharges in inverter-fed motor were characterized as corona discharges. Thus, the wire having greater withstanding capability to these discharges is named “corona-resistant” winding wire [22] and [23]. Corona is a form of partial discharges, and after Stone [24], “the term corona is reserved for the visible PDs that can occur on bare metal conductors operating at high voltage, which ionize the surrounding air”. Thus, this term should not be used for PDs within the machine’s winding.

Regarding to the twisted pair construction the arising partial discharges may be characterized as Dielectric Barrier Discharges (DBD) in accordance with their definition: “DBD are electric discharges between two metallic electrodes, with at least one of them covered by a dielectric material” [25]. We suggest, that PDs within the turn insulation occurs in air gaps between barriers composed of impregnation and enamel insulation.

Barrier discharges based generators are widely investigated and used for ozone

electrochemical synthesis, UV light generation and surface treatment [25], [26], [27], [28], [29] and [30]. Basing on the accumulated knowledge and experience in this domain, the new approaches to study partial discharges in electrical machine windings may be proposed. The using of these approaches will be discussed in the following sections.

2.3 Modelling of dielectric barriers in twisted pair

As shown in the Section 2.1, the twisted pair can be represented as a part of electric circuit and the parameters of the equivalent circuit can be calculated using the transmission line approach. With the objective to study partial discharges in the twisted pair we propose to model its insulation as a solid dielectric with air voids where PDs will occur.

From the point of view of classical partial discharges theory [31], the solid dielectric having an inclusion (*e.g.*, an air void or insulation defect) with lower electric strength can be represented by its capacitance C_x . This capacitance is defined by (V.14) and schematically shown in Figure V.9.

$$C_x = C_a + \frac{C_{in}C_d}{C_{in} + C_d} \quad (V.14)$$

where C_{in} is the inclusion capacitance, C_d is the capacitance of a part of solid dielectric containing the inclusion (C_d is connected in series with the C_{in}), and C_a is the capacitance of another part of solid dielectric without inclusions. Partial discharge will occur when the voltage applied at the inclusion reaches the breakdown voltage of this inclusion, which is defined as the partial discharge inception voltage.

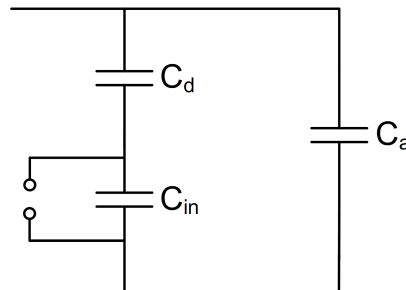


Figure V.9: Equivalent circuit when studying partial discharges in solid dielectric [20].

Coming now to the twisted pair specimen construction, it consists of two copper conductors covered by enamel insulation. These conductors are the metal electrodes, and the enamel film creates dielectric barriers between these electrodes and air gaps in turns of twisted pair (see Figure V.10). Therefore, the twisted pair under partial discharges can be modelled by corresponded capacitances: dielectric barriers capacitances C_{b1} and C_{b2} (capacitance between conductor and polarized outer dielectric surface), and air gaps capacitance C_{air} in parallel with a variable resistance R_d as shown in Figure V.10b.

The variable resistance is used in order to take into account the changing of electric circuit parameters due to PD inception. This model is proposed basing on the scheme used for barrier discharge study presented in [25], [26], [27], [28] and [32].

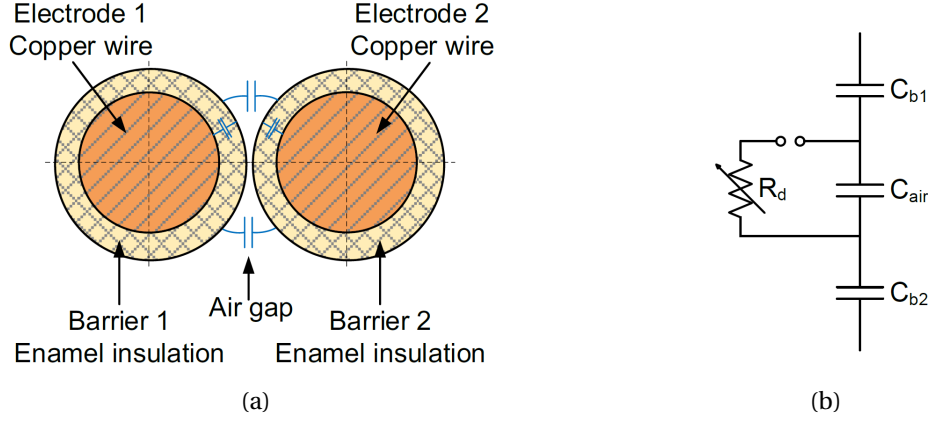


Figure V.10: Twisted pair structure (a) and corresponded equivalent circuit (b) when studying partial discharges in twisted pair.

In the absence of partial discharges, the twisted pair is modelled by its equivalent capacitance C_{tp} defined in (V.16). When the applied voltage reaches the PDIV, a breakdown of the discharger shown in Figure V.10b occurs commuting the variable resistance of discharges arising in air gaps.

$$C_b = \frac{C_{b1}}{2} = \frac{C_{b2}}{2} \quad (\text{V.15})$$

$$C_{tp} = \frac{C_b C_{air}}{C_b + C_{air}} \quad (\text{V.16})$$

Parameters of the proposed model are derived from capacitance measurements performed using a LCR meter E7-13 (see Appendix V-A). To this purpose, twisted pairs are made of the conventional enamelled wire PETD-180. The geometry is given in Table V.1. The measured capacitance of twisted pair $C_{tp} = 14$ nF. This value is close to the capacitance calculated in Section 2.1 (see Table V.2). To determine the capacitance of dielectric barriers C_b , wires forming the twisted pair are metallized – covered by conducting paste (liquid metal composition “indium – gallium”). The metallized twisted pair is shown Figure V.11. It should be noted, that only the “active” (twisted) length $l = 0.125$ m of specimen is metallized. In this case, the capacitor C_{air} is short-circuited and the effect of air gaps between turns can be neglected, while the dielectric barriers capacitances C_{b1} and C_{b2} are connected in series.

The measured capacitance of dielectric barriers $C_b = 96$ pF. Thus, the capacitance of air voids can be derived from (V.16): $C_{air} = 16.39$ pF.

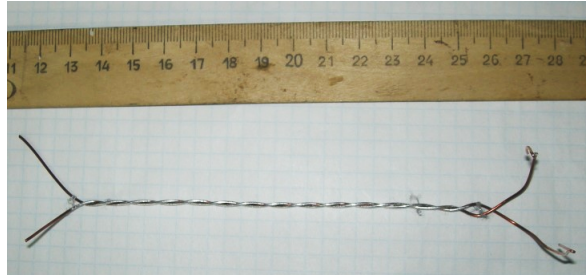


Figure V.11: Twisted pair covered by conducting liquid metal paste.

The capacitance of solid dielectric in series with air gaps capacitance represent a capacitive divider as shown in Figure V.12, where the maximum of voltage drops on minimal capacitance, *i.e.*, on air gaps.

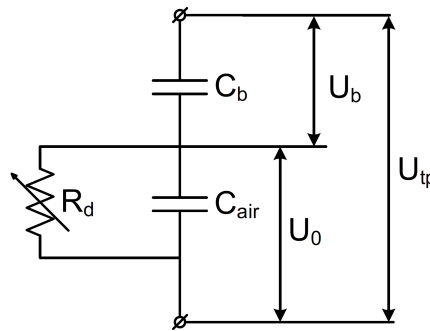


Figure V.12: Voltage in the equivalent circuit:

U_{tp} – voltage at twisted pair, U_b – voltage at dielectric barriers, U_0 – voltage at air gaps.

Voltage divider ratio k is defined by (V.17) [33] and equal to 1.171.

$$k = \frac{U_{tp}(t)}{U_0(t)} = \frac{C_b + C_{air}}{C_b} \quad (\text{V.17})$$

where $U_{tp}(t)$ is the instantaneous voltage applied to the twisted pair and $U_0(t)$ is the instantaneous voltage at air gaps. Therefore, 85.4% of the total voltage applied to the twisted pair drops on the air gaps. It put into evidence the risk of partial discharges appearance in poorly impregnated stator winding in presence of repetitive surges.

From the point of view of barrier discharge theory the current-voltage curve is one of the most important characteristics of discharge. The proposed model allows to analyse current-voltage characteristics of twisted pair and partial discharges comparing it with experimental observations as presented in the next section.

2.4 Current-voltage characteristics of twisted pair

2.4.1 Theoretical current-voltage characteristics

The study of current-voltage characteristics of twisted pair is based on the method described in [32]. The discharge current in the air gap between the dielectric barriers of twisted pair is equal to the current of the external circuit according to the condition of the total current continuity. In air gaps, the current is transported by electrons and ions, and the current through dielectric barriers flows to the external circuit due to a displacement current I_d . According to [35] the displacement current density is written by:

$$j_d = \epsilon_0 \epsilon_r \frac{\partial E}{\partial t} = \epsilon_0 \frac{\partial E}{\partial t} + \frac{\partial P}{\partial t} \quad (\text{V.18})$$

where E is the electric field strength, and P is the dielectric polarization. In this equation, the first term corresponds to displacement current in vacuum and the second term corresponds to displacement current in dielectric caused by displacement rate of charges in dielectric. In addition to the displacement (capacitive) current, a conduction current I_{cond} flows through dielectric barriers, thus the total current is defined by V.19. In our case, the conduction current may be neglected.

$$I_{tot} = I_{cond} + I_d \quad (\text{V.19})$$

In the absence of barrier discharges the current flows through the capacitance of air gaps and dielectric barriers as shown in Figure V.13a. When the electric field is strong enough to start the air ionization, the active resistance is connected in parallel to the air gaps capacitance. Corresponding to the scheme given in Figure V.13b, the current through dielectric barriers I_b is equal to the current in the air gaps I_{air} , and is equal to the vector sum of active I_a (discharge active current) and reactive I_r (capacitive current in the air gaps) current components as written in (V.20).

$$I_{tp} = \sqrt{I_a^2 + I_r^2} \quad (\text{V.20})$$

If the impulse voltage is applied to the twisted pair, when the maximum capacitive current $i_{c \max}$ will be defined by (V.21).

$$i_{c \max} = C \frac{dV}{dt} \quad (\text{V.21})$$

Therefore, knowing capacitance values of twisted pair's equivalent circuit and impulse voltage rate we can plot the theoretical current-voltage characteristics. In the calculations of maximum capacitive currents, the voltage changing rate is approximately defined by the voltage rise from 0 to its amplitude in steady state during the time equal to 25 ns.

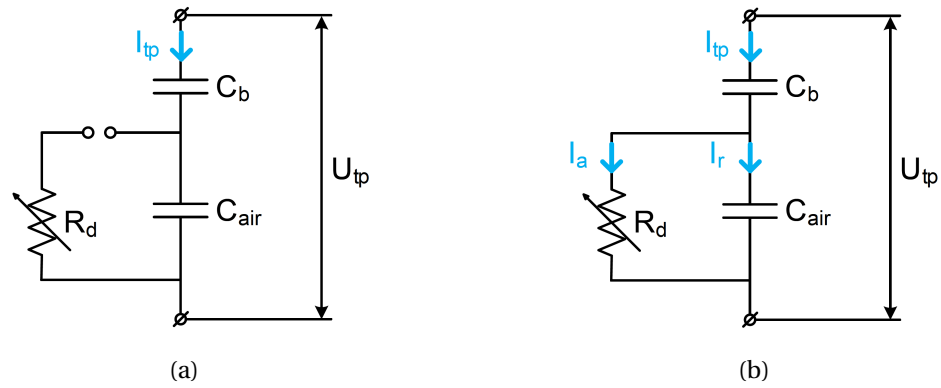


Figure V.13: Equivalent circuits of twisted pair indicating the currents:
(a) without barrier discharges and (b) with barrier discharges.

The current-voltage characteristic of dielectric barriers is described by $I_b = C_b \cdot dV/dt$; points are provided in Table V.3. The equivalent circuit is shown in Figure V.14a and the obtained characteristic corresponds to the line AB in Figure V.15.

Table V.3: Theoretical points of dielectric barriers' current-voltage characteristic.

Voltage, V	0	600	900	1400
Current, A	0	2.304	3.456	5.376

The current-voltage characteristic of twisted pair without discharges is described by $I_{tp} = C_{tp} \cdot dV/dt$; points are provided in Table V.4. The equivalent circuit is shown in Figure V.14b and the obtained characteristic corresponds to the line AC in Figure V.15.

Table V.4: Theoretical points of twisted pair's current-voltage characteristic.

Voltage, V	0	600	900	1400
Current, A	0	0.336	0.504	0.784

The current-voltage characteristic of twisted pair with barrier discharges is obtained in accordance with [32]. This characteristic starts at the voltage value corresponded to PDIV (point D) and it should be parallel to the line AB. Most of the time during the experiments, PDIV value were close to 900 V (DC bus voltage value). The obtained characteristic corresponds to the electric circuit of Figure V.14c and it is drawn by the line DE in Figure V.15. Thus, the resulting current-voltage characteristic of twisted pair is described by the curve ADE having a salient point at voltage value corresponding to PDIV. The current-voltage characteristic related to the air gaps capacitance without discharges (line AF) can be calculated by analogy with the previous characteristics using the equation (V.21) and C_{air} value or defined graphically by subtraction of the line AF from the line AB.

In the absence of air ionization, the obtained characteristic is very close to the characteristic of the twisted pair due to their similar capacitance values. To obtain the

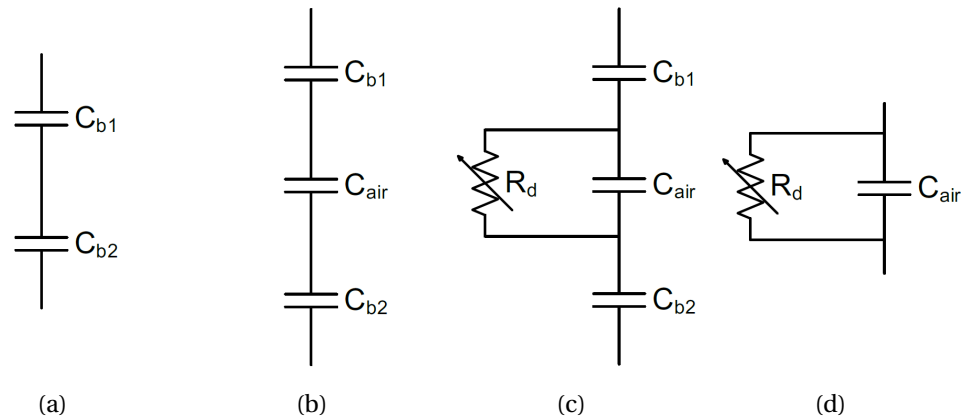


Figure V.14: Equivalent circuits of twisted pair for current-voltage characteristics: (a) – line AB (dielectric barriers), (b) – line AC (twisted pair without discharges), (c) – line DE (twisted pair with discharges), and line MN (discharges in air gaps).

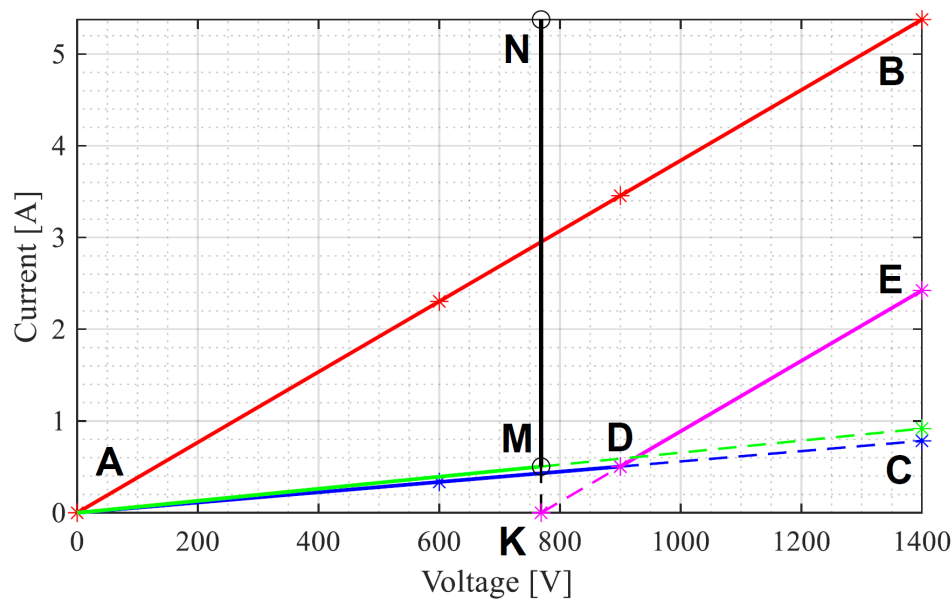


Figure V.15: Current-voltage characteristic of twisted pair:
 AB – current-voltage characteristic of dielectric barriers,
 AC – current-voltage characteristic of twisted pair without discharges,
 DE – current-voltage characteristic of twisted pair with discharges,
 AF – current-voltage characteristic of air gaps without discharges and
 MN – current-voltage characteristic of discharges in air gaps

current-voltage characteristic of discharges in air gaps corresponded to the equivalent circuit of Figure V.14d, the line DE is continued till reaching the voltage axis at voltage value equal to 768.75 V, point K in Figure V.15. Then the direct dashed line is plotted perpendicularly till crossing the line AF in the point M. The direct line MN is the current-voltage characteristic of discharges in air gaps. It also corresponds to the result of subtraction of the characteristic of twisted pair with discharges (line DE) from the characteristic of dielectric barriers in twisted pair (line AB).

2.4.2 Empirical current-voltage characteristics

With the purpose to compare the theoretical current-voltage characteristics and the experimental ones, current measurements are performed. The sketch of the test setup is drawn in Figure V.16. As in previous tests, the full bridge inverter topology is used to generate bipolar pulses, where the peak-to-peak inverter voltage corresponds to the double of DC bus voltage. The twisted pairs are only tested at room temperature in this experiment, thus the cable connections length can be reduced to 0.15 m) that allows to decrease the transient overvoltage and oscillations. However, the partial discharges occurred at voltage amplitude $V_{dc} > 1200$ V and switching frequency $f = 50$ kHz provokes high di/dt causing activation of SiC MOSFET drivers' over current protection and turning-off the transistors. In this regard, the resistor $R = 56 \Omega$ and toroidal ferrite core are added to decrease the current rate. The voltage waveforms measured by the high-voltage differential probe Tektronix THDP0100 100 MHz and the Oscilloscope Tektronix MDO3024 are given in Figure V.17.

It should be noticed, that all the experiments have been conducted with cooling (air velocity is equal to 2.4 m/s) of the tested specimen as shown in Figure V.16. It allows to slow down the temperature rise of twisted pairs caused by discharges and, consequently, to increase the time to breakdown. Otherwise, a thermal runaway and drastically accelerated failure in very short time occurred at high switching frequency as it was shown in Chapter IV.

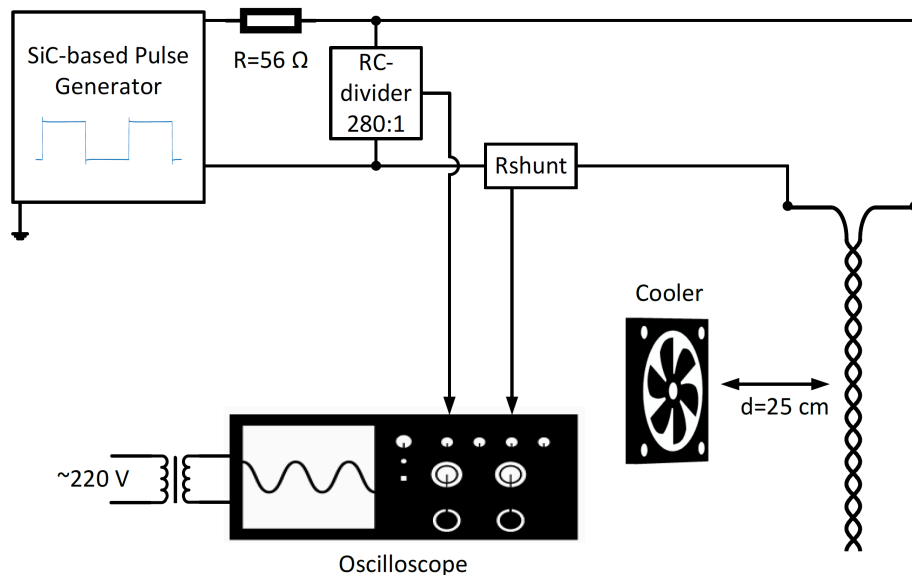


Figure V.16: Sketch of the test setup for current measurements.

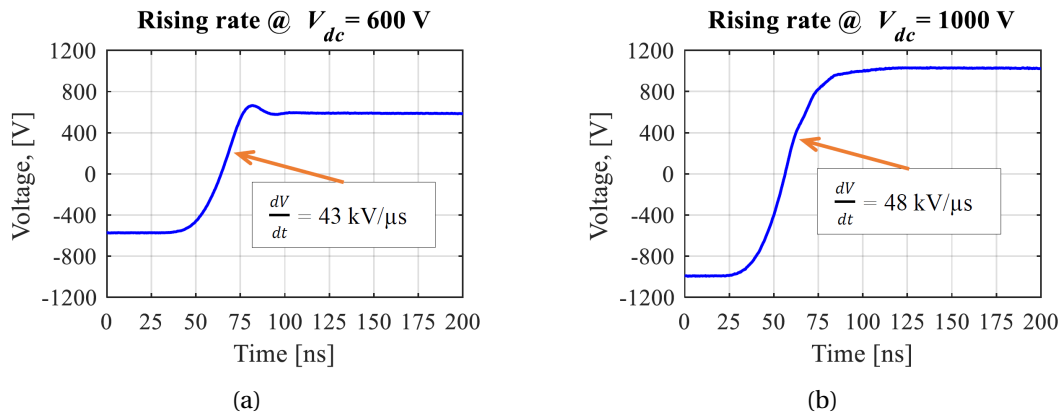


Figure V.17: Voltage waveforms measured on the twisted pair by high-voltage differential probe (with damping resistor and toroidal ferrite core at the inverter output, cable length is equal to 0.15 m).

In full-bridge inverter topology, the tested specimen is connected to inverter's mid-points that complicates the current measurements. Therefore, to measure currents on twisted pair the oscilloscope was powered via an isolation transformer having a shielded secondary winding. Thus, a current shunt can be placed in one of the inverter's leg. This shunt is made with low inductive ceramic encased resistors placed on round copper plate. It is connected to the oscilloscope Tektronix TDS 2014C via a coaxial cable and impedance match resistors. One of the ends of the twisted pair is connected to the pulse generator output via this shunt that allows to measure its current. During the current measurements the voltage on the twisted pair was recorded using the designed RC-divider with ratio 280:1. Figure V.18 and Figure V.19 show the installation and connections of measurement means. Appendix V-B provides more details about the construction of the current shunt and RC-divider.

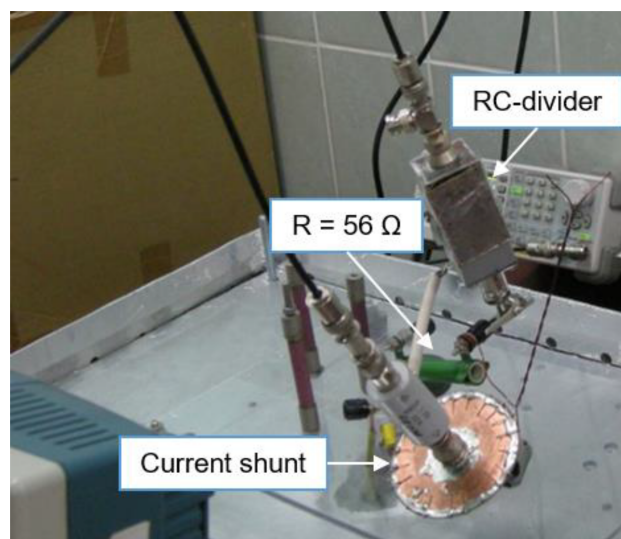


Figure V.18: Photograph of used measurement means.

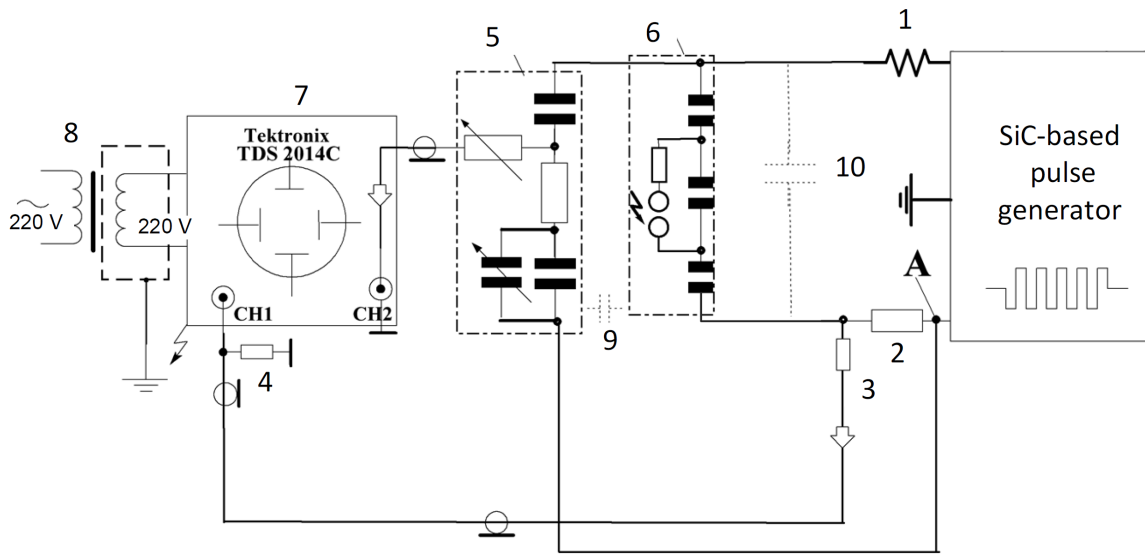


Figure V.19: The scheme of current and voltage measurements on the twisted pair subjected to PD.

- 1 – damping resistor $R = 56 \Omega$, 2 – current shunt resistance $R_{sh} = 1.03 \Omega$,
3 and 4 – current shunt impedance matching resistors, 5 – RC-divider 280:1,
6 – tested twisted pair (barrier discharge model), 7 – oscilloscope, 8 – isolation transformer.

Current of dielectric barriers

With the purpose to measure current through dielectric barriers the metallized twisted pair (as used in barrier capacitance measurement) is tested at high dV/dt impulse voltage with switching frequency $f = 50 \text{ kHz}$. The current pulse on the rising rate of impulse voltage is recorded as shown in Figure V.20. Table V.5 provides amplitude value of currents measured on metallized twisted pair depending on the applied voltage. The given voltage values correspond to the DC bus voltage and also to the steady-state voltage amplitude applied to the twisted pair.

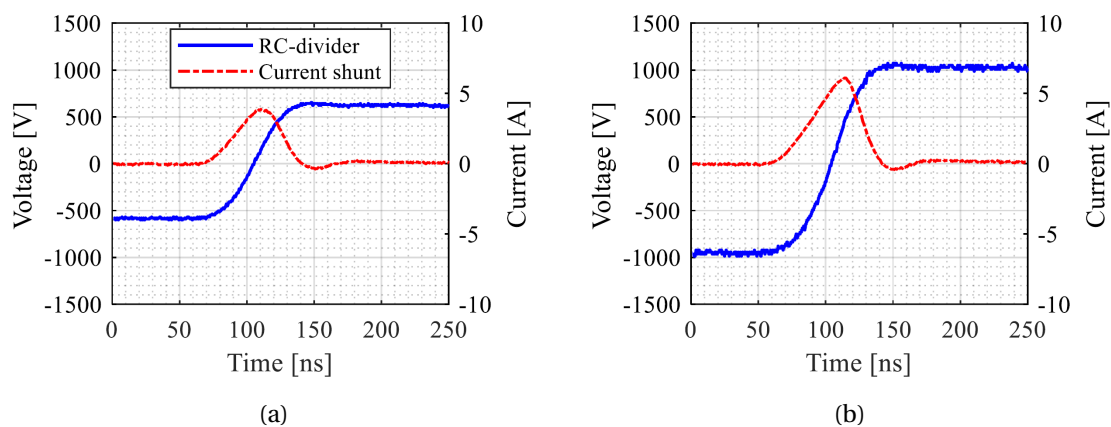


Figure V.20: Current pulse waveforms measured on the metallized twisted pair tested under impulse voltage $f = 50 \text{ kHz}$: (a) $V_{dc} = 600 \text{ V}$, (b) $V_{dc} = 1000 \text{ V}$.

Table V.5: Theoretical points of dielectric barriers' current-voltage characteristic.

Voltage, V	200	300	400	500	600	700	800	900	1000
Current, A	1.631	2.408	2.990	3.379	3.884	4.544	4.893	5.049	6.097

Current of twisted pair

Then, the current is measured on twisted pair (without metallization) also tested at high dV/dt impulse voltage with switching frequency $f = 50$ kHz. Figure V.21 gives current pulse waveforms below (a) and above PDIV level (b) on the rising rate of impulse voltage. A capacitive current of the tested twisted pair is observed in Figure V.21a; whereas the total current including capacitive one and PD pulse current is observed in Figure V.21b. Table V.6 provides the mean of peak values of current pulses observed during two impulse voltage periods depending on the voltage amplitude.

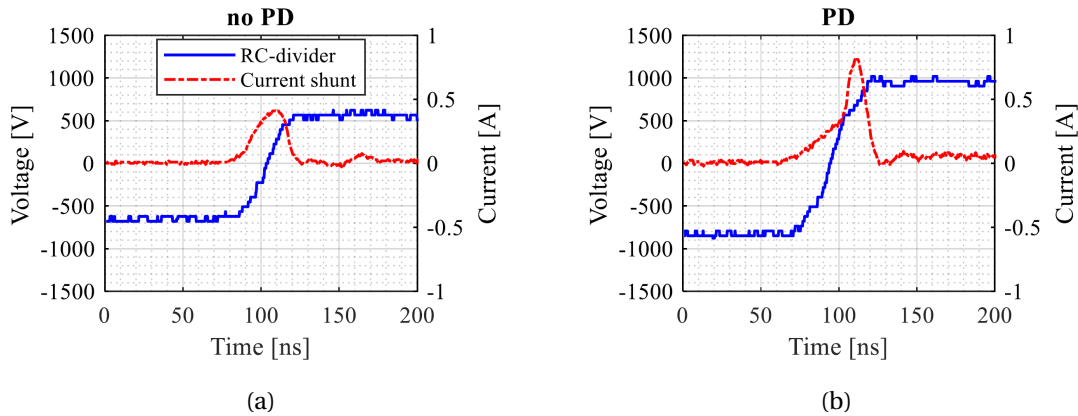


Figure V.21: Current pulse waveforms measured on the twisted pair tested under impulse voltage $f = 50$ kHz: (a) $V_{dc} = 600$ V, (b) $V_{dc} = 1000$ V.

Table V.6: Experimental points of twisted pair's current-voltage characteristic.

Voltage, V	600	700	800	900	1000	1100	1200	1300	1400
Current, A	0.394	0.539	0.673	0.683	0.730	2.563	2.874	3.314	3.754

Basing on the method described in the Section 2.4.1, the experimental current-voltage characteristic of twisted pair is plotted as shown in Figure V.22. Measured points are shown by asterisks.

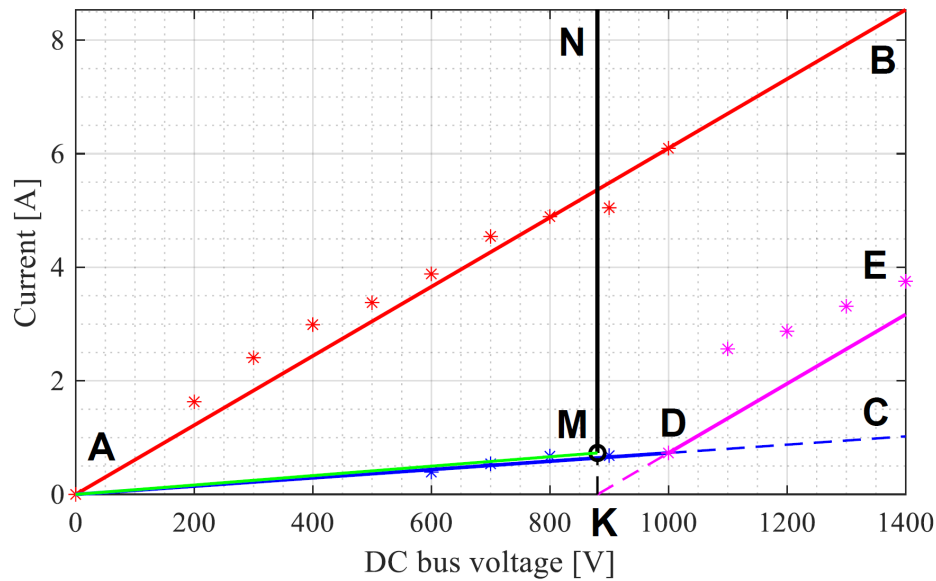


Figure V.22: Current-voltage characteristic of twisted pair:
 AB – current-voltage characteristic of dielectric barriers,
 AC – current-voltage characteristic of twisted pair without discharges,
 DE – current-voltage characteristic of twisted pair with discharges,
 and MN – current-voltage characteristic of discharges in air gaps.

The obtained theoretical and experimental current-voltage characteristics do not perfectly match but they are similar. Considering the stochastic nature of partial discharges and large range of observed currents values this study may be refined by further measurements collecting currents on longer acquisition time. The discharge current depends not only on the applied voltage. It may be increased by internal processes, such as a photo-ionization forming new charges. On the other hand, the characteristic salient point corresponded to PDIV may be shifted because this value depends on experimental conditions such as temperature, atmospheric pressure, humidity. Moreover, the voltage redistribution at damping resistor and twisted pair occurs at the moment of discharges ignition that causes fluctuations of measurement results. The real capacitive current is different from the theoretical one due to parasitic capacitances of the experimental setup not considered in calculations.

The conducted study shows that the method based on the barrier discharge theory may be applied to the twisted pair in further investigations.

3 Study of turn insulation deterioration

The previous sections show that enamel destruction mechanism can be investigated basing on the barrier discharges approach. In this regard, the further study of the destruction mechanism of enamel insulation when subjected to fast and high switching frequency voltage pulses is proposed. The twisted pair specimens have been tested un-

der impulse voltage at $600 \div 1400$ V peak voltage range and $20 \div 70$ kHz frequency range. Specimens' temperatures, currents and light emission spectra are measured. In addition, microscopic images and electrostatic simulations were made with the purpose to link the discharges arising between enamelled wires and erosion on their surface.

3.1 Experimental study

Experimental study was carried out on the twisted pairs made of conventional enamelled wire PETD-180, the same as that used in previous sections. The sketch of the experimental setup complemented with additional equipment is given in Figure V.23. As in previous tests a full bridge inverter topology is used to generate bipolar pulses and the tested specimen is connected to inverter's midpoints. The transient overvoltage and oscillations are limited using the damping resistor and the toroidal ferrite core at the inverter output. The current shunt $R_{sh} = 1.03 \Omega$ and RC-divider 280:1 described in Section 2.4.2 and Appendix V-B are used to measure voltage and current on the twisted pair. The heating of specimen subjected to barrier discharges was evaluated by means of the infrared camera Fluke Ti100. The Ocean optics USB2000 Spectrometer is used to analyse discharges light emission. The experiments were conducted at an atmospheric pressure, a temperature of 25°C and a relative humidity of 30%.

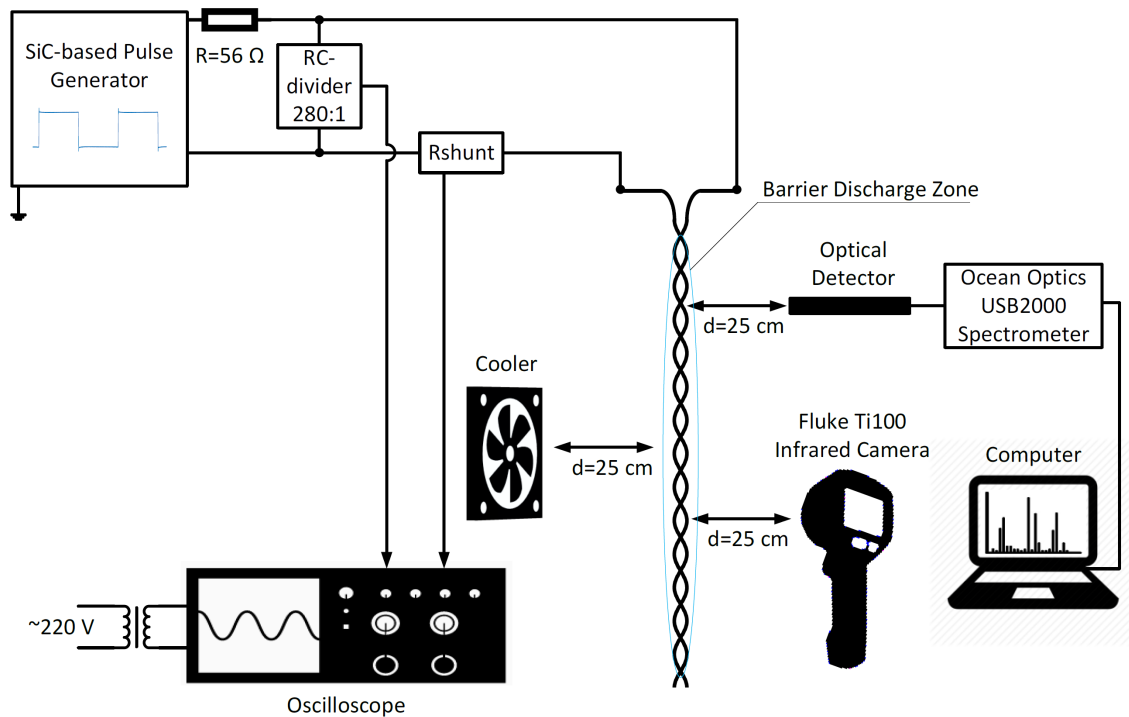


Figure V.23: Experimental setup sketch for barrier discharges study.

Study of current in the twisted pair

The twisted pair currents are measured at different voltage levels and switching frequencies. The current pulses are recorded during two impulse voltage periods as shown in Figure V.24. The maximum of positive and negative peak values of current pulses (on the rising and falling voltage rate) are plotted against voltage measured on DC bus as shown in Figure V.25. As previously mentioned, the DC bus voltage almost corresponds to the steady-state voltage amplitude applied to the twisted pair as it can be seen from measurements performed by means of the differential probe Tektronix THDP0100 (see Figure V.17). The designed RC-divider 280:1 does not provide the same measurement accuracy but allows to conduct the measurements using the the oscilloscope Tektronix TDS 2014C powered via the isolation transformer.

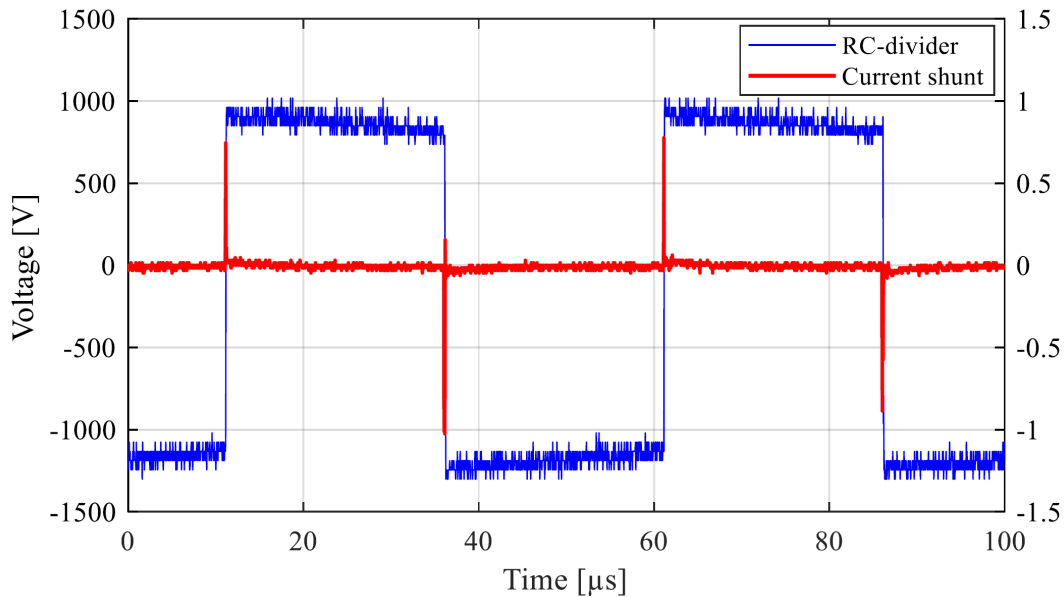


Figure V.24: Current pulses at rising and falling voltage rates $V_{dc} = 1000$ V and $f = 50$ kHz.

The performed measurements allow to conduct an analysis of frequency and voltage amplitude effects, which can be extended by further measurements collecting currents on longer acquisition time considering the stochastic nature of partial discharges. The rise of twisted pair's current can be noticed above the voltage level $V_{dc} = 1000$ V that means the start of a PDs activity (PDIV). The effect of voltage amplitude can be observed clearly, while the effect of switching frequency on current amplitude is not obvious.

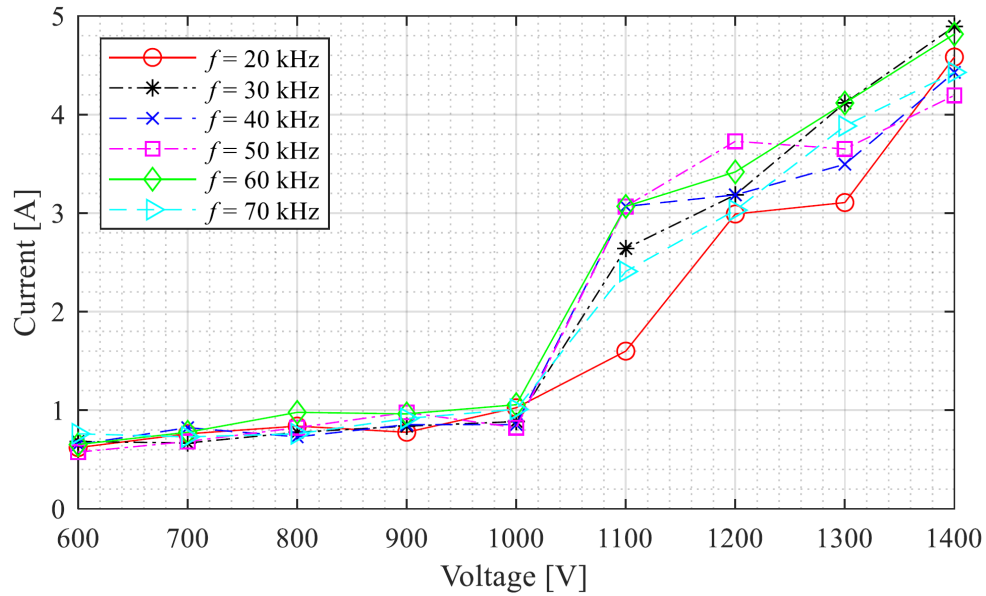


Figure V.25: Current peak values at different voltage levels and switching frequencies.

Thermal study

Basing on consideration that an important part of PD energy transforms into heat, the discharges intensity can be evaluated by temperature monitoring during the tests. The Figure V.26 gives the temperature values measured on twisted pair depending on voltage amplitudes and switching frequencies. These measurements are performed with cooling fan in order to limit it below a critical value that increase the time to breakdown.

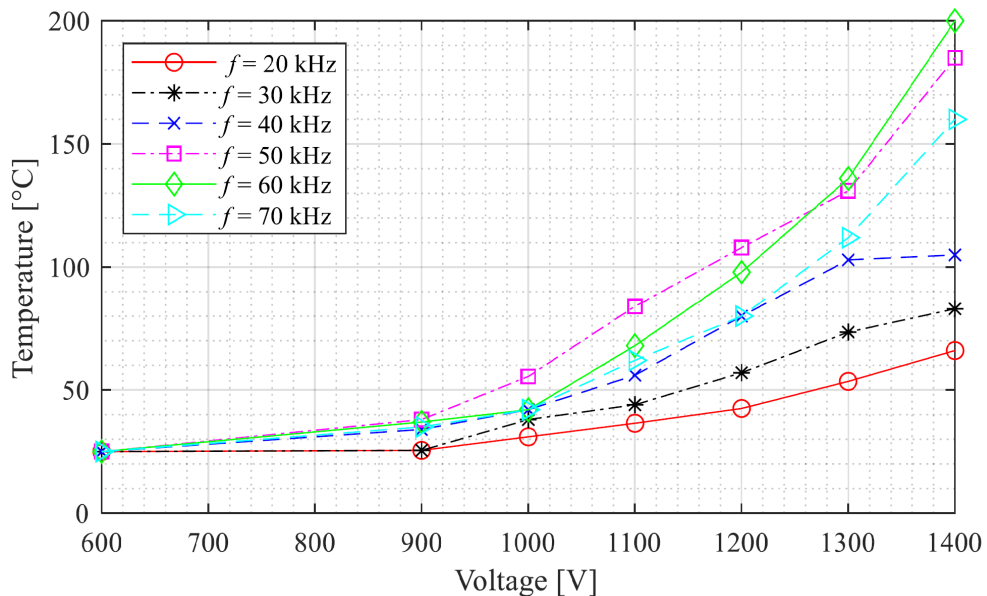


Figure V.26: Temperature measurement results at different impulse voltage amplitudes and switching frequencies.

The rapid insulation breakdown at high voltage amplitude complicates the measurements. Despite this, the obtained results put into evidence the influence of both voltage and frequency variations on the twisted pair heating by discharges, considering the fact that this heating started in the presence of PDs.

As mentioned above, the main part of discharge energy transforms into heat, the rest of this energy consumes for chemical reactions, *e.g.*, for nitrous oxide and ozone generation, and dissipates in light and sound. Basing on that, one of the methods used for study DBDs characteristics is the optical emission spectroscopy.

Optical emission study

In the light of the information provided below, this experimental study includes the analysis of light emission spectra of barrier discharges in the tested twisted pair. As in the previous tests, light spectra are measured on different voltage levels and switching frequencies. In obtained spectra the same peaks (on the same corresponding wavelengths), but of different intensities were observed. Figure V.27 reports the spectrum obtained at $V_{dc} = 1400$ V and $f = 50$ kHz. Figure V.28 summarizes the values of peak corresponded to 336.51 nm of wavelength depending on voltage amplitudes and switching frequencies. As is the case with tested specimen's temperatures, the higher frequency leads to the higher emission intensity.

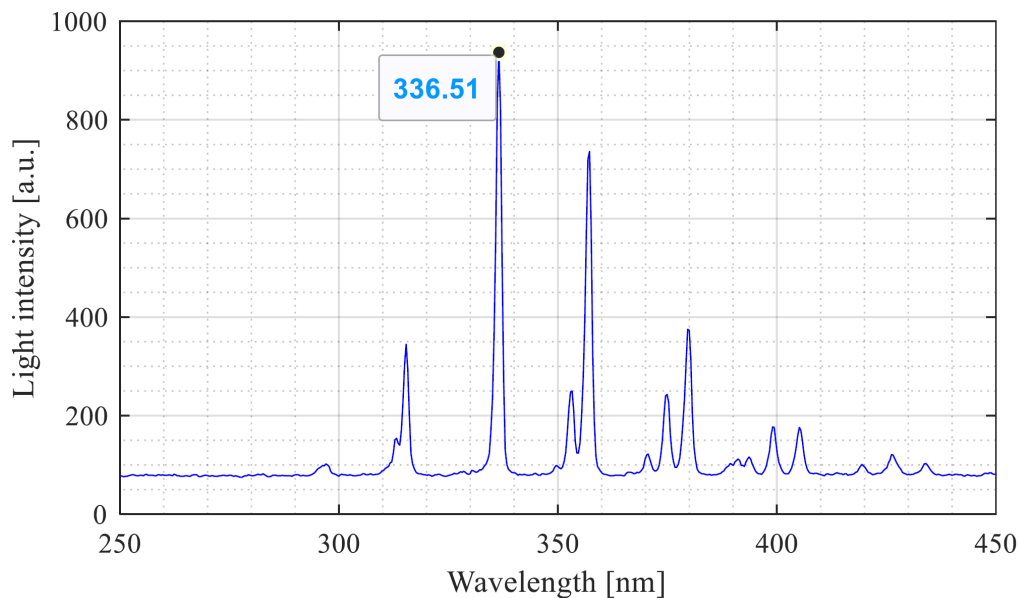


Figure V.27: Emission spectrum of barrier discharges in twisted pair at $V_{dc} = 1400$ V and $f = 50$ kHz.

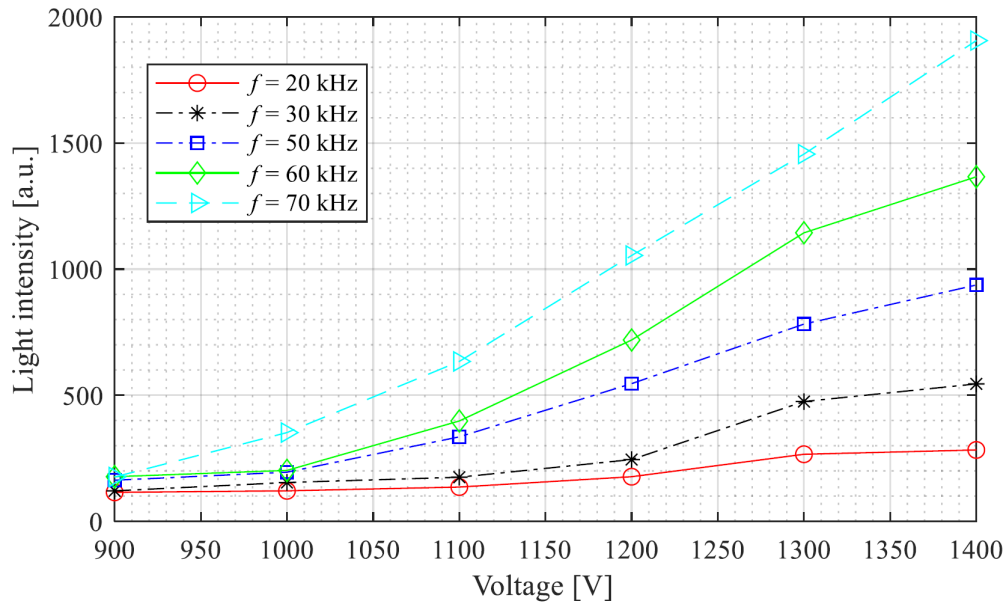


Figure V.28: Peak values of emission spectra at 336.51 nm of wavelength at different voltage levels and switching frequencies.

Microscopic study

With the purpose to study the structure of barrier discharges, photographs are taken through an optical microscope. Figure V.29 and Figure V.30 demonstrate DBDs between two enamelled wires in the tested twisted pair under impulse voltage with recorded voltage of DC bus equal to 1200 V and 1400 V and switching frequency $f = 50$ kHz. A large number of microdischarges (filaments) distributed on the dielectric surface is observed in the air gap between enamelled wires. The filaments build up surface charges which create electric field opposite to that of the applied voltage leading to the discharge extinction till the following voltage rate. The obtained images reveal the presence of repetitive filamentary structure of barrier discharges, the rise of light intensity and the propagation of discharges from the central axe between wires' turns to the wires' surface with the increasing of the applied voltage.

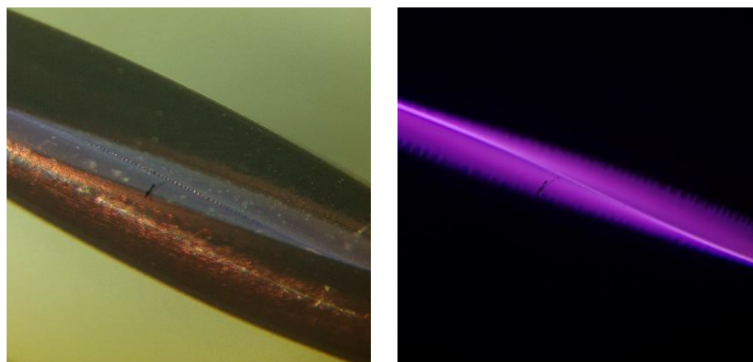


Figure V.29: Microscopic images of twisted pair turns tested at $V_{dc} = 1200$ V, $f = 50$ kHz showing filamentary structure of DBDs (twisted pair is exposed to light at left figure).

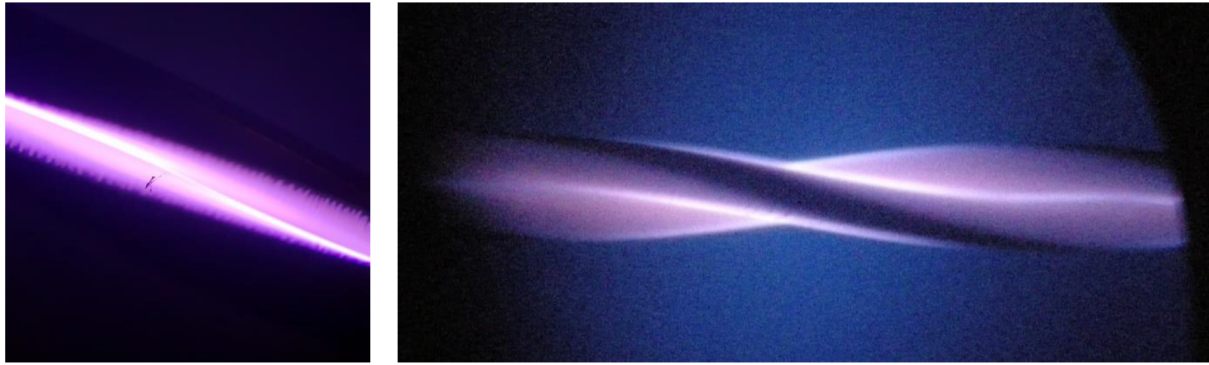


Figure V.30: Microscopic images of twisted pair turns tested under impulse voltage $V_{dc} = 1400$ V, $f = 50$ kHz showing filamentary structure of DBDs and their propagation.

Figure V.31 demonstrates the wires surface after testing at 1200 V peak amplitude of impulse voltage with switching frequency $f = 50$ kHz during 4 minutes (with cooling). The enamel erosion pattern is deep and clear (up to tenths of a millimetre), craters corresponds to tracks of observed DBDs filaments. It put into evidence a memory effect of filament and shows their role in the insulation destruction which seems to be due to the chemical reactions with the ions and radicals created by discharges. The residual electron concentration in the filament region is high enough for the next air gap breakdown followed by filament production occurring again in this region.

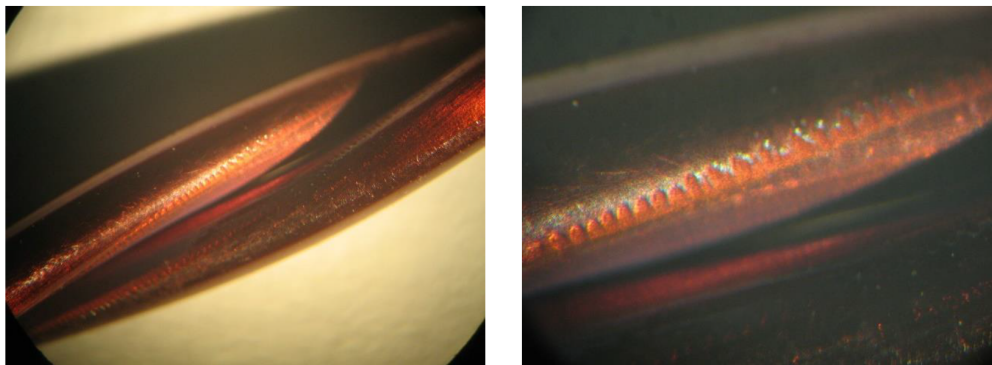


Figure V.31: Microscopic images of insulation surface with filaments track erosion.

The abrasive effect of barrier discharges on enamel insulation can be clearly observed on microscopic image given in Figure V.32 representing a cross-section of tested twisted pair placed in the epoxy resin.

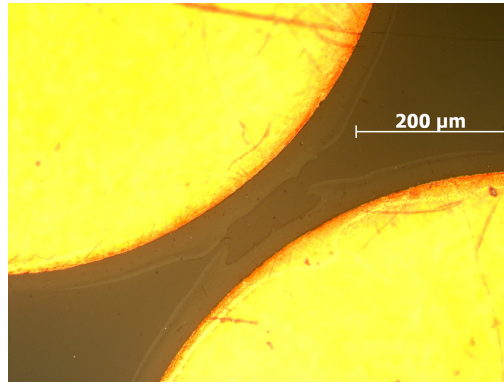


Figure V.32: Microscopic image of twisted pair cross-section.

3.2 Finite element modelling

Electrostatic simulations using FEM finds application in works dedicated to partial discharges in inverter-fed motors, *e.g.*, for evaluate PDIV within two parallel winding wires [14] or to localize the maximum electric field strength in air gaps of twisted pair [36]. In this thesis, the FEM modelling was performed with the purpose to link the areas of high electric field between wires' turns giving rise to barrier discharges and damaged insulation areas.

The electric field distribution in the twisted pair is calculated using ANSYS Maxwell 2D Electrostatic solver. The twisted pair is modelled by two copper conductors coated with polyimide insulation layer surrounded by air (without impregnation). The relative permittivity of polyimide used in the simulations is $\epsilon_r = 3$, and $\epsilon_{air} = 1.003$ was set for the air. The wire's diameter and insulation thickness corresponds to tested specimens' dimensions. Two cases were studied: firstly, when the two wires touched one another $d_{gap} = 0$ and secondly, than there was a distance between insulation layers $d_{gap} = 0.003$ mm (microgap in zone A) as shown in Figure V.33a and V.33b respectively. The excitation corresponding to various voltage levels from 600 to 1400 V was set on the one copper conductor and 0 V (ground) on the other.

The electrostatic calculation of electric field distribution cannot provide the information about frequency effect, but highlights the voltage amplitude influence, which can be correlated with experimental results and observations. Figure V.34 shows the simulation of the electric field distribution between two twisted pair turns. Figure V.35 and Figure V.36 gather simulation results of the electric field intensity E distribution in air along line 1-2 (shown in Figure V.34) at $600 \div 1400$ V voltage range.

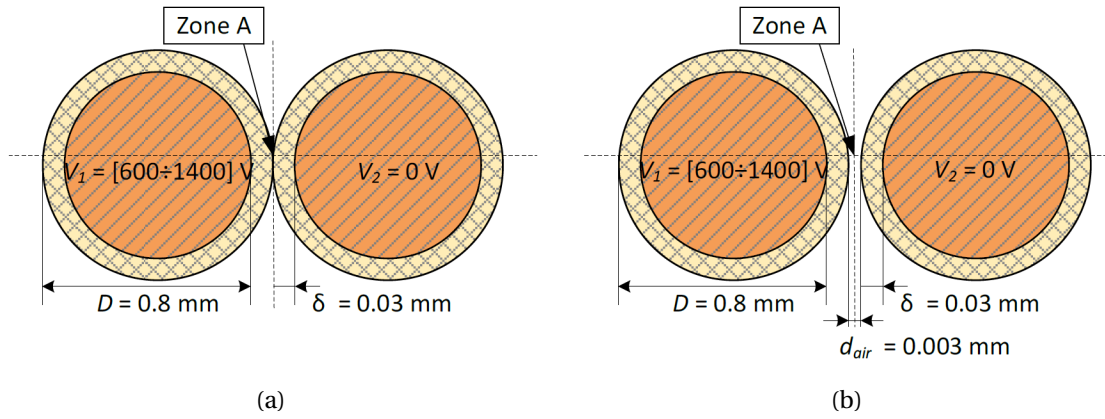


Figure V.33: Geometry of twisted pair turns in electrostatic calculations:
(a) two wires touched one another, (b) microgap between wires.

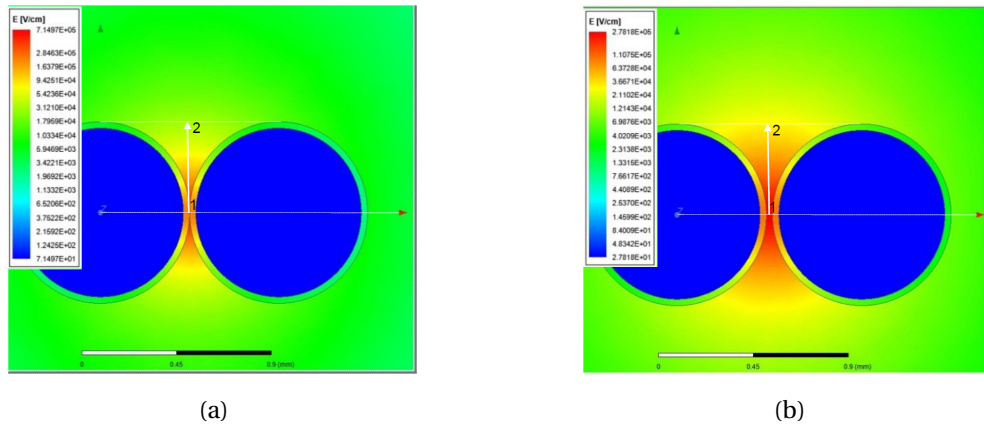


Figure V.34: Electric field between twisted pairs turns at 1400 V excitation voltage (a) when $d_{gap} = 0$ and (b) when $d_{gap} = 0.003$ mm.

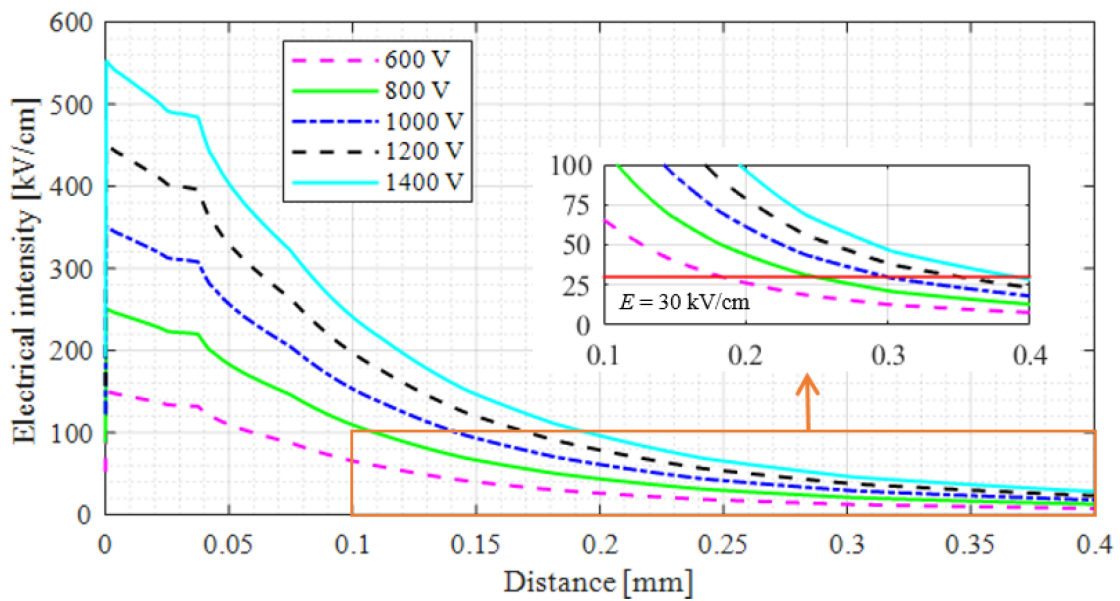


Figure V.35: Electrical intensity distribution in air along the line 1-2 when $d_{gap} = 0$.

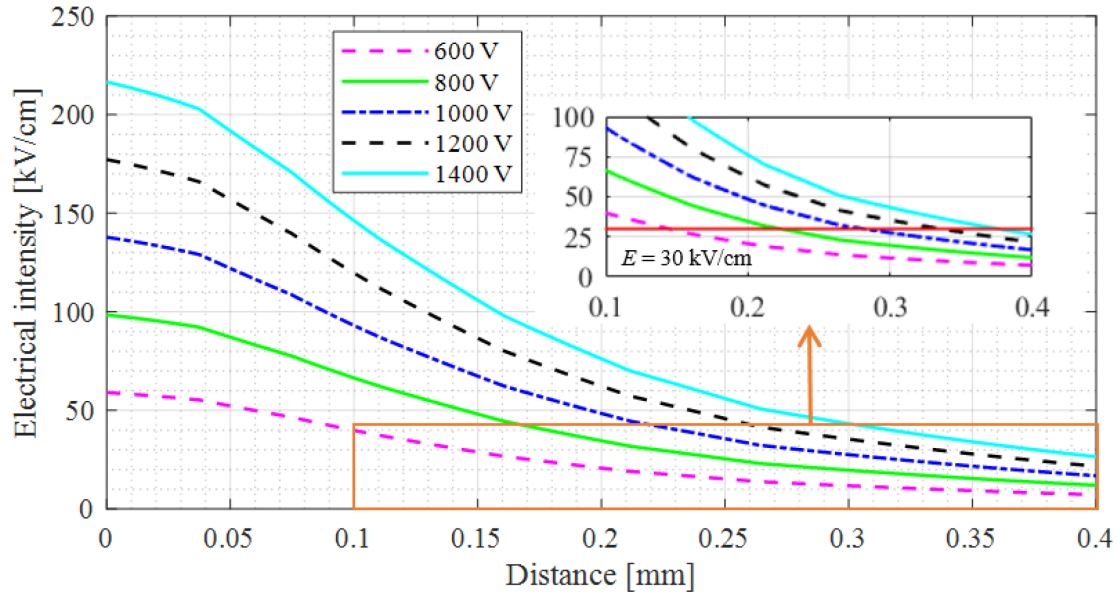


Figure V.36: Electrical intensity distribution in air along the line 1-2 when $d_{gap} = 0.003$ mm.

Modelling results show that the voltage starting from 600 V might be sufficient for air ionization in microgaps and the further voltage rise will enlarge the ionization zone between wires. The discharge inception criteria is define here as the air dielectric strength 30 kV/cm under uniform and weakly nonuniform electric fields (red line in Figure V.35 and Figure V.36). The electric field is weakened in presence of the microgap between enamelled wires but high enough to provoke the air ionization. Moreover, the propagation length of the filaments correlates with FEM simulation results where the electric field at 1400 V is high enough that a discharge may probably occur at the distance up to 0.4 mm.

On the basis of the results obtained by numerical simulation and experimentally, several results have been highlighted. The impulse voltage having steep dV/dt and switching frequency from 20 to 70 kHz provokes higher air volume ionization favouring filamentary mode. It leads to an erosion craters formation on enamel insulation as result of filaments' tracks. The propagation of damaged zone correspond to zones of high electric field between wires' turns simulated by FEM. The same peaks of light emission spectra were observed on various frequencies. On the other hand, in presence of DBDs the increase of switching frequency results in higher discharge repetition rate and their higher energy as seen from temperature and spectrum measurements. The heating of tested specimen increases capacitive currents, intensifying the electric field that enlarges filaments, acting on the insulation surface, and accelerates insulation destruction.

4 Synthetic experimental setup for turn insulation testing

The experimental study discussed above was performed at room temperature. If the additional heating should be provided the utilization of the thermal chamber as shown in Chapter III would complicate the access to the tested specimen. To overcome this drawback a synthetic test bench with two different voltage sources is proposed. The idea consists in the implementation of sinusoidal voltage source to heat the tested specimen by currents at the same time with the application of the impulse (or sinusoidal) voltage provoking the partial discharges. It also gives a possibility to conduct tests at nominal current. The performed tests show that the electric circuit for wires heating is not disturbed by PDs activity or breakdown of twisted pairs. The sketch of the experimental setup is shown in Figure V.37 and photographs of practical realisation are given in Figure V.38. The easy access to the tested specimen allows to observe it using infrared camera, microscope and spectrometer.

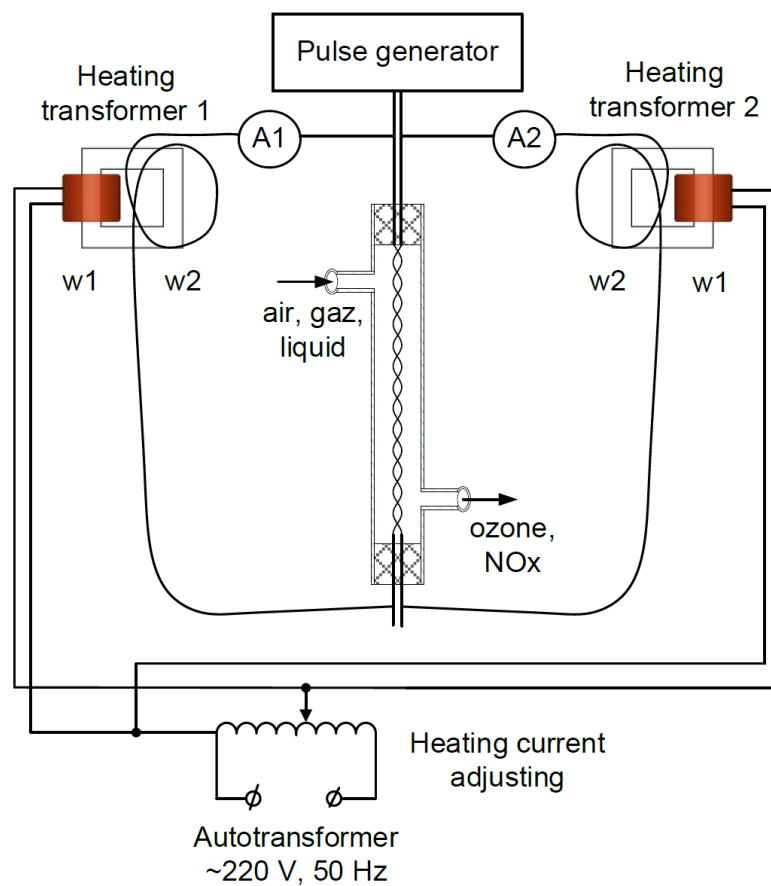


Figure V.37: Sketch of the proposed synthetic experimental setup.

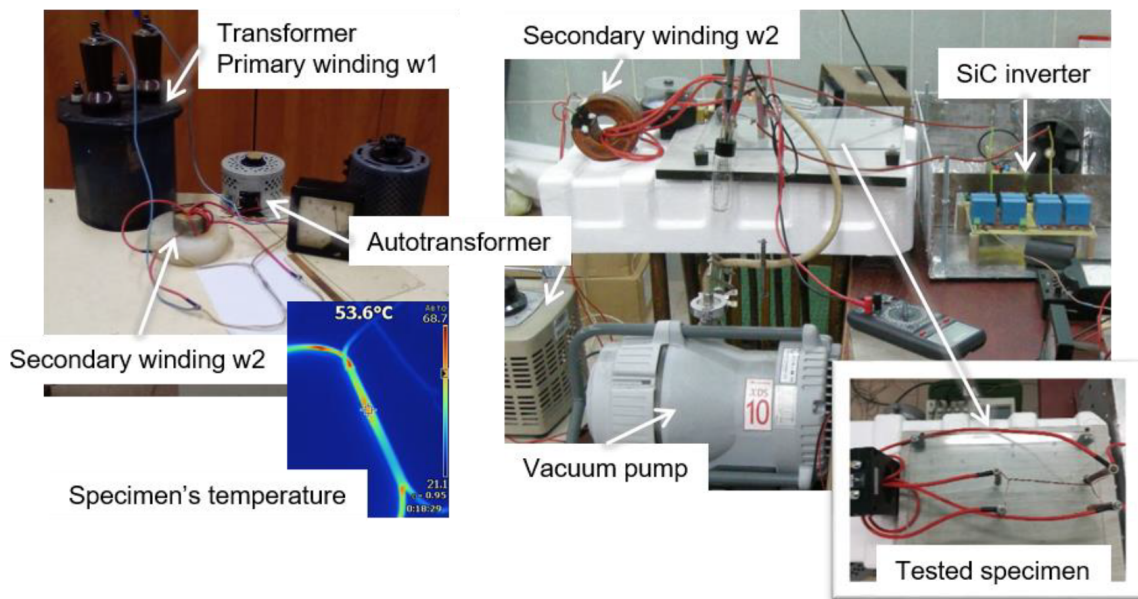


Figure V.38: Photographs of the synthetic experimental setup realisation.

Moreover, if the tested specimen is placed in the hermetical glass tube, the influence of a gas or a liquid on PDs may be investigated, or chemical products produced by PDs activity may be extracted and analysed. The quartz glass should be utilized because it is acid-resistant, transmits almost 100% of ultraviolet, visible and infrared light, it is also heat-resistant and excellent insulator.

The utilization of the hermetic glass tube also offers a possibility to conduct tests at low pressure using a vacuum pump as demonstrated in Figure V.38 and Figure V.39. The experimental study at low pressure is a relevant task for characterization of partial discharges and insulation destruction of electrical equipment in aerospace applications. If a vacuum chamber is not available, the proposed setup may be used. It also allows to keep easy access to the tested specimen for observations.

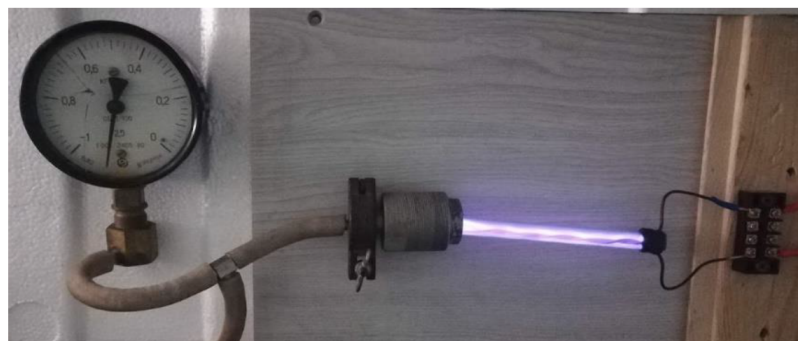


Figure V.39: Partial discharges on twisted pair tested under low pressure.

One of the tests conducted at low pressure was the estimation of pressure level corresponded to a minimum of PDIV of twisted pair. Firstly, the pressure in the glass

tube with the tested twisted pair is decreased to 9×10^{-2} mm Hg. This pressure level excludes the ignition of partial discharges at voltage level up to 1400 V (high dV/dt test bench). Then, the atmospheric air is injected into the tube, the pressure is measured, and the impulse voltage applied to the twist pair is progressively increased from 0 to 1400 V, $f = 50$ kHz, at a fixed pressure. The partial discharge ignition is determined observing the twisted pair current and the optical emission. Therefore, PDs were observed at minimum voltage level of 370 V when the pressure in the glass tube was equal to 38 mm Hg.

In the absence of PD, the heating of tested specimen (observed by the infrared camera) is only due to its dielectric losses: conductivity and relaxation losses, while the ionization losses are omitted. The temperature measurements of specimen tested under 1300 V and 50 kHz at 38 mm Hg shows very slight heating without PD. It indirectly indicates that the observed high temperature rise of specimen in previous tests is mainly caused by partial discharges. At the same time, the temperature increase caused by PD leads to higher dielectric material conductivity and dielectric losses.

The conducted experimental study of PDs in twisted pairs under low pressure also shows that insulation defects can be put into evidence in certain conditions. Figure V.40 demonstrate the visualization of the point defects by partial discharges as a bright glow at the defective areas.

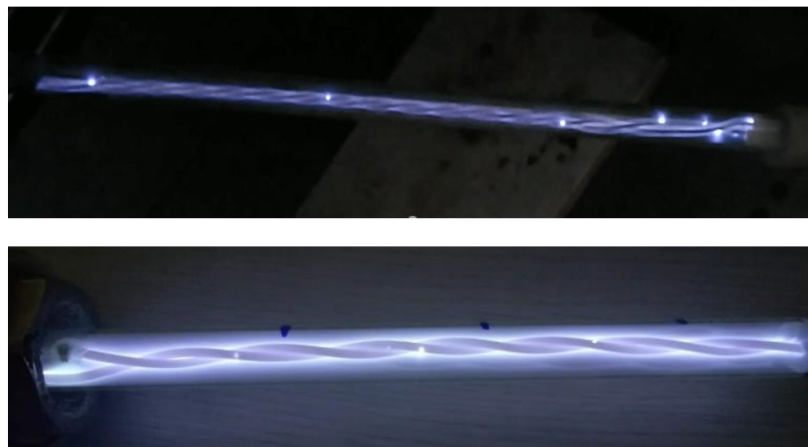


Figure V.40: Visualization of insulation defects in twisted pair tested under low pressure.

In the order to visualize the weakest insulation spots avoiding specimen destruction the energy of discharges should be limited by decreasing of voltage. Firstly, the minimum voltage level allowing clear defects visualization is determined varying the pressure in the glass tube. The optimal ranges are estimated as $500 \div 1000$ V of applied voltage and $1 \div 10$ mm Hg of pressure. Then, if the tested specimen destruction occurs, the current should be limited by adding a 1 M Ω resistor.

This additional experiments show the possible ways to use the high dV/dt impulse voltage for insulation defects detection, or to extend the present study considering the low pressure effect that may be interest for aeronautical applications.

5 Conclusion

To deal effectively with partial discharges in the turn insulation and to limit their consequences, these phenomena should be thoroughly investigated considering the characteristics of applied electric stresses, specifically for high dV/dt impulses, and studied specimens. For this purpose, the experimental test bench and the twisted pair are modelled using different approaches. Firstly, the impact of high voltage rate on the voltage transients even with short cable connections is analysed. To limit the transient overvoltage a damping resistor is added in the scheme for the following experiments.

On the other hand, the modelling of the twisted pair using the barrier discharge approach offers an opportunity to apply the methods developed for plasma and ozone generators in our study revealing common aspects. Thus, the current-voltage characteristics of twisted pair in the absence and presence of barrier discharges are given. These characteristics can be used for the discharges energetic aspects study. However, the current measurements method should be improved. The proposed equivalent circuit of twisted pair with barrier discharges allows to separate discharge current and capacitive current, especially significant at high dV/dt . This model can be refined by additional series and parallel resistors taking into account conductivity and relaxation losses.

The performed current, temperature and spectra measurements show high energy of barrier discharges increasing with the electric field strength and the switching frequency. The total energy of barrier discharges is mainly divided between generation of ozone and NO_x, heating of tested specimen and heat transfer by convection, and UV radiation. Higher is this energy, faster will be the insulation degradation. Depending on energy distribution between different processes, the electro-chemical or the electro-thermal destruction will predominate. For the first time, the filamentary structure of barrier discharges in the twisted pair subjected to high dV/dt is put into evidence that allows to relate the enamel insulation destruction with chemical etching by repetitive filaments. Moreover, the rise in switching frequency and voltage amplitude increase filaments propagation zone enlarging the deteriorated insulation surface.

To go further in the experimental study, the synthetic test bench is proposed. It provides a possibility to combine different electrical stresses using two voltage sources, and to control the media of tested specimen, changing the gas or adding a liquid, varying the pressure. Furthermore, the possibility of the insulation weakest spots visualization by barrier discharges at low pressure is demonstrated.

The observations made on the twisted pair may be used for understanding of turn insulation destructions mechanisms as long as this insulation has defects and air gaps. In this case, layers of enamel insulation and impregnating varnish compose the dielectric barriers and the air gap ionization between these barriers may occur depending on the machine's operation conditions.

References

References

- [1] *IEC 60851-5:2008. Winding wires - Test methods - Part 5: Electrical properties.* Ed. 4.0 edition, 2008.
- [2] *IEC 60851-6:2012. Winding wires - Test methods - Part 6: Thermal properties.* Ed. 3.0 edition, 2012.
- [3] *IEC 60851-4:2016. Winding wires - Test methods - Part 4: Chemical properties.* Ed. 3.0 edition, 2016.
- [4] *IEC 60851-3:2009. Winding wires - Test methods - Part 3: Mechanical properties.* Ed. 3.0 edition, 2009.
- [5] J. F. Dexter. Thermal evaluation of enameled magnet wire. *Electrical Engineering*, 75(3):258–263, mar 1956.
- [6] D.J. Barta. Revisions of the periodic conformance testing procedures in the NEMA MW 1000 magnet wire standard. In *Proceedings Electrical Insulation Conference and Electrical Manufacturing Expo, 2005.*, pages 1–4. IEEE, 2005.
- [7] M. Fenger, S.R. Campbell, and J. Pedersen. Motor winding problems caused by inverter drives. *IEEE Industry Applications Magazine*, 9(4):22–31, jul 2003.
- [8] Peng Wang, Hongying Xu, Jian Wang, Wanya Zhou, and Andrea Cavallini. The influence of repetitive square wave voltage rise time on partial discharge inception voltage. In *2016 IEEE Conference on Electrical Insulation and Dielectric Phenomena (CEIDP)*, pages 759–762. IEEE, oct 2016.
- [9] Peng Wang, Hongying Xu, Jian Wang, Andrea Cavallini, and Gian Carlo Montanari. Temperature effects on PD statistics and endurance of inverter-fed motor insulation under repetitive square wave voltages. In *2016 IEEE Electrical Insulation Conference (EIC)*, pages 202–205. IEEE, jun 2016.
- [10] Gian Carlo Montanari, Fabrizio Negri, and Fabio Ciani. Partial Discharge and life behavior of rotating machine wire insulation under PWM waveforms: The influence of inverter characteristics. In *2017 IEEE Electrical Insulation Conference (EIC)*, pages 161–164. IEEE, jun 2017.

-
- [11] Francesco Guastavino, Alessandro Ratto, Eugenia Torello, and Giovanna Biondi. Aging Tests on Nanostructured Enamels for Winding Wire Insulation. *IEEE Transactions on Industrial Electronics*, 61(10):5550–5557, oct 2014.
- [12] Farah Salameh, Antoine Picot, Marie Chabert, and Pascal Maussion. Parametric and Nonparametric Models for Lifespan Modeling of Insulation Systems in Electrical Machines. *IEEE Transactions on Industry Applications*, 53(3):3119–3128, may 2017.
- [13] Daniel Roger, Sonia Ait-Amar, and Ewa Napieralska. A method to reduce partial discharges in motor windings fed by PWM inverter. *Open Physics*, 16(1):599–604, 2018.
- [14] Loucif Benmamas, Philippe Teste, Guillaume Krebs, Emmanuel Odic, Franck Vangraefscheppe, and Tahar Hamiti. Contribution to partial discharge analysis in inverter-fed motor windings for automotive application. In *2017 IEEE Electrical Insulation Conference (EIC)*, pages 348–351. IEEE, jun 2017.
- [15] Steven Ellingson. *Electromagnetics, Volume 1*. VT Publishing, aug 2018.
- [16] Sina Ebnesajjad. *Fluoroplastics. Melt Processible Fluoropolymers - the Definitive User's Guide and Data Book Book*, volume 2. Elsevier, 2nd edition, 2016.
- [17] Alain ANTON. Caractéristiques électriques des matériaux isolants. Ref: TIP510WEB - "Constantes physico-chimiques", nov 2003.
- [18] Власов, Ю.А. Анализ влияния внешних факторов на диэлектрическую проницаемость работающего масла. *Современные проблемы науки и образования*, 6, 2013.
- [19] Yugong Wu, Xuanhe Zhao, Fei Li, and Zhigang Fan. Evaluation of Mixing Rules for Dielectric Constants of Composite Dielectrics by MC-FEM Calculation on 3D Cubic Lattice. *Journal of Electroceramics*, 11(3):227–239, dec 2003.
- [20] H.A. Wheeler. Formulas for the Skin Effect. *Proceedings of the IRE*, 30(9):412–424, sep 1942.
- [21] Mike Melfi, A.M.J. Sung, Sidney Bell, and G.L. Skibinski. Effect of surge voltage rise-time on the insulation of low-voltage machines fed by PWM converters. *IEEE Transactions on Industry Applications*, 34(4):766–775, 1998.
- [22] F-R. Bohm, Klaus Nagel, Heinz Schindler, Frank Rainer Böhm, Klaus Nagel, and Heinz Schindler. A new generation of wire enamel for the production of magnet wires with outstanding corona resistance. In *Proceedings: Electrical Insulation Conference and Electrical Manufacturing and Coil Winding Technology Conference (Cat. No.03CH37480)*, pages 109–113. IEEE, 2003.

- [23] Xin Zhong, Akram Shakeel, Yan Yang, Guoqiang Gao, and Guangning Wu. Preparation and corona-resistance characteristics of double-layer polyimide/Al₂O₃ nanocomposite film. In *2016 IEEE International Conference on High Voltage Engineering and Application (ICHVE)*, pages 1–4. IEEE, sep 2016.
- [24] Greg C. Stone, Ian Culbert, Edward A. Boulter, and Hussein Dhirani. *Electrical Insulation for Rotating Machines*. John Wiley & Sons, Inc., Hoboken, NJ, USA, jul 2014.
- [25] Hubert Piquet, Sounil Bhosle, Rafael Diez, and Michael V Erofeev. Pulsed Current-Mode Supply of Dielectric Barrier Discharge Excilamps for the Control of the Radiated Ultraviolet Power. *IEEE Transactions on Plasma Science*, 38(10):2531–2538, oct 2010.
- [26] Ломаев, М. И. Определение энерговыхода в эксилампах с возбуждением барьерным разрядом. *Оптика атмосферы и океана*, 14(11):1091–1095, 2001.
- [27] M. I. Lomaev, E. A. Sosnin, V. F. Tarasenko, D. V. Shits, V. S. Skakun, M. V. Erofeev, and A. A. Lisenko. Capacitive and barrier discharge excilamps and their applications (Review). *Instruments and Experimental Techniques*, 49(5):595–616, oct 2006.
- [28] Пикулев, АА and Цветков, ВМ. Моделирование процесса разряда в ячейке барьерного разряда на основе трехпараметрической модели. *Журнал технической физики*, 77(9):22–27, 2007.
- [29] A.V. Avanesov, S.G. Dambrauskas, A.T. Rakhimov, and V.B. Saenko. Generation of UV radiation and electrosynthesis of ozone at the barrier discharge with new electrode structure. *Preprint MSU SINP*, 6/827:23, 2007.
- [30] N. Mericam-Bourdet, M. J. Kirkpatrick, F. Tuvache, D. Frochot, and E. Odic. Effect of voltage waveform on dielectric barrier discharge ozone production efficiency. *EPJ Applied Physics*, 57(3):1–10, 2012.
- [31] Кучинский, Георгий Станиславович. Частичные разряды в высоковольтных конструкциях. Л.: Энергия. Ленинград, 1979.
- [32] Самойлович, Вадим Георгиевич and Гибалов, Валентин Иванович and Козлов, Кирилл Вадимович. Физическая химия барьерного разряда. МГУ, 1989.
- [33] Шваб, Адольф. Измерения на высоком напряжении: измерительные приборы и способы измерения. Энергоатомиздат, 1983.
- [34] Тэнэеску, Ф. and Крамарюк, Р. Электростатика в технике. Энергия, 1980.
- [35] Тареев, Борис Михайлович. Физика диэлектрических материалов: Учебное пособие. Энергоиздат, 1982.

- [36] Marek Florkowski, Barbara Florkowska, and Pawel Zydron. Partial Discharges in Insulating Systems of Low Voltage Electric Motors Fed by Power Electronics—Twisted-Pair Samples Evaluation. *Energies*, 12(5):768, feb 2019.

Conclusion and future work

Conclusion and future work

The experimental investigation and numerical simulation study performed in this work are essentially focused on the effects of impulse voltage with high dV/dt and high switching frequency on winding insulation robustness of inverter-fed electrical machines. Therefore, the work covers a number of issues related to electric drives, power electronics, electrical machines, dielectric materials and partial discharges. Its relevance is due to the implementation of wide bandgap semiconductors, such as Silicone Carbide, in power electronic inverters that may intensify the electric stresses in motor drives, accelerating motor's winding insulation failure.

Chapter I provides a literature survey devoted to low voltage electrical machines and their insulation system. It synthesizes the factors affecting electrical machines winding insulation during their fabrication (compatibility of winding wires and impregnating composition) and operation (thermal, electrical, ambient and mechanical stresses). Particular attention should be paid to electrical stresses due to impulse supply voltage in inverter-fed motors. As can be seen from the literature, the electrical machines driven by power converters with pulse width modulation are subjected to repetitive surges due to fast changing voltage pulses and reflection phenomena in supply cable, as well as non-uniform voltage distribution in the stator winding. The overvoltage at motor terminals leads to partial discharge inception accelerating winding insulation degradation and causing its premature failure, that is especially critical for Type I insulation used in low voltage machines (up to 700 V RMS rated voltage).

At the same time, power electronics technology does not stand still. The development of Silicon Carbide technology for power electronics offers better performances than demonstrated by Silicon-based power semiconductor devices. SiC-based power converters show high power density, fast and high frequency switching. However, the use of SiC-based power electronics in the electric drive increases electrical stresses in controlled electrical machine. Machine's windings may experience higher overvoltage caused by very short impulse rising and falling times (ns-level), electrical insulation is subjected to steep voltage changing rates, that may increase a risk of PD and accelerate insulation ageing and destruction. In this regard, constraints related to high dV/dt impulse voltage waveform generated by SiC-based inverters and their effects on winding insulation should be thoroughly investigated.

Following up upon the literature survey, Chapter II deals with the study of transient overvoltage in motor fed by inverter that allows to estimate the electrical stresses causing the motor winding insulation degradation. For this purpose, a high frequency model from the literature has been used for electric drive simulations. High frequency models found in literature are typically intended to examine and predict transient phenomena in induction motors being the most widely used electrical machines. At the same time, other machines' types, which are used in electric drives, also need to be considered. Therefore, our study focuses on the modelling of the switched reluctance machine which is particularly interesting due to its redundant and fault tolerant construction, particular control using asymmetric bridge converter and concentrated winding construction by contrast with induction motors. Moreover, an absence in literature of SRM models for analysis of high frequency behaviour makes it a crucial task.

Basing on the existing models developed for three-phase induction motors, the studied switched reluctance motor (3-phase, 6-slot, and 4-pole, $V_{dc} = 300\text{ V}$) has been modelled by equivalent circuits with lumped parameters. Model parameters have been derived from impedance measurements in frequency range from 30 kHz to 30 MHz. Performing a model validation in frequency-domain, we have observed a good correlation between measured and simulated results. We have studied the transient overvoltage in motor winding combining the suggested motor equivalent circuit and a multi-cell model of feeding cable proposed in the literature. Owing to the fact, that the phases of SRM may be energized independently, single-phase and single commutation simulations have been performed approximating the inverter voltage by an ideal pulse generator with specified rise/fall times and dV/dt . Simulation results confirm that the steeper voltage rates leads to the greater overvoltage. It should be noted, that in case of extremely short rise time up to 10 ns, even one meter of power cable represents a critical length. Furthermore, the increasing in cable length intensifies the transient overvoltage, affects the oscillation frequency and makes the transient oscillations longer. However, the overvoltage value do not reach two times of pulse generator voltage that may be related to cable losses presented in the model. The performed study correlates with the previous works and highlights the importance of high dV/dt effects characterisation.

In order to investigate the effects of voltage waveform parameters, such as dV/dt and switching frequency, on winding insulation, different testing methods are proposed in Chapter III. Considering the fact, that the turn insulation is the weakest element of electrical machine winding, endurance tests have been carried out on standard twisted pair specimens made by conventional and corona resistant enamelled wires for random wound winding type. As for the concentrated winding made with rectangular wire, a novel specimen's shape representing a coil is proposed for testing enamelled rectangular section winding wires.

First of all, the breakdown voltage and endurance testing under sinusoidal voltage of 50 Hz nominal frequency is described. Then, the endurance tests under PWM-like impulse voltage having considerably low dV/dt up to 0.4 kV/ μ s with rise time of 4 μ s is presented. This experimental bench previously developed and installed at TPU (Russia) contains a pulse generator allowing an adequate reproducing of stresses typical for inverter-fed motors with electronic devices based on Silicon technology. Associating this pulse generator with a thermal chamber makes it possible to combine electrical and thermal stresses for endurance tests.

With the purpose to apply the electrical stresses on turn insulation engendering by Silicone Carbide high-speed switches, we have developed an experimental bench integrating a SiC-based pulse generator at SATIE laboratory (France). Firstly, a half-bridge inverter have been designed with modern SiC MOSFET transistors having ns-level rise time with maximum voltage amplitude up to 1200 V and switching frequency up to 64 kHz. It already allowed us to apply very steep voltage rates and served us as a first prototype for the high dV/dt test bench. Consequently, a full bridge topology SiC-based pulse generator has been designed at SATIE laboratory, and the high dV/dt test bench containing the thermal chamber and measuring tools has been assembled in TPU. The pulse generator provides high dV/dt impulse voltage (up to 60 kV/ μ s applied to tested specimen), voltage amplitude up to 1700 V and maximum switching frequency up to 125 kHz. Adjusting the voltage waveform parameters, we can study their effect on enamel insulation degradation. Considering the fact that the overvoltage in inverter-fed motor may exceed the value of partial discharge inception voltage, all the insulation endurance tests have been conducted in presence of partial discharges representing the main ageing factor. The PDs activity has been detected using optical, electromagnetic and chemical methods. The weakest partial discharges have been observed when applying sinusoidal voltage and the high dV/dt impulse voltage given rise to intensive, bright PDs.

The experimental protocols followed by the obtained results and their analysis are provided in Chapter IV. Tests have been conducted on unimpregnated specimens made of winding wires different in enamel compositions in order to evaluate and compare their resistance to PDs applying various voltage waveforms: sinusoidal, impulse with low dV/dt , impulse with high dV/dt , and to choose the optimal insulation type for inverter-fed motors. The mean time to breakdown has been used as the end-point criterion for the insulation endurance evaluation. In line with expectations, the corona resistant wire mainly shown better endurance comparing with the conventional wires. The rectangular section wire also demonstrated higher mean time to breakdown than other conventional wires that may be related to its higher thermal index and thicker insulation.

The study of influence of defects on turn insulation endurance has been carried out. For this purpose, non-defective unimpregnated, defective unimpregnated and defective impregnated by different compositions specimens were tested under impulse volt-

age with low dV/dt . Comparing the obtained mean times to breakdown, we noticed that, firstly, independent defects critically affect the turn insulation when subjected to PDs and, secondly, the impregnation may not provide sufficient defects “healing” that highlights the importance of compatibility of enamel insulation and impregnating composition.

The experimental results presented in this Chapter illustrate the following:

- heating of specimens in the thermal chamber at temperature corresponding to their thermal index significantly accelerates the insulation destruction when subjected to PDs (electro-thermal failure mechanism);
- in specimens tested under sinusoidal voltage with frequency of 50 Hz and under low dV/dt PWM-like impulse voltage with carrier frequency of 5 kHz, breakdown mainly occurred at defective area; the “frost effect” and localized damages were observed on the insulation surface (domination of electrical and chemical failure mechanisms);
- in specimens tested under high dV/dt voltage with switching frequency of 50 kHz the effect of carbonization and sticking of turns were observed (domination of thermal destruction mechanism).

These observations put into evidence the effect of impulse voltage having short rise time and high switching frequency on partial discharges leading to higher ozone concentration and significant temperature rise extremely shortening the insulation life time. Unfortunately, the effects of high dV/dt and high switching frequency could not be separated that complicates the analysis of dV/dt effect. On the other hand, the interest of higher frequency operation is linked to fast switching SiC transistors enabling the conduction losses reduction.

The presented above experimental results motivated me to examine more thoroughly deterioration processes in turn insulation subjected to high dV/dt impulse voltage as well as the features of arising partial discharges as described in Chapter V. The twisted pair specimens have been used for conducting this phenomenological study.

Firstly, the overvoltage caused by cable connections between the laboratory-designed SiC-based pulse generator and the tested twisted pair has been modelled and analysed basing on electromagnetic approach and low-loss transmission line approximation. The obtained results highlight the importance to minimize the cable line length to limit the voltage oscillations and surges that correlates with the observations described in Chapter II. Secondly, considering partial discharges arising in air gaps between twisted pair turns as barrier discharges, the dielectric barriers in twisted pairs have been modelled. It allowed us to analyse numerically and experimentally obtained current-voltage characteristics, linking the specimen geometry and relative permittivity with the inception voltage, and separating barrier discharges current and capacitive current, especially significant at high dV/dt . However, the current and voltage measurements when applying the

impulse voltage with very short rising time is a challenge to overcome because it requires an accuracy which may be difficult to achieve with the available and laboratory-designed probes.

The performed current, temperature and emission spectra measurements show high energy of barrier discharges increasing with the switching frequency rise and the electric field strength (also demonstrated by performed electrostatic calculations using finite element modelling). The obtained microscopic images of barrier discharges and enamel insulation surface erosion put into evidence the filamentary structure of discharges relating to the insulation destruction with chemical etching by repetitive filaments. Thus, the destruction mechanism of turn insulation subjected to high dV/dt impulse voltage corresponds to ionization breakdown. The discharge between the dielectric barriers produces heat and UV radiation, generates ozone and NO_x, leads to accelerated charged electrons and ions bombarding and additional heating of the dielectric surface (dielectric barriers). Depending on energy distribution between different processes the electrochemical breakdown or the electro-thermal breakdown will occur. To go further in the experimental study, we propose a synthetic test bench containing two voltage sources (the sinusoidal voltage source providing the specimen heating and the pulse generator to apply the impulse voltage) and providing a possibility to control the pressure and the media (gas, liquid) of tested specimens. The tests performed on twisted pairs under impulse voltage and low pressure allowed us to visualize the weakest insulation spots by partial discharges that could be used for insulation defectiveness estimation.

The main results and contributions of the present thesis:

- high frequency model intended to study of transient overvoltage in inverter-fed switched reluctance machine's winding has been proposed;
- test bench containing SiC-based pulse generator providing high dV/dt impulse voltage (up to 60 kV/ μ s applied to tested specimen), voltage amplitude up to 1700 V and maximum switching frequency up to 125 kHz has been designed;
- novel specimen's shape for testing rectangular section wires has been designed;
- synthetic test bench containing two voltage sources offering a possibility to apply desired impulse voltage waveform to the tested specimen and at the same time to control its temperature, pressure and media has been proposed;
- estimation of insulation defectiveness using defects visualization when tested specimens subjected to high dV/dt impulse voltage exceeding the partial discharge inception level and low pressure has been suggested;
- partial discharges in air gaps between turns of tested twisted pairs have been characterized as the dielectric barrier discharges; having regard that the twisted pair represents a physical model of machine's winding part, the PDs within the winding may be also considered and studied as dielectric barrier discharges;

- dielectric barrier discharges in twisted pairs tested under high dV/dt impulse voltage with high switching frequency have a filamentary structure creating periodical erosion tracks on the enamel surface;
- in case of barrier discharges occurred on twisted pairs subjected to high dV/dt impulse voltage with high switching frequency, the electro-thermal insulation destruction may predominate the electro-chemical one even in the absence of the external heating.

Regarding to the future work, the following points would be advisable thereafter:

- to improve the accuracy of the proposed high frequency model of the inverter-fed switched reluctance machine and the feeding cable extending the frequency range considering the possible very short impulse voltage rise time up to 10 ns;
- to develop a model to simulate the turn-to-turn voltage distribution of electrical machine's winding (distributed and concentrated);
- to study the probable distribution of defects in winding insulation which in association with the voltage distribution will make it possible to more accurately predict the zones with risk of partial discharges inception;
- using the high dV/dt test bench to establish the test procedure allowing to investigate simultaneously and separately the effects of thermal and electrical stresses;
- to enlarge this experimental study of turn insulation endurance and destruction mechanism under low pressure using a vacuum chamber or proposed in this work setup with hermetical tube and vacuum pump, in order to simulate altitude conditions of aeronautic motors operation;
- to suggest a corona resistance criteria basing on endurance tests results: *e.g.*, maximal time to breakdown or without breakdown, or number of ageing cycles;
- to develop a mathematical model of insulation life time considering high dV/dt and high switching frequency as well as electro-thermal and electro-chemical ageing processes in turn insulation in presence of dielectric barrier discharges;
- regarding the obtained experimental results under high frequency impulse voltage, to propose new nanostructured corona-resistant enamels with higher thermal index that may improve wires temperature stability and extend the winding life time;
- to enlarge the performed study of dielectric barrier discharges in turn insulation determining a balance of discharges power evaluating the power for heating and UV radiation, the power needed to ionization processes and ozone generation, as well as dielectric losses;

- to examine the effect of relative permittivity and wires' capacitance on barrier discharges inception;
- to improve the dielectric barrier model of twisted pair considering a dynamic capacitance changing in presence of discharges as well as variable resistance characterizing the air ionization.

Appendices

Appendices

Contents

Appendix III-A. Wires characteristics	IV
Appendix III-B. RC-divider characteristics	V
Appendix IV-A. Endurance tests results under sinusoidal voltage	VI
Appendix IV-B. Endurance tests results under PWM impulse voltage with low dV/dt	VIII
Appendix IV-C. Endurance tests results under PWM impulse voltage with low dV/dt: effect of defects “healing” by the impregnation	XI
Appendix IV-D. Endurance tests results under rectangular impulse voltage with high dV/dt	XII
Appendix IV-E. Thermal imaging of specimens subjected to PDs under dif- ferent voltage waveform parameters	XVI
Appendix V-A. LCR meter E7-13	XVII
Appendix V-B. Current shunt and RC-divider	XVIII

Appendix III-A. Wires characteristics

The characteristics of enameled wires given in Table 1 are issued from data sheets available in products catalogues of cables manufacturers and suppliers.

Table 1: Tested wires characteristics.

	PETD2K-180	PETD-180	APX 1	APX 2
Corona resistant	yes	no	no	no
Section	round	round	round	rectangular
Core's material	Cu	Cu	Cu	Cu
Insulation composition	tris(hydroxyethyl)cyanuric varnish comprising nanoparticles of silicon + polyamide-imide (PAI)	polyesterimide (PEI) + polyamide-imide (PAI)	modified polyurethane (PU) + polyamide (PA)	Tris(2-Hydroxyethyl) Isocyanurate (THEIC) modified polyesterimide (PEI) + polyamide-imide (PAI)
Insulation grade	2	2	2	2
Thermal class	180(H)	180(H)	180(H)	200(H)
Breakdown voltage	4.5 kV	4.7 kV	170 - 180 V/ μ m	40 V/ μ m
Application	inverter-driven electrical machines, apparatus and appliances	electrical machines, apparatus and appliances	relay, motors, transformers	electrical machines, transformers

Appendix III-B. RC-divider characteristics

The RC-divider used for voltage measuring in the high dV/dt test bench is commercially available probe designed to measure and control parameters in high voltage electrophysical and technological installations. Its technical characteristics are given in Table 2; the photographs are shown in Figure 1.

Table 2: Tested wires characteristics.

Parameters	Values
Reference	ДНВ-25 (Russia)
Measuring voltage	DC, AC and impulse voltage
Operating voltage	25 kV
Input resistance	100 MΩ
Input capacitance	≈ 3 pF
Division ratio	3000:1
Bandwidth	35 MHz
Test voltage:	
• DC voltage	30 kV
• impulse voltage	40 kV
Measurement accuracy	3 %
Coaxial cable length	3 m

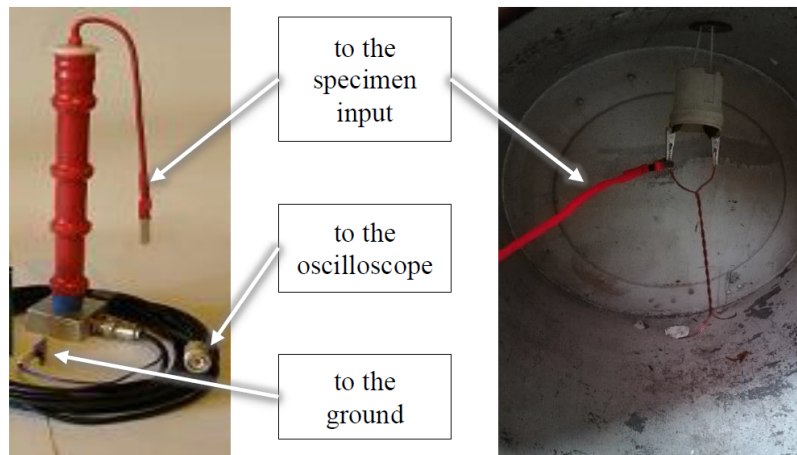


Figure 1: RC-divider general view.

Appendix IV-A. Endurance tests results under sinusoidal voltage

Table 3: Time to breakdown of bent wires specimens in “wire-shot” electrode system under sinusoidal voltage.

Winding wires	Test conditions			Time to breakdown, s										μ	σ
	f , Hz	V , kV	T , °C	t_1	t_2	t_3	t_4	t_5	t_6	t_7	t_8	t_9	t_{10}		
<i>PETD2K-180</i>		4		2 568	4 327	6 214	2 189	9 100	5 218	3 643	2 128	2 579	2 312	4 027.80	2 268.76
	50	4.5	180	3 643	1 107	1 768	1 542	2 352	1 117	993	2 128	2 351	3 110	2 011.10	884.97
		5		1 365	567	723	1 981	1 671	937	1 641	3 103	787	1 082	1 385.70	760.99
<i>PETD-180</i>		4		3 553	6 264	4 921	5 740	2 682	3 992	2 867	4 865	2 337	2 648	3 986.90	1 396.91
	50	4.5	180	496	2 487	2 684	648	3 348	2 149	2 212	2 253	1 696	2 985	2 095.80	925.81
		5		252	1 642	1 822	615	2 125	2 207	512	638	721	1 350	1 188.40	725.15

Table 4: Time to breakdown of twisted pairs and coils under sinusoidal voltage.

Winding wires	Test conditions			Time to breakdown, s										
	f , Hz	V , kV	T , °C	t_1	t_2	t_3	t_4	t_5	μ	σ				
<i>PETD-180</i>	50	5	25	6 459	7 261	7 934	10 302	9 252	8 241.60	1 541.10				
			180	3 874	4 191	4 789	5 909	6 989	5 150.40	1 288.04				
<i>APX-1</i>	50	5	25	2 606	3 028	3 295	4 718	8 294	4 388.20	2 323.01				
			180	1 772	991	1 484	1 368	1 695	1 462.00	308.85				
<i>APX-2</i> (coils)	50	5	25	54 735	86 920	49 858	69 434	63 258	64 841.00	14 471.57				
			180	3 139	3 576	2 221	2 260	3 531	2 945.40	665.69				

Appendix IV-B. Endurance tests results under PWM impulse voltage with low dV/dt

Table 5: Time to breakdown of twisted pairs and coils under PWM impulse voltage with surges.

Winding wires	Test conditions						Time to breakdown, s						
	f_m , Hz	f_s , Hz	V_a , kV	V_{os} , V	dV/dt , kV/ μ s	T , °C	t_1	t_2	t_3	t_4	t_5	μ	σ
<i>PEIT2-K-180</i>	400					25	167 543	207 220	209 040	-	-	194 601.00	23 450.58
		5	1.2	900	0.40	180	10 645	12 124	12 427	12 802	12 845	12 168.60	901.23
						190	4 421	5 287	5 517	5 657	5 748	5 326.00	534.95
						200	2 812	3 454	3 608	3 620	3 713	3 441.40	363.91
<i>PEIT-180</i>						25	11 400	11 460	11 580	11 820	13 560	11 964.00	906.58
						100	1 763	1 910	2 445	2 505	2 638	2 252.20	389.34
		5	1.2	900	0.40	180	1 618	1 735	1 805	1 865	1 962	1 797.00	130.19
						190	1 405	1 740	1 857	1 711	1 922	1 727.00	199.40
<i>APX-1</i>						200	1 419	1 599	1 618	1 690	1 704	1 606.00	113.82
						25	1 840	2 045	2 212	2 330	2 387	2 162.80	222.89
		5	1.2	900	0.40	100	1 245	1 393	1 490	1 542	1 629	1 459.80	147.39
						180	789	827	915	953	1 024	901.60	94.93
<i>APX-2</i> (coils)						25	8 913	14 865	16 039	16 866	22 521	15 840.80	4 864.72
		5	1.2	900	0.40	180	1 383	1 431	1 752	1 933	1 278	1 555.40	275.40

Table 6: Time to breakdown of twisted pairs under PWM impulse voltage with surges and when surges are limited.

Winding wires	Test conditions					Time to breakdown, s							
	f_m , Hz	f_c , Hz	V_a , kV	V_{os} , V	dV/dt , kV/ μ s	T , °C	t_1	t_2	t_3	t_4	t_5	μ	σ
PETD-180	400	5	1.2	900	0.40	180	1 618	1 735	1 805	1 865	1 962	1 797.00	130.19
				300	0.18		1 784	1 950	2 032	2 523	2 589	2 175.60	359.32
APX-1	400	5	1.2	900	0.40	180	789	827	915	953	1 024	901.60	94.93
				300	0.18		987	1 235	1 261	1 524	1 653	1 332.00	261.43

Table 7: Time to breakdown of two types' coils made of rectangular wire under PWM impulse voltage with surges.

Winding wire	Test conditions					Time to breakdown, s							
	f_m , Hz	f_c , Hz	V_a , kV	V_{os} , V	dV/dt , kV/ μ s	T , °C	t_1	t_2	t_3	t_4	t_5	μ	σ
APX-2 (coils)	400	5	1.2	900	0.40	180	1 383	1 431	1 752	1 933	1 278	1 555.40	275.40
APX-2 (double coils)							3 011	3 059	3 190	3 205	3 294	3 151.80	115.05

Appendix IV-C. Endurance tests results under PWM impulse voltage with low dV/dt : effect of defects “healing” by the impregnation

Table 8: Time to breakdown of twisted pairs under PWM impulse voltage with surges ($V_{os} = 900$ V).

Winding wires	Defect	Impregnating varnish	Time to breakdown, s										μ	σ	
			t_1	t_2	t_3	t_4	t_5	t_6	t_7	t_8	t_9	t_{10}			
PETD2-K-180	no defect	no impregnation	10 645	12 124	12 427	12 802	12 845	10 645	10 645	12 184	8 880	10 800	10 873	11 422.50	1 263.61
	ring	no impregnation	2 725	1 852	2 210	2 413	2 390	1 761	2 371	2 569	2 700	3 405	2 439.60	467.19	
	ring	KO-916K	3 270	3 412	4 230	2 793	2 700	1 105	1 234	1 979	2 060	2 504	2 528.70	974.62	
	ring	KP-55-5	5 949	5 323	6 345	6 872	6 014	4 721	5 987	4 796	6 013	6 559	5 857.90	710.00	
	ring	KP-50	9 888	10 229	10 663	10 783	12 261	7 391	7 897	9 494	11 013	11 954	10 157.30	1 574.52	

Table 9: Time to breakdown of twisted pairs made of PETD2-K-180 under rectangular impulse voltage with high dV/dt .

Winding wire	Test conditions					Time to breakdown, s						
	f_s , kHz	V_{dc} , kV	V_{os} , V	dV/dt , kV/ μ s	T , °C	t_1	t_2	t_3	t_4	t_5	μ	σ
PETD2-K-180	20	1.4	500	60	25	862	477	521	519	476	571.00	164.12
	20	1.0	500	60	180	6 910	7 779	8 760	7 805	7 827	7 816.20	654.52
		3 948				3 555	3 892	3 180	4 810	3 877.00	605.24	
		120				103	71	72	68	86.80	23.38	
	50	1.0	500	60	25	627	628	841	528	746	674.00	121.15
		418				308	495	214	298	346.60	110.18	
44		34				31	29	30	33.60	6.11		

Table 10: Time to breakdown of twisted pairs made of PETD-180 under rectangular impulse voltage with high dV/dt .

Winding wire	Test conditions					Time to breakdown, s						
	f_s , kHz	V_{dc} , kV	V_{os} , V	dV/dt , kV/ μ s	T , °C	t_1	t_2	t_3	t_4	t_5	μ	σ
PETD-180	20	1.0	500	60	25	563	596	605	641	642	609.40	33.22
		1.2				319	306	310	329	408	334.40	42.09
		1.4				239	223	240	241	186	225.80	23.45
	20	1.2	500	60	100	193	215	235	217	217	215.40	14.93
		1.0				360	251	272	263	249	279.00	46.23
		1.2				213	248	237	290	191	235.80	37.47
50	1.4	500	60	25	82	131	75	128	89	101.00	26.50	
	1.0				146	124	144	156	124	138.80	14.25	
	1.2				118	117	116	101	109	112.20	7.19	
		1.4				38	32	33	38	37	35.60	2.88

Table 11: Time to breakdown of twisted pairs made of APX-1 under rectangular impulse voltage with high dV/dt .

Winding wire	Test conditions					Time to breakdown, s						
	f_s , kHz	V_{acs} , kV	V_{os} , V	dV/dt , kV/ μ s	T , °C	t_1	t_2	t_3	t_4	t_5	μ	σ
APX-1	20	1.0	500	60	25	396	338	315	313	346	341.60	33.61
		1.2				85	105	94	103	92	95.80	8.23
		1.4				46	47	47	44	44	45.60	1.52
	20	1.2	500	60	100	39	34	31	30	39	34.60	4.28
		1.0				39	33	38	37	35	36.40	2.41
		1.2				14	14	13	14	15	14.00	0.71
	50	1.4	500	60	25	6	8	7	8	7	7.20	0.84
		1.0				58	39	40	38	35	42.00	9.14
		1.2				18	16	17	17	18	17.20	0.84
			1.4				12	12	12	12	12.20	0.45

Table 12: Time to breakdown of coils made of APX-2 under rectangular impulse voltage with high dV/dt .

Winding wire	Test conditions				Time to breakdown, s							
	f_s , kHz	V_{dc} , kV	V_{os} , V	dV/dt , kV/ μ s	T , °C	t_1	t_2	t_3	t_4	t_5	μ	σ
APX-2	20	1.0	500	60	25	6158	6327	5590	5671	6381	6025.40	370.87
		1.2				1000	686	592	967	1028	854.60	200.77
		1.4				491	331	393	335	471	404.20	74.61
	20	1.2	500	60	100	713	887	823	625	735	756.60	101.36
		1.0				1628	1363	1536	1510	1874	1582.20	188.84
						1.2	1142	1267	1340	1102	1117	1193.60
	50	1.4	500	60	25	298	296	313	363	348	323.60	30.32
		1.0				592	595	1147	824	757	783.00	227.31
		1.2				440	503	470	373	532	463.60	61.31
		1.4				140	165	128	124	148	141.00	16.46

Appendix IV-E. Thermal imaging of specimens subjected to PDs under different voltage waveform parameters

Table 13: Temperature measurements results.

Test conditions			Temperature, °C							
Voltage waveform	V , kV	f , kHz	T_0	T_1	T_2	T_3	T_4	T_5	μ	σ
<i>Twisted pairs (PETD2-K-180)</i>										
Sinusoidal voltage	3.0	0.05	22.00	24.2	24.3	24.6	24.9	25.3	24.66	0.45
	5.0			25.3	25.8	25.8	26.0	26.3	25.84	0.36
Low dV/dt impulse voltage	1.2	5.00	22.50	33.2	32.7	32.9	33.4	33.5	33.14	0.34
High dV/dt impulse voltage	1.00	20.0	24.0	27.3	27.8	28.3	39.1	40.2	32.54	6.51
	1.20			54.1	54.1	54.7	58.6	61.1	56.52	3.18
	1.40			83.2	84.1	84.5	86.4	87.9	85.22	1.90
	1.00	50.00		79.4	80.6	83.0	85.7	91.3	84.00	4.74
	1.20			145.0	145.0	147.0	148.0	150.0	147.00	2.12
	1.40			144.0	146.0	150.0	150.0	150.0	148.00	2.83
<i>Coils (APX-2)</i>										
Sinusoidal voltage	3.0	0.05	22.00	24.6	25.1	25.2	26.0	26.3	25.44	0.69
	5.0			28.0	30.0	30.0	30.1	30.2	29.66	0.93
Low dV/dt impulse voltage	1.2	5.00	22.50	75.6	76.1	76.8	78.6	79.8	77.38	1.77
High dV/dt impulse voltage	1.00	20.0	24.0	37.1	39.0	40.0	41.4	41.9	39.88	1.93
	1.20			116.0	118.0	119.0	120.0	124.0	119.40	2.97
	1.40			185.0	186.0	189.0	191.0	191.0	188.40	2.79
	1.00	50.00		73.5	75.3	76.2	76.3	78.4	75.94	1.78
	1.20			245.0	247.0	250.0	251.0	251.0	248.80	2.68
	1.40			303.0	310.0	318.0	326.0	334.0	318.20	12.34

In table 13, V corresponds to the RMS value at sinusoidal voltage and steady-state amplitude at impulse voltage; f is the sinusoidal voltage frequency, the carrier frequency at low dV/dt impulse voltage and the switching frequency at high dV/dt impulse voltage; T_0 is the ambient temperature.

Appendix V-A. LCR meter E7-13

LCR meter E7-13 is intended to measure capacitance, inductance and resistance of the alternating current, as well as the parameters of the complex impedance of capacitive and inductive nature in a wide range of measurement of phase angle.



Figure 2: LCR meter E7-13.

Technical characteristics:

- Capacity – from 0.1 pF to 10 μ F;
- Inductance - from 1 μ H to 100 H;
- Conductance - from 10 nS to 100 mS;
- Active resistance - from 0.01 Ω to 1 M Ω ;
- Test frequency – 1 kHz.

Appendix V-B. Current shunt and RC-divider

Current shunt

The current shunt having equivalent resistance $R_{sh} = 1.03 \Omega$ is made with low inductive ceramic encased resistors placed on round copper plate as shown in Figure 3 and Figure 4.

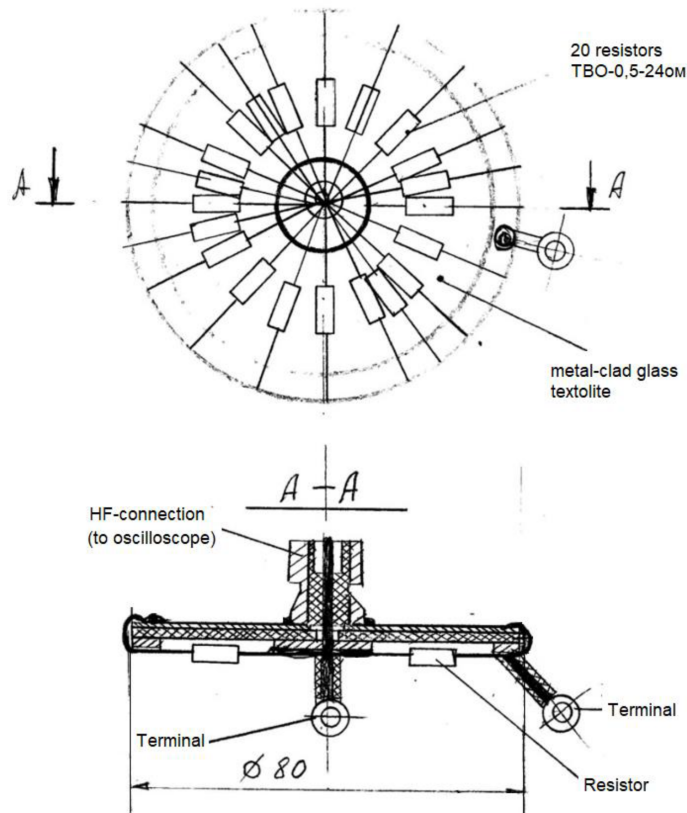


Figure 3: Sketch of current shunt.



Figure 4: Photograph of current shunt.

The shunt is connected to the oscilloscope via a RF coaxial cable $50\ \Omega$ with impedance matching resistors $R_1 = 50 - R_{sh} = 49\ \Omega$ and $R_2 = 50\ \Omega$. It is necessary to match the coaxial cable and the shunt impedances in order to damp oscillations and reflected waves due to steep edge pulses. The matching resistor R_1 connected in series with the central core of coaxial cable and the resistor R_2 at the end of the cable connected to the cable shield, form an active voltage divider for the signal of the shunt. Since the resistors are almost identical, the divisor coefficient is 2:1.

Before starting partial discharges measurements, the shunt characteristics were tested. Firstly, the shunt resistance was measured using the DC Milli-Ohm Meter Instek GOM – 802. The resistance measured on shunt terminals is equal to $1.03\ \Omega$. Then, this shunt was compared with a reference resistor (low inductive resistor $R_{ref} = 0.86\ \Omega$) under pulse voltage. The measured amplitude and edges were compared. The standard pulse generator produced impulse peak-to-peak voltage of $10\ \text{V}$, $50\ \text{kHz}$ and $10\ \mu\text{s}$ pulse duration. The scheme of the calibration test bench and scopes are provided in and respectively.

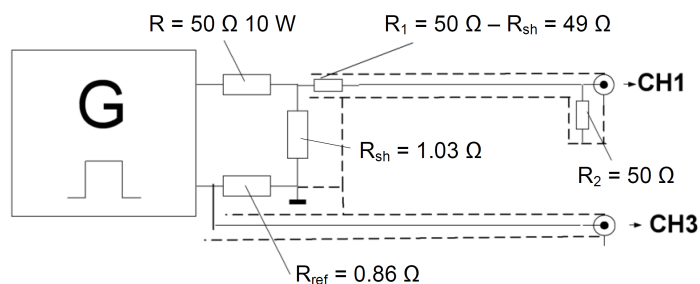


Figure 5: Scheme of shunt calibration test bench.

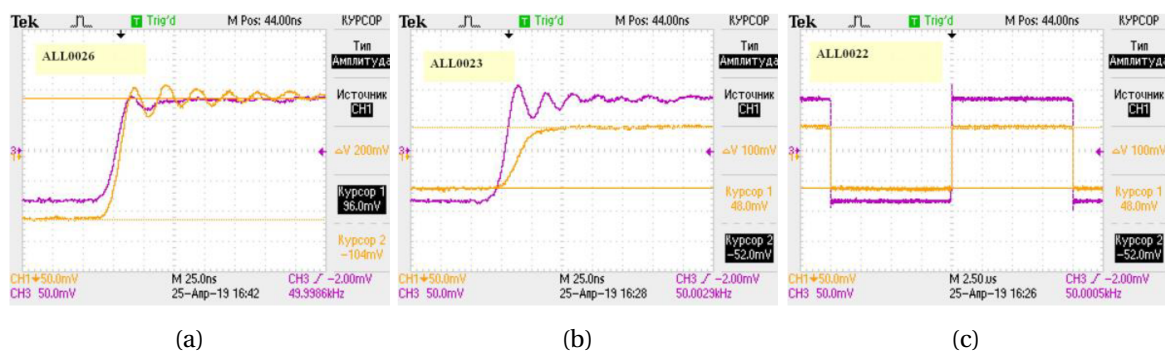


Figure 6: Calibration test scopes CH1 – current shunt, CH3 reference resistor:

- (a) measurement without matching resistors R_1 and R_2 ,
- (b) and (c) measurement with matching resistors R_1 and R_2 at different time-base.

RC-divider

The RC-divider has been designed with the purpose to measure high dV/dt impulse voltage produced by the SiC-based generator as the differential probe Tektronix THDP0100 was not always available. The RC-divider can be used to measure the impulse voltage on one of the inverter's legs and the use of two identical dividers allows to conduct differential measurements.

The construction of the RC-divider is shown in Figure 7 and Figure 8. In the scheme: $C_1 = 1$ pF is a vacuum capacitor in upper arm of the divider, $R_1 = 4 \Omega$ is a damping low-inductive resistor, $C_2 = 56$ pF is a ceramic capacitor, $C_3 = 5 \div 25$ pF is an adjustable capacitor, $R_2 = 0 \div 100 \Omega$ is an adjustable matching resistor, $R_2 = \rho - R_1$, where ρ is equal to the coaxial cable impedance, U_1 is an input signal, and U_2 is an output signal of the RC-divider. The terminal of upper divider's arm is connected directly to the tested specimen, and the terminal of the lower arm is connected to the oscilloscope via the coaxial cable.

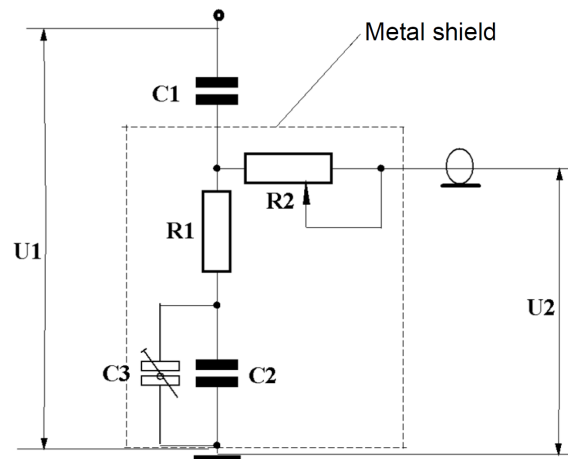


Figure 7: RC-divider scheme.

The ratios of two RC-dividers were determined experimentally at the same time with calibration and adjusting of variable capacitors and resistors. The output voltage U_2 was compared with the reference signal of the standard pulse generator. For this purpose, the RC-divider is connected to the standard pulse generator and the oscilloscope via the same cables and connectors which are utilized for measurements on twisted pairs. The impulse voltage of 50 kHz and 10 μ s pulse duration is applied at the RC-divider input and at the oscilloscope channel CH1. The output signal of RC-divider is displayed on the oscilloscope channel CH2. Divider ratios are estimated by $k = \frac{U_g}{U_{g2}}$, where U_g is the voltage of the standard pulse generator. The maximum k_{max} , minimum k_{min} , and operational k_{op} ratios of two RC-dividers are estimated and provided in Table 14 and Table 15. Figure 9 shows examples of scopes recorded during the dividers calibration.

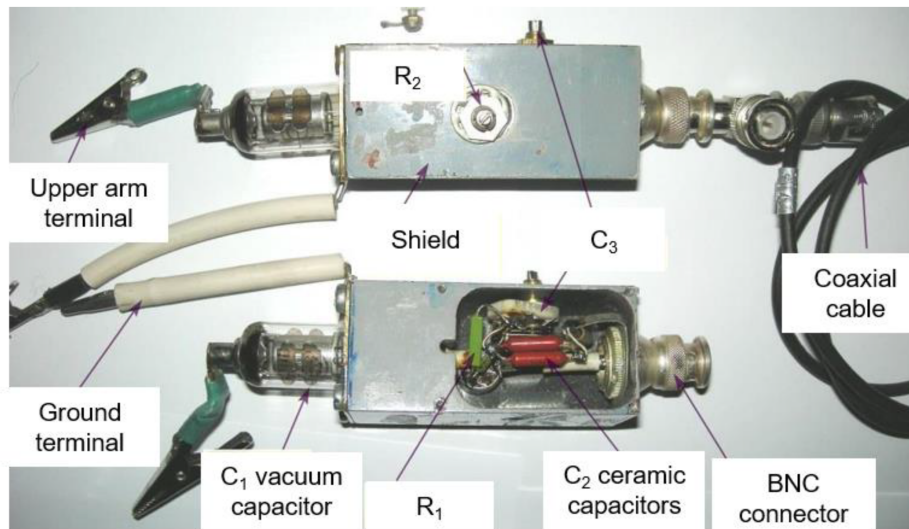


Figure 8: Photograph of two identical RC-dividers.

Table 14: Parameters of RC-divider #1.

$U_g, V(CH1)$	18.6	18.6	18.6
$U_2, mV(CH2)$	60.8	65.6	63.2
k_1	$k_{1max} = 306$	$k_{1min} = 283$	$k_{1op} = 294$

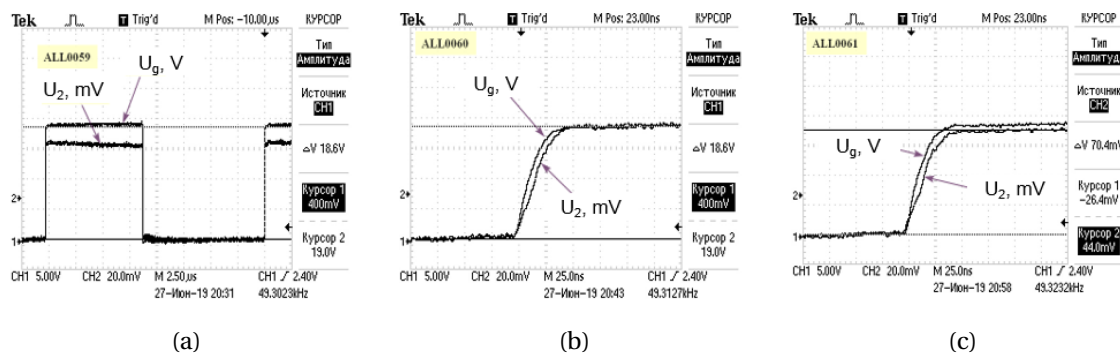


Figure 9: Scopes of calibration and dividers ratios estimation:

(a) and (b) correspond to the RC-divider #1, and (c) corresponds to the RC-divider #2.

Table 15: Parameters of RC-divider #2.

$U_g, V(CH1)$	18.6	18.6	18.6
$U_2, mV(CH2)$	68.8	71.2	70.4
k_1	$k_{1max} = 270$	$k_{1min} = 261$	$k_{1op} = 264$

List of Figures

I.1 Typical motor drive system with a long supply cable	12
I.2 Traction and charging power trains on-board of Renault's electric vehicle: ZOË	13
I.3 Michelin Active Wheel System	13
I.4 SiC Application areas presented in AgileSwitch SiC Product Overview	14
I.5 Si and SiC inverters comparison	15
I.6 Chart of possible motor choices for HEVs and EVs	16
I.7 Machine options for the MEA drive system	16
I.8 Performance comparison of motor technologies	17
I.9 Construction of an induction motor (dissected view)	18
I.10 Magnetic circuit of induction motor's stator and rotor	18
I.11 Three-phase SR Drive® stator and rotor (graphic of NIDEC Motors)	19
I.12 Three-phase SRM driven by asymmetric half-bridge converter	20
I.13 Conventional excitation and bipolar overlapping excitation	20
I.14 Section of stator winding	21
I.15 Distributed stator winding	21
I.16 Distributed and concentrated winding configurations	22
I.17 Concentrated winding configuration of a Hyundai Sonata 2011 motor	23
I.18 Difference between rectangular and round conductors placed in stator slot	23
I.19 Enamelled wire with double layer insulation	24
I.20 Scanning electron microscopy image of enamelled wire, chemical composition PAI and PEI	25
I.21 Turn insulation microstructures microscopy images	28
I.22 Crack propagation mechanism in turn insulation	28
I.23 Crack propagation in turn insulation microscopy images	29
I.24 Main factors affecting winding insulation during electrical machines manufacturing and operational processes	30
I.25 Expected insulation life vs. operating temperature for different thermal classes	31
I.26 Insulation damage caused by inter-turn short circuit of the stator windings in three-phase induction motors	32

I.27 Principle of induction motor adjustable speed drive with its schematic voltage characteristic	33
I.28 Voltage impulse waveform parameters	33
I.29 Different definitions of impulse rise time	34
I.30 Inverter fed motor pu overvoltage vs. cable length and impulse voltage risetime	34
I.31 Phase-to-phase voltage waveforms during motor operation at the motor input with a 30 m, 25 m and 15 m length connecting cable	35
I.32 Electrical discharges in stator windings	36
I.33 Microscopy images of turn insulation aged by PDs	37
I.34 Five step phase to phase voltage at the terminals of a machine fed by a 3-level converter	38
I.35 Electrical breakdown path through inorganic filler spherical particles	39
II.1 HF equivalent circuit of a random wound coil	59
II.2 Single-phase HF equivalent circuits	60
II.3 Induction motor HF model	61
II.4 HF model approach based on impedance measurements	61
II.5 Induction motor HF model	62
II.6 Measured and simulated voltage waveforms at the motor terminals for 70-m cable	62
II.7 Overvoltage evolution as function of the inverter's rise time for different cable lengths	63
II.8 High frequency per phase equivalent circuits	65
II.9 Studied switched reluctance motor: front-view and setup for impedance measurement	65
II.10 Common mode impedance measurement: per phase circuit connections and winding coils connections	66
II.11 Differential mode impedance measurement: per phase circuit connections and winding coils connections	66
II.12 Measured CM impedance of SRM	67
II.13 Measured DM impedance of SRM	68
II.14 Simplified HF per phase circuit motor model basing on [9]	71
II.15 Comparison of measured and simulated by simplified HF model motor impedances	71
II.16 Extended HF per phase circuit motor model basing on [11]	72
II.17 Comparison of measured and simulated by extended HF model motor impedances	72
II.18 Two-wire shielded cable: cable's structure and HF equivalent circuit model basing on [12]	75
II.19 Voltage waveforms for pulse generator voltage rise time $t_R = 30$ ns (10 kV/ μ s) and cable length $L = 1$ m simulated with two proposed motor models	77

II.20 Voltage waveforms for different pulse generator voltage rise times simulated with the extended motor model	78
II.21 Voltage waveforms at the motor terminals for pulse generator voltage rise time $t_R = 30$ ns and different cable lengths: $L = 5$ m and $L = 10$ m	78
III.1 Examples of motorette test setup configurations	91
III.2 Samples for hairpin motors insulation qualification tests	91
III.3 Device for twisting the specimen for breakdown voltage test	92
III.4 Two crossed enamelled wires creating one-point contact specimen	92
III.5 Geometry of winding wire	95
III.6 Bent wire specimen for breakdown voltage tests	96
III.7 Twisted pair specimen	97
III.8 Coupled bar specimen	97
III.9 Coil specimen	98
III.10 Sketch and photograph of the specimen placed in “wire – shot” test	99
III.11 Voltage on specimens while insulation endurance testing	101
III.12 Experimental setup for sinusoidal voltage tests	102
III.13 Simplified electric scheme and voltage waveform measured on the tested specimen	103
III.14 Scheme of the low dV/dt pulse generator: Si IGBT inverter	104
III.15 Sketch of the low dV/dt experimental bench	104
III.16 Low dV/dt experimental bench photographs	105
III.17 Bipolar impulse voltage waveform parameters	106
III.18 Electrical scheme of the high-frequency RC-divider 1000:1	106
III.19 Low dV/dt PWM impulse voltage scopes.	107
III.20 Enlarged plot showing impulse voltage parameters	107
III.21 Voltage measured at the pulse generator output without specimen and voltage measured on the tested specimen	108
III.22 General view of the high dV/dt experimental bench and SiC inverter	109
III.23 Scheme of pulse generator for high dV/dt tests: SiC half-bridge inverter	110
III.24 High dV/dt impulse voltage scopes: half-bridge inverter topology.	111
III.25 Scheme of experimental setup for high dV/dt tests: SiC full bridge inverter	112
III.26 General view of the high dV/dt experimental bench, SiC inverter and tested specimen installation	114
III.27 High dV/dt impulse voltage scopes	115
III.28 Voltage measured at the pulse generator output without specimen and voltage measured on the tested specimen	116
III.29 Electron-optical defectoscope Filin-7	117

III.30 “Wire-shot” test under sinusoidal voltage: specimen’s photograph and PDs optical image	117
III.31 Test under low dV/dt PWM impulse voltage: twisted pairs’ installation, PDs photograph and PDs optical image	118
III.32 Test under low dV/dt PWM impulse voltage	118
III.33 Test under high dV/dt impulse voltage	118
III.34 Photograph of antenna detecting PD on the coil tested under high dV/dt impulse voltage	119
III.35 Voltage waveforms measured at high dV/dt test bench	120
III.36 Voltage waveforms measured at high dV/dt test bench above the PDIV . . .	121
III.37 Experimental setup for ozone detection	122
III.38 Photographs of chemical reactions resulting from PDs on tested specimen	122
III.39 Photographs of chemical reactions of iodine and starch solution	123
IV.1 Photograph of a broken specimen made of APX-1 (CV)	138
IV.2 Comparison among different PDF plots of breakdown voltage data	140
IV.3 Histogram of mean breakdown voltages issued from tests and breakdown voltage given in wires’ specifications	141
IV.4 Time to breakdown of bent wires specimens tested in “wire-shot” electrode system	143
IV.5 Comparison among different probability distribution plots of time to break- down data of PETD2-K-180 and PETD-180	144
IV.6 Time to breakdown of twisted pairs and coils under sinusoidal voltage: tem- perature effect	146
IV.7 Photograph of the coil specimen after being tested	147
IV.8 Time to breakdown of two specimens’ types made of PETD-180	148
IV.9 PWM impulse voltage waveform	150
IV.10 Time to breakdown of twisted pairs and coils under PWM impulse voltage .	151
IV.11 Time to breakdown of twisted pairs under PWM impulse voltage	152
IV.12 Time to breakdown of two specimens’ types made of rectangular wire APX-2 under PWM impulse voltage with surges	153
IV.13 Views of specimens made of corona resistant wire PETD2-K-180 and con- ventional wire APX-2 after being tested under PWM impulse voltage with surges	154
IV.14 Possible defects in turn insulation system	155
IV.15 Twisted pair having a ring defect on the one turn	156
IV.16 Time to breakdown of twisted pairs made of CR wire tested under PWM impulse voltage with surges	157
IV.17 Views of twisted pairs’ insulation breakdown in defective area	158

IV.18 Model of turn insulation destruction mechanism in presence of partial discharges	158
IV.19 Rectangular impulse voltage waveform having high dV/dt	159
IV.20 Time to breakdown of twisted pairs and coils under impulse voltage with high dV/dt	161
IV.21 Time to breakdown of twisted pairs made of PETD2-K-180 under impulse voltage with high dV/dt	163
IV.22 Time to breakdown of twisted pairs made of PETD-180 under impulse voltage with high dV/dt	163
IV.23 Time to breakdown of twisted pairs made of APX-1 under impulse voltage with high dV/dt	164
IV.24 Time to breakdown of coils made of APX-2 under impulse voltage with high dV/dt	164
IV.25 Winding wires' photograph and microscopic images after testing under high dV/dt impulse voltage	166
IV.26 Winding wires' microscopic images after testing under high dV/dt impulse voltage	166
IV.27 Microscopic images of rectangular winding wire after testing under high dV/dt impulse voltage	166
IV.28 Photographs and thermal images of twisted pair and coil tested under PWM-like low dV/dt impulse voltage	167
IV.29 Photographs and thermal images of twisted pair and coil tested under high dV/dt impulse voltage	168
IV.30 Temperature of twisted pairs and coils tested under different voltage waveforms	168
V.1 Inverter's voltage waveforms measured at different contact points	180
V.2 Scheme of experimental setup presented measurement points	181
V.3 Test setup modelled by an equivalent circuit	181
V.4 Coaxial strictures corresponding to enamelled wires and cables configurations	182
V.5 Variation of effective relative permittivity with distance between two cables .	184
V.6 Inverter's voltage waveforms measured at contacts in the thermal chamber (twisted pair connected) and simulated by equivalent RLC-circuit using LT-Spice	185
V.7 Simulated voltage waveforms for different pulse rise times, $l = 1$ m	186
V.8 Simulated voltage waveforms for two cable lengths, $t_R = 27$ ns ns	187
V.9 Equivalent circuit when studying partial discharges in solid dielectric	188
V.10 Twisted pair structure and corresponded equivalent circuit when studying partial discharges in twisted pair	189

V.11 Twisted pair covered by conducting liquid metal paste	190
V.12 Voltage in the equivalent circuit	190
V.13 Equivalent circuits of twisted pair indicating the currents	192
V.14 Equivalent circuits of twisted pair for current-voltage characteristics	193
V.15 Current-voltage characteristic of twisted pair	193
V.16 Sketch of the test setup for current measurements	194
V.17 Voltage waveforms measured on the twisted pair by high-voltage differential probe	195
V.18 Photograph of used measurement means	195
V.19 The scheme of current and voltage measurements on the twisted pair subjected to PD	196
V.20 Current pulse waveforms measured on the metallized twisted pair tested under impulse voltage	196
V.21 Current pulse waveforms measured on the twisted pair tested under impulse voltage	197
V.22 Current-voltage characteristic of twisted pair	198
V.23 Experimental setup sketch for barrier discharges study	199
V.24 Current pulses at rising and falling voltage rates $V_{dc} = 1000$ V and $f = 50$ kHz .	200
V.25 Current peak values at different voltage levels and switching frequencies . .	201
V.26 Temperature measurement results at different impulse voltage amplitudes and switching frequencies	201
V.27 Emission spectrum of barrier discharges in twisted pair at $V_{dc} = 1400$ V and $f = 50$ kHz	202
V.28 Peak values of emission spectra at 336.51 nm of wavelength at different voltage levels and switching frequencies	203
V.29 Microscopic images of twisted pair turns tested	203
V.30 Microscopic images of twisted pair turns tested under impulse voltage . . .	204
V.31 Microscopic images of insulation surface with filaments track erosion	204
V.32 Microscopic image of twisted pair cross-section	205
V.33 Geometry of twisted pair turns in electrostatic calculations	206
V.34 Electric field between twisted pairs turns at 1400 V excitation voltage	206
V.35 Electrical intensity distribution in air along the line 1-2 when $d_{gap} = 0$	206
V.36 Electrical intensity distribution in air along the line 1-2 when $d_{gap} = 0.003$ mm	207
V.37 Sketch of the proposed synthetic experimental setup	208
V.38 Photographs of the synthetic experimental setup realisation	209
V.39 Partial discharges on twisted pair tested under low pressure	209
V.40 Visualization of insulation defects in twisted pair tested under low pressure	210

List of Tables

II.1	Calculated parameters of switched reluctance motor HF model	70
II.2	Influence of model parameters on the CM and DM impedance magnitude curves	73
II.3	HF cable model parameters basing on [12]	76
III.1	The enamel insulation thickness measurement results for round section wires	95
III.2	The enamel insulation thickness measurement results for rectangular section wire.	96
III.3	Main components of high dV/dt experimental bench with pulse generator having H-bridge topology	113
III.4	Parameters of radio frequency cable PK 150-7-11	119
IV.1	Breakdown voltage under progressive voltage stress on winding wires	139
IV.2	Normal distribution parameters of breakdown voltage data	141
IV.3	Normal distribution parameters of breakdown voltage data	143
IV.4	Experimental protocol of endurance tests under PWM voltage with low dV/dt	149
IV.5	Experimental protocol of endurance tests under rectangular impulse voltage with high dV/dt	160
IV.6	Time to breakdown ratios of studied wires depending on test conditions . . .	165
V.1	Electrical and geometrical parameters of cable connections and tested winding wire	182
V.2	Calculated electrical parameters for electrical circuit simulations	184
V.3	Theoretical points of dielectric barriers' current-voltage characteristic	192
V.4	Theoretical points of twisted pair's current-voltage characteristic	192
V.5	Experimental points of dielectric barriers' current-voltage characteristic . . .	197
V.6	Experimental points of twisted pair's current-voltage characteristic	197

Université Paris-Saclay

Espace Technologique / Immeuble Discovery

Route de l'Orme aux Merisiers RD 128 / 91190 Saint-Aubin, France

Titre : Caractérisation des isolants de bobinage des machines électriques alimentées par des ondes de tension à forts dV/dt

Mots clés : semi-conducteurs grand gap, machines électriques, isolation entre spires, décharges partielles

Résumé : L'isolation des bobinages des moteurs alimentés par des convertisseurs statiques basés sur la modulation de largeur d'impulsion est soumise à des contraintes électriques provenant de la forme d'onde de la tension d'alimentation. Les phénomènes de nuisances électromagnétiques sur l'ensemble de la chaîne de conversion, les ondes réfléchies dans le câble d'alimentation, ainsi que la non-adaptation des impédances du câble et de l'enroulement de la machine peuvent conduire à l'apparition de surtensions aux bornes de la machine suffisamment élevées pour dépasser la tension d'apparition des décharges partielles. Il en résulte une dégradation de l'isolation entre les spires qui, à terme, peut engendrer la défaillance de la machine. La mise en œuvre de composants à semi-conducteurs grand gap, tel que le Carbure de Silicium, permet la réalisation de convertisseurs de forte densité de

puissance pour les systèmes d'entraînement à vitesse variable des machines électriques. Les vitesses et les fréquences de commutation élevées de ces composants conduisent à des contraintes électriques en dV/dt plus sévères sur l'isolation des enroulements des moteurs alimentés par de tels convertisseurs. L'étude expérimentale et les simulations numériques réalisées dans le cadre de cette thèse se concentrent essentiellement sur les effets des ondes de tension à forts dV/dt et de la fréquence de commutation élevée sur la robustesse de l'isolation du bobinage des machines électriques alimentées par des onduleurs. Par conséquent, les travaux touchent un certain nombre de questions liées à l'entraînement à vitesse variable, à l'électronique de puissance, aux machines électriques, aux matériaux diélectriques et aux décharges partielles.

Title : Characterization of winding insulation of electrical machines fed by voltage waves with high dV/dt

Keywords : wide-bandgap semiconductors, electrical machines, turn insulation, partial discharges

Abstract : The insulation of electrical machines driven by power converters with pulse width modulation are subjected to repetitive surges due to fast changing voltage pulses and reflection phenomena in supply cable, as well as non-uniform voltage distribution in the stator winding. The overvoltage at motor terminals may lead to partial discharge inception accelerating winding insulation degradation and causing its premature failure. The implementation of wide bandgap power semiconductors as Silicon Carbide allows to create converters with high power density for variable frequency drive applications. The fast and high frequency switching of electronic devices based on

wide bandgap semiconductors increase electrical stresses caused by steep voltage changing rates in controlled electrical machine. It may increase a risk of partial discharges and accelerate insulation aging and destruction. The experimental investigation and numerical simulation study performed in this work is essentially focused on the effects of impulse voltage with high dV/dt and high switching frequency on winding insulation robustness of inverter-fed electrical machines. Therefore, the work covers a number of issues related to electric drives, power electronics, electrical machines, dielectric materials and partial discharges.